

**Study of the medium produced in the d+Au  
collisions at 200 GeV using single electron  
observable by PHENIX detector at RHIC**



*Thesis submitted for the degree of*  
**DOCTOR OF PHILOSOPHY**

*in*

**PHYSICS**

*by*

**Sourav Tarafdar**

*Supervisor*

**Dr. Venktesh Singh**

*Nuclear Physics Section*

*Department of Physics*

*Banaras Hindu University*

*Varanasi-221005*

*India.*

Enrollment No. 275301



**DEPARTMENT OF PHYSICS  
BANARAS HINDU UNIVERSITY  
VARANASI-221005, INDIA**

**UNDERTAKING**

I, hereby declare that I have completed the research work for the full time period prescribed under the clause VIII.1 of the Ph.D. ordinances of the Banaras Hindu University, Varanasi and that the research work embodied in this thesis entitled **Study of the medium produced in the d+Au collisions at 200 GeV using single electron observable by PHENIX detector at RHIC** is my own work.

Date: \_\_\_\_\_ (Signature of the candidate)

Place: Varanasi **Sourav Tarafdar**

## CANDIDATE'S DECLARATION

I, **Sourav Tarafdar**, certify that the work embodies in this Ph.D. thesis is my own bonafide work carried out by me under the supervision of **Dr. Venktesh Singh** for a period of \_\_\_\_\_ from \_\_\_\_\_ to \_\_\_\_\_ at Banaras Hindu University. The matter embodies in this Ph.D. thesis has not been submitted for the award of any other degree/diploma.

I declare that I have faithfully acknowledged, given credit to and referred to the research workers wherever their works have been cited in the text and the body of the thesis. I further certify that I have not willfully lifted up some others work, para, text, data, results etc. reported in the journals, books, magazines, reports, dissertations, theses, etc., or available at web-sites and included them in this Ph.D. thesis and cited as my own work.

Date: \_\_\_\_\_ (Signature of the candidate)

Place: Varanasi **Sourav Tarafdar**  
(Name of the candidate)

---

### Certificate from the Supervisor

This is to certify that the above statement made by the candidate is correct to the best of my knowledge.

---

**Dr. Venktesh Singh**  
**Assistant Professor**

(Signature of the HOD/Coordinator of the School with seal)

## **PRE-SUBMISSION SEMINAR COMPLETION CERTIFICATE**

This is to certify that Sri. **Sourav Tarafdar**, a bonafide research scholar of this department, has satisfactorily completed the pre-submission seminar requirement which is a part of his Ph.D. programme, on his thesis entitled **Study of the medium produced in the d+Au collisions at 200 GeV using single electron observable by PHENIX detector at RHIC**.

(Signature of the Head of the Department)

Date:

*Place: Varanasi*

## **COPYRIGHT TRANSFER CERTIFICATE**

Title of the Thesis: **Study of the medium produced in the  $d+Au$  collisions at 200 GeV using single electron observable by PHENIX detector at RHIC.**

Candidate's Name : **Sourav Tarafdar**

### **COPYRIGHT TRANSFER**

The undersigned hereby assigns to the Banaras Hindu University all rights under copyright that may exist in and for the above thesis submitted for the award of the Ph.D. degree.

### **Signature of the candidate**

Note: However, the author may reproduce or authorize others to reproduce material extracted verbatim from the thesis or derivative of the thesis for author's personal use provided that the source and the University's copyright notice are indicated.

*To My Family*

## Acknowledgements

The long journey of attaining Ph.D. is not being covered by a individual person, rather it's a collective effort of many people during the journey to support the person. I would like to thank my supervisor Dr. Venktesh Singh for putting me on this track after seeing the desire in me to join the world of research and providing me all kinds of working facilities. I am grateful to my friends and group mates, Lakhwinder Singh, Prakhar Garg, Prashant Srivastava, Arun Prakash and Arun Kumar Soma for making this journey a pleasant one in Banaras Hindu University apart from having fruitful Physics discussion. I am grateful to our group leader Prof. C. P. Singh for his useful discussions with us related to the world of quarks and gluons.

The first time I became familiar with PHENIX computing facility was in Wiesmann Institute of Science by Prof. Itzhak Tserruya and Illia Ravinovich. I thank them and the other members of Wiesmann Institute of Science for showing me the first step of starting up analysis. I am greatly indebted to Prof. Yasuyuki Akiba (Akiba san) in the PHENIX collaboration for his informative suggestions and constant help in my analysis work without which probably this work would not have been possible. Besides that Akiba san showed me different ways of solving a same problem and also opened in front of me the various mysteries involved in analysis work. I am also grateful to Cesar Luiz da Silva and Matt Durham in the collaboration for their suggestions in the PHENIX analysis group meeting. Also my huge thanks to whole of the PHENIX collaboration for making my stay in the collaboration a wonderful and pleasant experience during this journey. Last but not the least I want to thank my parents for showing their faith in me through out this journey and encouraging me for doing better. Without their moral support and love for me it would not have been possible to stay on this course.

## Preface

The thesis is divided into five chapters. The **first** chapter is Introduction which gives theoretical background of High Energy Physics, Collider Physics and about different ways of measuring the properties of medium produced during heavy ion collisions. It also reflects the motivation for selecting d+Au collision. In Au+Au collision strong medium effect is observed which is absent in p+p collision. The question arises, what happens in d+Au collision in which the collision system are asymmetric and the size is in between Au+Au and p+p collision systems.

The **second** chapter is about RHIC and PHENIX experiment/detector giving the details of detector subsystems. As PHENIX detector is an agglomeration of several sophisticated detectors each meant for different purpose, so more emphasis is given on the set of detectors used in my analysis. In addition, the basic operation of RHIC has been discussed in this chapter.

The **third** chapter has details of the analysis work done concerning to the topic of this thesis. The important information that has to be extracted from raw data is the invariant yield of single electron from heavy flavor decay in  $d + Au$  collisions. The steps involved in extracting this information has been detailed in this chapter.

The final results has been discussed in **fourth** chapter. It shows, the nuclear modification factor of single electron from heavy flavor in  $d + Au$  collision at  $\sqrt{s_{NN}} = 200$  GeV. Further, it has been compared with a theoretical model calculation based on KKT model and the present analysis result matches qualitatively with the theoretical prediction. The result for nuclear modification factor in this thesis is important in terms of finding the cold nuclear matter effect in

$d + Au$  collision at  $\sqrt{s_{NN}} = 200$  GeV for heavy flavor. Further, I tried to give a simple model to entangle the cold nuclear matter effect in  $Au + Au$  collisions. The calculation of invariant cross section from the invariant yield of single electron heavy flavor has been shown here and compared with the number of  $d + Au$  binary collision scaled FONLL  $p + p$  results.

**Chapter 5** summarises the whole thesis along with future prospect of heavy flavor measurement in PHENIX at RHIC.

# Contents

<b>List of Figures</b>	<b>XXV</b>
<b>List of Tables</b>	<b>XXVI</b>
<b>1 Introduction and Motivation</b>	<b>1</b>
1.1 Heavy quark production and its role as a probe for matter produced at RHIC . . . . .	10
1.2 Measurement of Heavy Flavor cross sections using FONLL . . . . .	14
1.3 Methodology of heavy flavor measurements in PHENIX . . . . .	15
1.4 Brief overview of heavy flavor measurement by PHENIX central arm	17
<b>2 PHENIX experiment: A Brief Review</b>	<b>19</b>
2.1 Relativistic Heavy Ion Collider (RHIC) . . . . .	19
2.2 The PHENIX detector . . . . .	21
2.2.1 PHENIX coordinate system . . . . .	22
2.2.2 PHENIX Global detectors . . . . .	24
2.2.3 Central detectors . . . . .	29
2.2.4 Muon Arm Detectors . . . . .	45
<b>3 Data Analysis</b>	<b>46</b>

3.1	Data files . . . . .	47
3.2	Event selection . . . . .	47
3.3	Fiducial cuts . . . . .	48
3.4	Electron identification, track matching and track quality . . . . .	51
3.5	Quality Analysis (QA) of MB events . . . . .	54
3.6	Run Q/A of ERT trigger events . . . . .	56
3.7	Correction factors . . . . .	58
3.7.1	ERT trigger Efficiency . . . . .	58
3.7.2	Electron identification correction . . . . .	59
3.7.3	Acceptance Uncorrected Inclusive Electron Spectra . . . . .	63
3.7.4	Acceptance correction . . . . .	65
3.8	Cocktail Calculation . . . . .	73
3.8.1	Cocktail input . . . . .	76
3.8.2	Run8 d+Au electron cocktail . . . . .	81
3.9	Systematic Error on inclusive spectra of electrons . . . . .	81
3.9.1	High $p_T$ extension . . . . .	82
3.9.2	Acceptance X eID efficiency . . . . .	83
3.9.3	Geometrical Acceptance . . . . .	86
3.10	Cocktail Systematic Errors . . . . .	87
3.11	Converter Analysis; Extraction of photonic electrons . . . . .	88
3.11.1	Comparison of photonic electron invariant yield and cocktail photonic component . . . . .	103
3.11.2	Non-photonic single electron . . . . .	104
3.12	Systematic error on Converter analysis . . . . .	105
3.13	Analysis of electron spectrum . . . . .	108

3.13.1	Inclusive spectra . . . . .	108
3.13.2	Heavy Flavor spectra . . . . .	109
<b>4</b>	<b>Results and Discussions</b>	<b>115</b>
4.1	Heavy Flavor single electron . . . . .	116
4.1.1	Heavy Flavor single electron from cocktail subtraction method	116
4.1.2	Comparison of heavy flavor single electron invariant yield from converter and cocktail method . . . . .	116
4.2	Nuclear modification factor ( $R_{dA}$ ) . . . . .	117
4.2.1	Final Nuclear Modification for heavy flavor single electron in $d + Au$ collision . . . . .	119
4.3	Model Comparison . . . . .	122
4.4	Ratio of $R_{AA}$ and $R_{dA}^2$ at $\sqrt{S_{NN}} = 200$ GeV . . . . .	126
4.5	Heavy flavor invariant cross section . . . . .	129
4.6	Comparison between data and FONLL calculation . . . . .	130
<b>5</b>	<b>Summary and Outlook</b>	<b>134</b>
<b>Bibliography</b>		<b>137</b>
<b>A Appendix</b>		<b>145</b>
<b>B Appendix</b>		<b>147</b>
<b>List of Publications</b>		<b>148</b>

# List of Figures

1.1	Feynmann diagram for $q + \bar{q} \rightarrow l^+ + l^-$ reaction. The vertices (given by $\mu$ and $\nu$ ) and the momentum of the lines are labeled. . . . .	3
1.2	Feynmann diagram for annihilation process (top panels) and for Compton scattering (bottom panels). . . . .	5
1.3	Feynmann diagram for strangeness production. $q$ and $\bar{q}$ are the light quarks and antiquarks whereas the $Q$ and $\bar{Q}$ are the heavy quarks and antiquarks like strange quarks and antiquarks. . . . .	6
1.4	Conjectured QCD phase diagram. . . . .	7
1.5	Schematic heavy-ion collision from left to right. Two ions travelling towards each other with the velocity of the order of the velocity of light seems to be contracted because of Lorentz contraction. The two ions during collision smashes into one another and then passes through each other. Intense high temperature is produced making the quarks and gluons to unbound for a brief period of time. Just after collision the area cools off causing the quarks to recombine and form several particles detection of which gives us the glimpse of the properties of the matter produced during the collision process. . . . .	8
1.6	Schematic of space-time evolution in nucleus-nucleus collision where QGP is expected to form. . . . .	9

1.7	Schematic of space-time evolution in nucleus-nucleus collision where QGP is not expected to form. . . . .	10
1.8	Fragmentation of charm quark and semi-leptonic decay of charm meson. The decay mode on the left hand is of prime interest of this analysis.	12
1.9	Nuclear modification factor of light and heavy quarks as a function of number of participants $N_{part}$ [107]. . . . .	13
2.1	Schematic view of the ions going through the various accelerator stages before getting into the RHIC rings. . . . .	20
2.2	Layout of PHENIX detector. . . . .	22
2.3	Schematic view of PHENIX coordinate system. For details see the text.	23
2.4	PHENIX detector acceptance. x axis is rapidity ( $y$ ), and y axis is azimuthal angle. . . . .	24
2.5	PHENIX detector layout during 2008 data taking. . . . .	25
2.6	The left panel shows the BBC and the right panel shows photomultiplier tube (PMT) used in the BBC. The PMT is of 25.4 mm diameter and has a 3 cm quartz mounted on it. The quartz act as a Cherenkov radiator. . . . .	26
2.7	Top panel shows the cross sectional view of the location of ZDC. The z axis is perpendicular to the plane of the paper. The deflection of protons due to DX magnets is shown by green blob. The neutrons are shown by red blob and are being captured by ZDC. Bottom panel is the plane view of RHIC beampipe , location of ZDC and the collision region. . . . .	27

2.8	Correlation between total energy deposited in ZDC and total charge measured by BBC for $Au + Au$ collision. The various centrality classes are labelled in the figure. 0-5% centrality corresponds to most central collision whereas the extreme left region in the figure corresponds to peripheral collision.	28
2.9	Pictorial representation of Reaction Plane detector.	28
2.10	Left panel shows the 12 scintillators segments for RxNP detector. Right panel shows the division of the RXNP detector in 2 segments.	29
2.11	PHENIX central and muon arm magnets in ++ mode. The field direction is represented by the arrows on the inner field lines.	31
2.12	Schematic diagram of Drift chamber frame [74].	32
2.13	Schematic layout of the DC wire orientation [74].	34
2.14	Calculation of drift lines for the optimum electric field configuration [74]. Different types of wire are marked by letters: B - back, C - cathode, G - gate, P - potential, S - sense or anode wires.	35
2.15	Left hand side shows the pad and pixel geometry. The center of the right hand side figure shows a cell defined by three pixels [74].	36
2.16	Schematic diagram of TEC six-plane sector [74].	37
2.17	Schematic diagram of the operation inside TEC. The anode cathode configuration is shown together with the $\vec{E}$ -field lines [74] For details see the text.	38
2.18	RICH one arm cutaway schematic diagram [76].	39
2.19	Schematic diagram of one of the ToF panel [76].	41
2.20	PbSc module interior displaying a stack of scintillator and lead plates, wavelength shifting fiber readout and leaky fiber in the central hole [85].	42
2.21	Schematic view of PbGl supermodule.	43

2.22	The energy spectra of electrons, pions and protons of 0.5, 1 and 2 GeV/c measured in the PHENIX EMCal [85]. . . . .	44
3.1	$z_{vertex}$ distribution of events in $d + Au$ collision at $\sqrt{S_{NN}} = 200$ GeV. y axis is counts and x axis is the range of collision vertex along z axis of PHENIX in cm. The distribution is fitted with Gausian function in order to determine the full width at half maximum based on which events lying between particular range of $z_{vertex}$ are selected. . . . .	48
3.2	E/p distribution of single electrons before HBD support removal. . . . .	49
3.3	phi distribution with eID but without fiducial cut. Red colored distribution is for $E/p < 0.7$ and black colored is for $E/p > 0.7$ . Below $E/p = 0.7$ there are two spikes in phi. That is because most of the conversion takes place at $E/p < 0.7$ . . . . .	50
3.4	E/p distribution of single electrons after applying HBD support structure removal cut. . . . .	50
3.5	Cherenkov photons are being reflected by the RICH mirror on the PMT plane array. . . . .	52
3.6	PMT arrays of RICH detector along with the projected track and the predicted maximum and minimum radius. . . . .	52
3.7	$e^\pm$ per MB events in MB data set. x axis is the run number and y axis is the number of electrons per MB events. Converter run is shown by red markers and the green marker is for non-converter run. . . . .	55
3.8	The ratio of MB&ERT trigger in the MB data set and the ERT data set for the non-converter data set. One entry of the histogram is for one run. . . . .	57
3.9	$e^\pm$ per MB sampled events in ERT data set. . . . .	57

3.10 $p_T$ spectra of electrons in different sectors in MB dataset. y axis is the number of counts and x axis is $p_T$ . Red histogram is without ERT trigger condition while the blue histogram is with ERT trigger condition.	60
3.11 ERT trigger efficiency in different sectors. . . . .	61
3.12 $p_T$ distribution in different sectors before and after applying ERT trigger correction for standard eID. x axis is $p_T$ and y axis is number of counts. Sector1_3 don't have ERT triggered data. Red colored distribution is after applying trigger efficiency and black colored distribution is before applying trigger efficiency correction. . . . .	62
3.13 $p_T$ distribution in different sectors before and after applying ERT trigger correction for tight eID. x axis is $p_T$ and y axis is number of counts. Sector 1_3 don't have ERT triggered data. Red colored distribution is after applying trigger efficiency and black colored distribution is before applying trigger efficiency. . . . .	63
3.14 E/p distribution of single electrons in different $p_T$ bins starting from $0.8 \text{ GeV} < p_T < 1.0 \text{ GeV}$ at extreme left of top panel to $9.0 \text{ GeV} < p_T < 10 \text{ GeV}$ at extreme right of bottom panel. x axis is E/p and y axis is number of counts. . . . .	64
3.15 E/p magnified distribution in high $p_T$ bins. . . . .	65
3.16 $p_T$ spectra of electrons for tight and standard eID in different sectors before applying tight eID correction. y axis is number of counts normalized by the total number of events and x axis is $p_T$ . Red colored distribution is with tight eID and blue colored distribution is with standard eID in ERT trigger data set. Sector 1_3 is from MB trigger data set. . . . .	66
3.17 Correction for tight eID cut in different sectors. Sector1_3 is corrected for MB data as the final spectra contains only MB data from this sector. . . . .	67

3.18 Electron $p_T$ distribution in different sectors from ERT and MB data set after applying trigger efficiency and eID correction. y axis is number of counts normalized by the total number of events and x axis is $p_T$ . Red is ERT triggered data with tight eID cut corrected for trigger efficiency and tight eID correction, blue is ERT triggered data with standard eID corrected for ERT trigger efficiency and black is MB triggered data with standard eID. Sector 1_3 has MB triggered data in magenta with tight eID corrected for tight eID correction. . . . .	68
3.19 Stitched $p_T$ spectra from different sources in different sectors as mentioned in text. x axis is $p_T$ and y axis is number of electron counts scaled by total number of events. . . . .	69
3.20 Stitched $p_T$ spectra from different sources after adding all the sectors. . . . .	70
3.21 Fit to the $p_T$ spectra of electron in real data. The fit function is used as weight factor while filling the histograms in simulation. . . . .	70
3.22 Real data and MC comparison for Drift Chamber phi coordinate in $0.6 \text{ GeV} < p_T < 4.0 \text{ GeV}$ . Red is data and black is MC. The real data is rescaled such that the integral of the phi distribution in the real data and in the simulation agrees. y axis is the rescaled counts. Top panel includes both the sides. Middle panel is for North side of PHENIX. Bottom panel is for South side of PHENIX. . . . .	72
3.23 Real data and MC comparison for EMC z coordinate distribution. The real data is rescaled such that the integral of the EMC z distribution in the real data and in the simulation agrees. y axis is the rescaled counts. Red distribution is for real data and black distribution is for MC. Top panel panel is for North side of PHENIX. Bottom panel is for South side of PHENIX. . . . .	73

3.24 Real data and MC comparison for different eID cut and track matching parameters. The real data is rescaled such that the integral of the eID and track matching variables in the simulation and in the real data agrees. y axis is the rescaled counts. Red is data and black is MC. . . . .	74
3.25 $p_T$ spectra of single electron before passing through PISA (black curve) and after passing through PISA and reconstruction chain (red curve). . . . .	75
3.26 $e^+ + e^-$ acceptance X efficiency plot in PHENIX. This curve is used for the acceptance correction in real data for electrons as described in the text. . . . .	75
3.27 $\pi^\pm$ and $\pi^0$ fit. For details please see the text. . . . .	77
3.28 $\pi^\pm$ and $\pi^0$ fit quality. Red is for Hagedorn fit, blue is for power law fit and green open circle is for eqn. 3.14. . . . .	78
3.29 Top panel shows the $\eta$ $m_T$ scaled spectra and $\eta$ - $\pi^0$ normalization. Bottom panel shows the $\eta'$ $m_T$ scaled spectra and $\eta'$ - $\pi^0$ normalization. . . . .	79
3.30 Left panel starting from top shows the $\rho$ , $\omega$ , $\phi$ $m_T$ scaled spectra. Right panel starting from top $\rho$ - $\pi^0$ , $\omega$ - $\pi^0$ , $\phi$ - $\pi^0$ normalization. . . . .	80
3.31 Single electron cocktail for Run8 d+Au in minimum bias centrality. Mesonic contributions and $\gamma$ contribution has also been shown. . . . .	82
3.32 Single electron cocktail for Run8 d+Au in other centralities. Mesonic contributions and $\gamma$ contribution has been shown. . . . .	83
3.33 Ratio of single electron $p_T$ distribution with tight eID and standard eID. The spread of 2% for $p_T > 4.5$ GeV is taken as systematic error for $p_T > 4.5$ GeV. . . . .	84
3.34 Acceptance $\times$ eID efficiency curve for tight and standard eID cuts. Red is with tight eID cut and blue is with standard eID cut. . . . .	85

3.35 Acceptance $\times$ eID efficiency corrected $p_T$ spectrum of single electron for standard and tight eID. Blue colored distribution is for standard eID and red is for tight eID. . . . .	85
3.36 Ratio of tight eID $p_T$ spectra and standard eID $p_T$ spectra after applying Acceptance X eID efficiency correction. The spread in points gives us the idea of how much imperfect is the simulation for Acceptance X eID efficiency correction. The spread in point adds up as the systematic error. . . . .	86
3.37 Upper and lower relative systematic error on $d + Au$ single electron cocktail. . . . .	87
3.38 Total systematic error on $d + Au$ single electron cocktail in minbias centrality. The plot is obtained by taking the average of upper and lower curves in fig. 3.37. Also shown is the fit by the curve to the total cocktail systematic error plot. The fit function used is mentioned in the text. . . . .	88
3.39 Converter and non-converter active Drift Chamber in phi coordinate distribution in MB data set. The converter data is rescaled such that the integral of the phi distribution in the converter data and in the non-converter data agrees. y axis is the rescaled counts. . . . .	90
3.40 Converter and non-converter EMCAL active area in z coordinate distribution in MB data set. The converter data is rescaled such that the integral of the EMCAL z distribution in the converter data and in the non-converter data agrees. y axis is the rescaled counts. . . . .	91
3.41 Converter and non-converter active Drift Chamber in phi coordinate distribution in ERT data set. Red is for converter and black is for non-converter runs. The converter data is rescaled such that the integral of the phi distribution in the converter data and in the non-converter data agrees. y axis is the rescaled counts. . . . .	92

3.42 Converter and non-converter active EMCAL in z coordinate distribution in ERT data set for 7 different sectors of EMCAL. Red is for converter and black is for non-converter runs. The converter data is rescaled such that the integral of the EMCAL z distribution in the converter data and in the non-converter data agrees. y axis is the rescaled counts. . . . .	93
3.43 Converter and non-converter electron ( $e^+ + e^-$ ) yield. Left is from MB trigger data set and right plot is from ERT triggered data set. . . . .	94
3.44 $R_{CN}$ in minimum bias centrality. Left plot shows the overlay of $R_{CN}$ from MB and ERT data set. Right plot is the combined MB and ERT data set $R_{CN}$ . For $p_T \leq 1.6$ GeV MB data set is used and for $p_T > 1.6$ GeV ERT data set is used. The black curve in both the left and right hand plots shows the $R_\gamma$ . . . . .	94
3.45 $R_{NP}$ from ERT and MB data set. Left hand plot is the overlay of $R_{NP}$ from MB and ERT data set. Red points are from MB triggered data and blue points are from ERT triggered data. Right hand plot is the combined $R_{NP}$ from MB and ERT data. For $p_T \leq 1.6$ GeV MB data is used and for $p_T > 1.6$ GeV ERT data is used. . . . .	95
3.46 DC phi acceptance matching for simulation and MB triggered real data. Red is simulation and black is real data. The real data is rescaled such that the integral of the phi distribution in the real data and in the simulation agrees. y axis is the rescaled counts. Top panel is for combined North and South arm of DC. Central panel is for South arm of DC and the bottom panel is for North arm of DC. . . . .	97

3.47 EMCAL z acceptance matching for simulation and MB triggered real data. Red is simulation and black is real data. The real data is rescaled such that the integral of the EMCAL z distribution in the real data and in the simulation agrees. y axis is the rescaled counts. Top panel is for combined North and South arm of EMCAL. Central panel is for North arm of EMCAL and the bottom panel is for South arm of EMCAL.	98
3.48 DC phi acceptance matching for simulation and ERT triggered real data. Red colored distribution is simulation and black colored distribution is real data. The real data is rescaled such that the integral of the phi distribution in the real data and in the simulation agrees. y axis is the rescaled counts. Top panel is for combined North and South arm of DC. Central panel is for South arm of DC and the bottom panel is for North arm of DC.	99
3.49 EMCAL z acceptance matching for simulation and ERT triggered real data. Red colored distribution is simulation and black colored distribution is real data. The real data is rescaled such that the integral of the EMCAL z distribution in the real data and in the simulation agrees. y axis is the rescaled counts. Top panel is for combined North and South arm of EMCAL. Central panel is for North arm of EMCAL and the bottom panel is for South arm of EMCAL.	100
3.50 Spectra of single electron before passing through PISA (black curve) and after passing through PISA and reconstruction chain (red curve).	101
3.51 Acceptance plot for $e^+ + e^-$ with fiducial cuts for MB triggered acceptance match for non-converter and converter data set	101
3.52 Spectra of single electron before passing through PISA (black curve) and after passing through PISA and reconstruction chain (red curve).	102
3.53 Acceptance plot for $e^+ + e^-$ with fiducial cuts for ERT triggered acceptance match for non-converter and converter data set.	102

3.54 Invariant yield of photonic electrons obtained from converter method. Black curve is the photonic electrons from Cocktail method. . . . .	103
3.55 Ratio of the photonic electron invariant yield from converter method and the photonic cocktail component. The ratio is fitted with a constant value. . . . .	104
3.56 Non-photonic single electron from the converter analysis (black curve) in minimum bias centrality. Also shown are the single electron cocktail from $Ke_3$ (magenta), $\rho \rightarrow ee$ (blue) and $\omega \rightarrow ee$ (red) from the cocktail calculation as in section 3.8. . . . .	105
3.57 Left hand plot is the conversion pair( $e^+e^-$ ) invariant mass distribution in the real data from RUN4 of PHENIX. Right hand is for simulation. Red colored distribution is for converter and blue colored distribution is for non-converter. The data points for both the plots are taken from [95]. . . . .	106
3.58 Single electron inclusive spectra in minimum bias centrality. . . . .	109
3.59 Single electron heavy flavour spectra from cocktail subtraction method in minimum bias centrality for d+Au collision species. The vertical bars at each data point are the statistical error whereas the systematic error is given by the block around each data point. The curve is the fit to the single electron from heavy flavor data from p+p collision species.	110
3.60 Single electron heavy flavor spectra for Run8 d+Au in 0-20% centrality (left plot) and in 20-40% centrality (right plot) for d+Au collisions species from cocktail subtraction method. The vertical bars at each data point are the statistical error whereas the systematic error is given by the block around each data point. The curves are the fit to the single electron from heavy flavor data from p+p collision species. . . . .	111

3.61 Single electron heavy flavor spectra for Run8 d+Au in 40-60% centrality (left plot) and in 60-88% centrality (right plot) for d+Au collisions species from cocktail subtraction method. The vertical bars at each data point are the statistical error whereas the systematic error is given by the block around each data point. The curves are the fit to the single electron from heavy flavor data from p+p collision species. . . . .	112
3.62 Single electron heavy flavour spectra using converter method in mini- mum bias centrality. The vertical bars are the statistical error around the central values and the systematics is shown by the boxes. . . . .	113
3.63 Single electron heavy flavor spectra using converter method for different centralities. The vertical bars are the statistical error around the central values and the systematics is shown by the boxes. . . . . . . . .	114
4.1 Heavy flavor single electron spectrum in different centrality using cock- tail subtraction method. .	117
4.2 Heavy flavor single electron spectrum obtained from converter analysis and cocktail subtraction method. The statistical error is shown by the vertical bars around the central value. . . . . . . . . . . . . . . . . . .	118
4.3 Heavy flavor single electron spectrum obtained from converter analysis and cocktail subtraction method. The statistical error is shown by the vertical bars around the central value. For cocktail subtraction method the systematic error are shown by green blocks whereas for converter subtraction method the systematic errors are shown by the yellow blocks.	119
4.4 Heavy flavor single electron spectrum for different centrality. For $p_T <$ 1.0 GeV heavy flavor from converter analysis is used because of small systematic error in comparison to cocktail subtraction method. For $p_T > 1.0$ GeV heavy flavor from cocktail subtraction method is used.	120

4.5 $R_{dA}$ for minimum bias centrality using heavy flavor single electron invariant yield from cocktail subtraction method. The bars are statistical error and the systematic error is shown by boxes around the central value. . . . .	121
4.6 $R_{dA}$ for other centralities starting from 0-20% from extreme left in top panel to 60-88% centrality in the extreme right of the bottom panel. The bars are statistical error and the systematic error is shown by boxes around the central value. . . . .	122
4.7 $R_{dA}$ for minimum bias centrality from the converter method calculated heavy flavor single electron in $d + Au$ . The bars are statistical error and the systematic error is shown by boxes around the central value. . . . .	123
4.8 $R_{dA}$ for other centralities starting from 0-20% from extreme left in top panel to 60-88% centrality in the extreme right of the bottom panel. The bars are statistical error and the systematic error is shown by boxes around the central value. . . . .	124
4.9 Final $R_{dA}$ for minimum bias centrality. For $p_T < 1.0$ GeV, results from converter analysis is used and for $p_T > 1.0$ GeV results from cocktail subtraction method is used. The bars are statistical error and the systematic error is shown by boxes around the central value. . . . .	125
4.10 Final $R_{dA}$ for other centralities starting from 0-20% from extreme left in top panel to 60-88% centrality in the extreme right of the bottom panel. For $p_T < 1.0$ GeV, results from converter analysis is used and for $p_T > 1.0$ GeV results from cocktail subtraction method is used. The bars are statistical error and the systematic error is shown by boxes around the central value. . . . .	126

4.11 Nuclear modification factor in minimum bias centrality for $d + Au$ (top panel) and $Au + Au$ (bottom panel) at $\sqrt{S_{NN}} = 200$ GeV. The bars are statistical error and the systematic error is shown by boxes around the central value. For $d + Au$ collision enhancement in nuclear modification factor is seen as compared to the suppression in $Au + Au$ collision from $p_T > 2.0$ GeV. . . . .	127
4.12 $\frac{R_{AA}}{(R_{dA})^2}$ for single electron from heavy flavor. For comparison the light meson ( $\pi^0$ ) $\frac{R_{AA}}{(R_{dA})^2}$ is also shown. Heavy quarks suppression seems to be more than the light quark suppression. . . . .	128
4.13 Heavy flavor invariant cross section for single electron in $d + Au$ collisions at $\sqrt{S_{NN}} = 200$ GeV in minimum bias centrality. The boxes are systematic error around the central value. The vertical bars are statistical error. . . . .	131
4.14 Comparison of heavy flavor invariant cross section for single electron in $d + Au$ collisions at $\sqrt{S_{NN}} = 200$ GeV obtained in this analysis with the FONLL prediction. The data points are obtained in this analysis and the different curves are the FONLL predictions for different decay channels of heavy flavors. . . . .	132
4.15 Data/FONLL calculation. The upper curve is the ratio of FONLL value upped by it's systematic with the FONLL central value. The lower curve is the ratio of FONLL value lowered by it's systematic with the FONLL central value. The upper and lower curve shows the upper and lower limits in the FONLL uncertainty band. . . . .	133
B.1 Impact parameter. . . . .	147

# List of Tables

1.1	Heavy quark cross section experimental and theoretical estimates. The PHENIX data and theoretical values are for $\sqrt{s} = 200$ GeV in $p + p$ collisions. The STAR data is for $d + Au$ measurement. . . . .	11
3.1	Parametrization of ERT trigger efficiency for single electron in each sector . . . . .	59
3.2	Definition of the variables in Eqn. 3.16 and Eqn. 3.17 . . . . .	89

# Chapter 1

## Introduction and Motivation

Tremendous development has been made in order to understand the basic constituent of matter and the forces that binds them together after the discovery of nucleus. Until 1960s, it was believed that basic constituent of nucleus was protons and neutrons. However Gell-Mann's theoretical proposal of quarks (having fractional charges of  $2/3$  and  $-1/3$ ) being the constituent of protons made a huge revolution in High Energy Physics. Several theories were proposed to understand the properties of these basic constituent of nature and the interaction between these quarks. The proposed theories made it possible to understand various combinations of quarks giving rise to large number of particles found in nature.

The first experiment in order to prove the existence of quarks inside the protons was Deep Inelastic Scattering (DIS) at SLAC in 1968. Due to Gell-Mann's theory being still under dispute at that time, the constituents found in DIS experiment were named partons. However later experiments in SLAC, Fermilab and elsewhere showed the partons having fractional charges of  $2/3$  and  $-1/3$  and hence proving Gell-Mann's hypothesis to be correct. The interaction between the quarks with each other happens by the exchange of another particle called gluon, which are neutral bosons. Both the quarks and gluons carry charge

termed as *color* charge analogous to electrical charge [1].

Unlike positive and negative charge in electrical case, the quarks (anti-quarks) and gluons carry color charges named red, blue and green. Quarks carry color, antiquarks an anticolor and gluons carry one color and one anticolor [2]. Now it is quite established that the basic constituent of nucleus is quarks bounded together by gluons however the complete understanding of the nature of force making the gluons to bind the quarks together has not yet been possible.

In order to understand the nature of force making the gluons to bind quarks together, study of nucleon-nucleon collision is going on which is continuing to unfold this wonderful secret of nature. One of the most interesting fact is that the interaction between quarks is completely opposite to the electromagnetic interaction. Unlike electromagnetic interaction the force of interaction between quarks decreases as they are brought close to each other, this phenomenon is called *asymptotic freedom*. Once they are brought sufficiently close to each other the quarks can unbind giving rise to free quarks. This condition of free quarks can be achieved by bringing the quarks sufficiently close to each other which is possible if, either the temperature reaches of the order of sun's core temperature or the nuclear density becomes too high. No wonder why everything in nature is so stable.

It is believed that few microseconds after the Big Bang the medium consisted of free quarks and gluons. This deconfined state of quarks and gluons is called *quark-gluon plasma (QGP)*. As mentioned earlier, this condition of free quark can be achieved only if we manage to bring quarks sufficiently close together. At energy density of  $\epsilon = 1 \text{ GeV}/\text{fm}^3$  hadronic phase (confined quarks and gluons) undergoes phase transition and gives rise to QGP phase. Calculations based on lattice chromodynamics show us that this energy density can be achieved at a temperature of  $T = 170 \text{ MeV} = 10^{12} \text{ K}$  [3]. In laboratory, this condition can be achieved by head on smashing of heavy ions moving with the

velocity of the order of light and this event is termed as relativistic heavy ion collisions.

There are many signals proposed by various models for detecting **QGP**.

Some of the important signals are:

- i) **Effect on nuclear stopping power** due to creation of compressed hadronic matter. As the baryon rapidity distribution depends strongly on the baryon-baryon cross section [4], the change in nuclear stopping power due to compressed baryonic matter changes the shape of baryonic rapidity distribution.
- ii) **Dilepton (lepton-antilepton pair) production** makes it possible to understand the thermodynamic condition of the medium produced during heavy ion collisions. Interaction of quark and antiquark inside QGP gives rise to virtual photon ( $\gamma^*$ ) which further decays into a lepton ( $l^-$ ) and antilepton ( $l^+$ ). Fig. 1.1 shows the reaction  $q + \bar{q} \rightarrow l^+ + l^-$ . The particles and their momenta are denoted by  $q$ ,  $\bar{q}$ ,  $l$  and  $l^-$ . The photon momentum is denoted by  $q + \bar{q}$ .

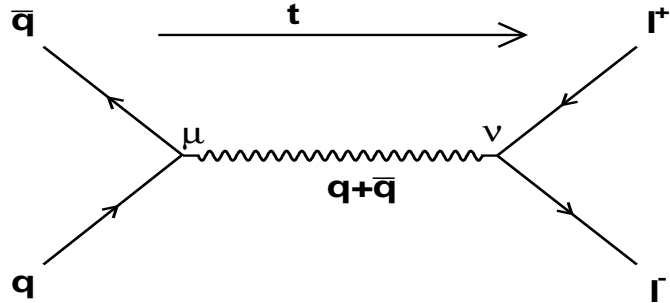


Figure 1.1: Feynmann diagram for  $q + \bar{q} \rightarrow l^+ + l^-$  reaction. The vertices (given by  $\mu$  and  $\nu$ ) and the momentum of the lines are labeled.

The lepton and antilepton pair after their production passes through the collision region and as their mean free path is quite large they are not expected to undergo collisions after their production as well as their production rate and momentum distribution are dependent on the quarks and antiquarks momentum distributions in the QGP which is governed by the thermodynamic condition of QGP [5, 6, 7, 8, 9, 10]. Thus they carry the information of momentum distribu-

tion of quarks and antiquarks.

**iii)  $J/\psi$  suppression** is caused by Debye screening. This signature of QGP was proposed by Matsui and Satz [11]. Many theoretical [12, 13, 14, 15, 16] and experimental studies [17, 18] were performed on this phenomenon. Due to the presence of quarks, antiquarks and gluons in *QGP* the color charge of quark is screened and this is termed as Debye screening.  $J/\psi$  being the bound state of  $c$  and  $\bar{c}$ , when present in the medium (produced during heavy ion collision) are found to be suppressed because of the weakened interaction between  $c$  and  $\bar{c}$  alongwith the vanishing of string tension between  $c$  and  $\bar{c}$  due to the deconfined quarks and gluons in *QGP*. However recent results on  $J/\psi$  measurement [18, 19] showed very different results than predicted by the models [20, 21] describing the SPS data [17]. According to the models larger suppression of  $J/\psi$  at RHIC compared to SPS and more suppression at mid rapidity than forward rapidity has been predicted. The  $J/\psi$  results at RHIC [18, 19] shows larger suppression at forward rapidity than at mid rapidity which cannot be explained by present models. Besides that the spectral shape function of  $J/\psi$  calculated by using lattice QCD calculations has shown that  $J/\psi$  can survive above the critical temperature of the QGP phase transition[22, 23]. Thus currently  $J/\psi$  suppression study in relativistic heavy ion collision is being used to study the property of *QGP*.

**iv) Photon production** in *QGP* takes place due to the possible interaction between quark and antiquark alongwith the production of gluon [24]. This process is called *annihilation* and can be represented by the equation  $q + \bar{q} \rightarrow \gamma + g$  where  $g$  is gluon. This process is represented in terms of Feynmann diagram by the top panel in Fig. 1.2. Other than annihilation process a gluon interacting with a quark or antiquark can also produce photon [24] which can be represented by the reactions

$$g + q \rightarrow \gamma + q$$

$$g + \bar{q} \rightarrow \gamma + \bar{q}$$

and the process is termed as *Compton scattering*. Bottom panel of Fig. 1.2 shows

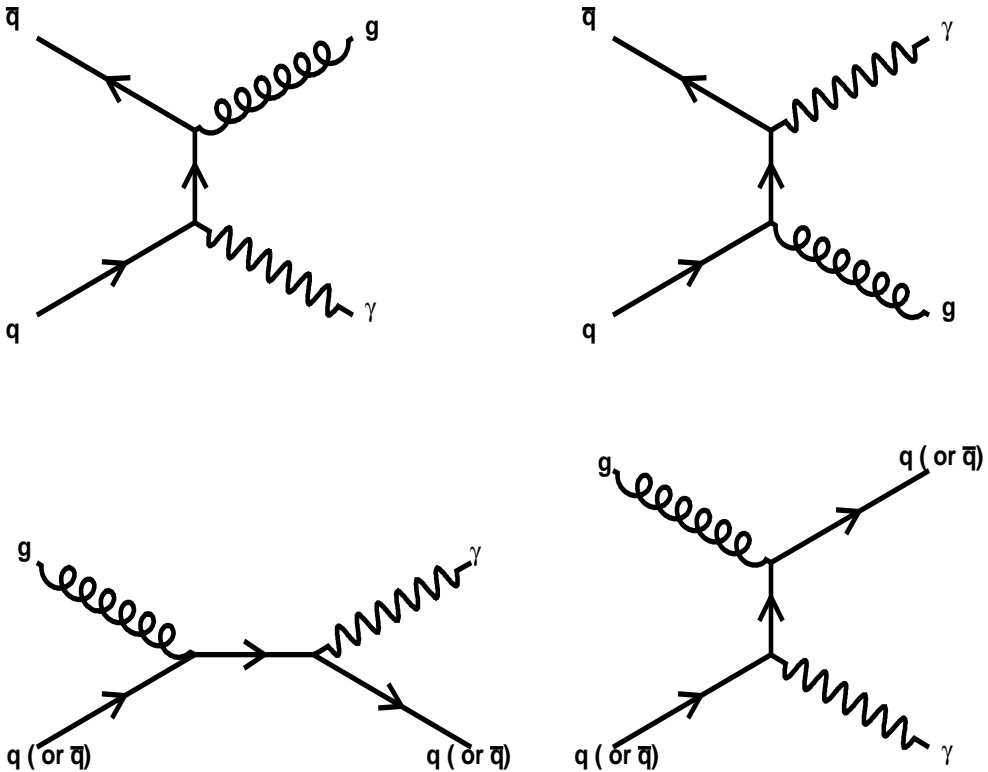


Figure 1.2: Feynmann diagram for annihilation process (top panels) and for Compton scattering (bottom panels).

the Feynman diagram of the Compton scattering. Experimental studies [25, 26] were made by collider experiments on these photon production in heavy ion collisions. The produced photon in the collision region interacts with the particles in that region via electromagnetic interaction, which being not so strong makes the mean free path of the photon large enough to avoid further interaction in the medium. Thus the escaped photon from the collision region carries thermodynamical information about the medium produced in the collision region.

v) **Strangeness enhancement** is expected to take place in case of existence of

*QGP* [27, 28, 29, 30, 31, 32, 33]. In QGP, collisions amongst the constituents of the medium can produce strange quarks and antiquarks. Interaction amongst light quarks and antiquarks can produce strange quarks and antiquarks as shown in Fig. 1.3. Other than this, collisions amongst the gluons in the medium can also produce strange quarks and antiquarks.

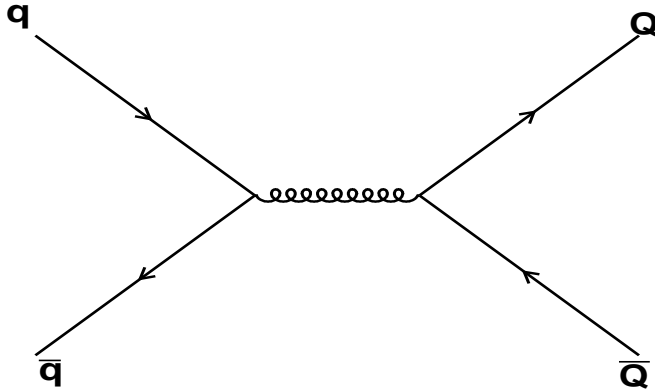


Figure 1.3: Feynmann diagram for strangeness production.  $q$  and  $\bar{q}$  are the light quarks and antiquarks whereas the  $Q$  and  $\bar{Q}$  are the heavy quarks and antiquarks like strange quarks and antiquarks.

Schwinger factor [34] describes the charm production rate under the non existence of chemical equilibrium. The mass dependence of this factor ( $A \exp(-km_q)$ ,  $A$  and  $k$  being constants and  $m_q$  being quark mass) shows that heavy quarks (like strange quarks) are suppressed due to the absence of chemical equilibrium. However during *QGP* phase when chemical equilibrium is achieved there is enhancement in the production of strange quarks.

Thus considering the above mentioned signatures of QGP the important probes for determining it are photons, dileptons and leptons. The leptons from heavy flavor decays (as described in section 1.1) is an important tool for understanding the nature of medium produced during the heavy ion collisions.

The Relativistic Heavy Ion Collider (RHIC) at Brookhaven National Laboratory (BNL) is dedicated to study the nuclear matter under extreme condition

and to explore the phase diagram of strongly interacting matter for new state of matter. This research presents the measurement of single electron from heavy flavor decay from  $d + Au$  collisions at  $\sqrt{s_{NN}} = 200$  GeV collected during the 2008 RHIC run with PHENIX (Pioneering High Energy Nuclear Interaction eXperiment) detector and calculates the nuclear modification factor for  $d + Au$  collisions.

RHIC is capable of colliding nuclei from  $p + p$  to  $Au + Au$  across a wide range of collision energies from center of mass energy per nucleon-nucleon collision of  $\sqrt{s_{NN}} = 22$  GeV to  $\sqrt{s_{NN}} = 200$  GeV for  $Au + Au$ . For  $p + p$  the collision energy is capable of going up to  $\sqrt{s_{NN}} = 500$  GeV.

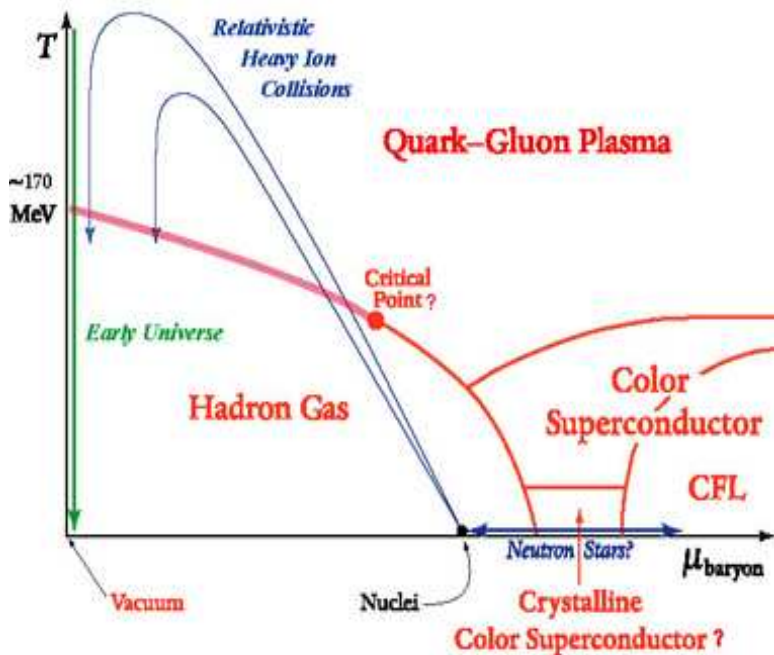


Figure 1.4: Conjectured QCD phase diagram.

Fig. 1.4 shows the conjectured phase diagram [36, 37] of QCD matter as a function of temperature ( $T$ ) and baryon chemical potential ( $\mu_{baryon}$ ). In the bottom left-hand corner of the phase diagram both  $T$  and  $\mu_{baryon}$  are small and the quarks and antiquarks combine with each other giving rise to hadrons. We

may call this region as hadronic phase. According to Lattice QCD calculation at about  $T = 175$  MeV [38, 39] there may occur phase transition where quarks may be found in deconfined state giving rise to the medium called QGP. The exact location of the critical point and the exact order of phase transition is not yet fixed but from the experimental data [40] it is confirmed that RHIC has the ability to explore the region where the quarks and gluons are being found in the deconfined state. According to the theoretical calculations the required energy density for a QCD phase transition is of the order of  $1 \text{ GeV}/\text{fm}^3$  [41]. The RHIC collisions produces energy densities of the order of  $5 \text{ GeV}/\text{fm}^3$  [40] showing RHIC having the ability to explore the new state of matter.

Heavy ion collisions are being described by parameter called impact parameter ( $b$ ). Impact parameter can be defined as the distance between the center of two nuclei colliding with each other and it basically gives us the information of overlapped region of the colliding nuclei. Collisions with smallest  $b$  are referred as the *most central collisions* whereas the ones with large  $b$  are termed as *peripheral collisions*.

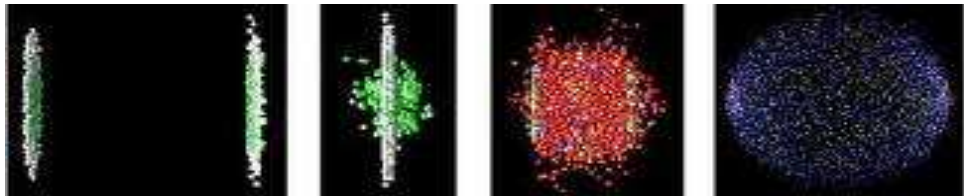


Figure 1.5: Schematic heavy-ion collision from left to right. Two ions travelling towards each other with the velocity of the order of the velocity of light seems to be contracted because of Lorentz contraction. The two ions during collision smashes into one another and then passes through each other. Intense high temperature is produced making the quarks and gluons to unbind for a brief period of time. Just after collision the area cools off causing the quarks to recombine and form several particles detection of which gives us the glimpse of the properties of the matter produced during the collision process.

Fig. 1.6 shows the schematic of the heavy ion collision where QGP is expected to form. As shown in the figure after the initial collision of heavy ions,

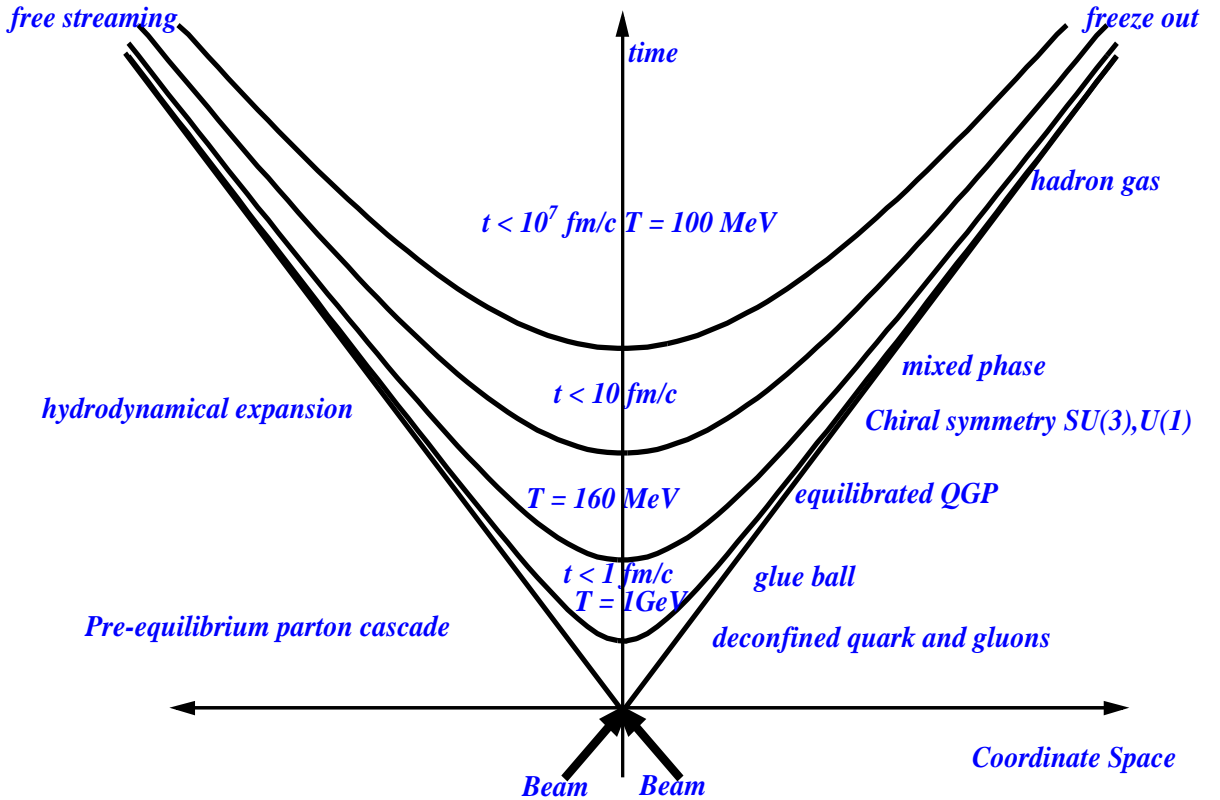


Figure 1.6: Schematic of space-time evolution in nucleus-nucleus collision where QGP is expected to form.

parton production is expected within a time of  $1 \text{ fm}/c$ . The system begins to expand and cool down because of the pressure making the local density go below the threshold for phase transition and according to QCD the partons become confined within hadrons. Fig. 1.6 is the schematic space-time diagram of the nucleus-nucleus collision. It shows the time scale of the various stages of medium produced after the collision takes place. Freeze out in the Fig. 1.6 is referred as the incidence when the interaction between the hadrons stops. The hadron-gas produced after collision continues to expand and interact until *chemical freeze-out* where the hadrons stops interacting inelastically. After further expansion and cooling, the last elastic interaction happens and *thermal freeze-out* occurs. The hadrons then undergoes decaying mechanism following their known modes of decay which can be detected experimentally.

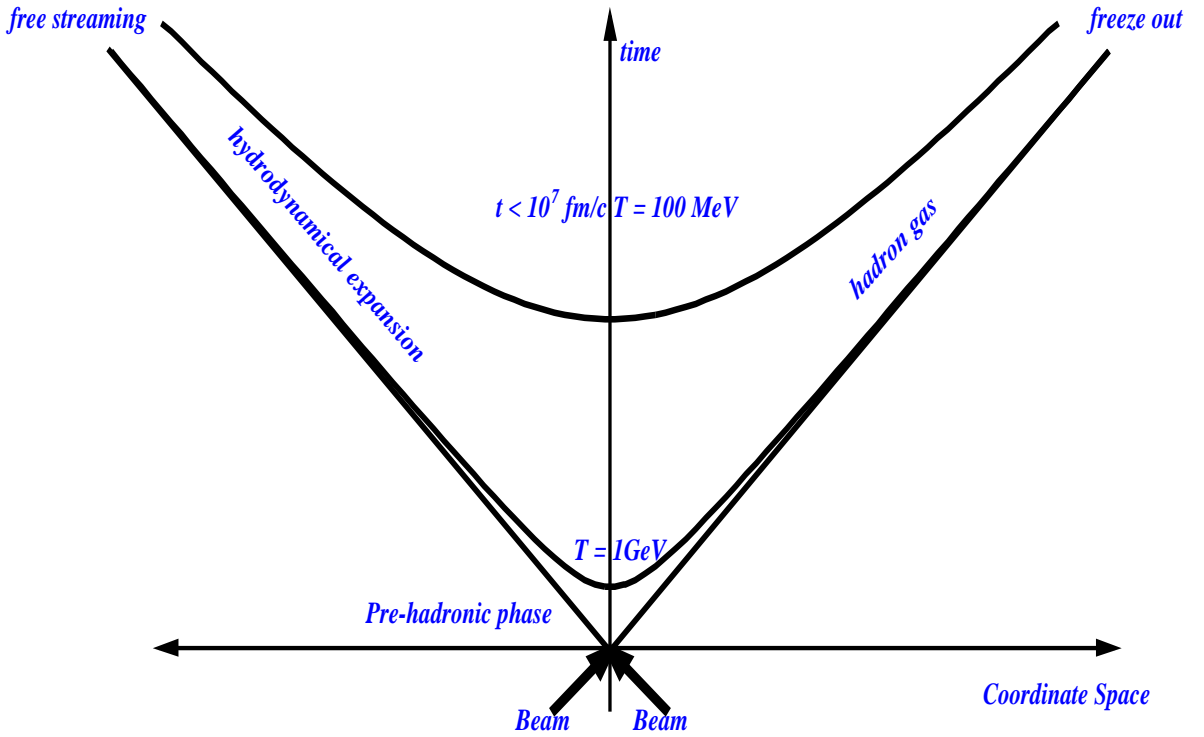


Figure 1.7: Schematic of space-time evolution in nucleus-nucleus collision where QGP is not expected to form.

Fig. 1.7 shows the schematic of the heavy ion collision where QGP is not expected to form. Comparing figures 1.6 and 1.7 it can be seen that only hadron gas is being produced in case where QGP is not expected to form.

## 1.1 Heavy quark production and its role as a probe for matter produced at RHIC

Heavy quarks are one of the most valuable probes for the matter produced at RHIC collisions mainly because of their masses ( $m_c \approx 1.3$  GeV,  $m_b \approx 4.2$  GeV) being quite large than the typically attained ambient temperatures or other non-perturbative scales,  $m_Q \gg T_C$ ,  $\Lambda_{QCD} = 0.2$  GeV<sup>3</sup> [42]. The mass scale of heavy quarks causes : (i) The production of heavy quarks constrained to the early,

primordial stages of heavy ion collision. (ii) Delay in thermalization of heavy quarks relative to light quarks. It is expected that the heavy quarks full thermalization time scale is longer than the life time of QGP resulting in retaining the information of the interaction history.

Table 1.1: Heavy quark cross section experimental and theoretical estimates. The PHENIX data and theoretical values are for  $\sqrt{s} = 200$  GeV in  $p + p$  collisions. The STAR data is for  $d + Au$  measurement.

Quark	$\sigma_{total}$ (mb)	Uncertainty on $\sigma$	Source
charm	0.256	+0.400 / -0.146	FONLL [62]
charm	0.244	+0.381 / -0.134	NLO [43]
charm	0.567	$\pm 0.057^{stat} \pm 0.224^{sys}$	PHENIX [96]
charm	1.3	$\pm 0.2^{stat} \pm 0.4^{sys}$	STAR [44]
bottom	0.00187	+0.00099 / -0.00067	FONLL [62]
bottom	0.0046	$\pm 0.0013^{stat} + 0.0026 / - 0.0022^{sys}$	PHENIX [45]
bottom	0.0039	$\pm 0.0025^{stat} + 0.003 / - 0.002^{sys}$	PHENIX [46]
top	$\sim 0$	N/A	N/A

RHIC energy is sufficient to produce heavy quarks, primarily for charm production. Bottom is also produced, however, the total production of bottom is significantly lower than that of charm production. It has been estimated that the total bottom cross section is about 1-2% of total charm cross section. The specific values are shown in table 1.1. PHENIX measurement shows that for  $\sqrt{s} = 200$  GeV  $p + p$  collisions, the charm cross section exceeds the bottom cross section until  $p_T \sim 4.0$  GeV/c, above which bottom dominates [97].

Different decay channels are used for detecting the heavy flavor hadrons. In the present work the measurement of the spectra of heavy flavors is based on the measurement of the spectra of heavy flavor electrons and positrons  $[(e^+ + e^-)/2]$  from the semi leptonic decays like  $D^0 \rightarrow K^- e^+ \nu_e$ ,  $D^+ \rightarrow \bar{K}^0 e^+ \nu_e$  etc. Fig. 1.8 shows the two decay channels of experimental interest in PHENIX. The center of the figure shows the charm/anti-charm quark pair produced in an initial inelastic hard collision. The right hand  $\bar{D}^0$  decay channel shows the hadronic decay to

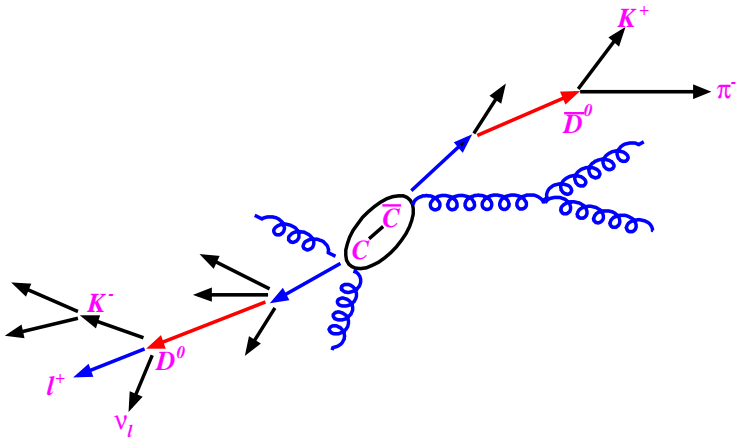


Figure 1.8: Fragmentation of charm quark and semi-leptonic decay of charm meson. The decay mode on the left hand is of prime interest of this analysis.

$K^+\pi^-$ . This hadronic decay mode is used for the study of charm production which is not the focus of this research. The left hand  $D^0$  decay mode shows the semi-leptonic decay of  $D^0$  to a lepton, the lepton's anti-neutrino and a  $K^-$ . The detection of this single lepton (electron) is the focus of this research.

The quantity *nuclear modification factor*, in heavy ion collisions provide us the information regarding the effects of medium on the particle yield. The nuclear modification factor is defined as the ratio between the particle yield in particular heavy ion collisions ( $dN_{A+B}$ ) to the particle yields in binary nucleon-nucleon collisions ( $dN_{p+p}$ ) scaled by the expected number of point-like binary nucleon-nucleon collisions  $\langle N_{coll} \rangle$ , for the centrality class considered. Thus nuclear modification factor,  $R_{AB}$  is

$$R_{AB} = \frac{dN_{A+B}}{\langle N_{coll} \rangle \times dN_{p+p}}. \quad (1.1)$$

The measurement of invariant differential yield/cross section for  $p + p$  provides the baseline for the Physics conclusion from the measurement of  $R_{AB}$  for other heavy ions collision species. One of the most interesting experimental results at RHIC is that of the significant energy loss of light quarks observed in the

QGP like medium. The light quarks are being observed through light mesons measurement like  $\pi^0$  while the heavy quarks are observed by single leptons.

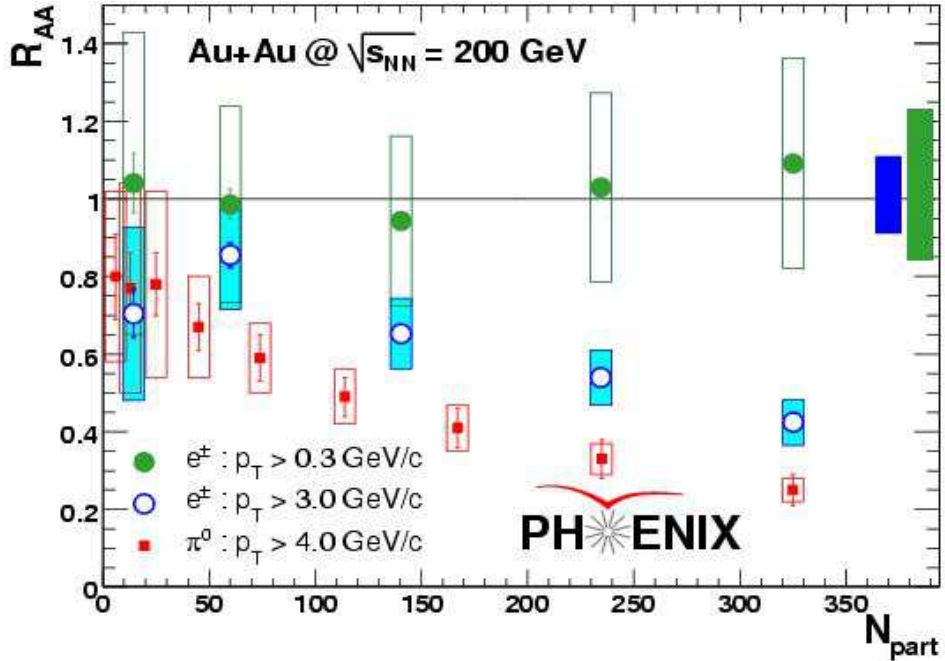


Figure 1.9: Nuclear modification factor of light and heavy quarks as a function of number of participants  $N_{part}$  [107].

Fig. 1.9 shows the nuclear modification factor,  $R_{AA}$ , in Au+Au for both light meson ( $\pi^0$ ) and heavy quarks (single electrons from decay channel of D's) for selected  $p_T$  bins as a function of  $N_{part}$ .  $N_{part}$  is the number of participants in heavy ion collisions and gives us the idea of collision centrality. The red points with filled rectangles in the Fig. 1.9 shows  $R_{AA}$  decreasing with increasing  $N_{part}$  (moving towards more central collision) for light mesons showing significant energy loss of the light quarks in the medium produced due to  $Au + Au$  collision. Gluon radiation (*emission of gluons due to acceleration of quarks*) and elastic-inelastic scattering of quarks in the medium can explain the Quark energy loss within the medium. The blue points with filled circles shows the  $R_{AA}$  for heavy flavor single electron with  $p_T > 0.3$  GeV. For  $p_T > 0.3$  GeV, there contains more than half of the heavy flavor decay electrons and the  $R_{AA} = 1.0$  is consistent

with the binary scaling of total heavy-flavor yield. The blue points with open circle shows the  $R_{AA}$  for heavy flavor single electron with  $p_T > 3.0 GeV/c$  and one can see the suppression in  $R_{AA}$  with the increase in  $N_{part}$ . Comparing this with the  $R_{AA}$  for  $\pi^0$  (red points with filled rectangles) it can be seen that the heavy quarks loses less energy than the light quarks but still it is greater than originally expected when taking into account *dead cone effect* [61]. The observed energy loss is yet to be understood fully. However the clear suppression of  $R_{AA}$  for  $Au + Au$  collision clearly shows medium is produced which is absent in  $p + p$  collision. Now the question arises what happens in  $d + Au$  collision which has the colliding species mass in between  $p + p$  and  $Au + Au$ ? Finding out the answer of this question is the main objective of this research.

## 1.2 Measurement of Heavy Flavor cross sections using FONLL

FONLL [62] which stands for Fixed-Order plus Next-to-Leading-Log, provides the means to calculate the heavy flavor single lepton  $p_T$  spectrum,  $E \frac{d^3\sigma_l}{dp^3}$  and also the total production cross section  $\sigma_{hv}$ . The heavy flavor single lepton  $p_T$  spectrum determined from FONLL can be directly compared with the measurement. The factorized lepton production cross section can be given schematically as

$$E \frac{d^3\sigma_l}{dp^3} = \frac{E_Q d^3\sigma_Q}{dp_Q^3} \otimes D(Q \rightarrow H_Q) \otimes f(H_Q \rightarrow l), \quad (1.2)$$

where,  $\otimes$  in the above expression denotes a generic convolution. It is to be noted that the above schematic expression of lepton spectrum consists of three main components. These are

- $\frac{E_Q d^3\sigma_Q}{dp_Q^3}$  : Heavy quark (Q)  $p_T$  and rapidity distributions at  $\sqrt{s_{NN}} = 200$  GeV which is calculated in perturbative QCD.

- $D(Q \rightarrow H_Q)$  : Heavy quarks fragmentation into heavy hadrons ( $H_Q$ ) which is described by phenomenological input extracted from  $e^+e^-$  data.
- $f(H_Q \rightarrow l)$  : The electron decay spectrum term where the heavy hadrons ( $H_Q$ ) decays into electrons. The spectrum for this case is available from other measurements.

The FONLL calculation apart from including the full fixed-order NLO result [63, 64, 65, 66], also re-sums [67] the large perturbative terms proportional to  $\alpha_S^n \log^k(p_T/m)$ . The re-summation is done to all orders with next-to-leading logarithmic (NLO) accuracy (i.e.,  $k = n, n - 1$ ) where the heavy quark mass is denoted by  $m$  here. The heavy quark by FONLL is being treated as an active light flavor for  $p_T \gg m$ . Thus, the number of light flavors for calculation of  $\alpha_s$  in FONLL is 4 for charm and 5 for bottom while in NLO calculation the produced heavy quark is not active flavor, so the  $\alpha_s$  is calculated with  $n_{1f} = 3, 4$  for charm and bottom respectively.

The parameters for FONLL calculation includes the heavy quark mass and the value of strong coupling,  $\alpha_s$ . These two terms are the perturbative parameters. Apart from these perturbative parameters the FONLL calculation depends on unphysical factorization ( $\mu_F$ ) and renormalization ( $\mu_R$ ) scales. The central values of these scales is given by  $\mu_F = \mu_R = \mu_O = \sqrt{p_T^2 + m^2}$ . In order to get the uncertainty the two scales ( $\mu_R$  and  $\mu_F$ ) are varied independently within fiducial region as described in [62].

### 1.3 Methodology of heavy flavor measurements in PHENIX

Charm quarks produced in the initial hard scattering processes between partons will hadronize into the family of open charm D mesons, which are combinations of

rare c or  $\bar{c}$  quarks with other light mesons. The fragmentation function describes the energy distribution of the final state D meson which is the fraction of energy inherited from the original c-quark. Both hadronization and fragmentation can only be measured experimentally. The non conservation of the charm quantum number in weak interaction causes the single charm quark D's decay weakly with the lifetime of  $\tau \approx 10^{-15}$  seconds. Fig . 1.8 is an example of the weak, semi-leptonic decay of a D meson where the resulting single lepton is either an electron or muon. The semi-leptonic decay of D mesons has been widely discussed in literature [47] to [57].

According to the weak interaction theory, certain decay modes of D mesons are highly favored than others. Other than the single lepton semi-leptonic decay mentioned earlier, other prominent decay modes like  $D^0 \rightarrow K^- \pi^+$  [58] and  $D^+ \rightarrow K^- \pi^+ \pi^-$  [59] result in light hadron daughters. Both semi-leptonic decay channels and light hadron decay channels are the convenient methods for measuring heavy quark production from heavy flavor mesons. Measurement using light hadron decay channels corresponds to the direct measurement as one can observe the D's as a peak from the invariant mass spectrum of the hadron daughters produced from the decay of D mesons. The semi-leptonic decay mode corresponds to indirect measurement as leptons are measured and it is used to infer the D meson and by extension the charm quark. The indirect method of heavy flavor measurement is the procedure employed in this research work. Here the observable is single electrons from the semi-leptonic decay of D mesons. The analysis procedure employed here to measure the single electrons is well established method [60].

The indirect method involves the measurement which is statistical in the sense it involves estimation of all backgrounds and then they got subtracted from all single lepton candidate tracks detected by the detector. Only after understanding the primary sources of backgrounds properly they are subtracted and the leftover particle tracks are attributed to the heavy flavor signal. In this

method one cannot identify a particular track as a background or a heavy flavor signal. It's only through the statistical estimation and subtraction of quantities that one can obtain any relevant physical quantity.

## 1.4 Brief overview of heavy flavor measurement by PHENIX central arm

The PHENIX detector, as will be explained in chapter 2, instead of having full  $4\pi$  coverage is designed to make measurements in two major kinematic regions. The two regions, according to the convention of measuring the angles relative to the beam axis, are : 1) mid-rapidity, with  $\pi/2$  acceptance centered at  $90^\circ$  polar angle in the central arm and 2) forward rapidity from about  $10^\circ$  to  $30^\circ$  polar angle in both forward and backward directions with full azimuthal coverage.

The central arm has particle identification detectors and has very low material within their acceptance making them to focus on the measurement of electrons. The particle identification detectors enables PHENIX to collect clean sample of electrons. However other than electrons from heavy flavor decay, several other sources also contributes to the electrons being detected by PHENIX detector. The  $\pi^0 \rightarrow \gamma\gamma$  decay and the subsequent photon decay has the maximum contribution towards the electron background. Dalitz decay also has significant contribution towards the electron. Direct photons, weak kaon decay and vector meson decay are the other less important sources of background electrons. Most of these background sources mainly  $\pi^0$  and  $\eta$ , have been independently measured by PHENIX detector providing an excellent input to the Monte Carlo detector simulation for the determination of background contribution. These contributions are well understood electromagnetic processes. The photon conversion contribution background is measured by adding extra conversion material in PHENIX detector acceptance and increment in the conversion takes place by a well deter-

mined factor. All these details when combined together gives precise information of the background in heavy flavor measurement.

# **Chapter 2**

## **PHENIX experiment: A Brief Review**

In this chapter description of the detectors used for the measurement of single electrons from heavy flavor decay has been given along with the steps involved in providing the collision species for relativistic heavy ion collisions at RHIC.

### **2.1 Relativistic Heavy Ion Collider (RHIC)**

The purpose of RHIC has been discussed in chapter 1. In this section some additional details of the accelerator has been provided. RHIC, a storage ring particle accelerator, has the dimension of 2.4 mile in circumference located at Brookhaven National Laboratory (BNL) in Upton, New York, U.S.A. It has two independent rings which are denoted arbitrarily by blue and yellow rings having six intersection points denoted by different clock positions. The accelerated ions orbit inside the blue and yellow rings in opposite direction and undergoes head-on collisions at each of the blue and yellow rings intersection points. The rings provide the facility to orbit ions of two different or same species. The ions which undergo collision inside the RHIC goes through several stages from their production to acceleration until the final stage of collision reaches. Fig. 2.1 shows the schematic

view of the stages involved from the beginning of accelerating the ions until the ions get into the rings.

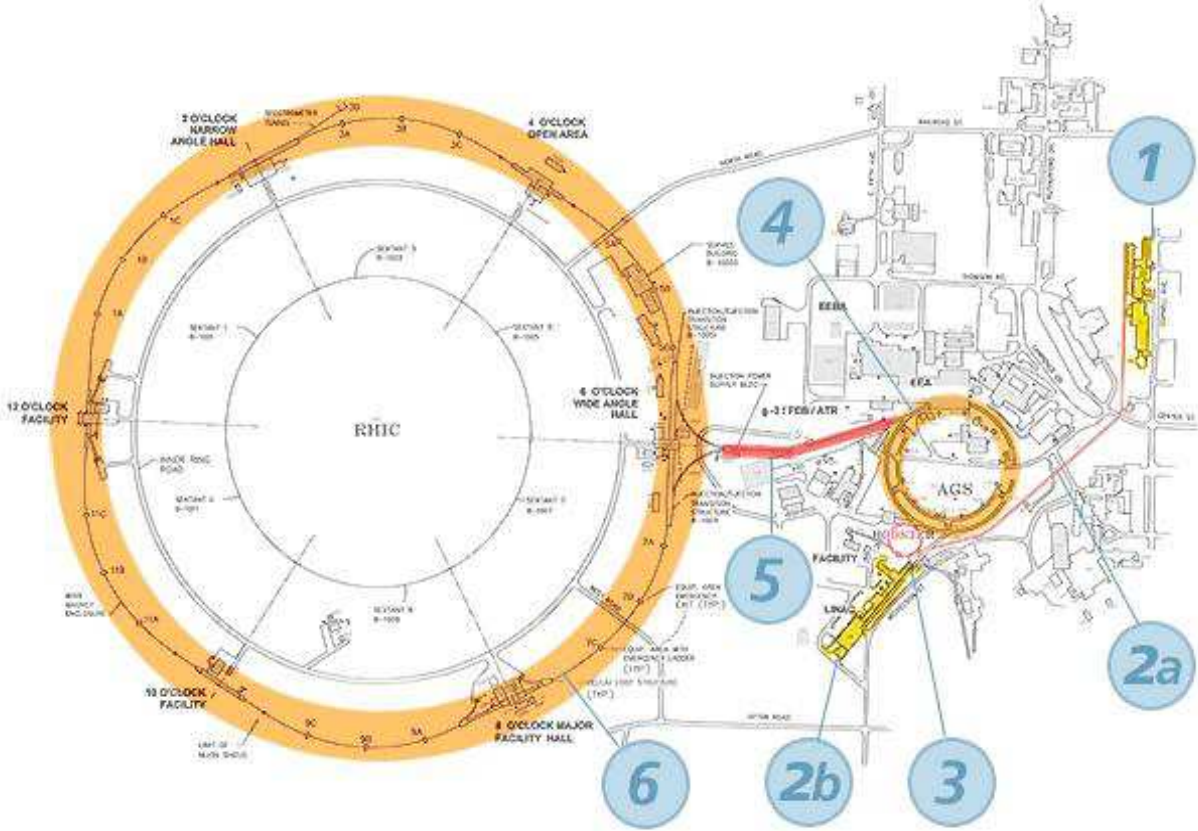


Figure 2.1: Schematic view of the ions going through the various accelerator stages before getting into the RHIC rings.

The first stage of the acceleration of heavy ions is the *Tandem Van de Graaff accelerator* (label (1) in the Fig. 2.1). The protons are accelerated by *Linear Accelerator (Linac)* (label 2a in the Fig. 2.1). For instance gold ions originating in the ion source at the front of the Tandem Van de Graaff are stripped of electrons with a foil and leave the Tandem Van de Graaff with the energy of about 1 MeV per nucleon and having charge of +32. The ions are then carried by the *Tandem-to-Booster line (TTB)*(label 2a in Fig. 2.1) to the *Booster Synchrotron* (label 3 in Fig. 2.1) where the ions are accelerated to an energy of 95 MeV per nucleon. The ions exiting from the booster are made to pass through ion stripper

making them to acquire a charge of +77 . The +77 charged ions are then injected into the *Alternating Gradient Synchrotron (AGS)* (label 4 in Fig. 2.1) with 37% of the speed of light. Inside AGS, they are accelerated and gains more energy and starts moving at 99.7% of the speed of light. The ions are passed through another ion stripper in the *AGS-to-RHIC Line* (label 5 in Fig. 2.1) and attains full charge of +79. The fully charged ions are then injected into the *RHIC rings* (label 6 in Fig. 2.1) and accelerated to the maximum energy of 100 GeV per nucleon. The beams in the RHIC are being steered by RHIC magnets around the rings making the collision between ions possible at the intersection points of the rings. Initially there were four experiments at the four intersection points of the rings. They are named as STAR (6 o'clock), PHENIX(8 o'clock), PHOBOS(10 o'clock) and BRAHMS(2 o'clock). PHOBOS completed its operation after 2005 and BRAHMS after 2006. Currently PHENIX and STAR are active.

## 2.2 The PHENIX detector

The PHENIX detector weighs 4,000 tons and is a collection of several small and large sized detectors, each performing a specific role during collection of data from RHIC collision. Fig. 2.2 shows the layout of the PHENIX detector. The detectors are grouped into *two central arms, two muon arms* and *event characterization detectors*. Central arms has detectors meant for measuring particles like *pions, protons, kaons, deuterons, photons and electrons*. Muon arms are dedicated for measuring muon particles and the event characterization detectors provide information about collision centrality and event vertex. Other than these a set of three huge magnets are used for bending the trajectories of the charged particles.

The data analyzed for this research work is from PHENIX data taking run during 2008. Further the measurement of heavy flavor single electrons is being

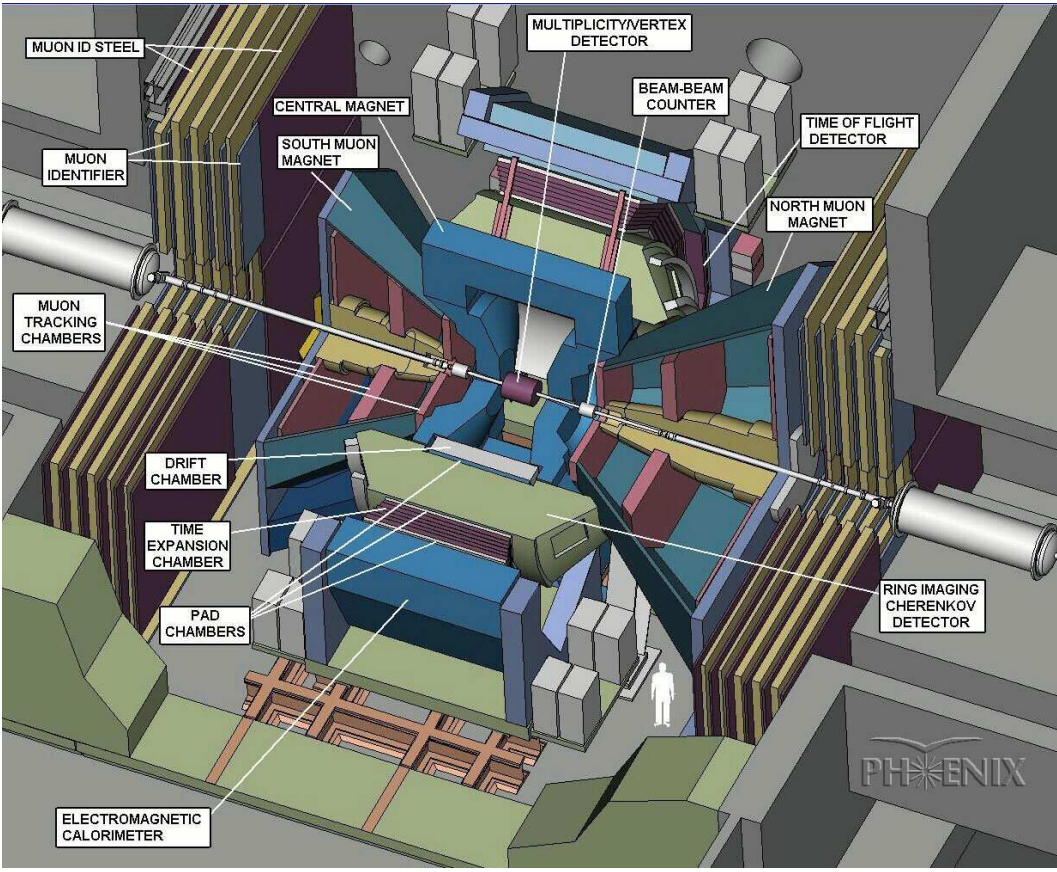


Figure 2.2: Layout of PHENIX detector.

done using the Central arm detectors along with event characterization detectors, so detailed explanation of the detectors in the PHENIX central arm and event characterization is being given here.

### 2.2.1 PHENIX coordinate system

Fig. 2.3 shows the PHENIX coordinate system. The beamline is along z axis. The collision point is at  $(0,0,0)$ . Both cartesian and cylindrical coordinate system is being used. Positive z axis is denoted by North, negative z axis is denoted by South, positive x axis is denoted by East and negative x axis is denoted by West. In cylindrical system the PHENIX coordinate system is denoted by  $(\theta, \phi, z)$ . The polar angle  $\theta$  is along the z axis such that it is  $90^\circ$  perpendicular to the z axis.

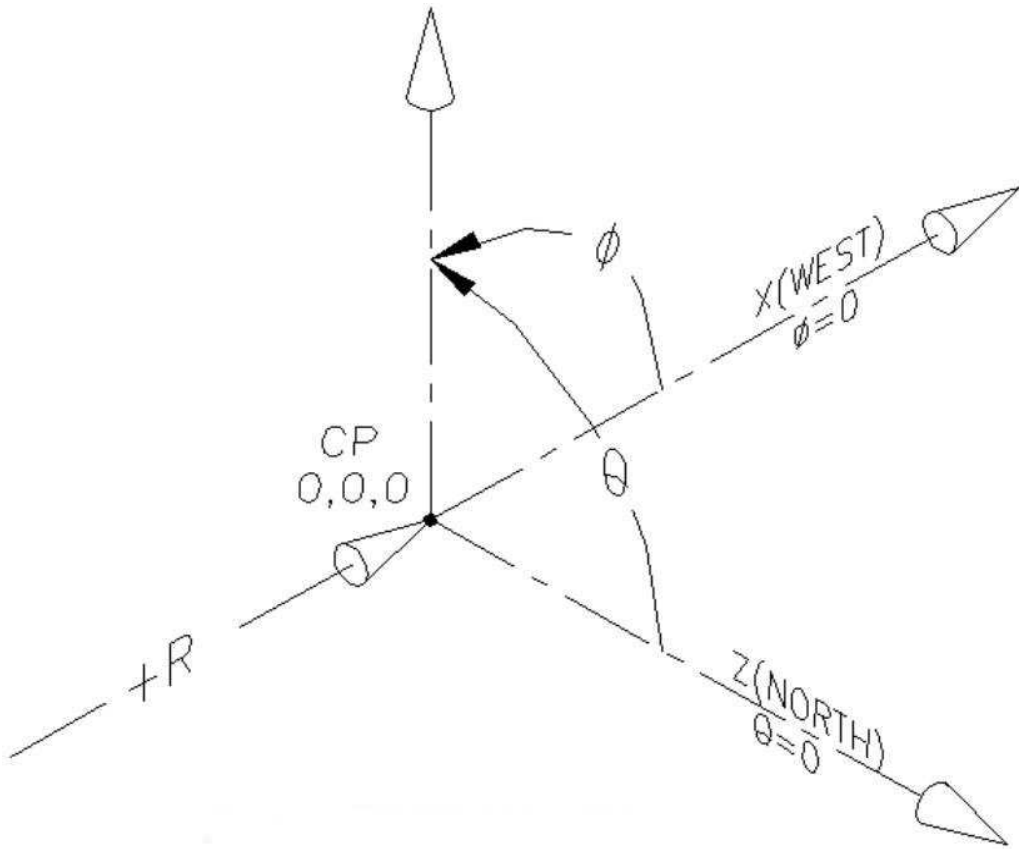


Figure 2.3: Schematic view of PHENIX coordinate system. For details see the text.

The azimuthal angle  $\phi$  is defined in the x-y plane perpendicular to the beam direction.

Fig. 2.4 shows the PHENIX detector acceptance in terms of azimuthal angle ( $\phi$ ) and rapidity ( $y$ ). The muon arms cover the full acceptance in azimuthal plane in the North and South arm while the Central arm tracking detectors like Drift Chamber, EMCAL and RICH has limited azimuthal region coverage at central rapidity. As shown in the Fig. 2.4 the central arm has coverage of  $180^\circ$  in  $\phi$  and  $-0.35 < \eta < 0.35$  whereas the muon arms has full  $\phi$  coverage and  $1.2 < |\eta| < 2.2$ .

Fig. 2.5 shows the PHENIX detector setup during the year 2008 data taking. The top panel is the cross sectional view of the detector with the beam axis (z axis) passing through the plane of the paper. The central arm detectors are on

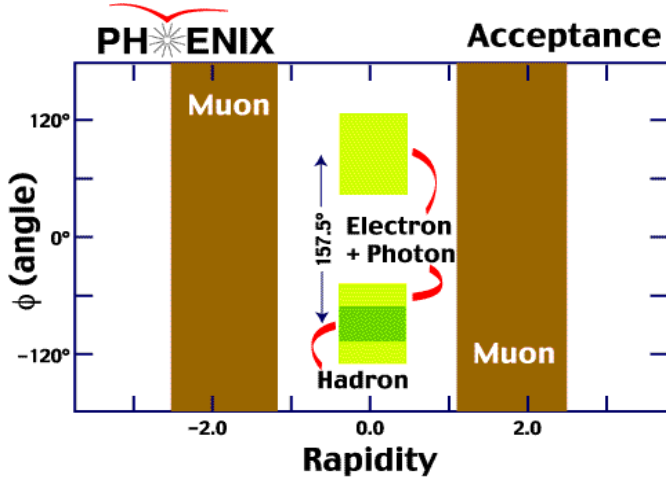


Figure 2.4: PHENIX detector acceptance. x axis is rapidity ( $y$ ), and y axis is azimuthal angle.

the left and right hand side of the beam axis. Lower panel shows the side view of the PHENIX detector.

### 2.2.2 PHENIX Global detectors

Beam-Beam counter (BBC), Zero Degree Calorimeter (ZDC) and Reaction Plane detector (RxNP) comprises the Global detector set, meant for centrality measurement, collision vertex determination and reaction plane measurement of each collision.

#### Beam-Beam Counters (BBCs)

The main purposes of BBCs are to act as a trigger to the collisions at the interaction region and to measure the collision vertex alongwith centrality of collision [68]. The BBC has two identical sets of counters located at 144 cm on both sides of the collision vertex (North and South side of PHENIX coordinate system) along the beam line at  $3.0 < \eta < 3.9$  and full azimuthal angle coverage. Two arrays of Cherenkov counters with quartz radiators and photomultiplier tubes makes the BBC. Fig. 2.6 shows the BBC and the PMT used in it.

2008

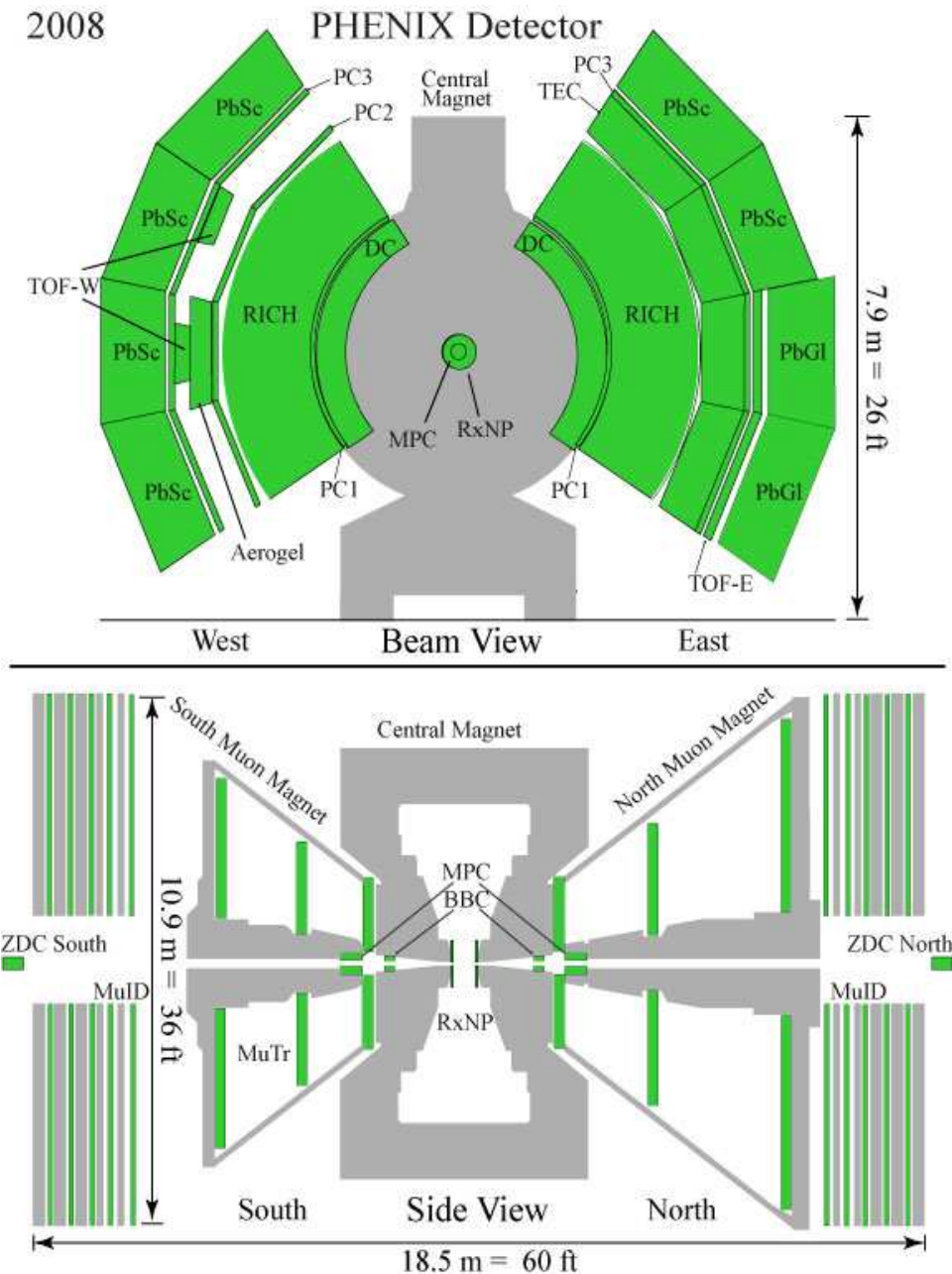


Figure 2.5: PHENIX detector layout during 2008 data taking.

Knowing the average hit timing for each set of BBC counters one can get the collision time and the z vertex position. The following equations are used for determining the collision time and z vertex position



Figure 2.6: The left panel shows the BBC and the right panel shows photomultiplier tube (PMT) used in the BBC. The PMT is of 25.4 mm diameter and has a 3 cm quartz mounted on it. The quartz act as a Cherenkov radiator.

$$T_0 = \frac{(T_S + T_N)}{2} \quad (2.1)$$

$$Z_{vertex} = \frac{c}{2}(T_S - T_N), \quad (2.2)$$

where,  $T_S$  and  $T_N$  are the average hit timing for each set of BBC counters located at the North and South of the PHENIX detector.

### Zero Degree Calorimeters (ZDCs)

The ZDCs [69] are hadronic calorimeters located at 18m from the interaction point along the downstream of the first accelerator DX dipole magnet [70] as shown in Fig. 2.7.

All the four experiments at RHIC have ZDCs installed. Since the charged particles (like spectator protons) are deviated by the DX magnets so ZDCs measure neutral energy of spectator neutrons which did not participate in the collision within a 2 mrad cone about the beam direction. These spectator neutrons still carry a significant fraction of the beam momentum. The measurement of neutral energy by ZDCs is basically counting the number of free spectator neutrons. This information is used in anti-correlation with the total charge deposited in the BBC to characterize the event centrality as shown in Fig. 2.8 . Other than event

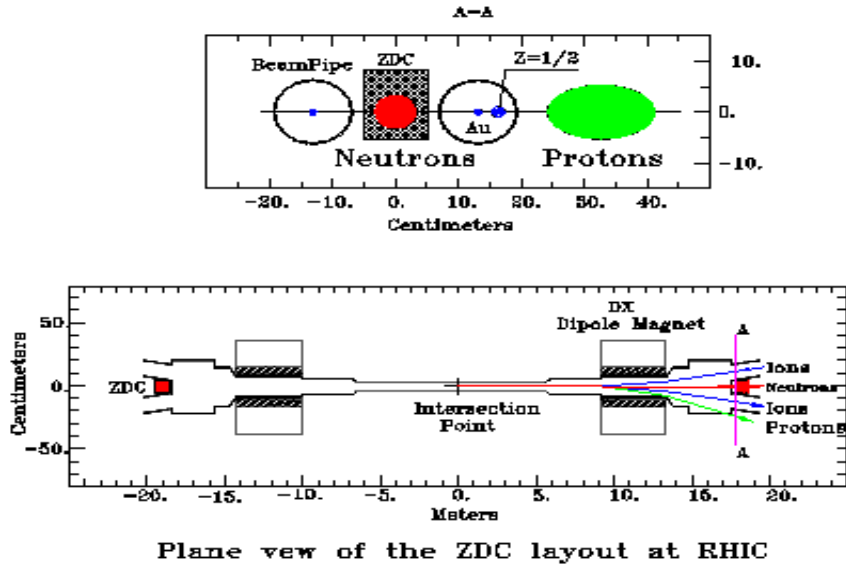


Figure 2.7: Top panel shows the cross sectional view of the location of ZDC. The  $z$  axis is perpendicular to the plane of the paper. The deflection of protons due to DX magnets is shown by green blob. The neutrons are shown by red blob and are being captured by ZDC. Bottom panel is the plane view of RHIC beampipe , location of ZDC and the collision region.

centrality determination the coincidence signals from the ZDCs on either side of the interaction region provides the luminosity monitoring.

### Reaction Plane detector (RxNP)

The Reaction Plane Detector [71] shown in Fig. 2.9 is meant for accurately measuring the reaction plane angle of heavy ions collisions. The RxNP detector comprises of scintillator paddle detector, optical fiber light guides and photomultiplier tubes. The optical fiber light guides carries the light produced by the paddle towards the PMT with minimum possible attenuation. Two sets of RxNP are placed on either side of the collision vertex ( $38 < |z| < 40$  cm). Each of them has 12 segments in  $\phi$  and 2 segments in  $\eta$  ( $1.0 < |\eta| < 1.5$  and  $1.5 < |\eta| < 2.8$  ) as shown in Fig. 2.10.

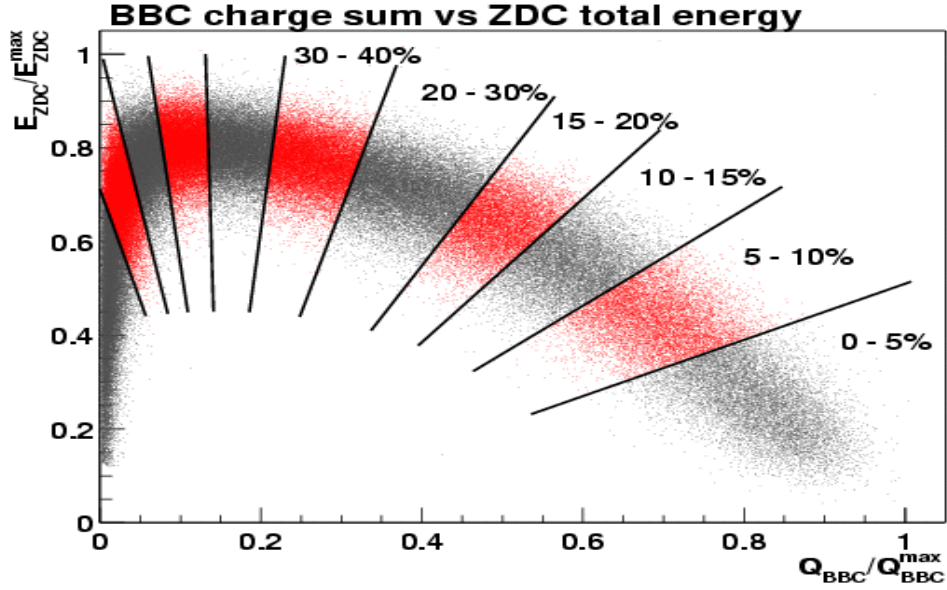


Figure 2.8: Correlation between total energy deposited in ZDC and total charge measured by BBC for  $Au + Au$  collision. The various centrality classes are labelled in the figure. 0-5% centrality corresponds to most central collision whereas the extreme left region in the figure corresponds to peripheral collision.

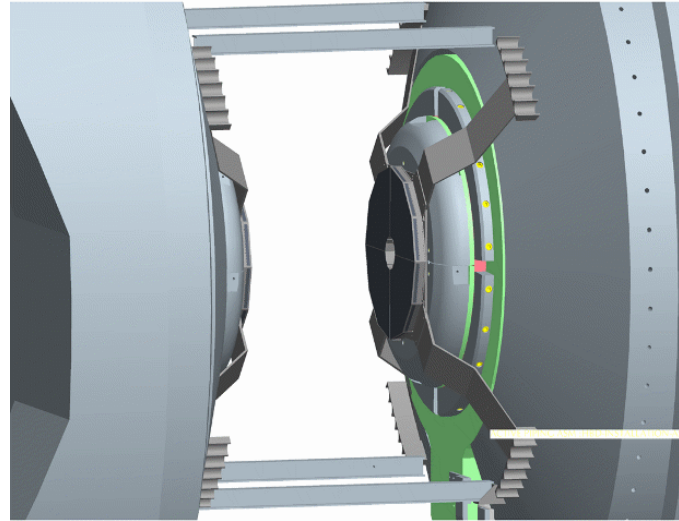


Figure 2.9: Pictorial representation of Reaction Plane detector.

The anisotropic flow of the produced particle is used by the RxNP to measure the reaction plane angle. The anisotropic flow can be expressed in the form

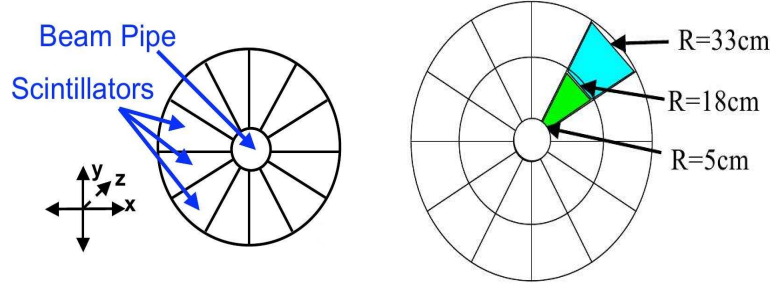


Figure 2.10: Left panel shows the 12 scintillators segments for RxNP detector. Right panel shows the division of the RXNP detector in 2 segments.

of Fourier expansion [72].

$$\frac{d(wN)}{d(\phi - \Psi_R)} = \frac{\langle wN \rangle}{2\pi} \left( 1 + \sum_n 2\nu_n \cos[n(\phi - \Psi_R)] \right), \quad (2.3)$$

where  $n$  is the  $n^{th}$  harmonic of the produced particle flow,  $N$  is the number of measured particles,  $\phi$  is the particle angle,  $w$  are weights and  $\nu_n$  is the anisotropy parameter. The same anisotropy is used for measuring the reaction plane angle using

$$\Psi_n = \frac{1}{n} \tan^{-1} \left( \frac{Y_n = \sum_i w_i \sin(n\phi_i)}{X_n = \sum_i w_i \cos(n\phi_i)} \right), \quad (2.4)$$

where  $v_n$  is the measured reaction plane angle from the  $n^{th}$  harmonic particle distribution and  $X_n$  and  $Y_n$  are the event flow vectors. Before the RxNP detector was installed the reaction plane angle was measured using the BBC detectors. However the low resolution of BBC for particles like photons,  $J/\psi$  and high  $p_T$  particles caused new discoveries difficult which made the installation of RxNP detector of utmost importance.

### 2.2.3 Central detectors

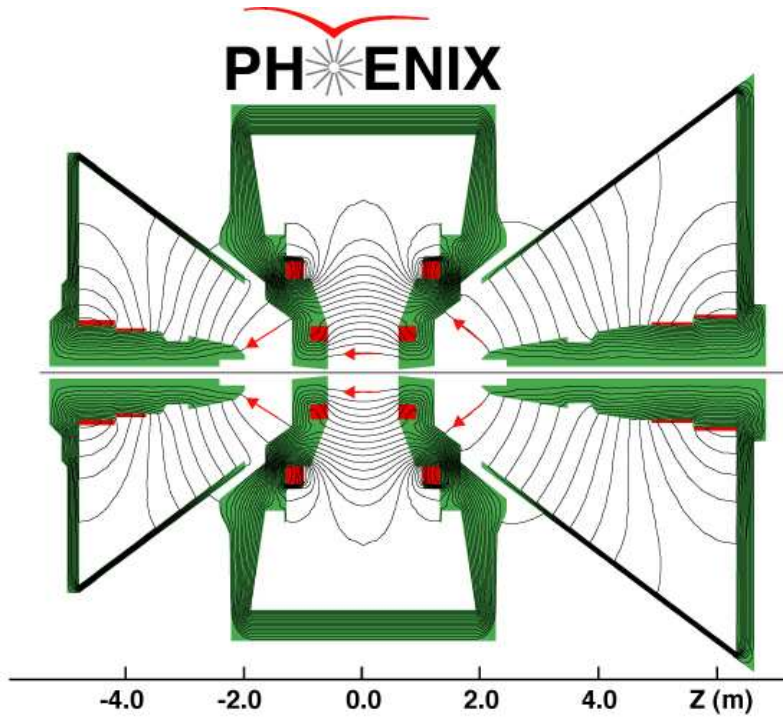
The PHENIX Central arm detector consists of a set of detectors meant for tracking the particles, to identify them and to measure the charge and momentum of

particles produced during the collision of ions. Central magnet present in the Central arm provides the magnetic field which helps in measuring the charge and momentum of particles. The Central arm is divided into East and West arms and each arm has the azimuthal coverage of  $|\phi| < 90^\circ$  and rapidity coverage of  $|\eta| < 0.35$ . The Central arm detectors can be divided into tracking detectors and particle identification detectors. Drift Chamber (DC), Pad chamber (PC) and Time Expansion Chamber (TEC) are the tracking detectors whereas Time of Flight (TOF), Ring Imaging Cherenkov detector (RICH), Electromagnetic Calorimeter (EMCAL) are the particle identification detectors.

## Central Magnet

The Central magnet [73] provides the magnetic field for bending the charged particles in order to determine the transverse momentum of the particles produced. It consists of an inner and outer pair of concentric Helmholtz coils inside a steel chamber providing axial field around the interaction point parallel to the beam direction as shown in Fig. 2.11. The central magnet is about 9 meters tall and weighs around 500 tons having acceptance of  $|\eta| < 0.35$ .

The two pairs of Helmholtz coils are capable of running with the same (++, --) or opposite (+-) polarity. The (++) configuration, which was present during the RHIC 2008 data taking, provides a total field integral of  $\int B dl = 1.5 \text{Tesla} - \text{meters}$  around the first 2 meters from the interaction point . For  $R > 2\text{m}$  where the tracking detectors are present, the magnetic field provided by the Central magnet is zero so that the tracking models for the tracking detectors, which assumes straight tracks, can make the tracking efficient. The zero field in the region of central arm detectors minimizes the smearing of Cherenkov rings in the RICH (Ring Imaging CHerenkov) as well.



Magnetic field lines for the two Central Magnet coils in combined (++) mode

Figure 2.11: PHENIX central and muon arm magnets in  $++$  mode. The field direction is represented by the arrows on the inner field lines.

### Drift Chambers

The Drift Chambers [74] are cylindrically shaped multiwire gas chambers each of which are located in the region from 2 to 2.4 m from the z axis and 2 m along the beam direction on both East and West arms of PHENIX detector, making them to experience the residual magnetic field with a maximum of 0.6 kG from PHENIX magnet system. The gas volume limit (active volume) for DC is defined by Al-myler windows and is being supported by a cylindrical titanium frame as shown in the Fig. 2.12.

The main purpose of the DC is to measure the charged particles trajectories in the  $r-\phi$  direction, determining the  $p_T$  of each particle with high resolution and the invariant mass of the particle pairs. The goal of DC is to measure the dielectron mass ( $e^+e^-$ ) from  $\phi$  decay having better resolution than its natural

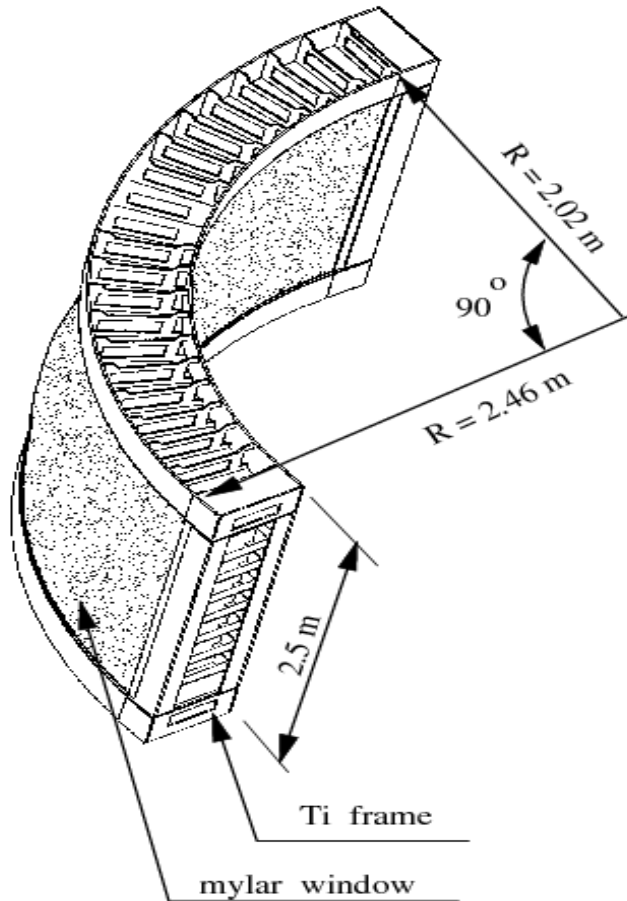


Figure 2.12: Schematic diagram of Drift chamber frame [74].

width of 4.4 MeV. Also the DC is expected to have a good tracking efficiency for the highest multiplicities at RHIC. All these factors imposes the following requirements on the DC :

- Single wire resolution better than  $150 \mu\text{m}$  in  $r-\phi$ .
- Single wire two track separation better than 1.5 mm.
- Single wire efficiency better than 99%.
- Spatial resolution in the z direction better than 2 mm.

Each drift chamber frame has modules divided in 20 equal sectors covering  $4.5^\circ$

in  $\phi$ . Each sector has six types of wire modules denoted by X1, U1, V1, X2, U2 and V2, stacked radially in each sector. Each module contains 4 anode or sense planes and 4 cathode planes with a 2-2.5 cm drift space in the  $\phi$  direction. The X1 and X2 wire cells running parallel to the beam measures the track precisely in  $r - \phi$  plane. Two sets of small angle U, V wire planes follows the X1 and X2 wire cells and are used in the pattern recognition. The z coordinate of the track is being measured by U1, V1, U2 and V2 wires having stereo angles of about  $6^\circ$  relative to the X wires. The selection of stereo angle is based on the requirement of minimizing track ambiguities by matching the z resolution of the pad chambers. Each of the X and U, V-stereo cells contain 12 and 4 sense wires, respectively resulting in 40 drift cell in the DC located at different radii. Fig. 2.13 shows the layout of the wires within one DC sector.

The Potential (P) wires separated the anode wires and the Gate (G) and Back (B) wires surrounds the anode wires. The strong electric field formed by the P wires separates the sensitive regions of each anode wires and the G wired terminates the unwanted drift lines by limiting the track sample length to roughly 3 mm. The G wires thus minimizes the time spread of drifting electrons from a single track causing decrease in the pulse width. The calculation based on this wire layout is shown in Fig. 2.14.

For the efficient track recognition for up to 500 tracks, each sense wire is separated in the center into two halves. Each half of a sense wire is then read out independently. These two halves of sense wire are electrically isolated by attaching a low mass central support (made of kapton with 100  $\mu\text{m}$  thickness) at the center. In total, DC system contains roughly 6500 anode wires and about 13,000 readout channels.

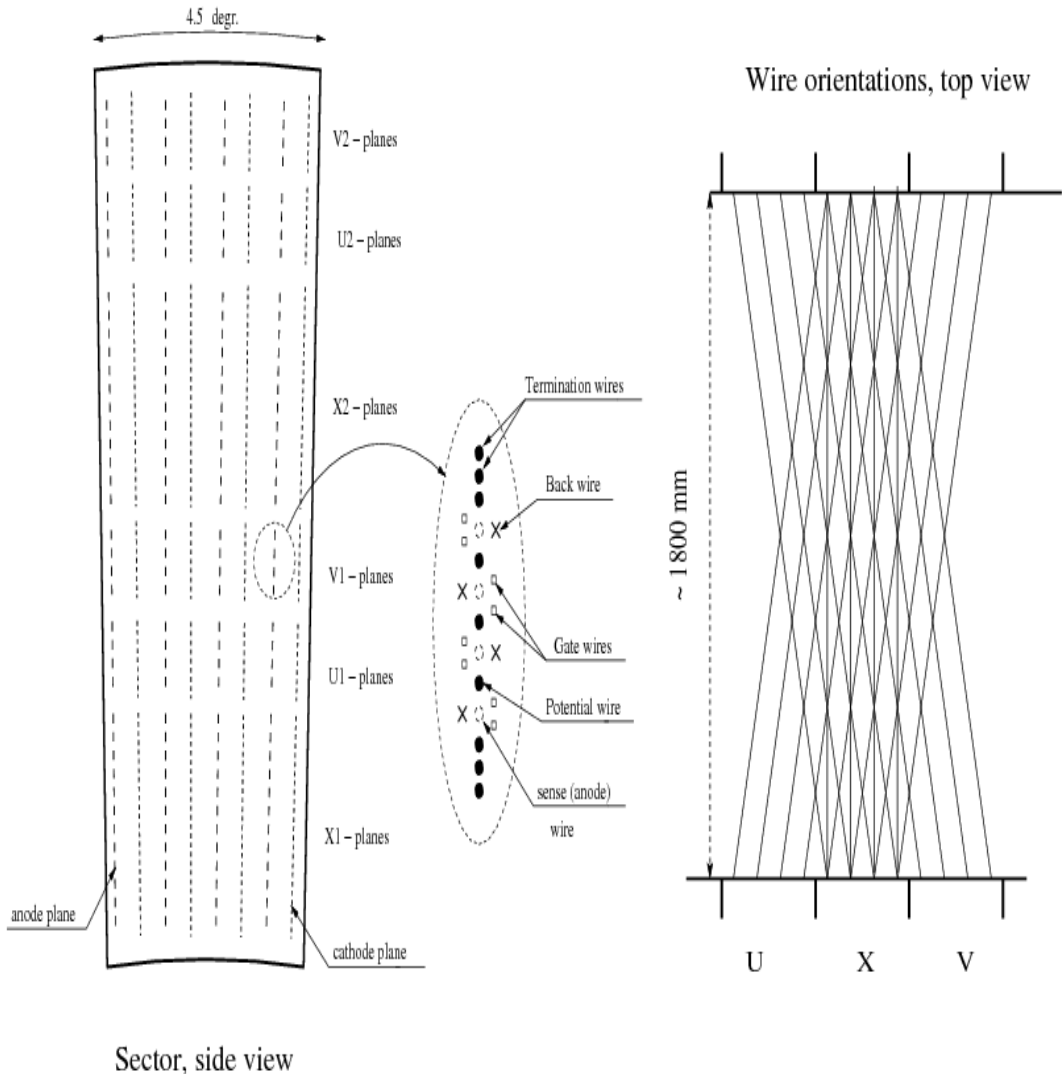


Figure 2.13: Schematic layout of the DC wire orientation [74].

### Pad Chambers

The PHENIX Pad Chambers (PC) are multiwire proportional chambers forming three separate layers of the PHENIX tracking system. Each detector contains a single plane of wires inside a gas volume bounded by two cathode planes. One of the cathode plane is segmented into an array of pixels as shown in Fig. 2.15.

The PC system determines space points along the straight line trajectories

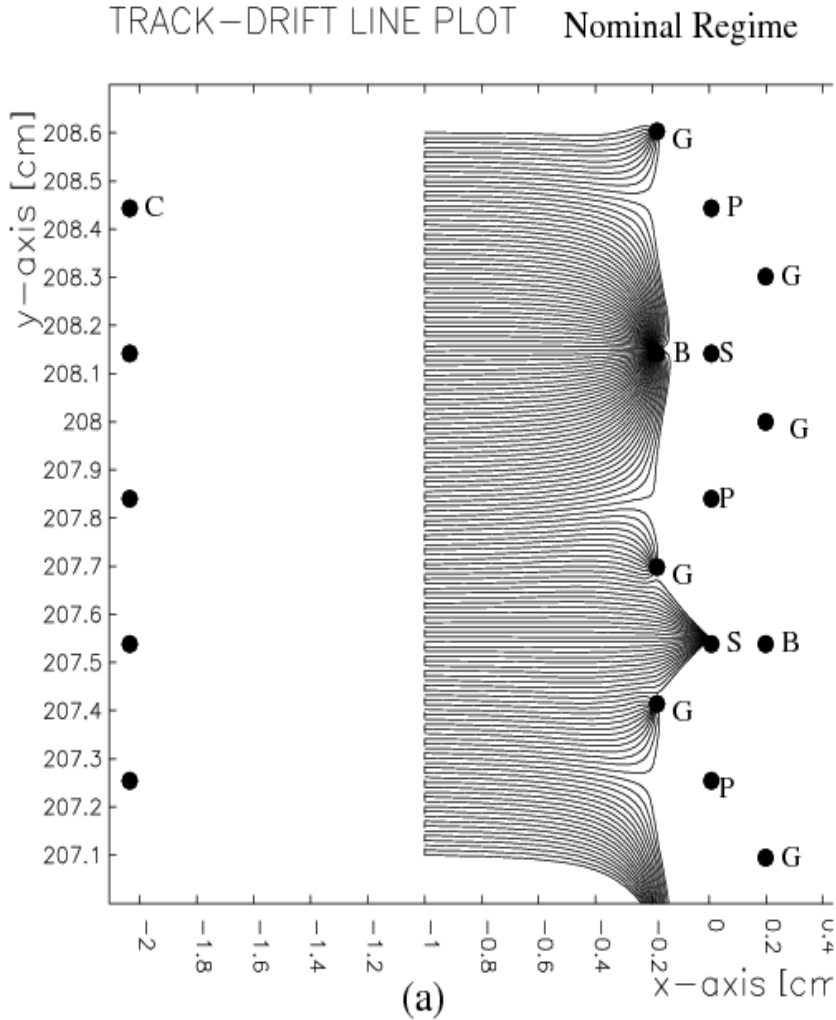


Figure 2.14: Calculation of drift lines for the optimum electric field configuration [74]. Different types of wire are marked by letters: B - back, C - cathode, G - gate, P - potential, S - sense or anode wires.

outside the magnetic field. PC system is divided into three parts named as PC1, PC2 and PC3, located in different locations of PHENIX detector. PC1 is located between DC and Ring Imaging Cherenkov Counter on both East and West arms and is essential for determining the three-dimensional momentum vector by providing the z-coordinate at the exit of DC. PC3 is in front of the EMCAL on both the East and West arms of PHENIX. PC2 is located only in the West arm behind the RICH. Particle identification information is also provided

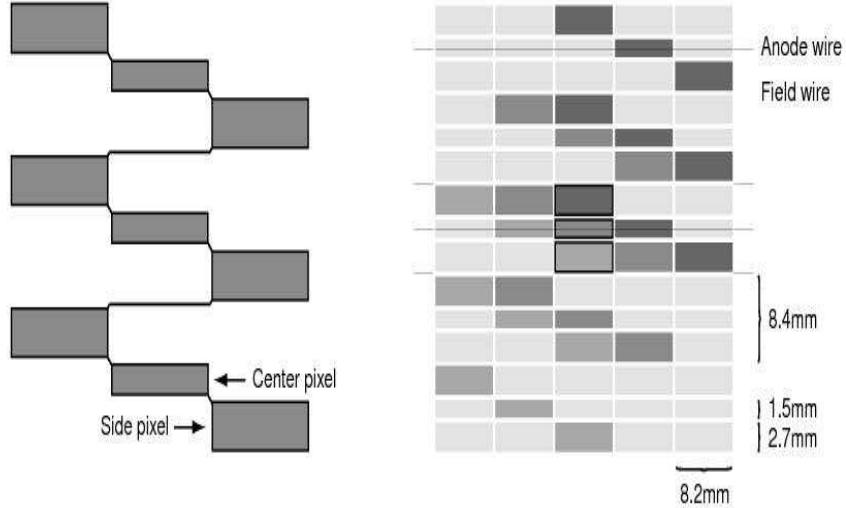


Figure 2.15: Left hand side shows the pad and pixel geometry. The center of the right hand side figure shows a cell defined by three pixels [74].

by PC particularly for electron identification. The DC and PC1 information gives direction vectors through RICH, while PC2 and PC3 resolves ambiguities in the outer detectors, arising from the secondary interactions inside EMCAL or from the particle decay outside the apperture of the DC and PC1 or bending of low momentum primary tracks around PC1 in the magnetic field and striking PC2 and PC3.

### Time Expansion Chamber (TEC)

The purpose of TEC is to provide the direction vectors which are matched to the additional track information from the DC's and PC's. The TEC is located at the East side of PHENIX between RICH and PC3 as shown in Fig. 2.5. It has the acceptance of  $\pi/2$  in azimuth and  $|\eta| < 0.35$ . It is divided into four sectors and each sector has coverage of  $\pi/8$  in azimuth and  $|\eta| < 0.35$ . Six independent chambers, made from the combination of machined graphite-composite, S2-glass and FR-4 components, are stacked together to form a wedge-shaped sector as shown in Fig. 2.16 which are the building blocks for TEC.

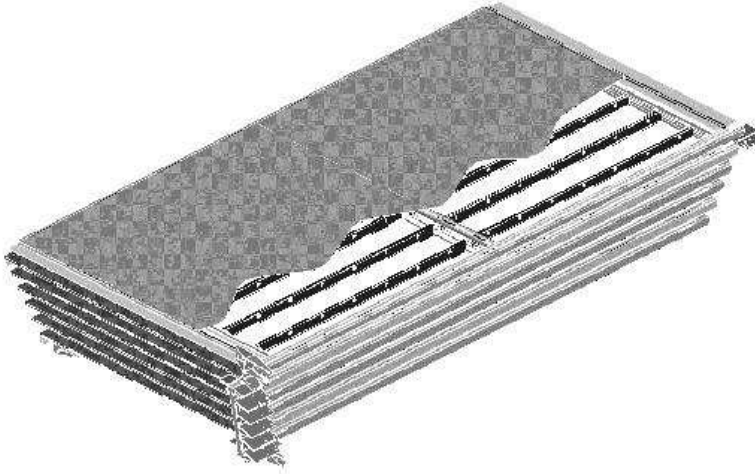


Figure 2.16: Schematic diagram of TEC six-plane sector [74].

The TEC wire chamber contains a combination of biased metalized-myler cathode planes and wire planes. The planes are biased for providing shape to the electric field and setting the gas gain. During the passage of a charged track through the TEC, the gas inside the TEC gets ionized and the resulting electron clusters gets drifted in the radial direction into the amplification region where the anode wires collects the signal as shown in the Fig. 2.17.

### **Ring Imaging Cherenkov Detector (RICH)**

Each central arms (East and West) of the PHENIX has RICH detector which works on the principle of Cherenkov radiation. Whenever a charged particle moves in a medium having refractive index  $n$ , with a velocity  $v$  greater than the velocity of light in the medium ( $c/n$ ), electromagnetic radiation, called Cherenkov radiation is emitted. The charged particle, traversing in the medium, polarises atoms on its track making them electric dipoles. As long as  $v < c/n$ , the arrangement of dipoles are symmetric around the charged particle path, making the integrated dipole field over all the dipoles to vanish. As soon as the charged

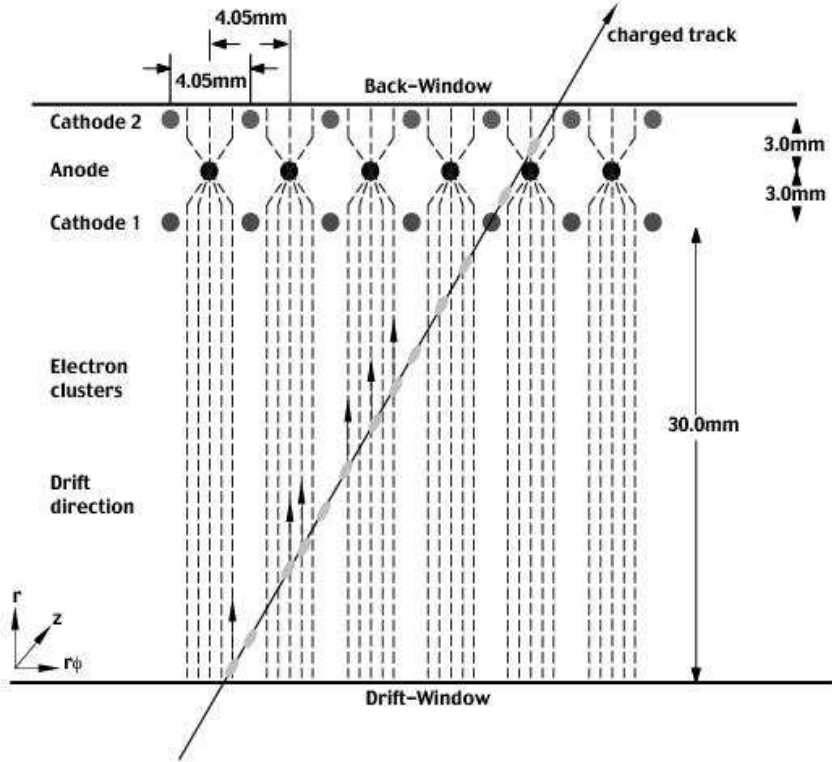


Figure 2.17: Schematic diagram of the operation inside TEC. The anode cathode configuration is shown together with the  $\vec{E}$ -field lines [74] For details see the text.

particle moves with  $v > c/n$ , the dipole field appears due to the broken symmetry in the alignment of dipoles. This causes the emission in Cherenkov photons making a cone around the track of charged particle with half angle given by

$$\cos\theta_c = \frac{1}{n\beta}. \quad (2.5)$$

The number of Cherenkov photons emitted per unit path length with wavelengths between  $\lambda_1$  and  $\lambda_2$  is given by [75]

$$\frac{dN}{dx} = 2\pi\alpha z^2 \int_{\lambda_1}^{\lambda_2} \left( 1 - \frac{1}{(n(\lambda))^2 \beta^2} \right) \frac{d\lambda}{\lambda^2}. \quad (2.6)$$

The goal of RICH along with TEC and EMCAL is to limit the false identification of hadrons as  $e^+$  and  $e^-$  to less than 1 per  $10^4$  for momenta below Cherenkov threshold.

Fig. 2.18 shows the cutaway diagram of one of the RICH detectors. The volume of each RICH detector is  $40m^3$  with an entrance window area of  $8.9m^2$  and an exit window area of  $21.6m^2$ .

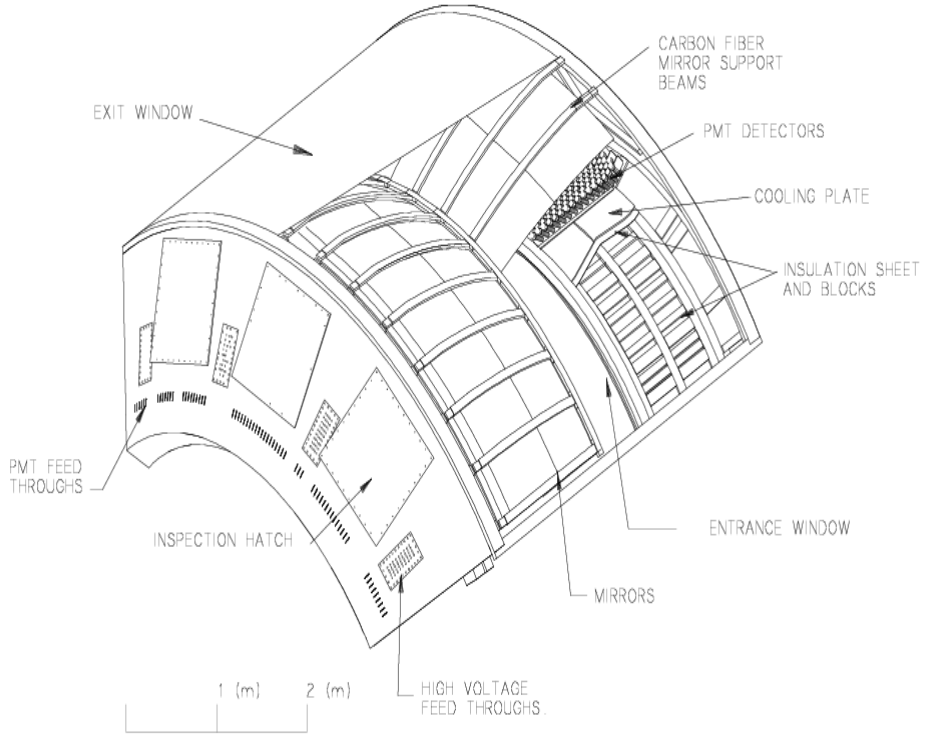


Figure 2.18: RICH one arm cutaway schematic diagram [76].

For heavy ion collisions ethane is considered to be the suitable radiator gas to be filled in the volume of RICH. It has the pion Cherenkov threshold of 3.71 GeV/c and produces an average of 20 photons per ring for  $\beta = 1$ . For  $p + p$  collisions or for light ions collisions  $CO_2$  is considered to be the suitable gas which has a pion Cherenkov threshold of 4.65GeV/c producing an average of 12

photons per ring for a  $\beta = 1$  particle. There are 48 composite mirror panels in each of the RICH detector which forms two intersecting spherical surfaces having total reflecting area of  $20m^2$ . The spherical mirrors focus Cherenkov light onto two arrays of 1280 Hamamatsu photomultiplier tubes located on either side of the RICH entrance window.

### **Time-of-Flight Counters (ToF)**

Time-of-Flight (ToF) is used for identifying particles by comparing the particle time of flight to the measured momentum of particles. The ToF is installed at a distance of 5.1 m from the collision vertex in between the Pad Chamber (PC3) and EMCAL in the East arm of the PHENIX detector. It covers  $70^\circ \leq \theta \leq 110^\circ$  and  $30^\circ$  in azimuth in the central arm. 10 panels of ToF walls builds up the ToF detector. Further each of the ToF wall consists of 96 segments equipped with a plastic scintillator slat and photomultiplier tubes readable at both ends. The slat provides the time and longitudinal position information of particles hitting it.

Fig. 2.19 shows a schematic view of one panel of ToF detector consisting of 96 plastic scintillation counters with photomultiplier tubes (PMT's) at both ends along with light guides and mechanical support. Aluminium foil wraps the scintillator rod and light guides. The scintillator rod and light guides are then glued on the honeycomb board which provides a rigid structure. In order to avoid geometrical conflicts between PMTs of neighboring slats scintillators with two different lengths (637.7 and 433.9 mm) are assembled in an alternating fashion.

### **Electromagnetic Calorimeter (EMCAL)**

The electromagnetic calorimeter measures the energy deposited by the photons and electrons in the EMCAL mass. The electrons and photons having high-energy loses energy in the matter by Bremsstrahlung [77, 78] and  $e^+e^-$  pair

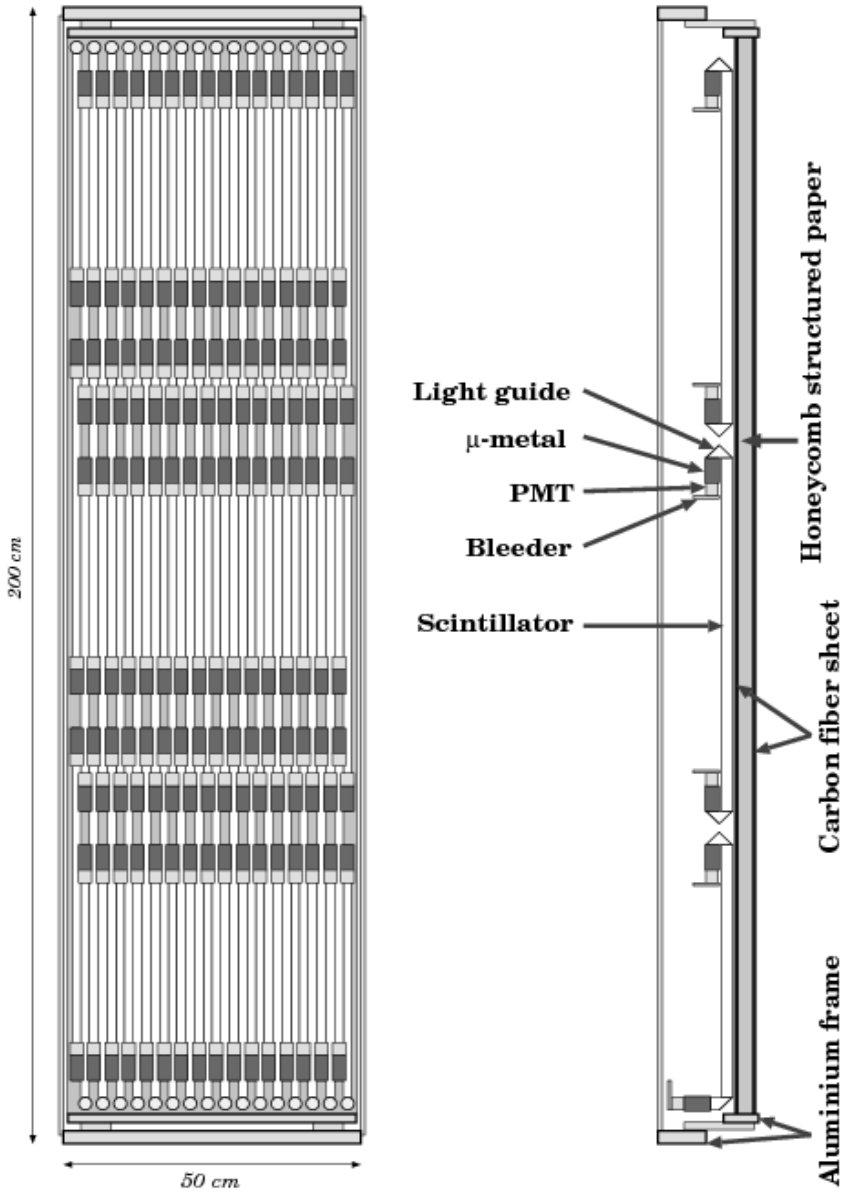


Figure 2.19: Schematic diagram of one of the ToF panel [76].

production [79, 80], respectively. The energy loss by them is defined by the radiation length  $X_0$  [81, 82, 83, 84], which is the mean length of the traversed particle in the matter after which an electron has lost  $1/e$  of its energy. Radiation length is also  $7/9$  of the mean free path for  $e^+e^-$  pair production by a photon. Other than that it also provides the trigger on rare events with high momentum

photons. The EMCAL is divided into eight sectors each has the coverage of  $22.5^\circ$  in azimuth and  $|\Delta\eta| = 0.35$  in pseudorapidity. The two top sectors of the West arm and all the four sectors in the East arm are lead-scintillator (PbSc) sampling calorimeter. The two bottom sectors are lead-glass (PbGl) Cherenkov calorimeters.

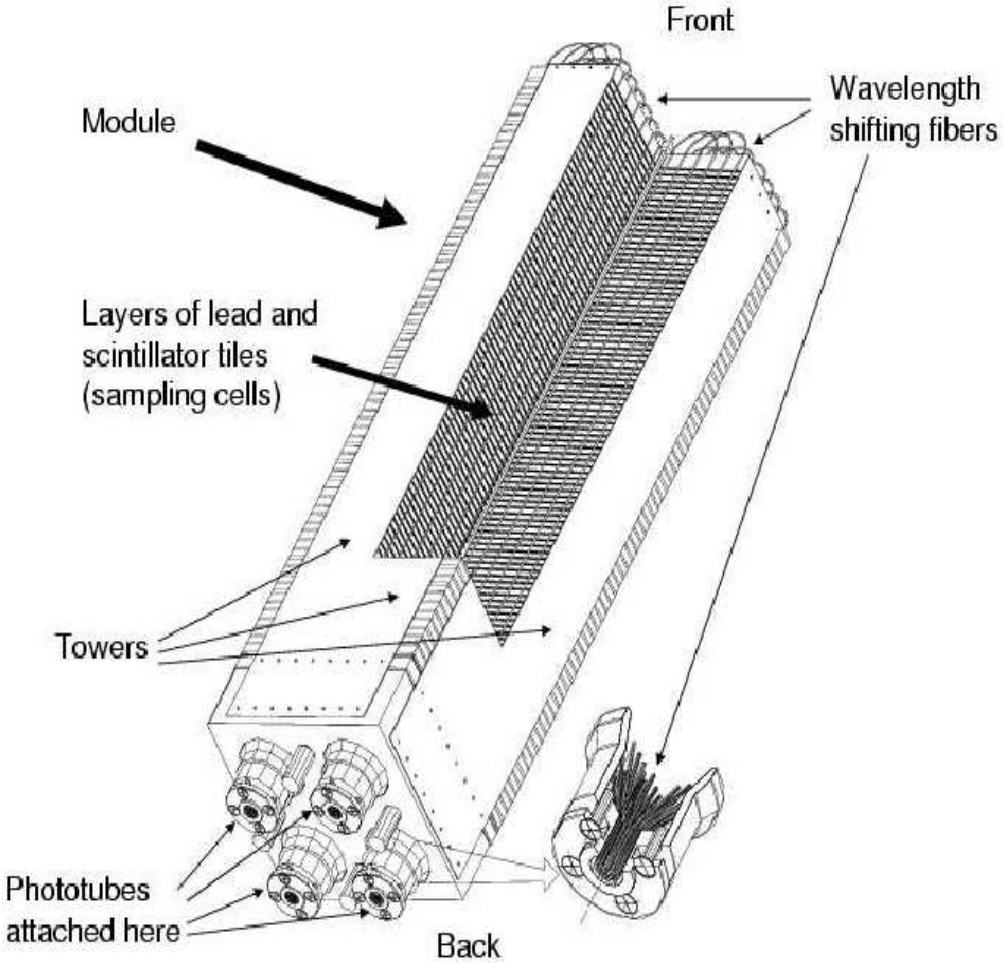


Figure 2.20: PbSc module interior displaying a stack of scintillator and lead plates, wavelength shifting fiber readout and leaky fiber in the central hole [85].

There are total of 15,552 individual towers in PbSc calorimeter which are made of 66 sampling cells with alternating layers of 1.5 mm Pb and 4 mm scintillator [85]. Fig. 2.20 shows a PbSc module having four towers, each of which are

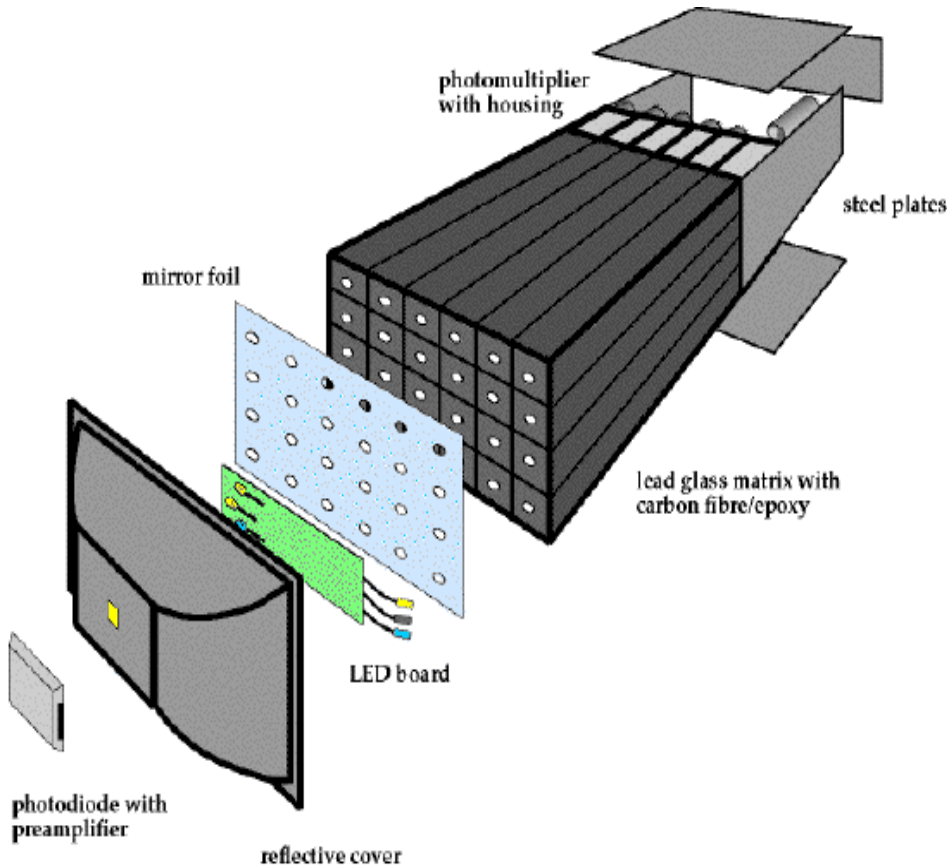


Figure 2.21: Schematic view of PbGl supermodule.

isolated optically and can be read out individually. Each tower has the dimension of  $5.535 \times 5.535 \text{ cm}^2$  in cross section and 37.5 cm ( $18X_0$ ) in length. A common support structure termed as super module holds 36 modules. 18 super modules form a sector. The energy resolution of the PbSc Calorimeter is

$$\frac{\sigma_E}{E} = \frac{8.1\%}{\sqrt{E}} \oplus 2.1\%. \quad (2.7)$$

Each sector of PbGl calorimeter has 192 supermodules (SM) each of which has 24 modules as shown in Fig. 2.21. Each module has cross section of  $4 \times 4 \text{ cm}^2$  and a length of 40 cm ( $14.3X_0$ ) with a photomultiplier as a read out at the end.

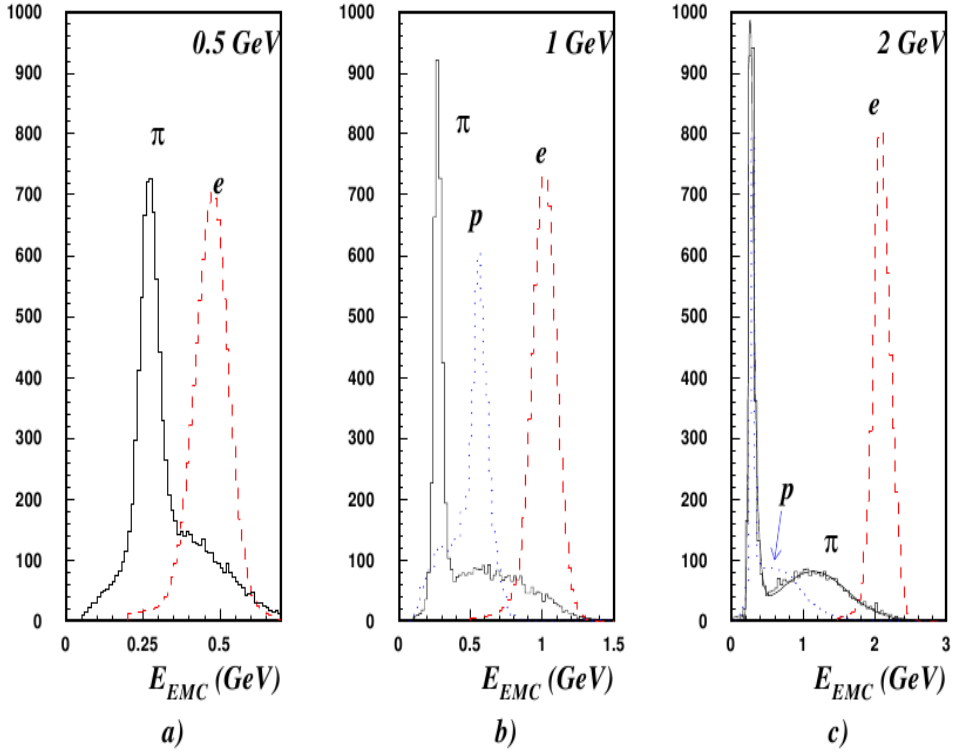


Figure 2.22: The energy spectra of electrons, pions and protons of 0.5, 1 and 2 GeV/c measured in the PHENIX EMC [85].

The energy resolution of the PbG1 Calorimeter is

$$\frac{\sigma_E}{E} = \frac{5.9\%}{\sqrt{E}} \oplus 0.76\%. \quad (2.8)$$

In the PbSc, the scintillation light produced by the electrons within the electromagnetic shower inside the Pb-layer is guided by the wavelength shifting fibres to the phototubes located at the back of each tower. The electromagnetic showers inside the PbG1 is being detected by Cherenkov light radiated by the electrons in the shower. The Cherenkov light is read out at the end of the Calorimeter by photomultiplier tubes.

The hadrons loses energy in the matter through ionization excitations. For

typical hadron energies ( $0.1 \leq E \leq 10$  GeV) the energy deposited in the matter is almost independent of the particle's energy, therefore these particles are called minimum ionizing particles (mip). The nuclear interaction length of PbSc  $\lambda_l = 0.85$  and of PbGl  $\lambda_l = 1.05$  causes few strong hadronic interaction depositing a significant fraction of their energy. The mip peak appears as in Fig. 2.22 for charged pions and protons. Electron peak is also shown for comparison.

The EMCAL serve as Level-1 trigger for events with high momentum photons, triggering when the energy deposited in an area of  $4 \times 4$  overlapping towers surpasses a defined threshold. Also the energy in a area of  $2 \times 2$  overlapping towers can be used in coincidence with the RICH trigger to trigger on events with electron candidates.

#### 2.2.4 Muon Arm Detectors

The present research work does not involve information from Muon Arms, so the description of Muon arms given here is in brief.

The PHENIX muon Arms [86] are located at North and South side of the PHENIX detector and has the rapidity coverage of  $1.1 \leq |\eta| \leq 2.4$  in North arm and  $1.2 \leq |\eta| \leq 2.2$  in the South Arm. Their main aim is to study the vector meson production, the Drell-Yan process (via muon pairs), and heavy quark production (through both muon pairs and single muons). Each muon arm has a muon magnet and two subsystem detectors which work together to measure muons.

# Chapter 3

## Data Analysis

This analysis describes the measurement of single electrons from heavy flavor decays in d+Au collisions at  $\sqrt{s_{NN}} = 200$  GeV. Whenever the term *single electrons* comes up then it has to keep in mind that it includes both electrons and positrons. The important steps of the analysis are briefly outlined here. This analysis begins with the selection of events as discussed in section 3.2. Section 3.4 has the discussion about various electron selection criteria. The  $p_T$  spectra of electrons was corrected for trigger efficiency as well as for tight eID correction which has been discussed in sections 3.7.1 and 3.7.2 respectively. Section 3.7.4 is about the acceptance correction to the ERT and tight eID corrected  $p_T$  spectra of single electron. Section 3.8 shows the single electron cocktail calculation which acts as a background in the heavy flavor single electron measurement. The extraction of the photonic component of single electrons from real data has been shown in section 3.11 along with the comparison of it with the cocktail method calculated photonic component of single electron. The analysis of the single electron spectra is being discussed in section 3.13.

### 3.1 Data files

This analysis has been done from the data taken by PHENIX for d+Au collisions at  $\sqrt{s_{NN}} = 200$  GeV during the year 2008. The data taken were stored in a specific file format called nano DSTs (nDSTs) which are easy to read on ROOT platforms. Two types of data sets are being used in the present analysis :

- data sample with Minimum Bias trigger (MB) condition known as EWG\_MB files
- data sample with electron trigger (ERT) condition known as EWG\_ERT files

EWG\_MB nDSTs are triggered by Minimum Bias (BBCLL1) triggers which requires the condition of at least two photomultiplier tubes of BBC simultaneously registering hits. However in order to study specific events containing, e.g. electrons, MB triggered events won't be of much use and that's why PHENIX has special triggers in order to study these kind of rare events. For electron measurement upto high  $p_T$  Electron trigger (ERTLL1\_E&BBCLL1) is used which is based on energy measurement by EMCAL and matched hits in the RICH. If the energy measured by the EMCAL tower is more than the set threshold along with a matched hit in the RICH then the trigger is fired. During the  $d + Au$  RUN in the year 2008 the ERT trigger thresholds were 600 MeV and 800 MeV. It is important to select events of our interest, proper fiducial cuts, identifying the proper electron selection criteria which has been discussed in sections 3.2, 3.3 and 3.4, respectively.

### 3.2 Event selection

Fig. 3.1 shows the  $z_{vertex}$  distribution of events in  $d + Au$  collision at  $\sqrt{s_{NN}} = 200$  GeV. Only those events are to be selected which lies near  $z_{vertex} = 0$  cm. This

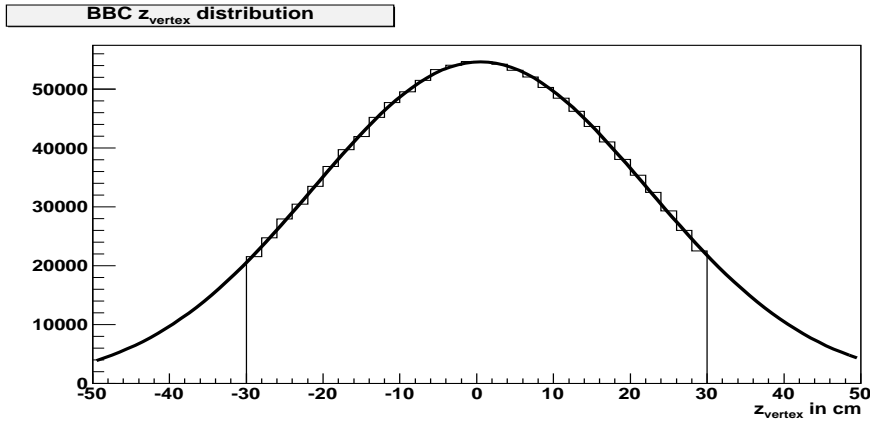


Figure 3.1:  $z_{vertex}$  distribution of events in  $d + Au$  collision at  $\sqrt{S_{NN}} = 200$  GeV. y axis is counts and x axis is the range of collision vertex along z axis of PHENIX in cm. The distribution is fitted with Gaussian function in order to determine the full width at half maximum based on which events lying between particular range of  $z_{vertex}$  are selected.

is because the events far away from the origin will have the higher probability to create particles hitting the nose cones of the PHENIX magnets. The distribution in the fig. 3.1 is centered at origin. In order to select the range of  $z_{vertex}$  within which we can select events, the  $z_{vertex}$  distribution is fitted with Gaussian. The full width at half maximum is around 20.0 cm. Thus only those events are selected which lies within the collision vertex ( $Z_{vertex}$ ) of :

#### **Zvtx cuts**

$$-20 \text{ cm} < z_{vtx} < 20 \text{ cm}$$

### **3.3 Fiducial cuts**

Due to continuous long operation of the detector the data taking ability gets reduced. Also due to various technical snags some of the areas of detector don't manage to take high quality of data. These areas which don't manage to take data are called dead areas of the detector and these areas, if not removed, contributes to the background. The data associated with dead areas of detector are being removed in this analysis by applying suitable fiducial cuts. List of the type

of fiducial cuts that has been applied in my analysis are below:

### Fiducial cuts

- HBD support removal  
 $\phi < 0.7$  or  $\phi > 2.41$
- DC, PC dead area

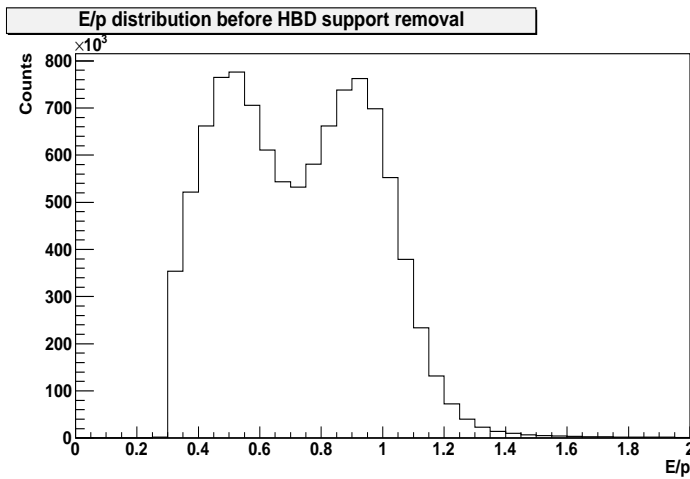


Figure 3.2: E/p distribution of single electrons before HBD support removal.

The Hadron Blind Detector (HBD) [87, 88] was present during Run7. Though it was removed after Run7, the support structure for that was still there during Run8 which produced electrons due to extra gamma conversion giving rise to background. Fig. 3.2 shows the E/p distribution of single electrons before HBD support removal. There is a big hump around E/p 0.5. This is because of the extra conversion electrons due to HBD support structure. This can be removed by applying the suitable Fiducial cut.

Fig. 3.3 shows the phi distribution for  $E/p > 0.7$  and for  $E/p < 0.7$ . For  $E/p < 0.7$  there are two peaks at  $\phi = 0.7$  and  $\phi = 2.5$ . These peaks are due to extra conversion electrons. These are removed by applying HBD support structure cut of  $\phi < 0.7$  or  $\phi > 2.41$ . Fig. 3.4 shows the E/p distribution of single electrons after applying the above mentioned condition resulting in the

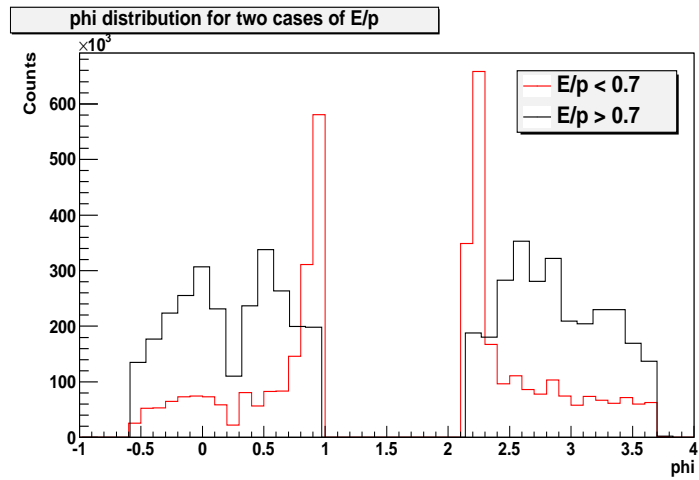


Figure 3.3: phi distribution with eID but without fiducial cut. Red colored distribution is for  $E/p < 0.7$  and black colored is for  $E/p > 0.7$ . Below  $E/p = 0.7$  there are two spikes in phi. That is because most of the conversion takes place at  $E/p < 0.7$ .

disappearance of hump.

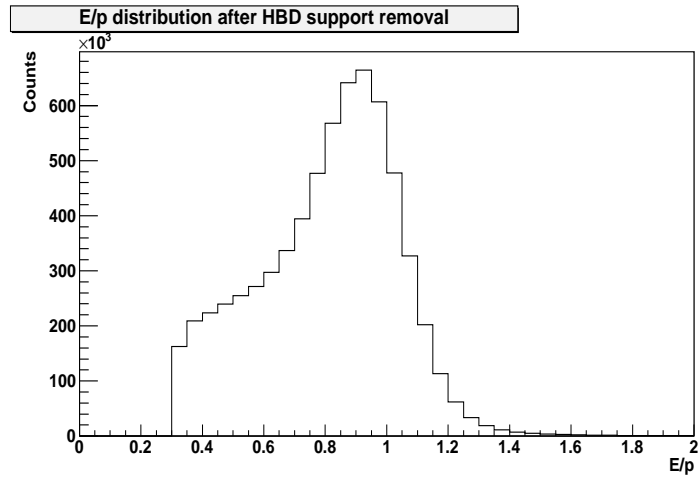


Figure 3.4:  $E/p$  distribution of single electrons after applying HBD support structure removal cut.

### 3.4 Electron identification, track matching and track quality

RICH and EMCAL are the primary electron identification detectors in PHENIX. The cherenkov photons emitted by the electrons with an angle  $\cos(\theta_c) = 1/(n\beta)$  in RICH are reflected by a concave mirror on a PMT plane as in Fig. 3.5. The reflected photons on the PMT plane makes a circular ring as shown in Fig. 3.6. Starting from the track the projected track point on PMT is stored onto the PMT plane given by  $P_{proj} = (z_{proj}, \phi_{proj})$ . As shown in Fig. 3.6, a maximum ( $R_{max} = 8.4$  cm) and minimum ( $R_{min} = 3.3$  cm) radius is defined around this projected point based on simulation study. This region with  $R_{min} < R < R_{max}$  is then scanned for several quantities like number of PMT hits ( $n_0$ ), number of cherenkov photons hits and ring shape. The number of photoelectrons ( $npe_i$ ) is determined from the pulse height measured by the PMT. The ring center is calculated by weighted mean position of hit PMTs. If  $R_i$  is the location of hit PMT and the number of photoelectrons in this area is  $\sum_i npe_i$  then the ring center is given by

$$R_{center} = \frac{\sum_i npe_i \cdot R_i}{\sum_i npe_i}, \quad (3.1)$$

which is stored in terms of  $R_{center} = (z_{center}, \phi_{center})$ . The distance between the ring center ( $R_{center}$ ) and the track projection ( $P_{proj}$ ) is termed as *displacement* (*disp*) and is given by

$$disp = \sqrt{(z_{proj} - z_{center})^2 - (\phi_{proj} - \phi_{center})^2}. \quad (3.2)$$

The energy and momentum of electrons are being measured by the EMCAL and DC. As mass of the electron ( $m_e = 511keV/c^2$ ) is negligible compared to the momentum of electron,  $p > 200$  MeV/c, so from the energy momentum relation

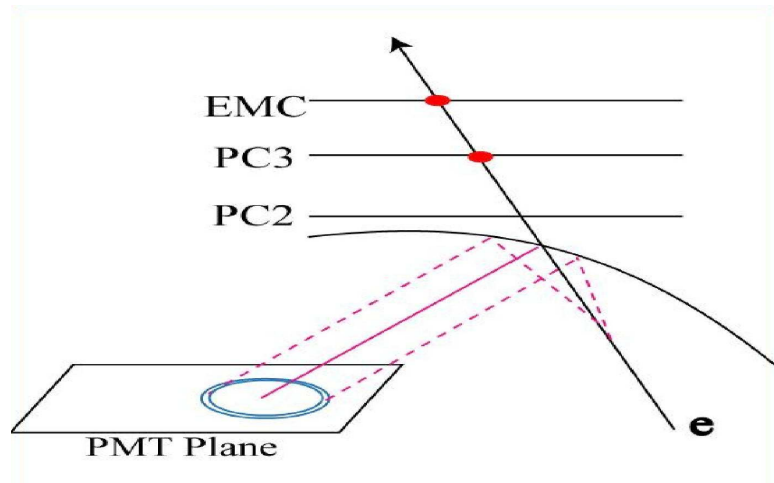


Figure 3.5: Cherenkov photons are being reflected by the RICH mirror on the PMT plane array.

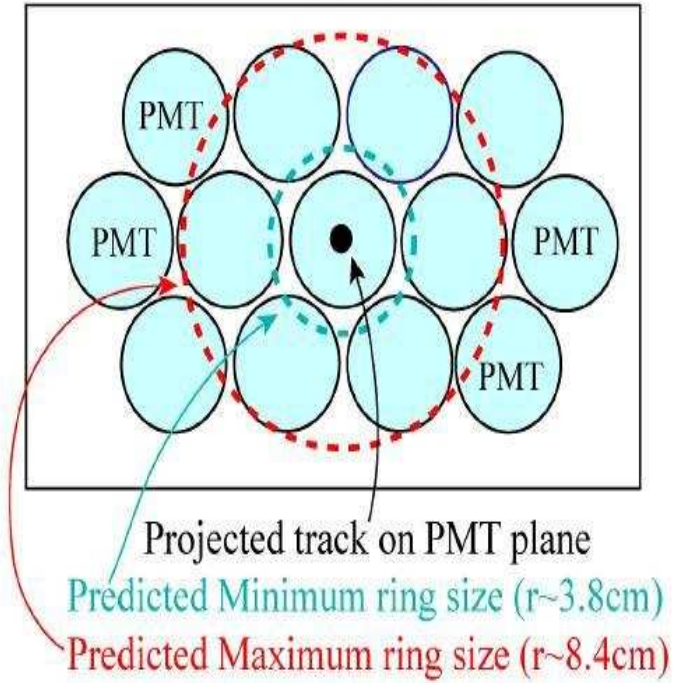


Figure 3.6: PMT arrays of RICH detector along with the projected track and the predicted maximum and minimum radius.

$(E = \sqrt{p^2 + m_e^2} \simeq p)$ , the energy deposited by electron in EMCAL should match with the momentum measured by DC. So  $E/p$  should be unity for electrons.

However the E/p peak width has momentum dependence and to correct it the variable dep which shows the deviation of E/p value from unity is being defined, given by  $dep = (E/p - 1) / \sigma_{E/p}$ . The E/p peaks for different momentum bins is shown in Fig. 3.14.

The distance between the projected track onto the EMCAL and position of the associated EMCAL cluster is calculated in azimuthal (emcdphi\_e) and z direction (emcdz\_e). These are further converted into one standard deviation ( $\sigma$ ) unit by Gaussian fit to the distribution and are stored as emcsdphi\_e and emcsdz\_e.

Hadronic and electromagnetic particles produces different energy sharing patterns between calorimeter towers. An analytical parametrization [89] was introduced meant for characterizing a shower to be electromagnetic which calculates

$$\chi^2 = \sum_i \frac{(E_i^{pred} - E_i^{meas})^2}{\sigma_i^2}, \quad (3.3)$$

where  $E_i^{meas}$  is the energy measured in the EMCAL tower and  $E_i^{pred}$  is the predicted energy from the parametrization. This  $\chi^2$  value characterizes a shower to be how much electromagnetic. Based on this  $\chi^2$ , variable named *prob* is defined as the probability of a shower to be electromagnetic and is used as another parameter for electron identification.

The quality of the track in reconstruction is determined from the bit pattern information in DC and PC and is given by the variable *quality*. The bit pattern is obtained from the front end electronics of the DC and PC and based on this bit pattern the hit pattern is determined. The bit pattern of (0,1) corresponds to X wires (runs parallel to the beam axis) and represents the lowest order bits. The UV stereo wires has bits of 2, representing hits being found and bits with value 3 represents hits being unique. The highest order bits are 4 showing hits being

found in PC1 and 5 for hits being unique in PC1. Based on these bits information the highest quality tracks has bit combinations which gives 63 or 31. Based on the above mentioned discussions the following track quality, track matching and electron identification criteria are being used, **Track Quality**

(quality == 31 || quality == 63)

### EMC Track Matching

$|emcsdphi\_e| < 2.0 \ \&\& |emcsdz\_e| < 2.0$

### eID cuts

#### Standard eID cuts

- $n0 >= 1$
- $prob >= 0.01$
- $|dep| < 2.0$
- $disp < 5.0$ .

#### Tight eID cut

In addition to the above standard eID following tighter electron identification criteria are used for removal of charged pions background at  $p_T > 4.7$  GeV.

$n0 >= 5 \ \&\& prob > 0.2$

## 3.5 Quality Analysis (QA) of MB events

During RHIC running period, the ion beam was not present continuously. Due to this, the data taking by PHENIX has been divided into several parts. Each part starts from the beam start up period until the beam is dumped. Technically these data taking periods are called runs. The quality analysis involves selecting only those runs which has good electron yield. Only electrons satisfying the base eID cuts alongwith the fiducial cuts are being counted. If electron yield is less

than  $2 \times 10^{-4}$ , the run is rejected as bad run. During 2008 RHIC RUN, a thin sheet of brass was wrapped up around the beam pipe near collision region in order to study electrons coming from conversion. The thin brass sheet is called converter and correspondingly some of the data taking runs were converter runs having large electron yield as compared to the runs without this converter. For converter runs the minimum yield is taken as  $4 \times 10^{-4}$ . After rejection of these bad runs, the average electron yields  $\langle N_e \rangle$  for the entire data set is calculated. After this the runs whose electron yield is more than  $3\sigma$  from  $\langle N_e \rangle$  is rejected as bad runs. Here  $\sigma$  value of the run is calculated from the electron yield run. This process underwent interaction for 4 times and the runs not being rejected by  $3\sigma$  cut are accepted as good runs. Fig. 3.7 shows the electron yield per MB events.

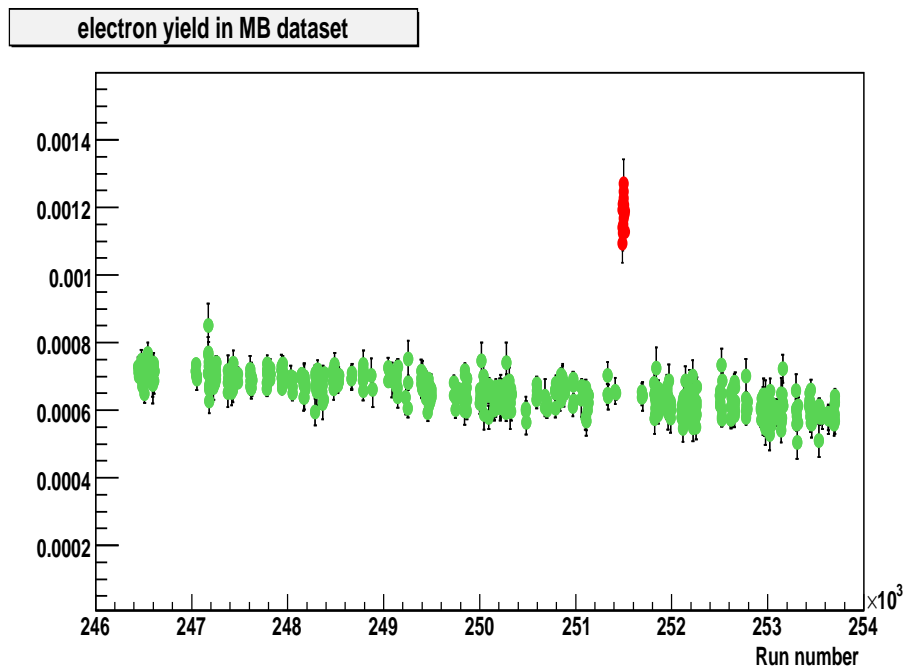


Figure 3.7:  $e^\pm$  per MB events in MB data set. x axis is the run number and y axis is the number of electrons per MB events. Converter run is shown by red markers and the green marker is for non-converter run.

The Converter run group is between run number 251485 and 251512.

### 3.6 Run Q/A of ERT trigger events

Similar process like that in Run Q/A for MB events is being applied for the ERT events. For each runs that passed the MB run Q/A check, the electron yield per MB sampled event is measured. The changing beam conditions causes the frequent adjustment scaledown factors on MB trigger. These frequently adjusted scaledown factors needs to be considered while calculating the MB sampled events recorded by ERT trigger. From the ERT trigger definition as it requires coincidence of the MB trigger the MB events sampled by ERT data set is given by

$$N_{MB}^{sampled} = N_{MB} * scale\_down\_factor. \quad (3.4)$$

The  $N_{MB}^{sampled}$  should be the number of sampled MB events in the ERT trigger file, if both of the MB and the ERT trigger file comes from the same set of DSTs. However sometimes some of the nDSTs are lost or crashed and these two data sets then contains different statistics. In order to check and correct for this problem, the number of MB trigger events in the ERT data set ( $N_{ERT}^{MB}$ ) and the number of ERT trigger event in the MB data set ( $N_{MB}^{ERT}$ ) are being compared. Since both of them are the number of ERT&MB<sub>sampled</sub> trigger event in the run, they should be identical if the original data set is identical. However, if some of the run file segments are crashed during the data processing, the ratio deviates from unity. The ratio then can be used for determining the true sampled MB triggers in ERT data set.

The distribution of ratio, Ratio\_ERT\_MB =  $N_{ERT}^{MB}/N_{MB}^{ERT}$ , is shown in Fig. 3.8. For Run8 the ratio is 1.0 which means no file segment is crashed in production of nDSTs. The sampled MB triggers in these runs are calculated as

$$N_{MB}^{sampled} = N_{MB} * scale\_down\_factor * Ratio\_ERT\_MB. \quad (3.5)$$

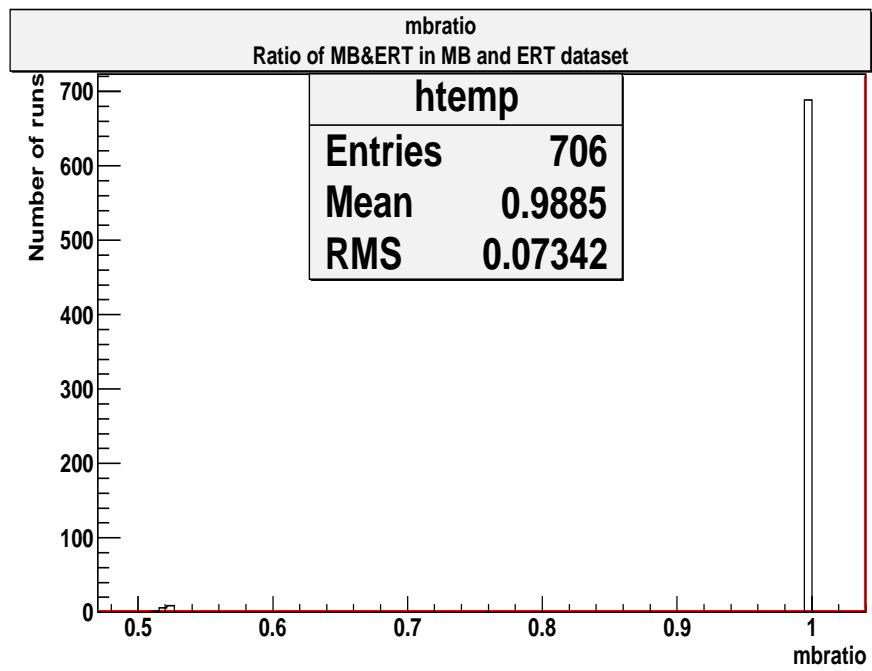


Figure 3.8: The ratio of MB&ERT trigger in the MB data set and the ERT data set for the non-converter data set. One entry of the histogram is for one run.

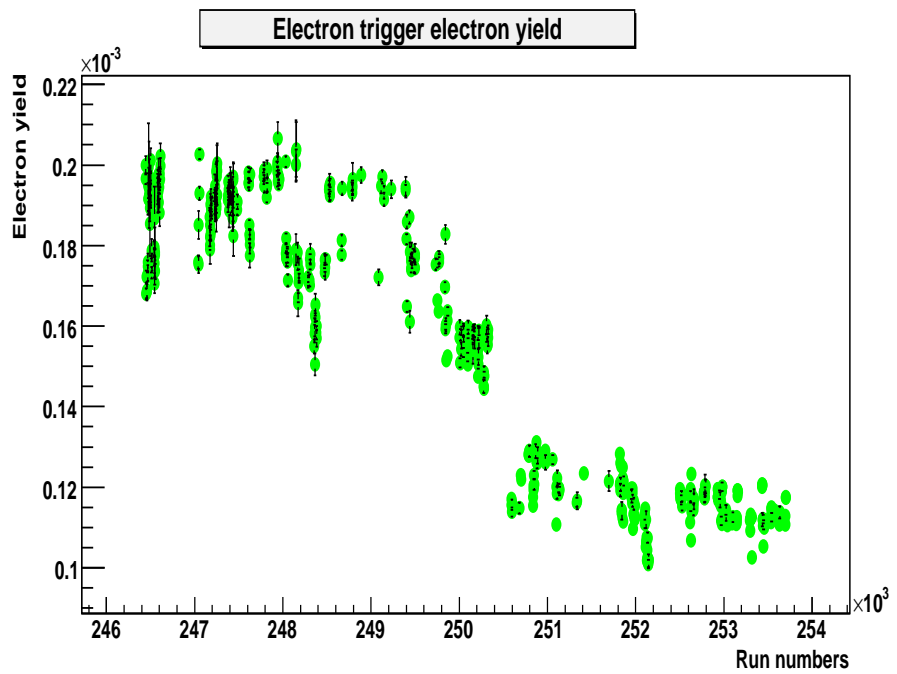


Figure 3.9:  $e^\pm$  per MB sampled events in ERT data set.

As Ratio\_ERT\_MB for Run8 is 1.0 [Fig. 3.8] so the above formula becomes

$$N_{MB}^{sampled} = N_{MB} * scale\_down\_factor. \quad (3.6)$$

The electron yield per sampled MB event for  $p_T > 600$  MeV is shown in Fig. 3.9. The yield after run number 249.4K decreases as the change in trigger threshold from 600 MeV to 800 MeV.

## 3.7 Correction factors

In order to make up for the lost electrons due to different kinds of technical problems during long run of data taking by the PHENIX detector various kinds of correction factors are applied to the raw electron counts. These correction factors has to be determined by analyzers during data analysis. The different kinds of correction factors that has been determined during this analysis are being described here.

### 3.7.1 ERT trigger Efficiency

For using the ERT data, the trigger efficiency correction has to be applied. The trigger efficiency is determined from the MB data set as a fraction of electrons that satisfies the ERTE electron trigger. The MB data set also records the ERT. In order to avoid the random benefit, the trigger tiles that fired the trigger has to be checked for getting hit by the electron.

The trigger efficiency has to be determined for each sectors. Fig. 3.10 shows the  $p_T$  spectra of electrons in different sectors and Fig. 3.11 shows the ERT trigger efficiency in different sectors. ERT trigger efficiency is obtained by dividing the red histogram by the blue histogram of Fig. 3.10. Sector1\_3 doesn't have ERT trigger, so in the final electron spectra only MB triggered data is used from this

sector. The trigger efficiency curves are fitted with Fermi function given by

$$f(p_T) = \frac{\epsilon_0}{e^{(p_0-p_T)/k} + 1}. \quad (3.7)$$

Table 3.1: Parametrization of ERT trigger efficiency for single electron in each sector

Sector	$\epsilon_0$	$p_0(\text{GeV}/c)$	$k(\text{GeV}/c)$
E0	0.6951	0.7668	0.1553
E1	0.7439	0.767	0.1331
E2	0.7298	0.7957	0.1651
E3	0.803	0.6621	0.1379
W0	0.8253	0.8051	0.1489
W1	0.6799	0.8381	0.1427
W2	0.2831	0.9376	0.2084

Fig. 3.12 shows the  $p_T$  distribution of electrons in each sector before and after applying ERT trigger efficiency correction for standard eID. Black colored distribution is before applying trigger efficiency correction and red colored distribution is after applying trigger efficiency correction. The same trigger efficiency corrected and non corrected spectra for tight eID is shown in Fig. 3.13.

### 3.7.2 Electron identification correction

The charged pions, having  $p_T$  above 4.7 GeV, starts emitting the Cerenkov light in  $CO_2$  gas radiator in RICH detector which reduces the pion rejection power of RICH. Thus a tighter eID cuts are applied on electrons for  $p_T > 4.7$  GeV.

Fig. 3.14 shows the E/p distribution in different  $p_T$  bins starting from low  $p_T$  (0.6-0.7 GeV/c, at the top left corner) to high  $p_T$  (9-10 GeV/c, at the bottom right corner). In each panel, the black histogram is the E/p distribution with standard cut ( $n0 >= 2$  and  $\text{prob} > 0.01$ ), and the red histogram is the E/p distribution with tighter eID cut( $n0 >= 5$  and  $\text{prob} > 0.2$ ).

From Fig. 3.14 it can be seen than below 5.0 GeV both black and red

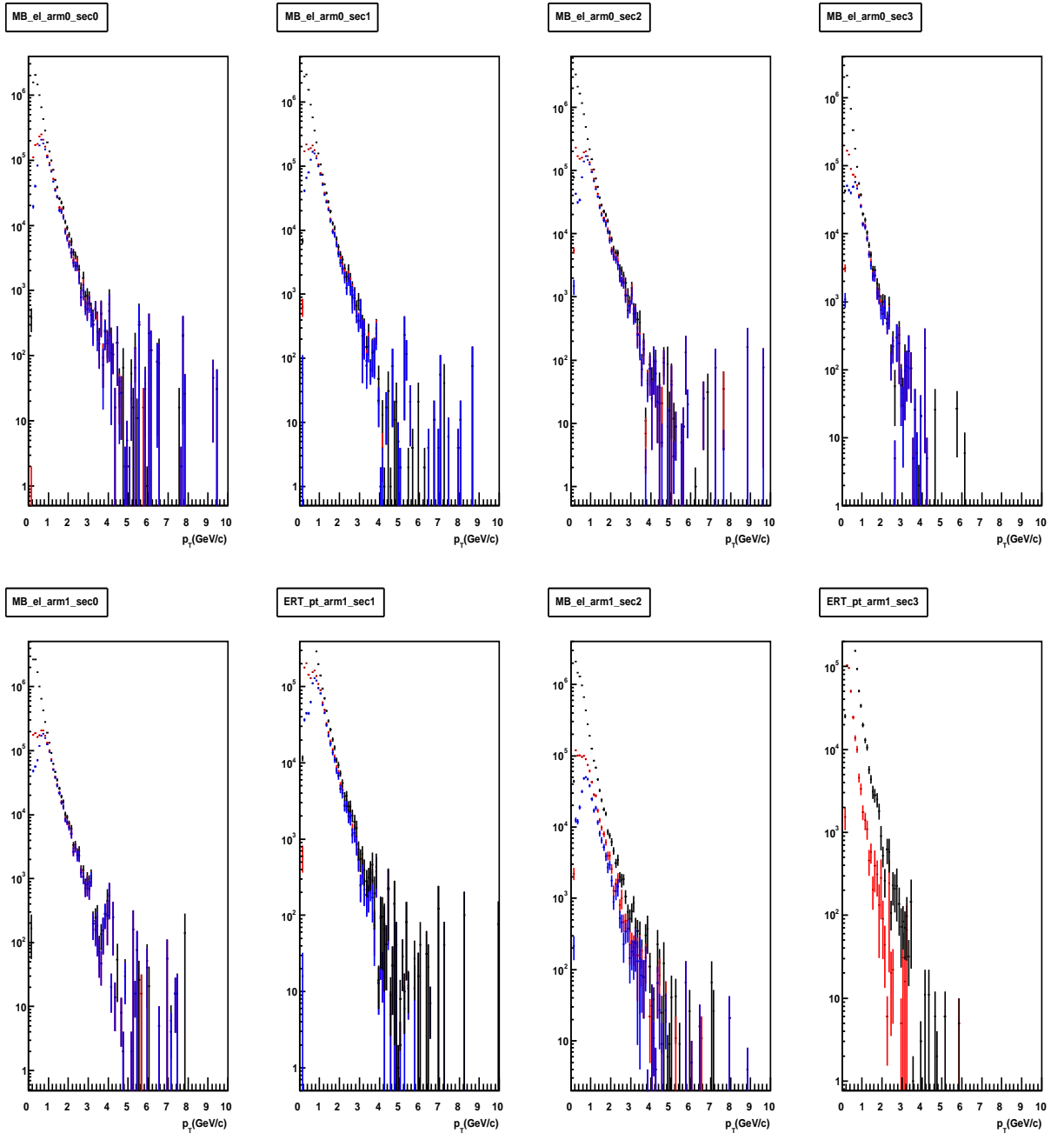


Figure 3.10:  $p_T$  spectra of electrons in different sectors in MB dataset. y axis is the number of counts and x axis is  $p_T$ . Red histogram is without ERT trigger condition while the blue histogram is with ERT trigger condition.

histograms show clear electron peak. Above 5.0 GeV the background in black histogram increases so much that the electron peak becomes rather invisible,

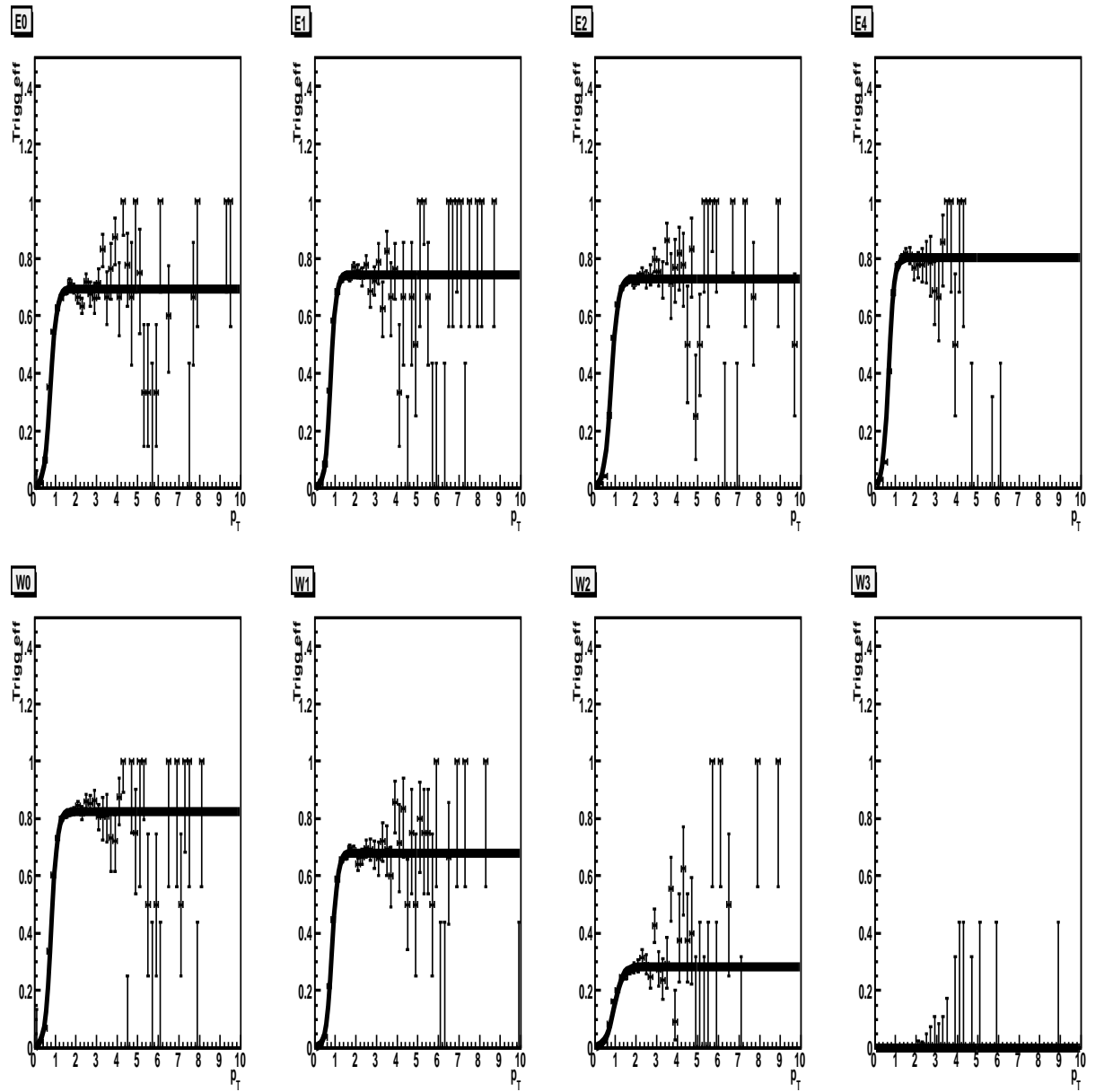


Figure 3.11: ERT trigger efficiency in different sectors.

whereas in the red histogram (with tight eID cut) the electron peak is visible even in the panel of 9.0–10.0 GeV.

The tight eID cut removes some fraction of electron in addition to the hadronic backgrounds. In order to account for this problem correction to the tight eID electron spectra has been applied. Fig. 3.16 shows the spectra from

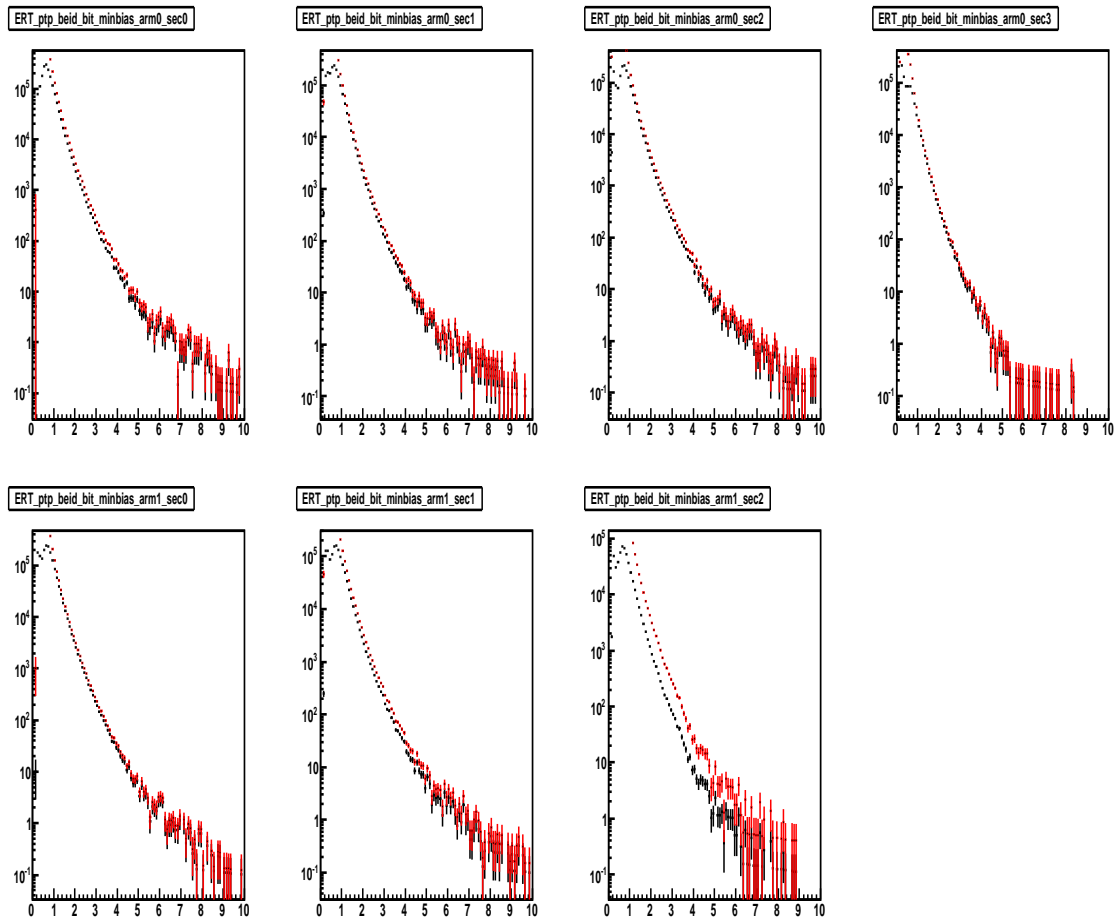


Figure 3.12:  $p_T$  distribution in different sectors before and after applying ERT trigger correction for standard eID. x axis is  $p_T$  and y axis is number of counts. Sector1\_3 don't have ERT triggered data. Red colored distribution is after applying trigger efficiency and black colored distribution is before applying trigger efficiency correction.

the ERT data set with tight and standard eID for different sectors. Fig. 3.17 shows this correction factor to be applied to the electron spectra with tight eID in different sectors. This is obtained by dividing the tight and standard eID spectra as shown in Fig. 3.16.

Fig. 3.18 shows the  $p_T$  distribution in each sector for MB and ERT triggered data set after applying the tight eID correction.

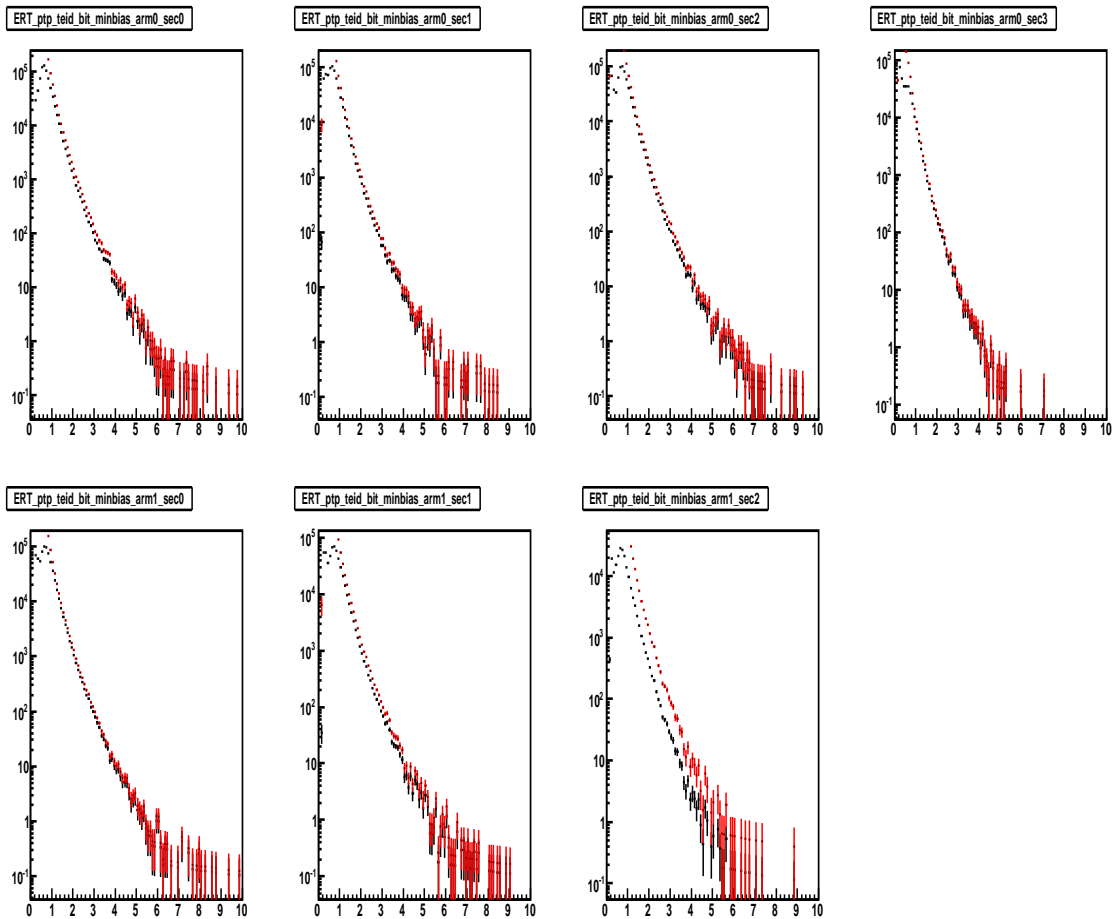


Figure 3.13:  $p_T$  distribution in different sectors before and after applying ERT trigger correction for tight eID. x axis is  $p_T$  and y axis is number of counts. Sector 1\_3 don't have ERT triggered data. Red colored distribution is after applying trigger efficiency and black colored distribution is before applying trigger efficiency.

### 3.7.3 Acceptance Uncorrected Inclusive Electron Spectra

In the final single electron inclusive spectra data from the following sources are being taken

- MB triggered data with standard eID upto  $p_T = 2.7$  GeV.
- ERT triggered data with standard eID corrected for trigger efficiency in each sector in  $2.7 \text{ GeV} \leq p_T \leq 4.5 \text{ GeV}$ .
- ERT triggered data with tight eID corrected for trigger efficiency and tight

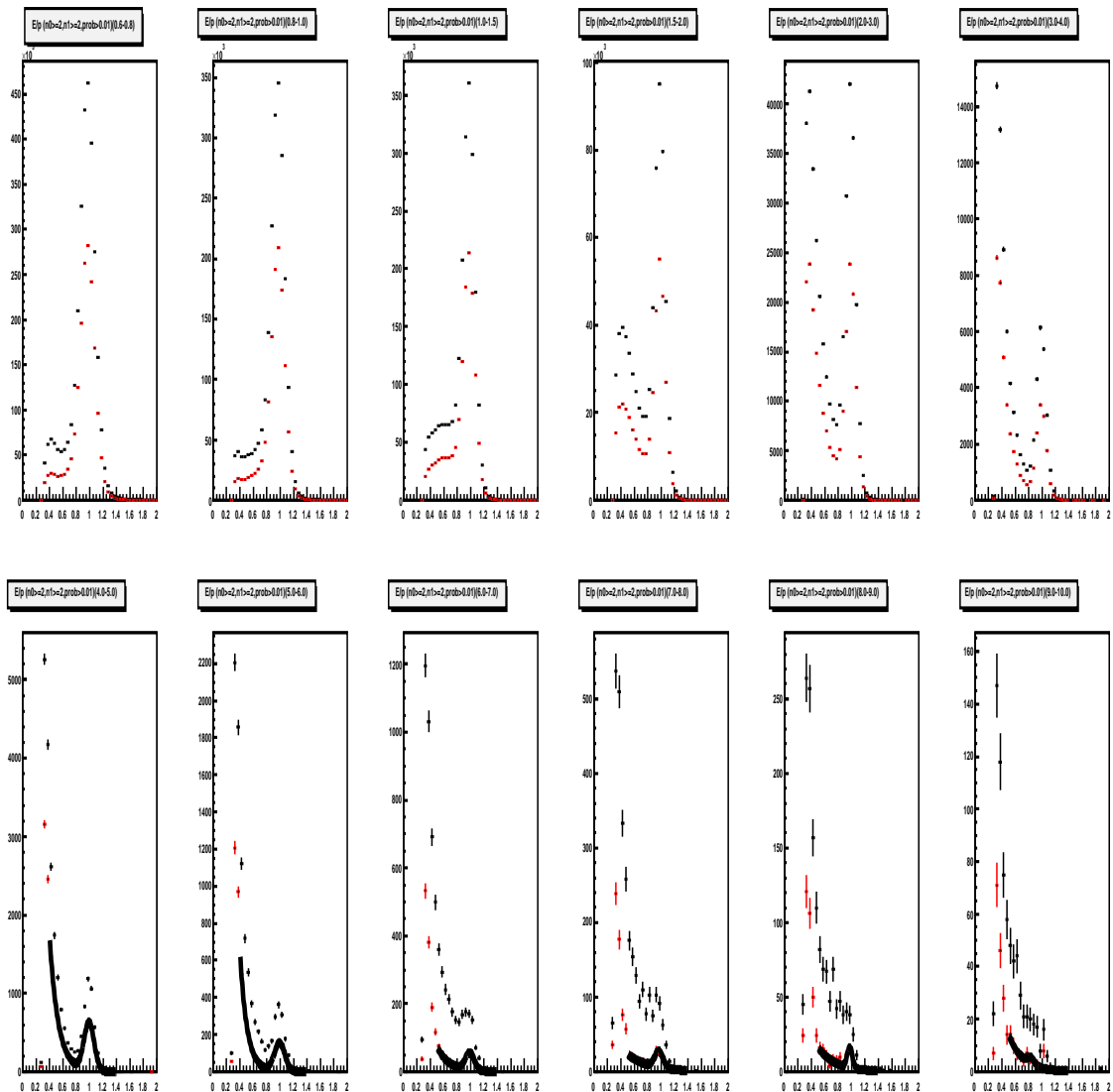


Figure 3.14: E/p distribution of single electrons in different  $p_T$  bins starting from 0.8 GeV  $< p_T <$  1.0 GeV at extreme left of top panel to 9.0 GeV  $< p_T <$  10 GeV at extreme right of bottom panel. x axis is E/p and y axis is number of counts.

eID for each sector in  $p_T > 4.5$  GeV.

- From sector 1\_3 only MB triggered data with standard eID for  $p_T \leq 4.5$  GeV and for  $p_T > 4.5$  GeV with tight eID.
- From sector 1\_2 MB triggered data with standard eID for  $p_T \leq 1.0$  GeV , ERT triggered data with standard eID for  $1.0 \text{ GeV} < p_T \leq 4.5$  GeV and

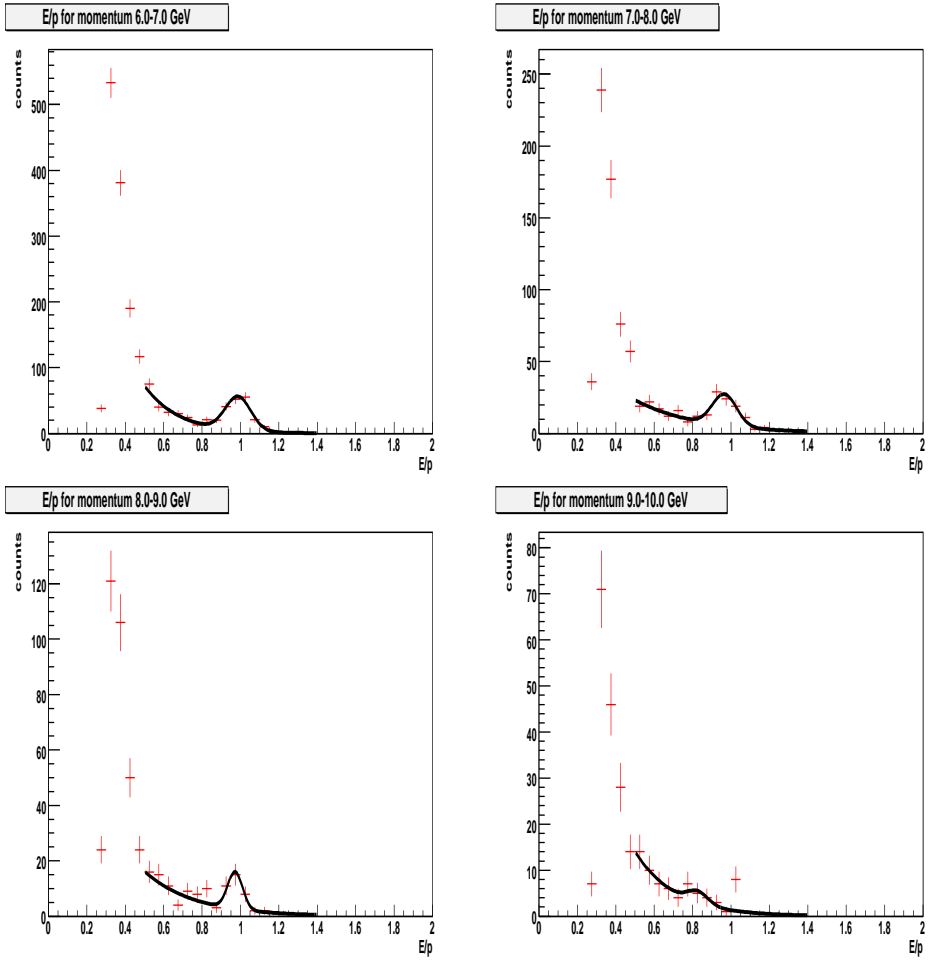


Figure 3.15:  $E/p$  magnified distribution in high  $p_T$  bins.

ERT triggered data with tight eID for  $p_T > 4.5$  GeV.

Fig. 3.19 shows the MB and ERT stitched single electron  $p_T$  distribution in different sectors for minimum bias centrality. Fig. 3.20 shows the single electron  $p_T$  distribution after adding different sectors for minimum bias centrality.

### 3.7.4 Acceptance correction

After the single electron  $p_T$  spectra has been corrected for trigger efficiency in section 3.7.2 and tight eID efficiency in section 3.7.1, the single electron  $p_T$  spectra has been corrected for acceptance X efficiency. This has been done because not

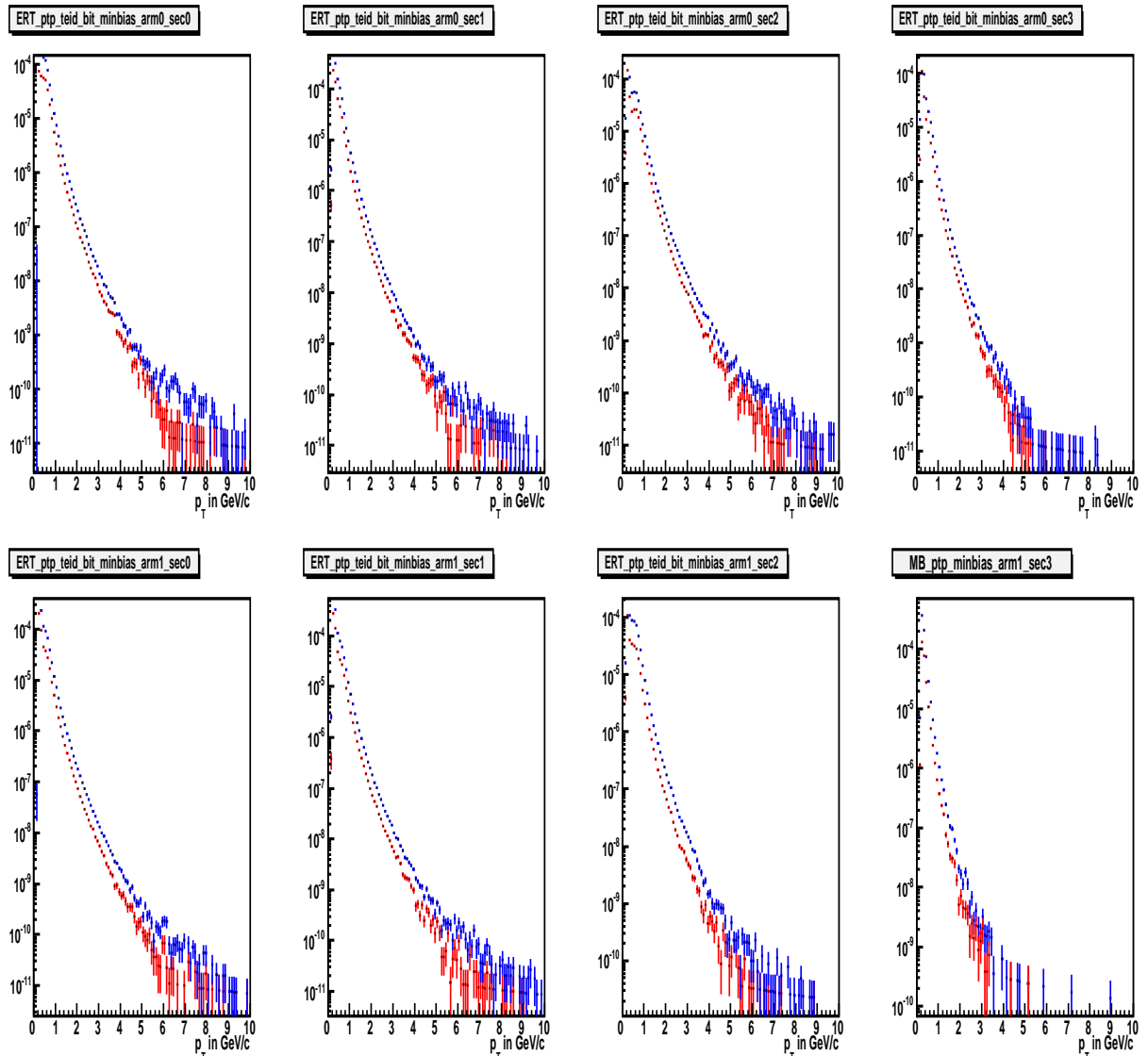


Figure 3.16:  $p_T$  spectra of electrons for tight and standard eID in different sectors before applying tight eID correction. y axis is number of counts normalized by the total number of events and x axis is  $p_T$ . Red colored distribution is with tight eID and blue colored distribution is with standard eID in ERT trigger data set. Sector 1\_3 is from MB trigger data set.

all of the created electrons gets reconstructed due to limited acceptance, dead areas, hot channels of detector and misreconstructed tracks. In order to calculate the acceptance X efficiency, Monte Carlo based simulation (MC) for pure single electrons has been done. The first step was generating single electrons and single

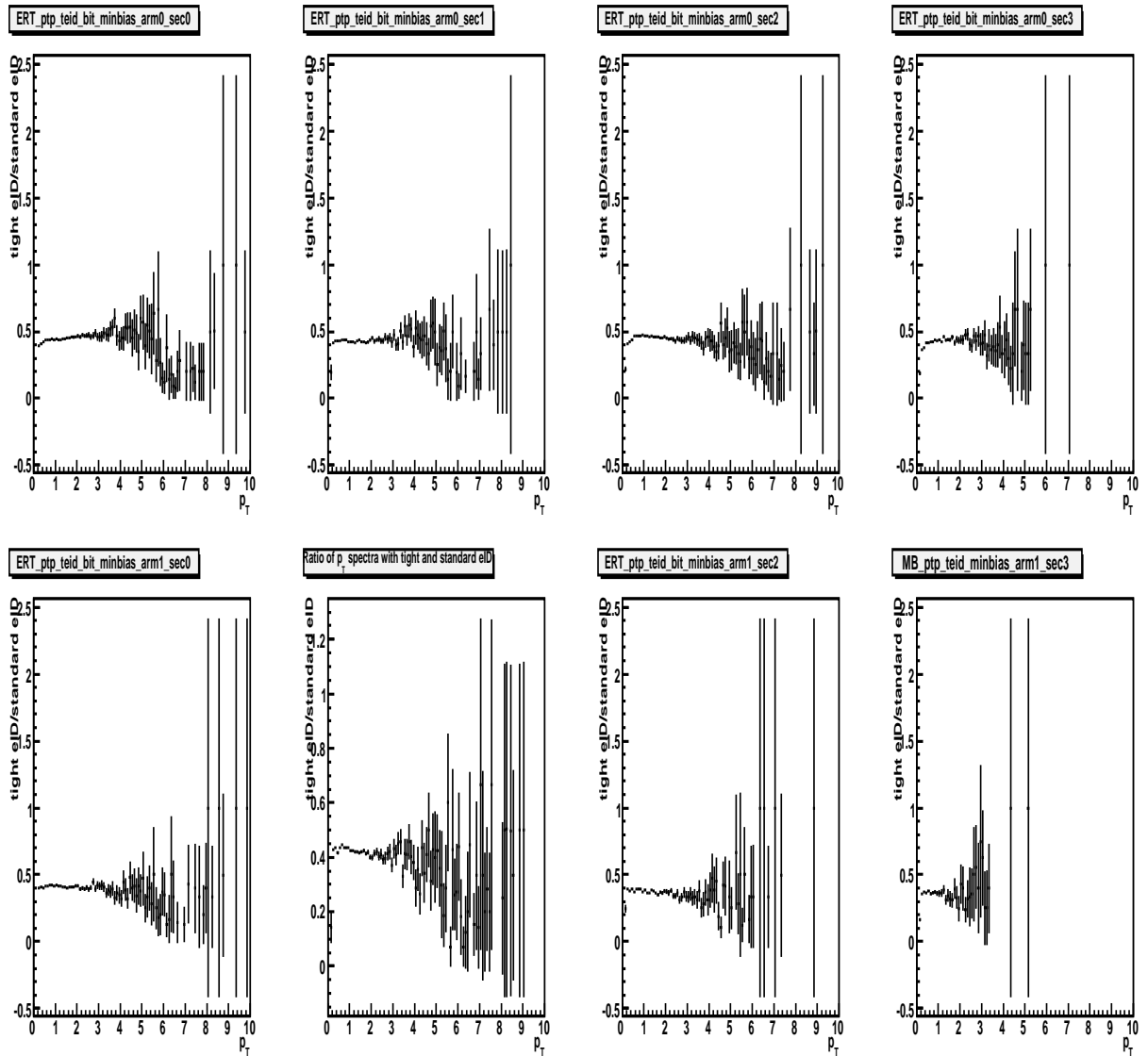


Figure 3.17: Correction for tight eID cut in different sectors. Sector1\_3 is corrected for MB data as the final spectra contains only MB data from this sector.

positrons in the following phase space in accordance with the PHENIX detector phase space using the single particle generator called EXODUS.

- $0 < p_T < 15 \text{ GeV}/c$  in flat  $p_T$
- $|\text{rapidity}| (|y|) < 0.5$
- $0 < \phi < 2\pi$

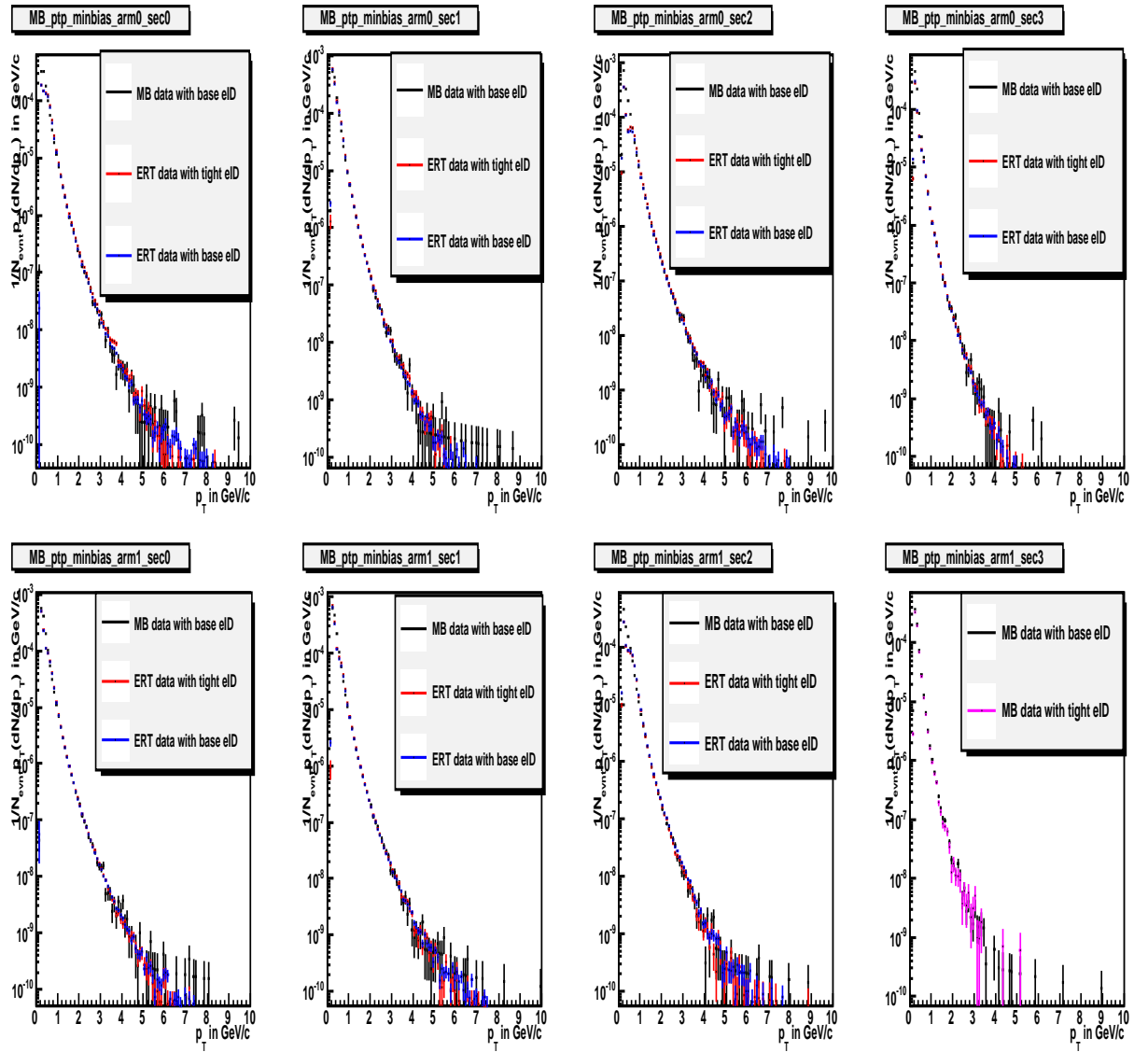


Figure 3.18: Electron  $p_T$  distribution in different sectors from ERT and MB data set after applying trigger efficiency and eID correction. y axis is number of counts normalized by the total number of events and x axis is  $p_T$ . Red is ERT triggered data with tight eID cut corrected for trigger efficiency and tight eID correction, blue is ERT triggered data with standard eID corrected for ERT trigger efficiency and black is MB triggered data with standard eID. Sector 1\_3 has MB triggered data in magenta with tight eID corrected for tight eID correction.

- $|z_{\text{vtx}}| < 40 \text{ cm}$

The generated single  $e^-$  and single  $e^+$  are passed through the Geant base PHENIX detector simulation package named PISA. The PISA was set to Run8

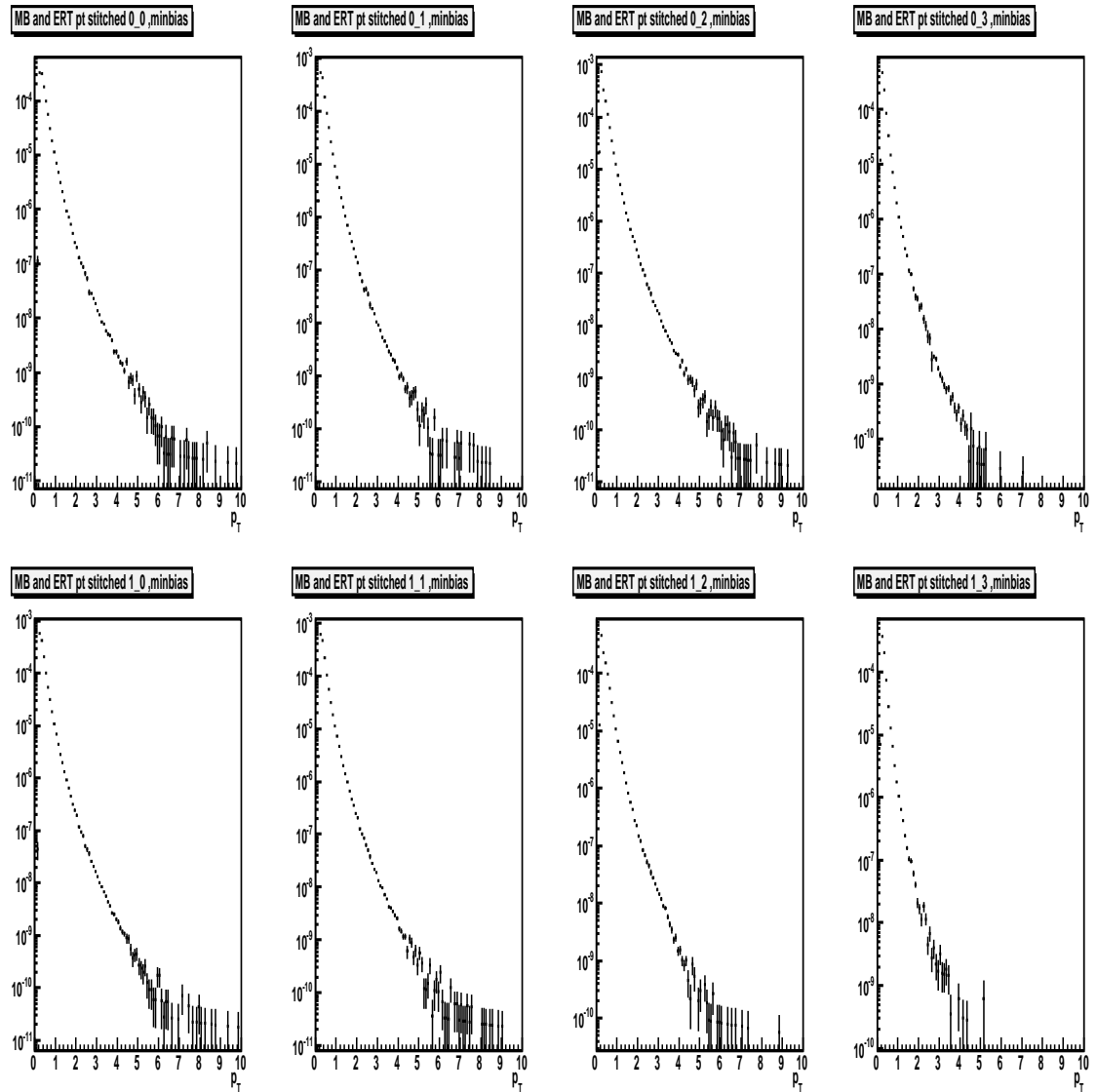


Figure 3.19: Stitched  $p_T$  spectra from different sources in different sectors as mentioned in text. x axis is  $p_T$  and y axis is number of electron counts scaled by total number of events.

d+Au configuration. The PISA output files are then passed through the reconstruction software PISAtodST. The information of the dead areas in DC and PC during Run8 d+Au is available and these real information are included in the code for running the reconstruction software.

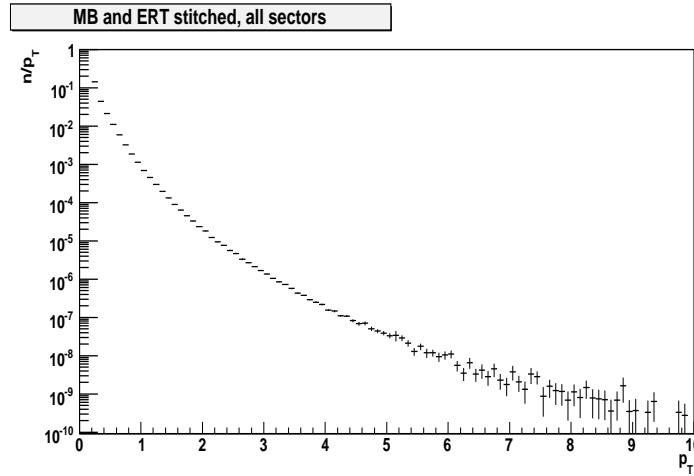


Figure 3.20: Stitched  $p_T$  spectra from different sources after adding all the sectors.

The DSTs of the PISAtoDST which we term as simDSTs are then analyzed by the analyzing code. The same fiducial and eID cuts like the real data analysis are being used for analyzing the simDSTs. As the simulated electrons are generated in the flat  $p_T$  distribution, standard weighting technique has been used for filling the electron histograms.

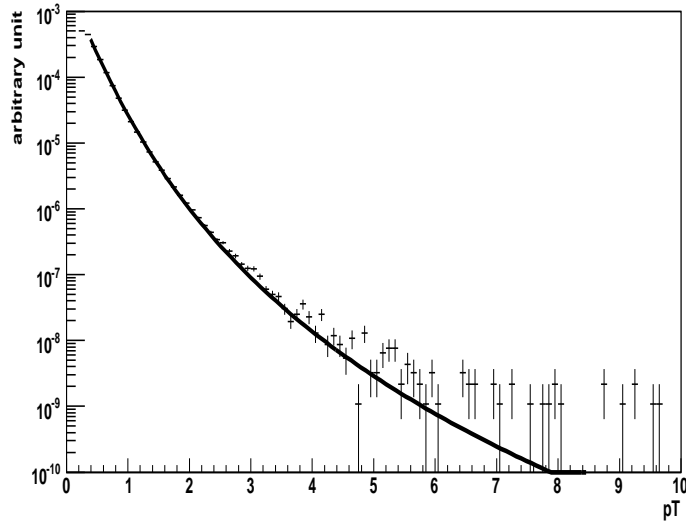


Figure 3.21: Fit to the  $p_T$  spectra of electron in real data. The fit function is used as weight factor while filling the histograms in simulation.

In order to find the proper weight factor, the real  $p_T$  spectra of single electrons is parametrized by the equation of the form :

$$Ap_T(b + p_T)^n. \quad (3.8)$$

Fig. 3.21 shows the fit to the real single electron which is applied as the weight factor. Before calculating the acceptance it is needed to make sure that the detector acceptance in MC and real data agrees.

In Fig. 3.22 and Fig. 3.23 the comparison of Drift Chamber phi variable and the EMCAL z coordinate variable (zed) between data and simulation are shown respectively. The MC and data overall agrees well.

Also it is needed to make sure the eID and track matching cuts used in data matches with that in simulation. Fig. 3.24 shows the comparison of these variables (n0, prob, dep, emcsdphi\_e, emcsdz\_e) between data and simulation.

Fig. 3.25 shows the  $p_T$  spectra of single electron before and after passing through PISA. Fig. 3.26 shows the acceptance which is calculated by dividing the output spectrum of the reconstructed electron by the input spectrum of generated electrons :

$$\epsilon = \frac{dN_{reco}/dp_T^{reco}}{dN_{gen}/dp_T^{gen}}, \quad (3.9)$$

where  $dN_{reco}/dp_T^{reco}$  is the yield of reconstructed single electron and  $dN_{gen}/dp_T^{gen}$  is the yield of generated single electron. The acceptance curve is parametrized with the function of the form :

$$\epsilon = A * \tan^{-1}(b * p_T + c). \quad (3.10)$$

The parametrization is further used for acceptance correction to the real data in order to make up for the lost electrons.

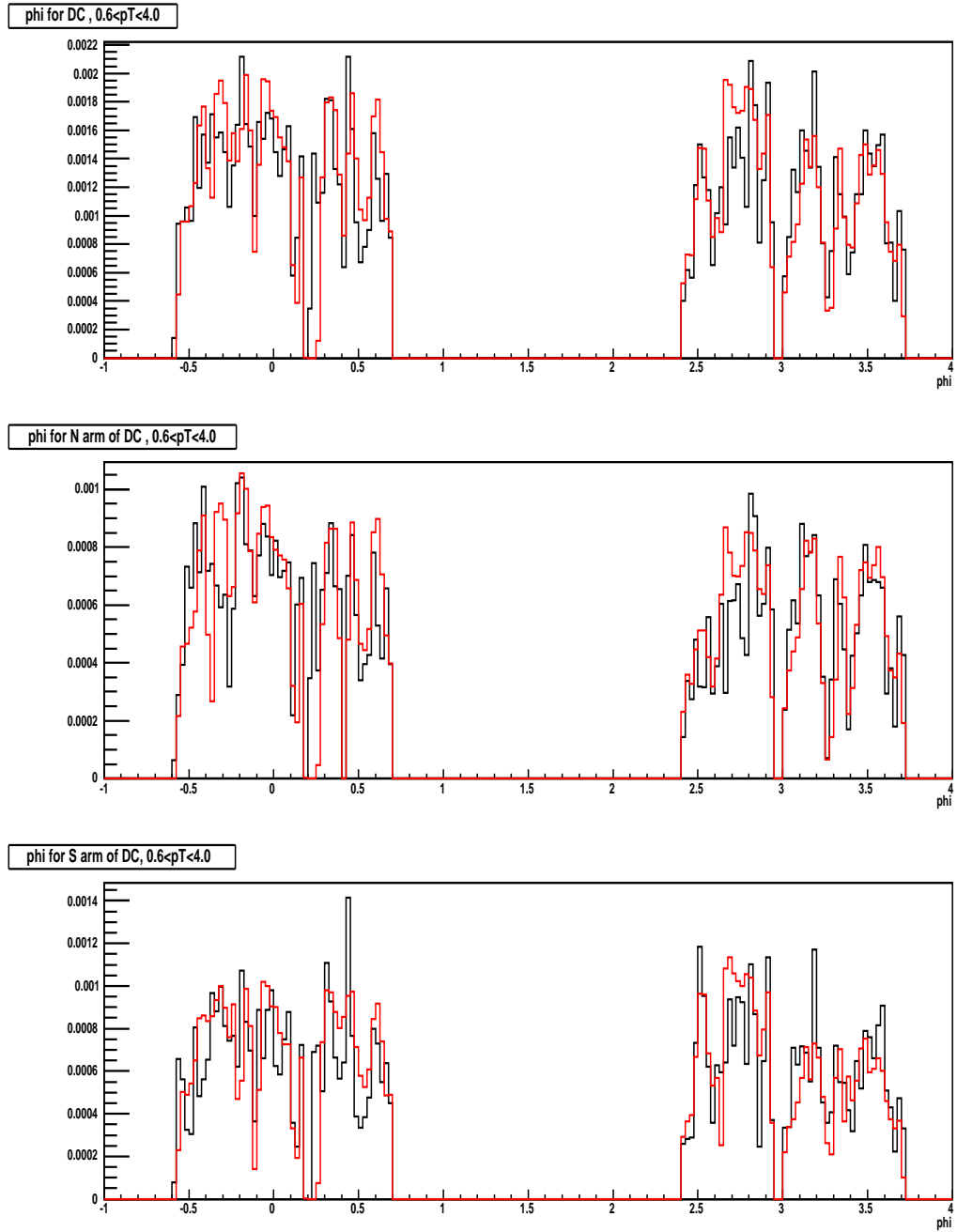


Figure 3.22: Real data and MC comparison for Drift Chamber phi coordinate in  $0.6 \text{ GeV} < p_T < 4.0 \text{ GeV}$ . Red is data and black is MC. The real data is rescaled such that the integral of the phi distribution in the real data and in the simulation agrees. y axis is the rescaled counts. Top panel includes both the sides. Middle panel is for North side of PHENIX. Bottom panel is for South side of PHENIX.

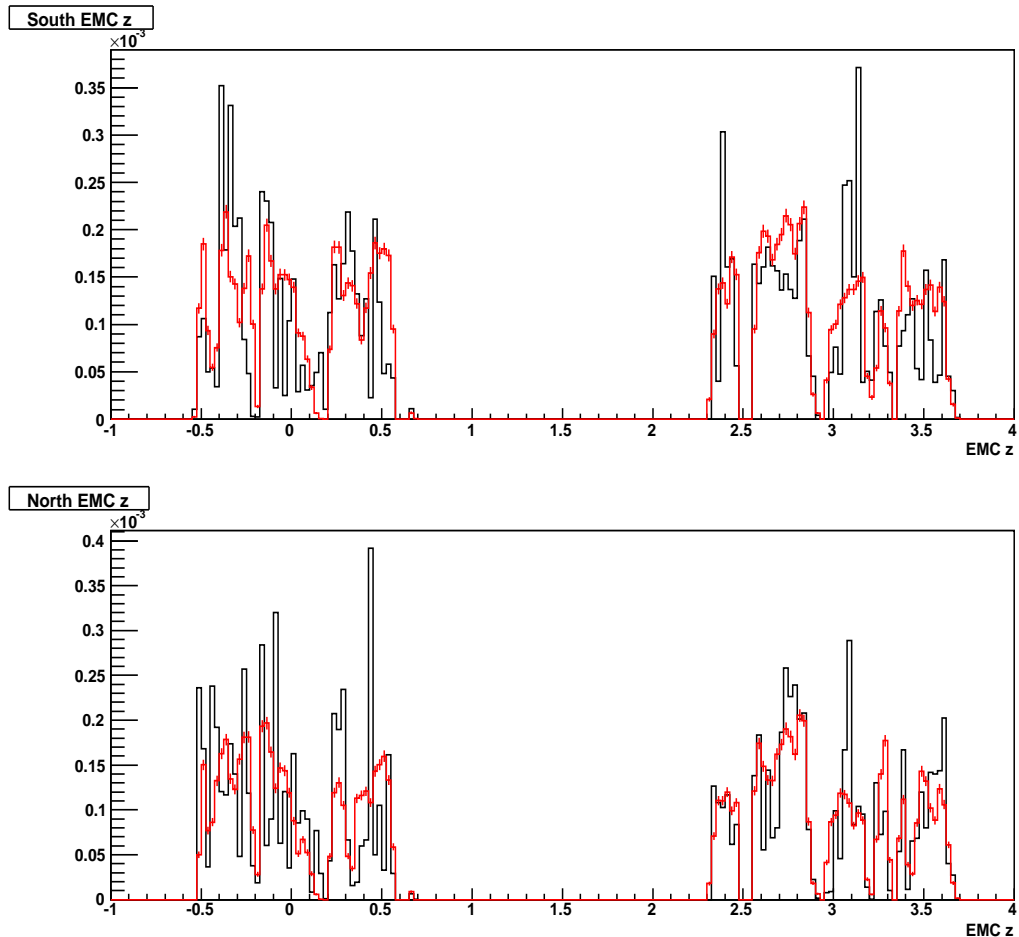


Figure 3.23: Real data and MC comparison for EMC  $z$  coordinate distribution. The real data is rescaled such that the integral of the EMC  $z$  distribution in the real data and in the simulation agrees.  $y$  axis is the rescaled counts. Red distribution is for real data and black distribution is for MC. Top panel is for North side of PHENIX. Bottom panel is for South side of PHENIX.

### 3.8 Cocktail Calculation

Once the measurement of inclusive single electron is done the measurement of background sources is done in order to subtract them from inclusive electrons to obtain electrons from heavy flavor decay. The electrons from background sources is known as single electron cocktail. The measurement of this cocktail is a simulation procedure in which the PHENIX single particle generator named EXODUS is being used. The various sources of the electrons contributing to

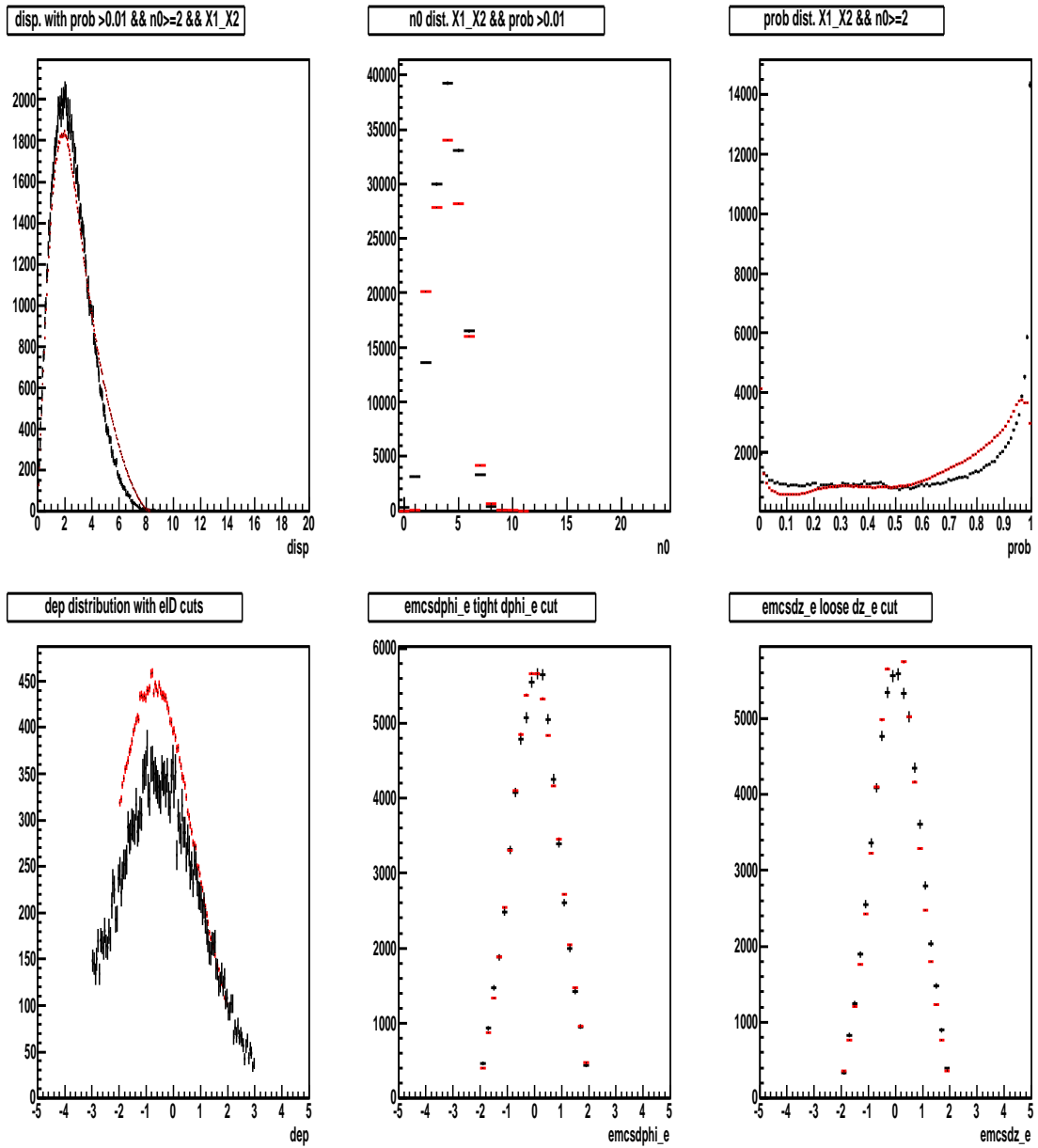


Figure 3.24: Real data and MC comparison for different eID cut and track matching parameters. The real data is rescaled such that the integral of the eID and track matching variables in the simulation and in the real data agrees. y axis is the rescaled counts. Red is data and black is MC.

this cocktail along with the procedure to calculate them is being discussed in section 3.8.1.

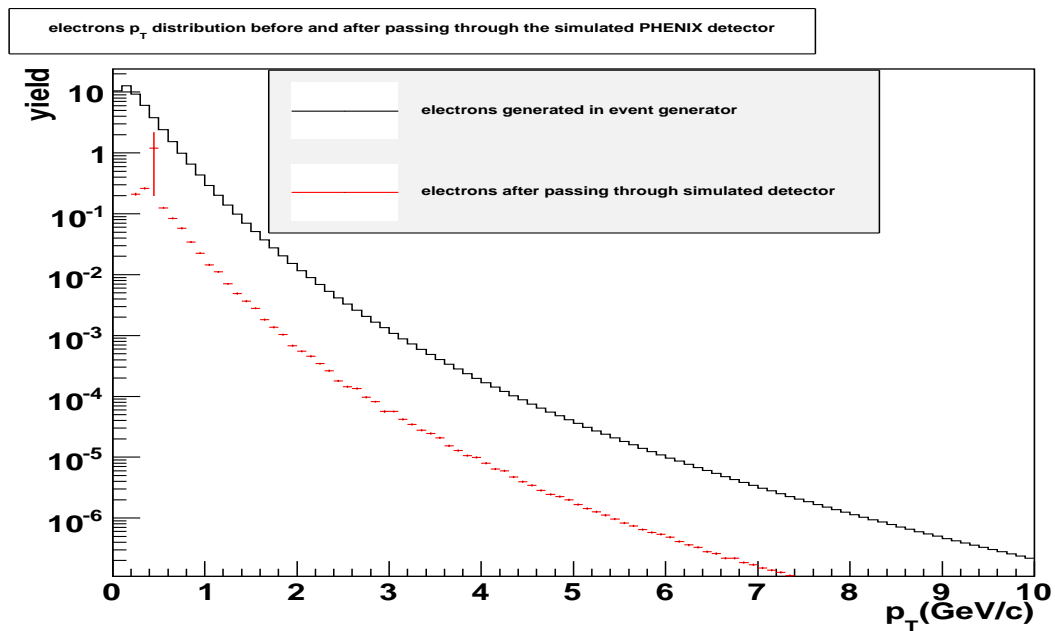


Figure 3.25:  $p_T$  spectra of single electron before passing through PISA (black curve) and after passing through PISA and reconstruction chain (red curve).

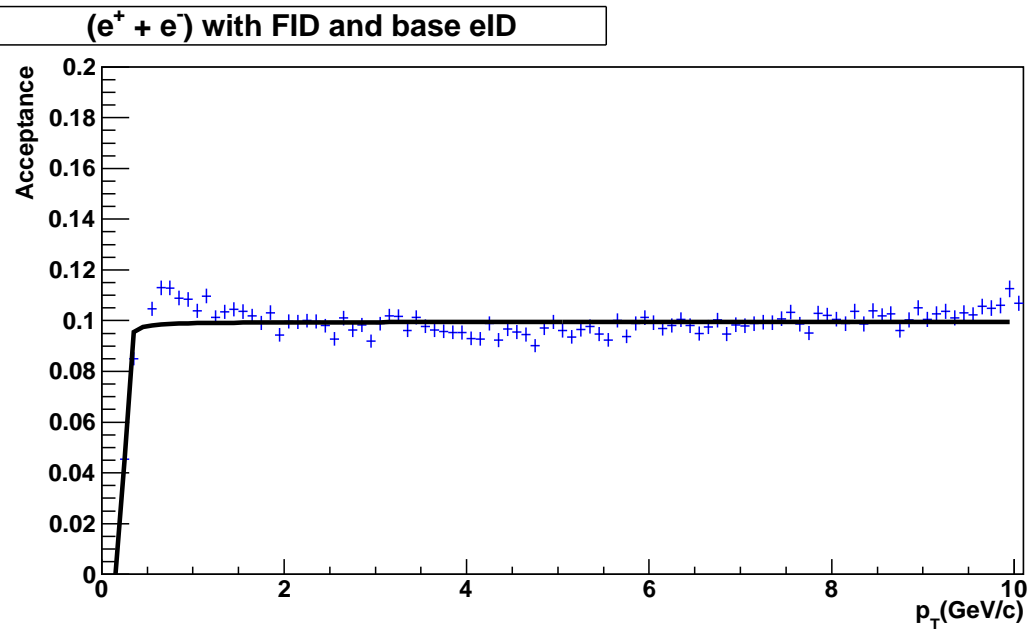


Figure 3.26:  $e^+ + e^-$  acceptance X efficiency plot in PHENIX. This curve is used for the acceptance correction in real data for electrons as described in the text.

### 3.8.1 Cocktail input

#### Neutral pions

The electron sources considered in the cocktail falls into two categories i.e. photonic and non-photonic sources. The following are the photonic sources

- Dalitz decays of light neutral mesons :  $\pi^0, \eta, \eta', \omega, \phi$ .
- Conversion of photons from decays of the above mentioned light neutral mesons inside the detector material.
- Conversion of direct photons, e.g. from quark gluon Compton scattering in material.

Non-photonic sources that are implemented in this analysis are

- Di-electron decays of light vector mesons :  $\rho, \omega, \phi$ .
- Weak kaon decays, referred as  $Ke_3$  decays.
- Virtual direct photons from initial hard scattering processes.

$\pi^0$  being the dominant electron source acts as the fundamental input for EXODUS. The first step is to parametrize  $\pi^0$  invariant yield or cross section spectra. The  $\pi^0$  [90] and charged  $\pi$  data [91] were taken from PHENIX published result. In low  $p_T$  region ( $p_T < 4.5$  GeV/c)  $\pi$  spectrum has been fitted by a Hagedorn function

$$\frac{dN}{p_T dp_T} = \frac{A}{(1 + p_T/p_0)^n} \quad (3.11)$$

and in high  $p_T$  region ( $p_T > 4.5$  GeV/c) spectrum was fitted by a modified power law function

$$\frac{dN}{p_T dp_T} = \frac{B}{(0.2 + p_T)^n} \quad (3.12)$$

and both the functions were connected by using the Woods Saxon form

$$T(p_T) = \frac{1}{1 + \exp\left(\frac{p_T - t}{w}\right)} \quad (3.13)$$

in order to fit the whole of charged and neutral  $\pi$  spectra. The combined charged and neutral  $\pi$  data have been fitted according to the following modified Hagedorn parametrization :

$$\frac{dN}{p_T dp_T} = T(p_T) \frac{A}{(1 + p_T/p_0)^n} + (1 - T(p_T)) \frac{B}{(0.2 + p_T)^n}. \quad (3.14)$$

Fig. 3.27 shows the fit to the  $\pi$  spectra in minimum bias centrality bins. Fig. 3.28 shows the comparison between quality of fits between only power law usage (blue triangles), only Hagedorn function (red squares) usage and while using eqn. 3.14 (green open circles). Using the eqn. 3.14 gives much more better fit result as compared to using only power law or only Hagedorn function as evident from Fig. 3.28.

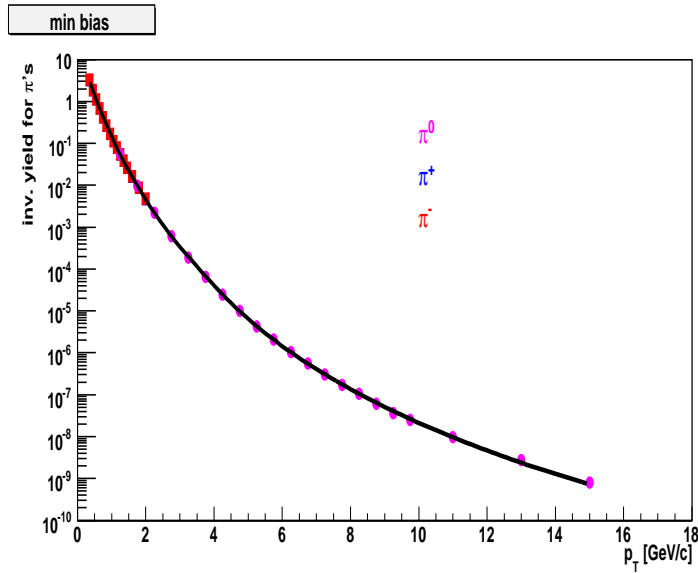


Figure 3.27:  $\pi^\pm$  and  $\pi^0$  fit. For details please see the text.

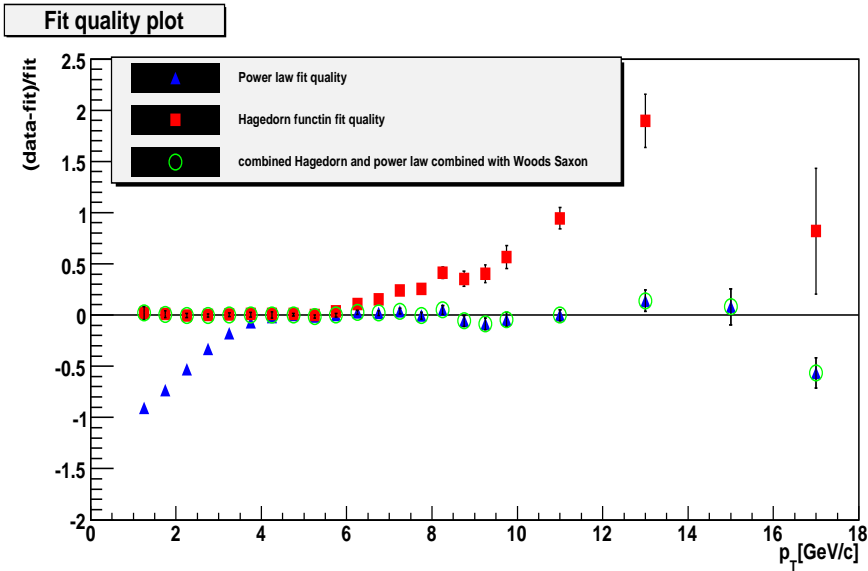


Figure 3.28:  $\pi^\pm$  and  $\pi^0$  fit quality. Red is for Hagedorn fit, blue is for power law fit and green open circle is for eqn. 3.14.

### Other light mesons

The next step is to determine the spectra of other light mesons based on the parametrization of pion spectra and  $m_T$  scaling i.e. the modified Hagedorn parametrization is used with  $p_T$  replaced by  $\sqrt{p_T^2 + m_{meson}^2 - m_{\pi^0}^2}$ .

The other light mesons (spectra obtained by  $m_T$  scaling) to  $\pi^0$  ratio is determined which is further scaled to the published particle ratios with the values

- $\eta/\pi^0 = 0.47 \pm 0.03$  [92]
- $\rho/\pi^0 = 1.0 \pm 0.3$  [94]
- $\omega/\pi^0 = 0.94 \pm 0.08$  [93]
- $\eta'/\pi^0 = 0.25 \pm 0.075$  [94]
- $\phi/\pi^0 = 0.40 \pm 0.12$  [94]

by suitable weight factor. This weight factor is then used as an input in EXODUS particle generator for generation of cocktail. Fig. 3.29 and Fig. 3.30 shows the

other light mesons  $p_T$  spectra obtained by  $m_T$  scaling and the relative normalization of other mesons to the pion.

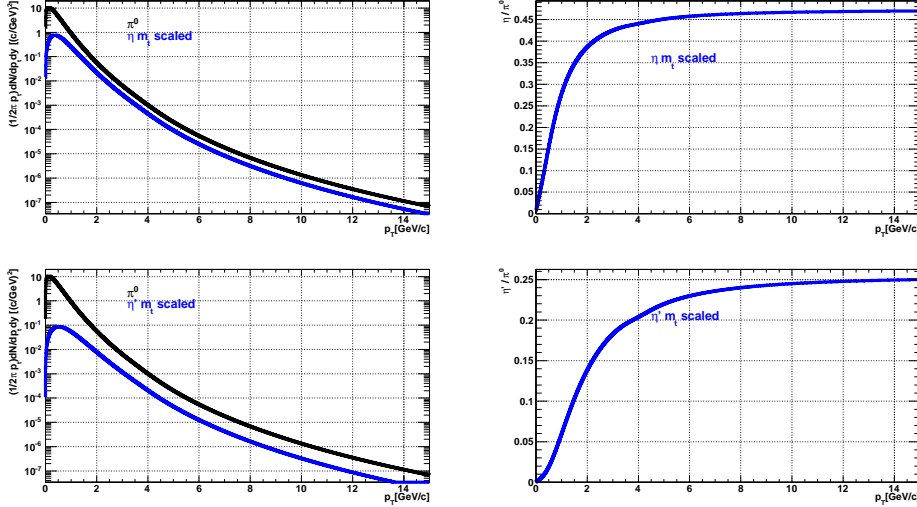


Figure 3.29: Top panel shows the  $\eta m_T$  scaled spectra and  $\eta$ - $\pi^0$  normalization. Bottom panel shows the  $\eta'$   $m_T$  scaled spectra and  $\eta'$ - $\pi^0$  normalization.

## Conversions

Electrons from conversion of photons (mainly from photon conversion of  $\pi^0 \rightarrow \gamma + \gamma$  in the detector material) contributes next to the  $\pi^0$  Dalitz decay towards the heavy flavor single electron. Even though the beam pipe is made of beryllium (low radiation length) still it contributes to the conversion along with the detector material. As electrons are coming from the conversions in Dalitz decays and photon external conversions, so their shapes are almost same. Thus simply by scaling the pion Dalitz decay contribution with proper factor, the conversion electron contribution is being estimated.

The first step involves generating the  $\pi^0 \rightarrow \gamma\gamma$  and  $\pi^0 \rightarrow \gamma e^+ e^-$  in EXODUS using the parametrization of  $\pi^0$  data as in equation 3.14. The generated  $\pi^0$  for both conversions and Dalitz decays are then fed to PISA and then passed through the reconstruction chain to get the simDSTs. The analysis code is then

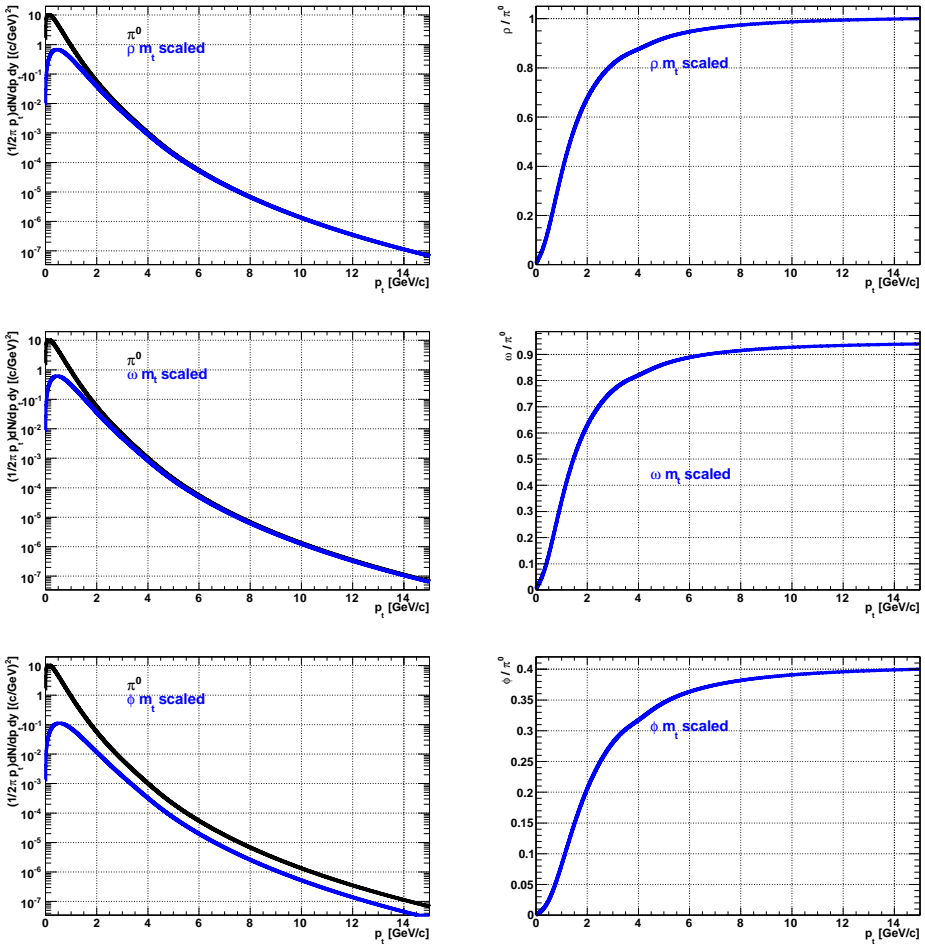


Figure 3.30: Left panel starting from top shows the  $\rho$ ,  $\omega$ ,  $\phi$   $m_T$  scaled spectra. Right panel starting from top  $\rho$ - $\pi^0$ ,  $\omega$ - $\pi^0$ ,  $\phi$ - $\pi^0$  normalization.

executed over these simDSTs for  $\pi^0$  conversions ( $\pi^0 \rightarrow \gamma\gamma$ ) and  $\pi^0$  Dalitz decays ( $\pi^0 \rightarrow \gamma e^+ e^-$ ) to get the single electron  $p_T$  spectra. The ratio of the single electron  $p_T$  spectra from conversions to that of the  $p_T$  spectra of single electron from  $\pi^0$  Dalitz decay gives the conversion factor. This conversion factor is then used for scaling the pion Dalitz decay to determine the contribution of conversion electrons towards the single electron cocktail.

### *Ke<sub>3</sub>* Decays

The electrons from the  $Ke_3$  decays are reconstructed with an incorrectly high momentum as they are generated away from the vertex. Even though these electrons are being rejected by the dep cut still some small amount pass and has to be removed completely. This has been done by full Geant simulation for p+p collisions at 200 GeV. As kaon nuclear modification factor don't differ too much from 1.0 so just by scaling p+p result by  $N_{coll}$  for each centrality bin of d+Au will produce the  $Ke_3$  contribution towards the d+Au single electron cocktail.

#### **3.8.2 Run8 d+Au electron cocktail**

The resulting cocktail for Run8 d+Au at 200 GeV is shown in Fig. 3.31 for minimum bias centrality and Fig. 3.32 for different centralities. The different colored lines are the single electron cocktail from various decay channels as mentioned before. The total background electron cocktail is obtained by summing the contributions from the different channels as shown in the Fig. 3.32. The black curve in the plot is the total background electron cocktail by summing the contribution from the different decay channels of the electron sources.

### **3.9 Systematic Error on inclusive spectra of electrons**

The systematic error arises from detector parameters. This is more important in experimental collider experiments because it reflects how much accurate is our detector in measuring any physical quantity precisely. Statistical errors can be reduced by taking more data. In this section, the determination of systematic error from different sources has been described.

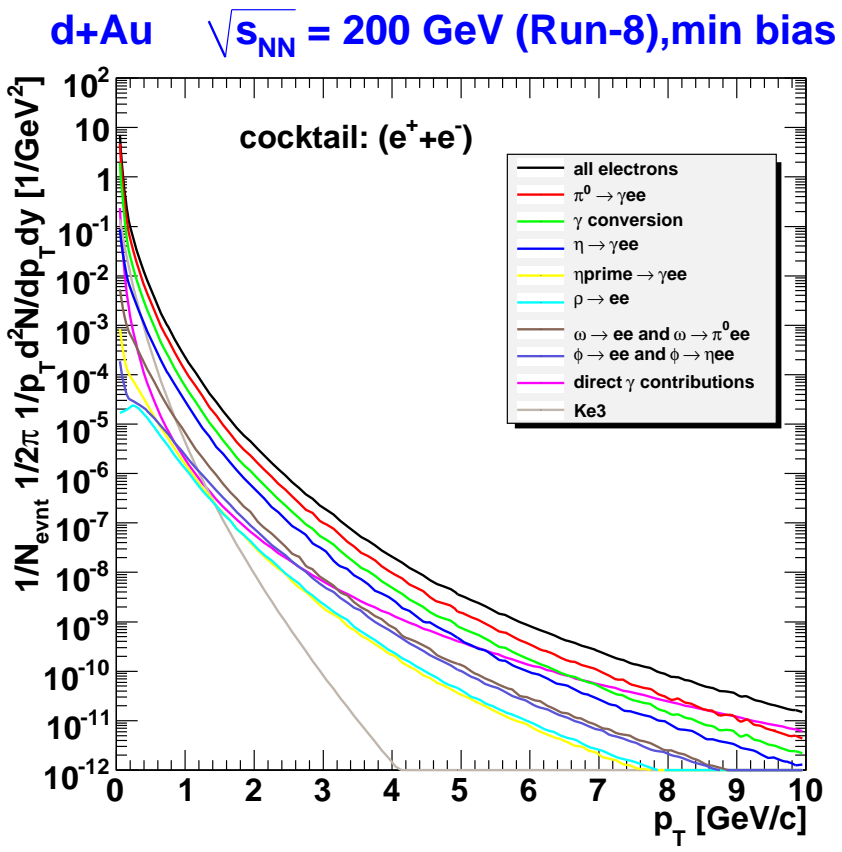


Figure 3.31: Single electron cocktail for Run8 d+Au in minimum bias centrality. Mesonic contributions and  $\gamma$  contribution has also been shown.

### 3.9.1 High $p_T$ extension

Tight eID cut (prob and n0) has been applied at  $p_T > 4.5$  GeV/c. In order to determine the systematic error involved in tight eID cut the ratio of single electron  $p_T$  distribution with tight and base eID is taken as shown in Fig. 3.33. Above  $p_T = 4.5$  GeV there is spread in the ratio of 2%. So systematic error of 2% has been assigned for the high  $p_T$  region for tight eID.

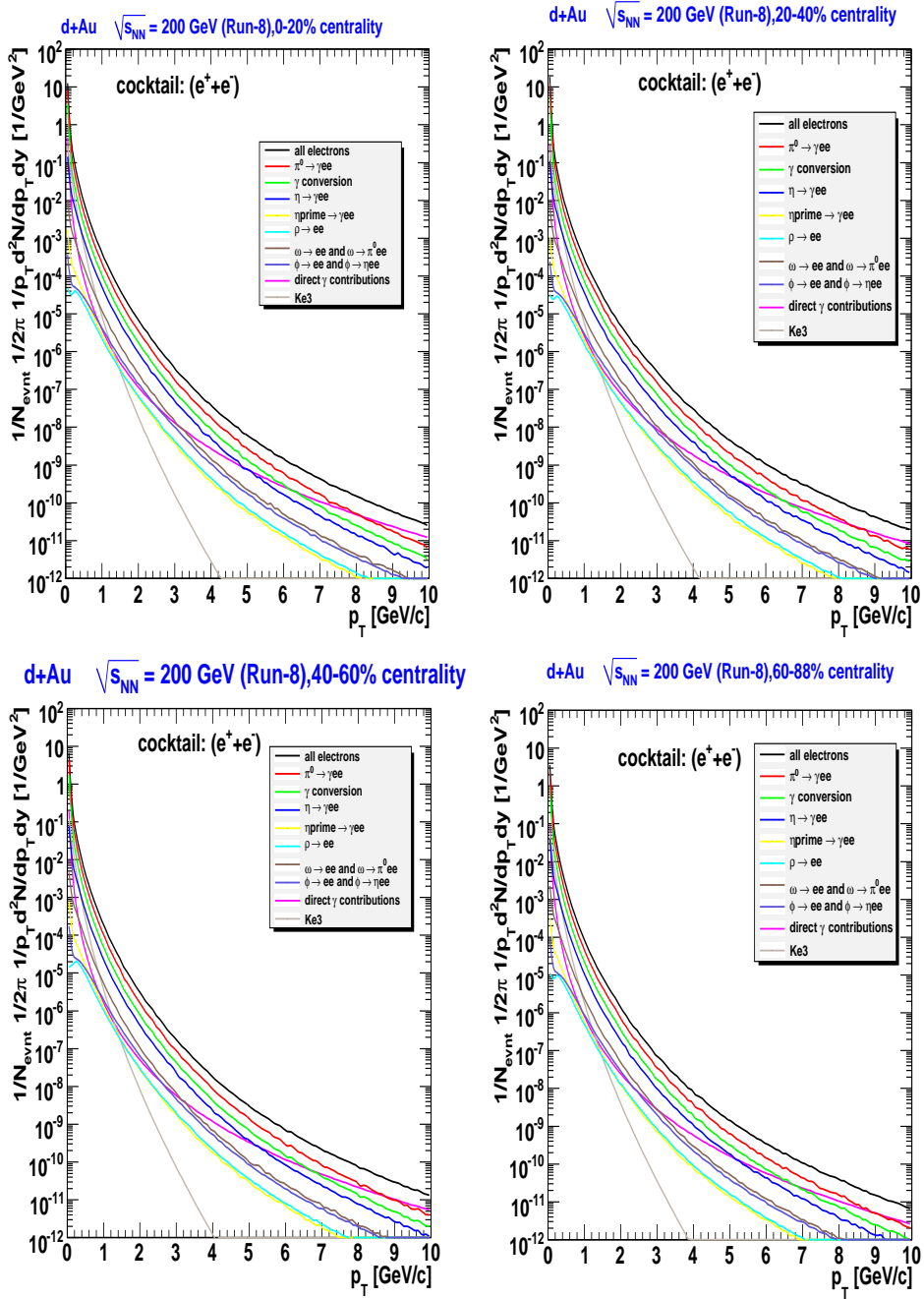


Figure 3.32: Single electron cocktail for Run8 d+Au in other centralities. Mesonic contributions and  $\gamma$  contribution has been shown.

### 3.9.2 Acceptance X eID efficiency

In order to determine the systematic uncertainty in Acceptance  $\times$  eID efficiency the Acceptance  $\times$  eID efficiency has been calculated for tight and standard eID

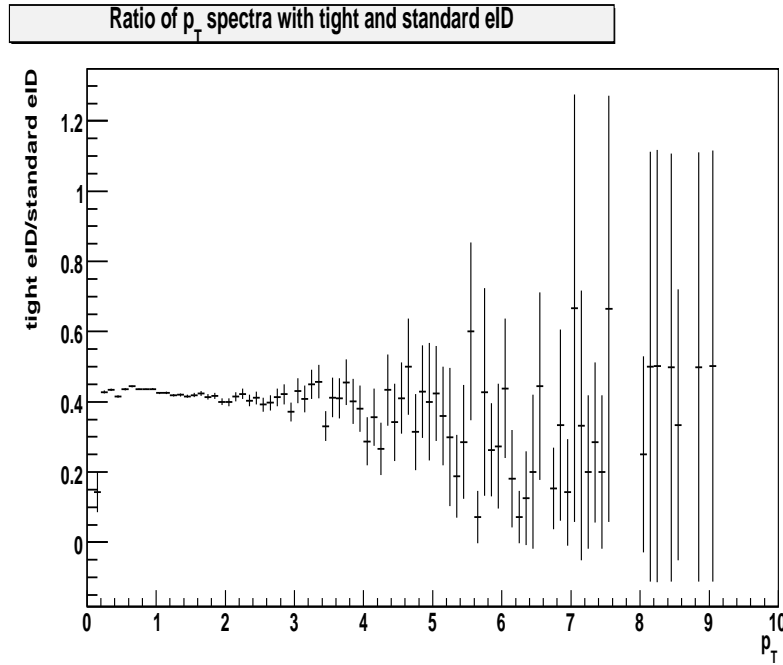


Figure 3.33: Ratio of single electron  $p_T$  distribution with tight eID and standard eID. The spread of 2% for  $p_T > 4.5$  GeV is taken as systematic error for  $p_T > 4.5$  GeV.

cuts. It is to be noted that in the acceptance of the electrons changes with the change in eID cuts. So in the acceptance calculation the eID efficiency is also present and it is reasonable to call the acceptance as Acceptance  $\times$  eID efficiency. The Acceptance  $\times$  eID efficiency curve for the two sets of eID parameters are shown in Fig. 3.34.

Applying these two Acceptance  $\times$  eID efficiency curves to the acceptance uncorrected single electron  $p_T$  spectrum with standard and tight eID cuts, the resulting standard and tight eID cuts  $p_T$  spectrum should become identical. The Acceptance  $\times$  eID efficiency corrected  $p_T$  spectrum for standard and tight eID cuts is shown in Fig. 3.35. However there is spread in the points which shows that the simulation is not modeled perfectly and this introduces the systematic error in calculation of Acceptance  $\times$  eID efficiency.

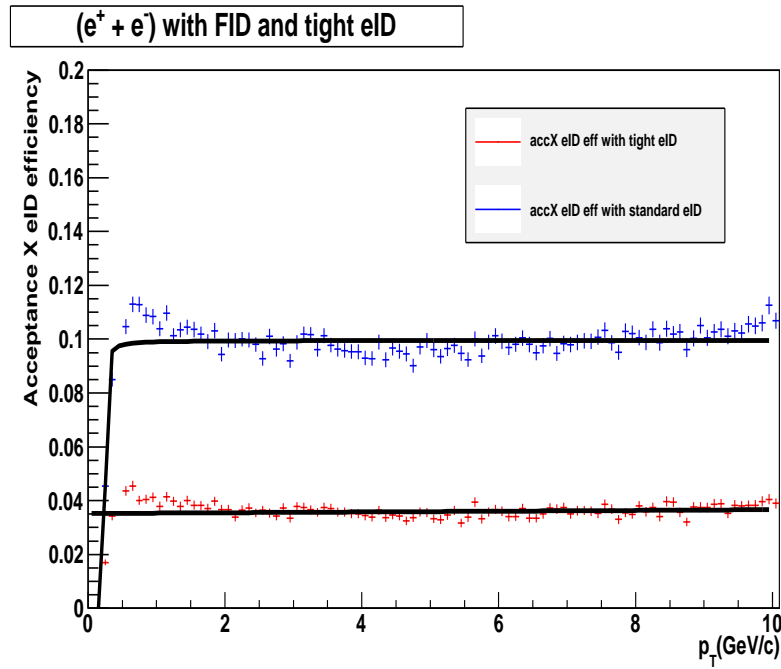


Figure 3.34: Acceptance  $\times$  eID efficiency curve for tight and standard eID cuts. Red is with tight eID cut and blue is with standard eID cut.

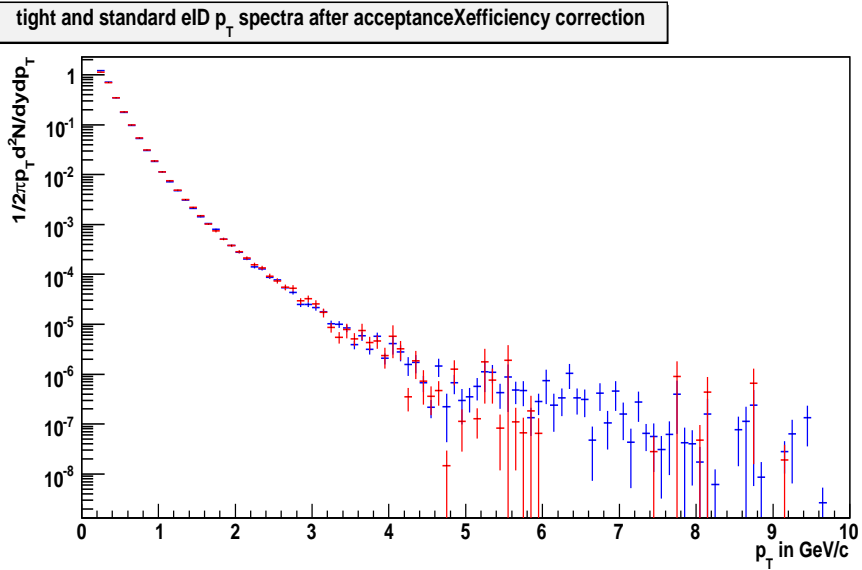


Figure 3.35: Acceptance  $\times$  eID efficiency corrected  $p_T$  spectrum of single electron for standard and tight eID. Blue colored distribution is for standard eID and red is for tight eID.

Taking the ratio of the curves in Fig. 3.35 gives the idea of spread in the points. Fig. 3.36 shows the ratio between the tight eID  $p_T$  spectra and standard

eID  $p_T$  spectra. There is a spread of 6%. So systematic uncertainty of 6% has been assigned to the Acceptance  $\times$  eID efficiency calculation.

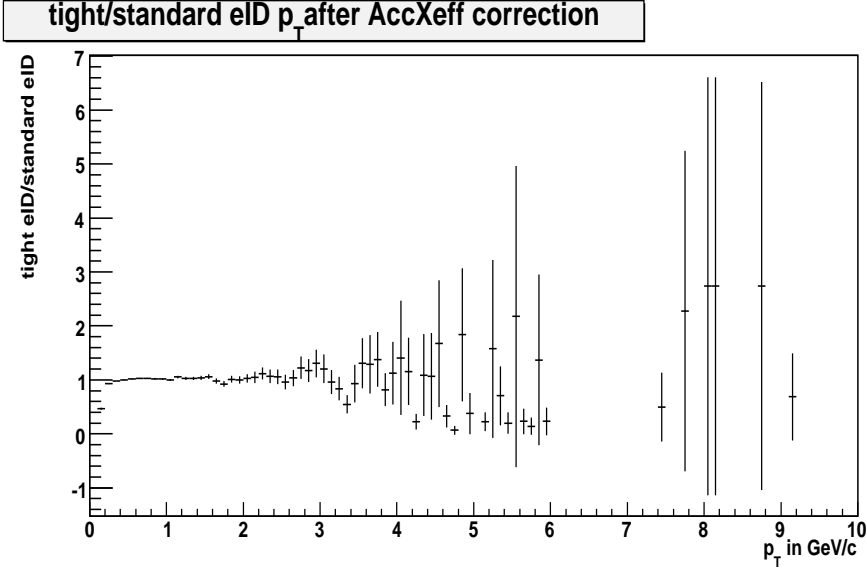


Figure 3.36: Ratio of tight eID  $p_T$  spectra and standard eID  $p_T$  spectra after applying Acceptance  $\times$  eID efficiency correction. The spread in points gives us the idea of how much imperfect is the simulation for Acceptance  $\times$  eID efficiency correction. The spread in point adds up as the systematic error.

### 3.9.3 Geometrical Acceptance

This uncertainty arises because of the mismatch in the real data and simulation acceptance. Figs. 3.22 and 3.23 shows the acceptance matching between data and simulation. Though there is a very good agreement, still it is needed to take into account the mismatch between them as systematic error in the measurement. This has been determined by taking the integral of the distributions in Figs. 3.22 and 3.23, for both data and simulation and then the ratio of data and simulation is taken. The r.m.s of the ratio, data/simulation, is 0.056 and the average is 1.0. Thus the systematic error for geometrical acceptance is taken as 6.0%.

### 3.10 Cocktail Systematic Errors

The input for the cocktail calculation is the pion data as discussed in section 3.8.1. The pion data taken as input has systematic error which introduces systematic error in the final cocktail calculation. In order to determine the systematic error in the cocktail, the pion data is moved up and down by it's systematic error, re-parametrized and then all the steps mentioned in section 3.8 for cocktail calculation are repeated in order to get the up cocktail (cocktail obtained by moving the pion data up by it's systematic error) and the down cocktail (cocktail obtained by moving the pion data down by it's systematic error). The upper and lower cocktail obtained from different photonic and non-photonic sources are added in quadrature to get total upper and lower systematic error on single electron cocktail. Fig. 3.37 shows the upper and lower relative systematic errors on single electron  $d + Au$  cocktail.

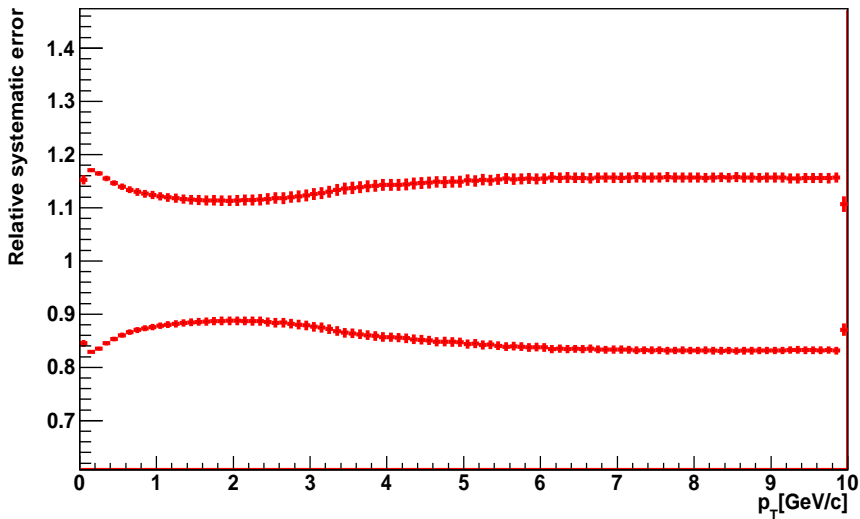


Figure 3.37: Upper and lower relative systematic error on  $d + Au$  single electron cocktail.

The final systematic error on single electron cocktail in  $d+Au$  is obtained by adding the magnitudes of upper and lower systematic errors as shown in fig. 3.37

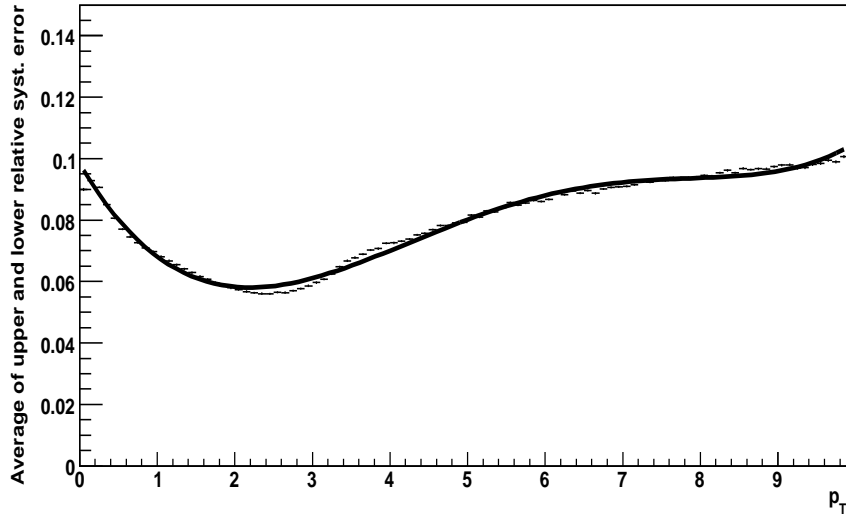


Figure 3.38: Total systematic error on  $d + Au$  single electron cocktail in minbias centrality. The plot is obtained by taking the average of upper and lower curves in fig. 3.37. Also shown is the fit by the curve to the total cocktail systematic error plot. The fit function used is mentioned in the text.

and then taking the average of it. Fig. 3.38 shows the final systematic error plot for  $d + Au$  single electron cocktail. The total relative systematic error plot is further fitted with the function of the form

$$f(p_T) = p_0 e^{p_1 p_T} + p_2 + p_3 p_T + p_4 p_T^2 + p_5 p_T^3, \quad (3.15)$$

where  $p_0$  to  $p_5$  are fit parameters and  $p_T$  is the transverse momentum of the single electron. The fit function is used for putting up the systematic error on the final single electron heavy flavor spectra.

### 3.11 Converter Analysis; Extraction of photonic electrons

During Run8, thin brass sheet was wrapped around beampipe in order to increase the contribution from conversion to the inclusive electron spectrum. This was

mainly done to determine the contribution of photonic electrons to the overall electron measurement.

The total yield of electron is from photonic ( $N^\gamma$ ) and non-photonic ( $N^{non-\gamma}$ ). Thus, without converter the total yield can be expressed as

$$N_e^{non-conv} = N^\gamma + N^{non-\gamma}. \quad (3.16)$$

The total yield of electrons with the converter-in is then given by

$$N_e^{conv} = R_\gamma N^\gamma + (1 - \epsilon) N^{non-\gamma}. \quad (3.17)$$

The various parameters in the above equations are defined in Table 3.11.

Table 3.2: Definition of the variables in Eqn. 3.16 and Eqn. 3.17

$N_e^{conv}$	The electron yield per MB event in converter run. For ERT data set this is electron yield per MB sampled event.
$N_e^{non-conv}$	The electron yield per MB event in non-converter run. For ERT data set this is electron yield per MB sampled event.
$N_e^\gamma$	The electron yield from photonic sources. This is the background removed by the converter method.
$N_e^{non-\gamma}$	The electron yield from non-photonic sources. It consists of the heavy flavor electron signal and the non-photonic background such as $Ke_3$ and the electrons from vector meson decays ( $\rho \rightarrow ee, \omega \rightarrow ee$ , etc)
$R_\gamma$	The ratio of photonic electron yield in converter run to that of the non-converter run determined by simulation.
$\epsilon$	Additional energy loss of electrons, due to converter. Determined from simulation.

By solving Eqn. 3.16 and Eqn. 3.17 we get  $N_e^\gamma$  and  $N_e^{non-\gamma}$  as

$$N_e^\gamma = \frac{N_e^{conv} - (1 - \epsilon) N_e^{non-conv}}{R_\gamma - 1 + \epsilon} \quad (3.18)$$

$$N_e^{non-\gamma} = \frac{R_\gamma N_e^{non-conv} - N_e^{conv}}{R_\gamma - 1 + \epsilon} \quad (3.19)$$

Before determining the photonic electron yield it is important to match the acceptance in converter and non-converter data set. If they don't match then additional fiducial cuts are to be applied to force match the acceptance. This has been done for both MB and ERT data set. Fig. 3.39 and Fig. 3.40 shows the comparison of Drift Chamber active area in phi and z coordinate respectively between converter and non-converter runs in MB data set. The acceptance appears to be matching within acceptance level. Fig. 3.41 and Fig. 3.42 shows the comparison of Drift chamber active area in phi and EMCAL active area in z coordinate respectively between converter and non-converter runs in ERT data set. Additional fiducial cuts has to be applied in order to match the acceptance for ERT converter and non-converter runs.

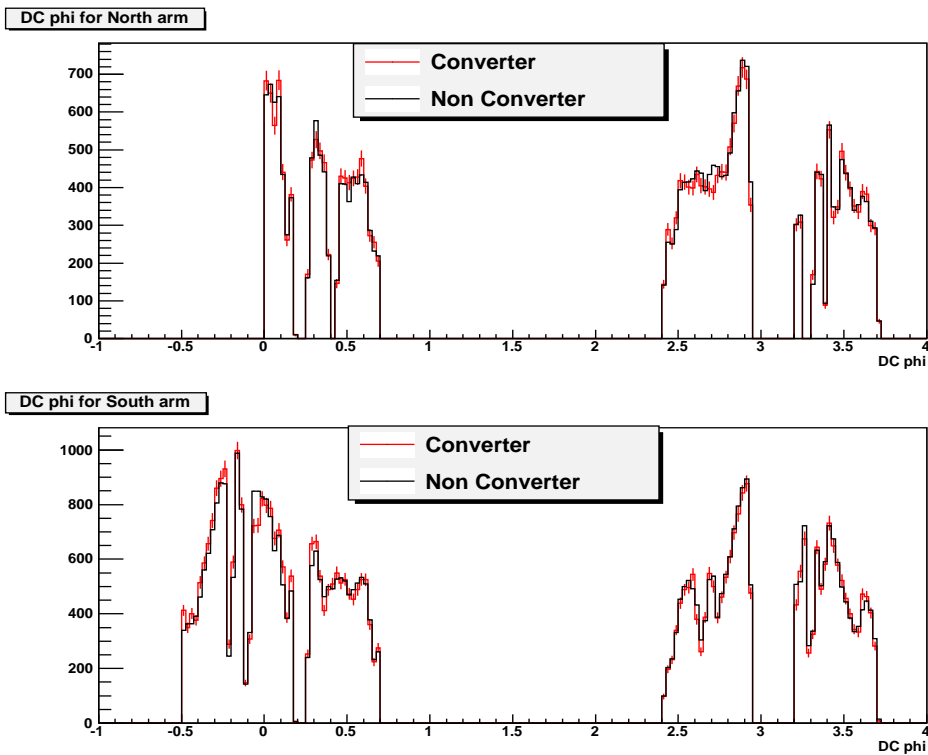


Figure 3.39: Converter and non-converter active Drift Chamber in phi coordinate distribution in MB data set. The converter data is rescaled such that the integral of the phi distribution in the converter data and in the non-converter data agrees. y axis is the rescaled counts.

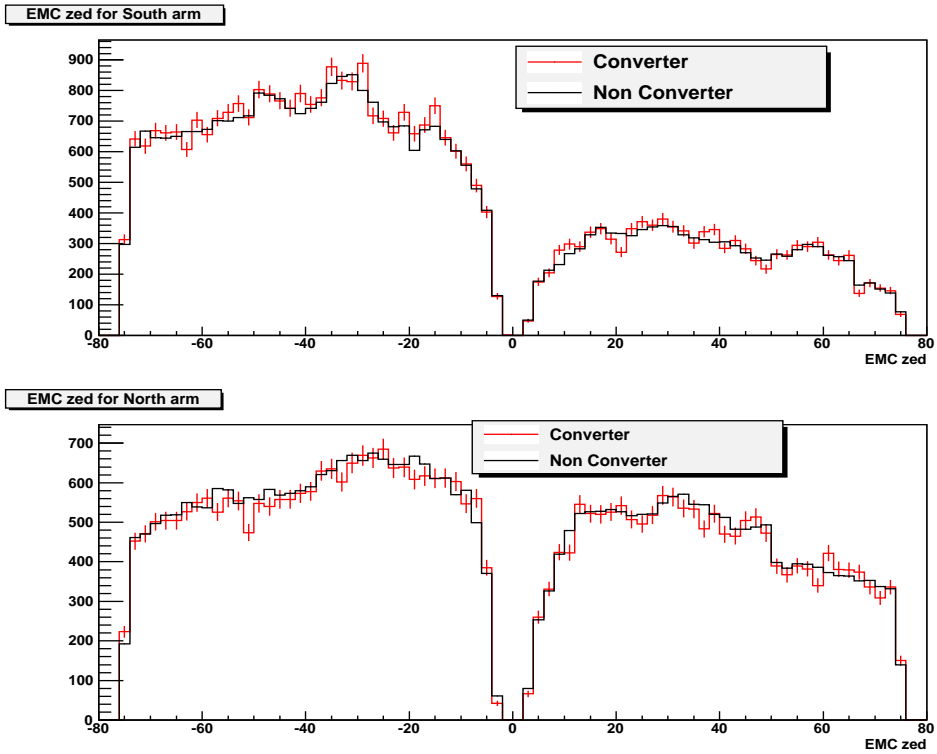


Figure 3.40: Converter and non-converter EMCAL active area in  $z$  coordinate distribution in MB data set. The converter data is rescaled such that the integral of the EMCAL  $z$  distribution in the converter data and in the non-converter data agrees.  $y$  axis is the rescaled counts.

In order to check the presence of non-photonic electrons another parameter named  $R_{CN}$  is being determined which is the ratio of converter and non-converter electron yield.

$$R_{CN} = \frac{N_e^{conv}}{N_e^{non-conv}} \quad (3.20)$$

Fig. 3.43 shows the converter and non-converter  $p_T$  spectra for MB data set and for ERT data set. Upto 1.6 GeV MB data set is used and for  $p_T > 1.6$  GeV ERT data set is used for getting the  $R_{CN}$ . Here the ERT data set has not been corrected for ERT trigger efficiency. As long as the ERT trigger data set is used well above the threshold the ERT trigger correction is not needed to apply as the effect of trigger efficiency cancels out while taking the ratio. Here the ERT data

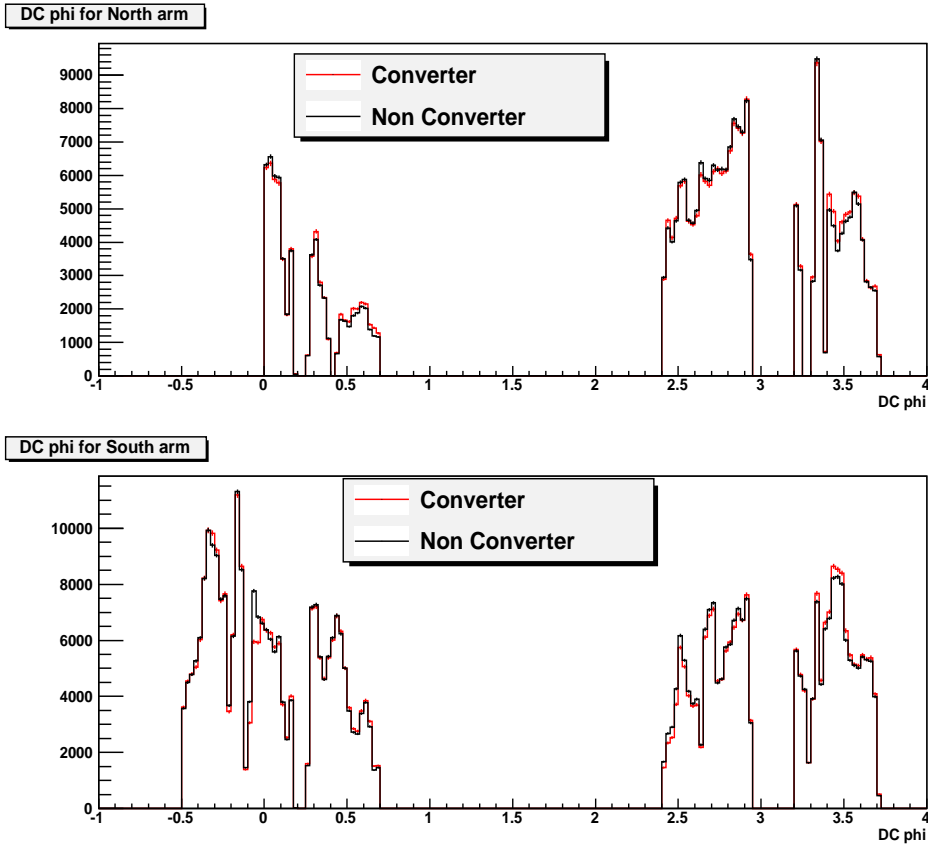


Figure 3.41: Converter and non-converter active Drift Chamber in phi coordinate distribution in ERT data set. Red is for converter and black is for non-converter runs. The converter data is rescaled such that the integral of the phi distribution in the converter data and in the non-converter data agrees. y axis is the rescaled counts.

set is used at  $p_T > 1.6\text{GeV}$  which is well above the ERT trigger threshold of 800 MeV.

Fig. 3.44 shows the ratio of converter and non-converter run electron yield ( $R_{CN}$ ) as a function of  $p_T$ . This has been obtained by taking the ratio of red over blue histogram in Fig. 3.43. The black curve in Fig. 3.44 is the  $R_\gamma$  obtained from simulation.  $R_\gamma$  is basically the expected  $R_{CN}$  for purely photonic electrons. However from Fig. 3.44 it can be seen that  $R_{CN}$  is below  $R_\gamma$  implying that non-photonic electrons are present in the data. The  $R_{CN}$  decreases with increasing  $p_T$  showing the non-photonic components increases with increasing  $p_T$ .

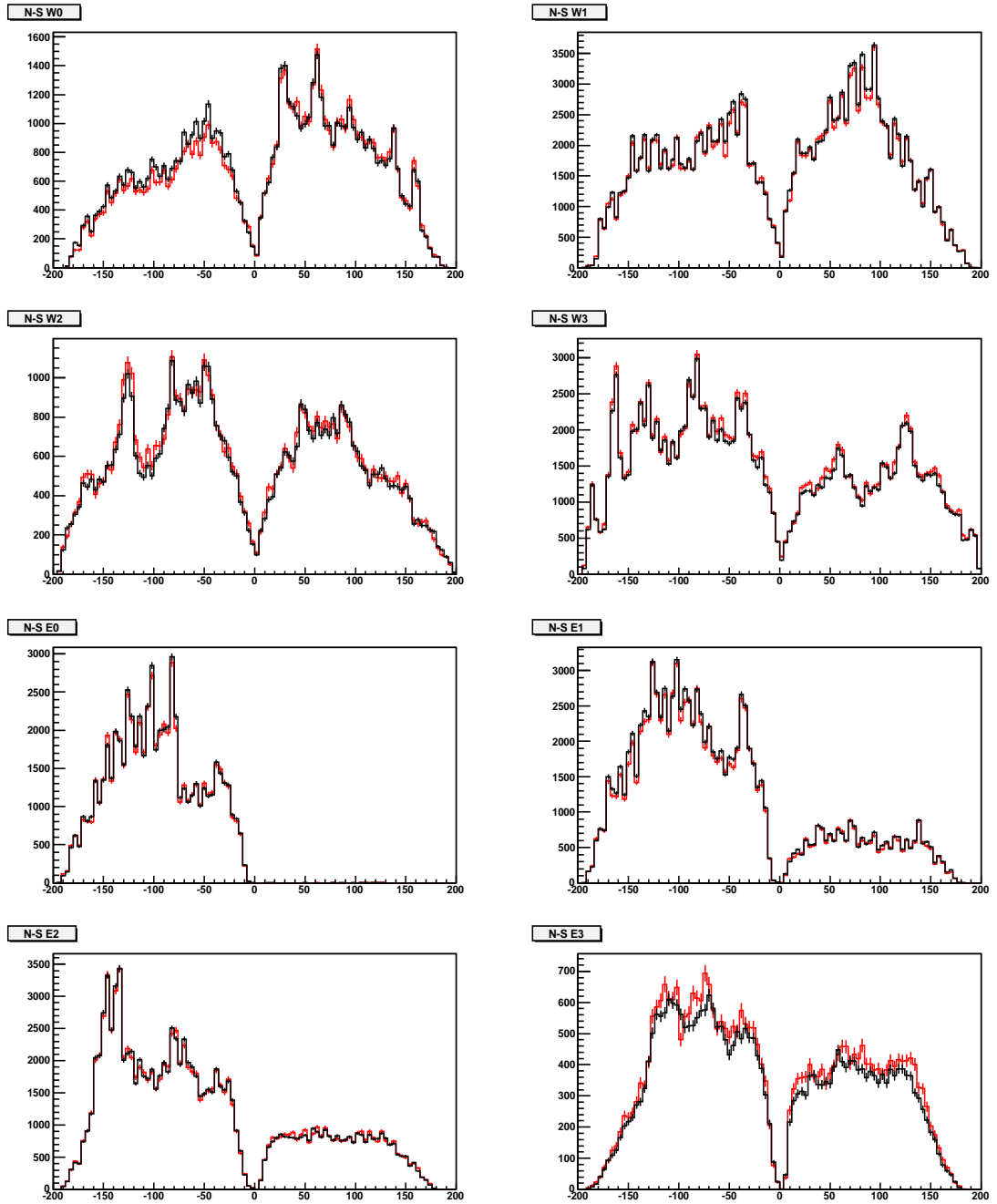


Figure 3.42: Converter and non-converter active EMCAL in z coordinate distribution in ERT data set for 7 different sectors of EMCAL. Red is for converter and black is for non-converter runs. The converter data is rescaled such that the integral of the EMCAL z distribution in the converter data and in the non-converter data agrees. y axis is the rescaled counts.

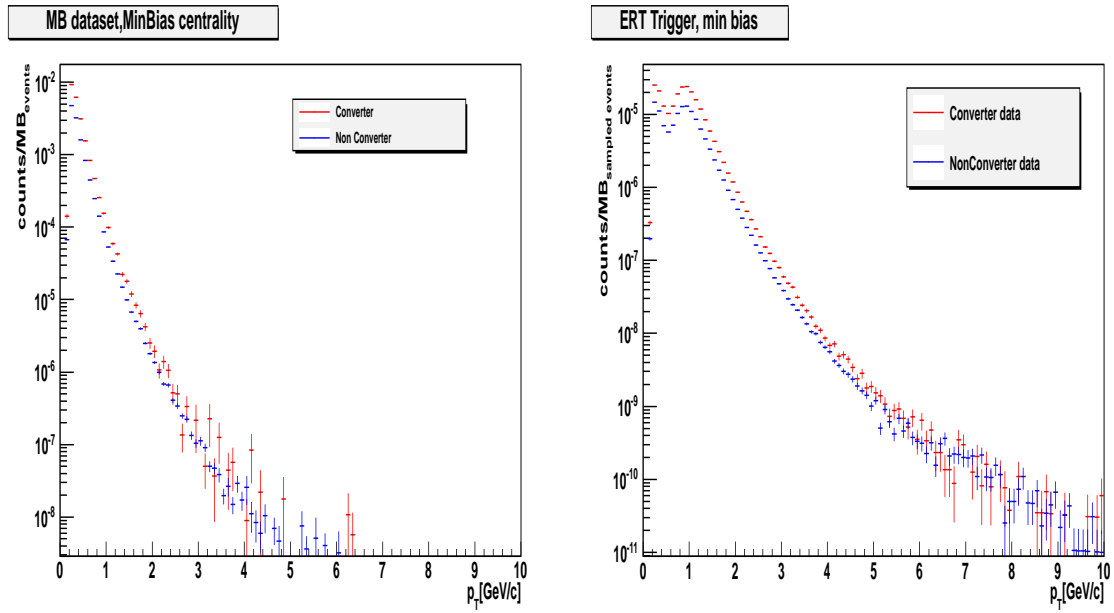


Figure 3.43: Converter and non-converter electron ( $e^+ + e^-$ ) yield. Left is from MB trigger data set and right plot is from ERT triggered data set.

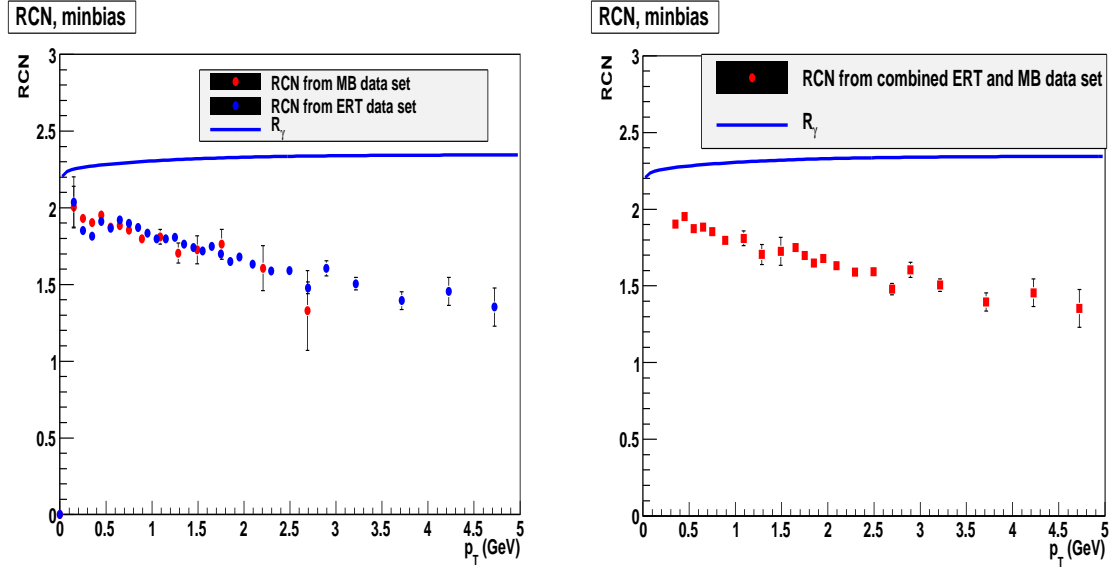


Figure 3.44:  $R_{CN}$  in minimum bias centrality. Left plot shows the overlay of  $R_{CN}$  from MB and ERT data set. Right plot is the combined MB and ERT data set  $R_{CN}$ . For  $p_T \leq 1.6$  GeV MB data set is used and for  $p_T > 1.6$  GeV ERT data set is used. The black curve in both the left and right hand plots shows the  $R_\gamma$ .

For evaluation of non-photonic electrons included in the photonic electrons in real data , the ratio,  $R_{NP} = N_e^{non-\gamma}/N_e^\gamma$  is defined. The expression of  $R_{NP}$  in terms of  $R_{CN}$  can is given by

$$R_{NP} = \frac{R_\gamma - R_{CN}}{R_{CN} - 1 + \epsilon} \quad (3.21)$$

Fig. 3.45 shows the  $R_{NP}$  for minimum bias centrality. The left hand plot is the overlay of  $R_{NP}$  from MB and ERT data set while the right hand plot is the combined  $R_{NP}$  from MB and ERT data set where for  $p_T \leq 1.6$  GeV MB data set is used and for  $p_T > 1.6$  GeV ERT data set is used.

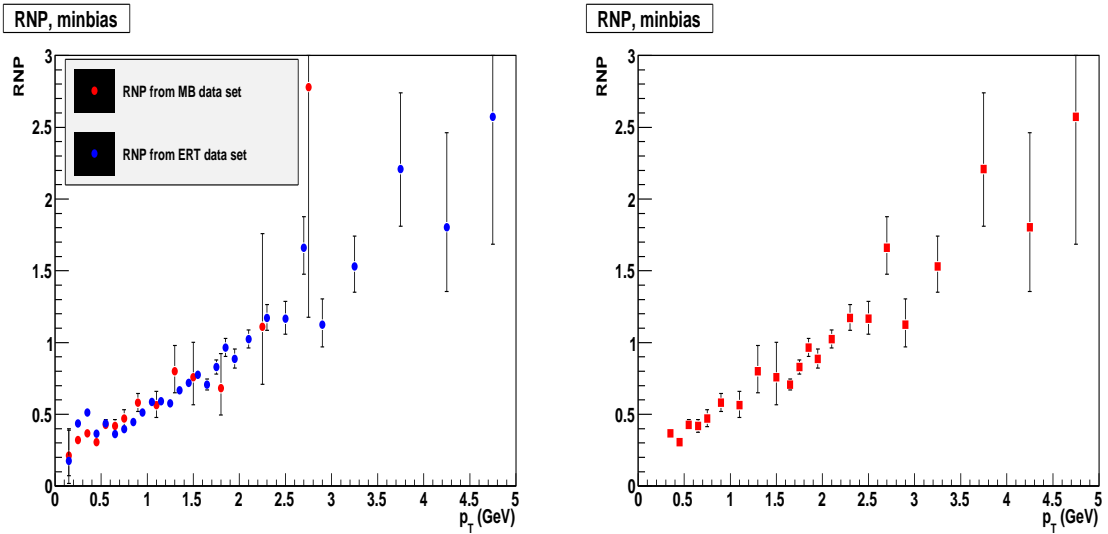


Figure 3.45:  $R_{NP}$  from ERT and MB data set. Left hand plot is the overlay of  $R_{NP}$  from MB and ERT data set. Red points are from MB triggered data and blue points are from ERT triggered data. Right hand plot is the combined  $R_{NP}$  from MB and ERT data. For  $p_T \leq 1.6$  GeV MB data is used and for  $p_T > 1.6$  GeV ERT data is used.

As different sets of additional fiducial cuts are being applied to MB and ERT dataset in order to match the acceptance for Converter and non-Converter data, so the acceptance with these fiducial cuts are being recalculated using these new sets of fiducial cuts. Same procedure as described in section 3.7.4 is being followed here as well. The difference is in the fiducial cuts used in the analysis

code. Like in section 3.7.4 the acceptance matching between the real data and the MC has to be checked for both in MB trigger data and the ERT trigger data as the MB and ERT triggered data has different sets of fiducial cuts here. Fig. 3.46 shows the real data and simulation phi distribution matching for the fiducial cuts applied in MB triggered data set.

Fig. 3.47 shows the real data and simulation EMCAL z distribution matching for the fiducial cuts applied in MB triggered data set.

The matching for the real data and simulated phi distribution in case of ERT dataset is shown in fig. 3.48.

Fig. 3.49 shows the real data and simulation EMCAL z distribution matching for the fiducial cuts applied in ERT triggered data set.

The  $p_T$  spectra of single electron before and after passing through PISA is shown in fig. 3.50. The fiducial cut here is for MB triggered data meant for matching the Converter and non-converter acceptance.

The acceptance is calculated by dividing the output spectrum of the reconstructed electron by the input spectrum of generated electrons and is shown in fig. 3.51 for MB datafiles with fiducial cuts meant for matching the acceptance in converter and non-converter data. The mathematical expression for acceptance calculation can be given by :

$$\epsilon = \frac{dN_{reco}/dp_T^{reco}}{dN_{gen}/dp_T^{gen}} \quad (3.22)$$

where  $dN_{reco}/dp_T^{reco}$  is the yield of reconstructed single electron and  $dN_{gen}/dp_T^{gen}$  is the yield of generated single electron.

Fig. 3.52 shows the  $p_T$  spectra of single electron before and after passing through PISA. The fiducial cut here is for ERT triggered data meant for matching the converter and non-converter acceptance.

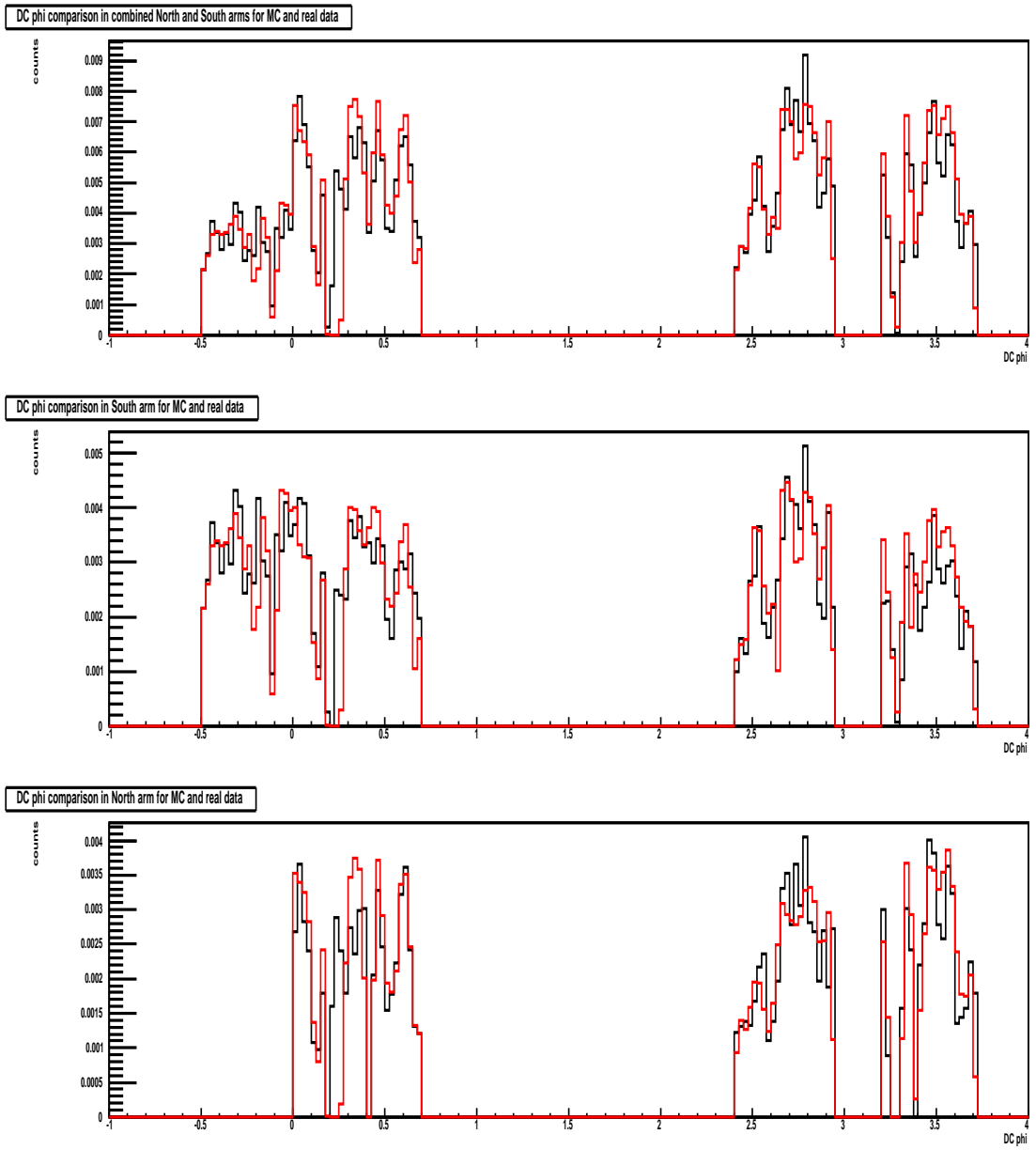


Figure 3.46: DC phi acceptance matching for simulation and MB triggered real data. Red is simulation and black is real data. The real data is rescaled such that the integral of the phi distribution in the real data and in the simulation agrees. y axis is the rescaled counts. Top panel is for combined North and South arm of DC. Central panel is for South arm of DC and the bottom panel is for North arm of DC.

Fig. 3.53 shows the acceptance plot with fiducial cuts meant for matching the acceptance in converter and non-converter data in ERT dataset. This has

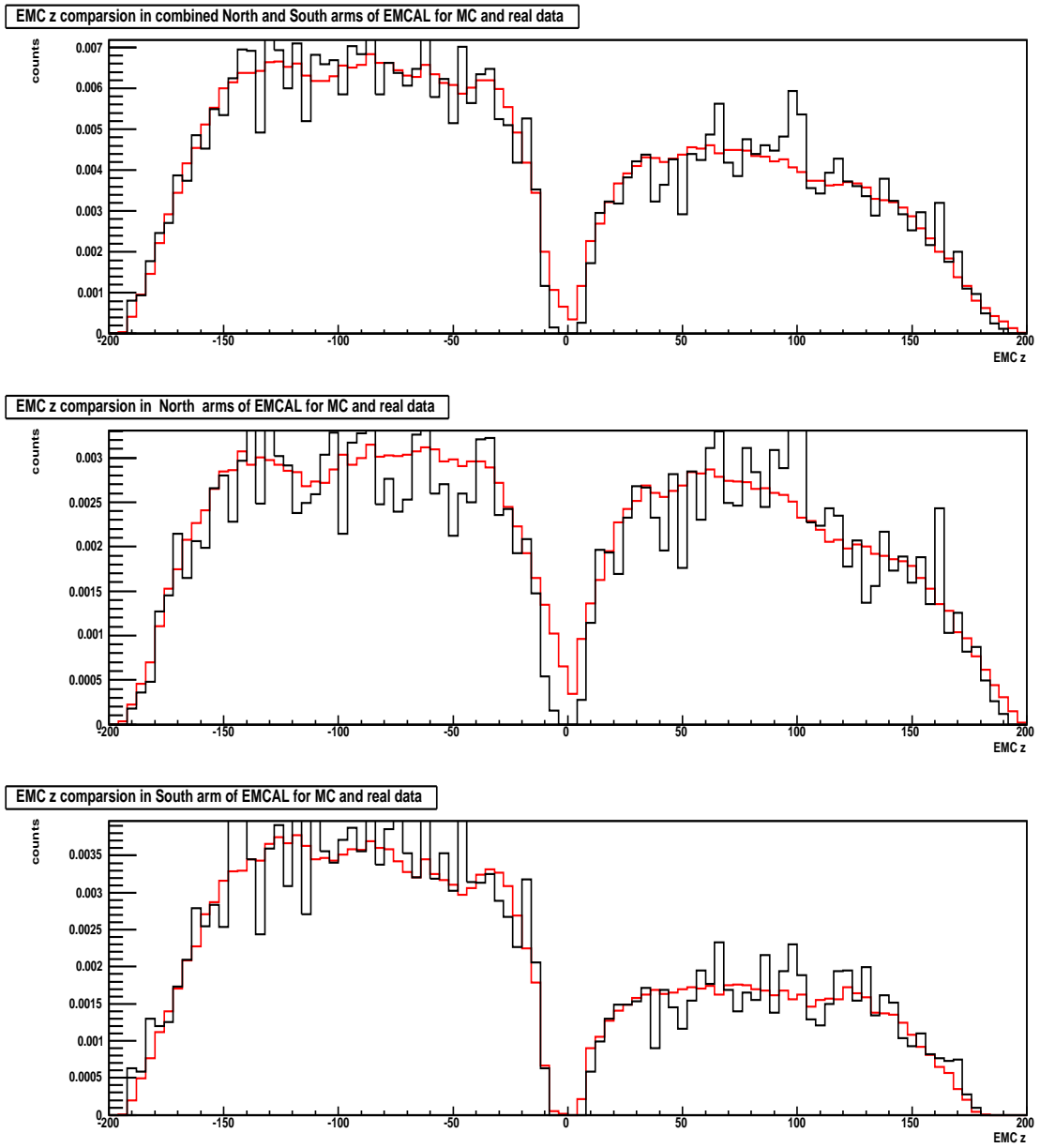


Figure 3.47: EMCAL z acceptance matching for simulation and MB triggered real data. Red is simulation and black is real data. The real data is rescaled such that the integral of the EMCAL z distribution in the real data and in the simulation agrees. y axis is the rescaled counts. Top panel is for combined North and South arm of EMCAL. Central panel is for North arm of EMCAL and the bottom panel is for South arm of EMCAL.

been calculated by dividing the output spectrum of the reconstructed electron by

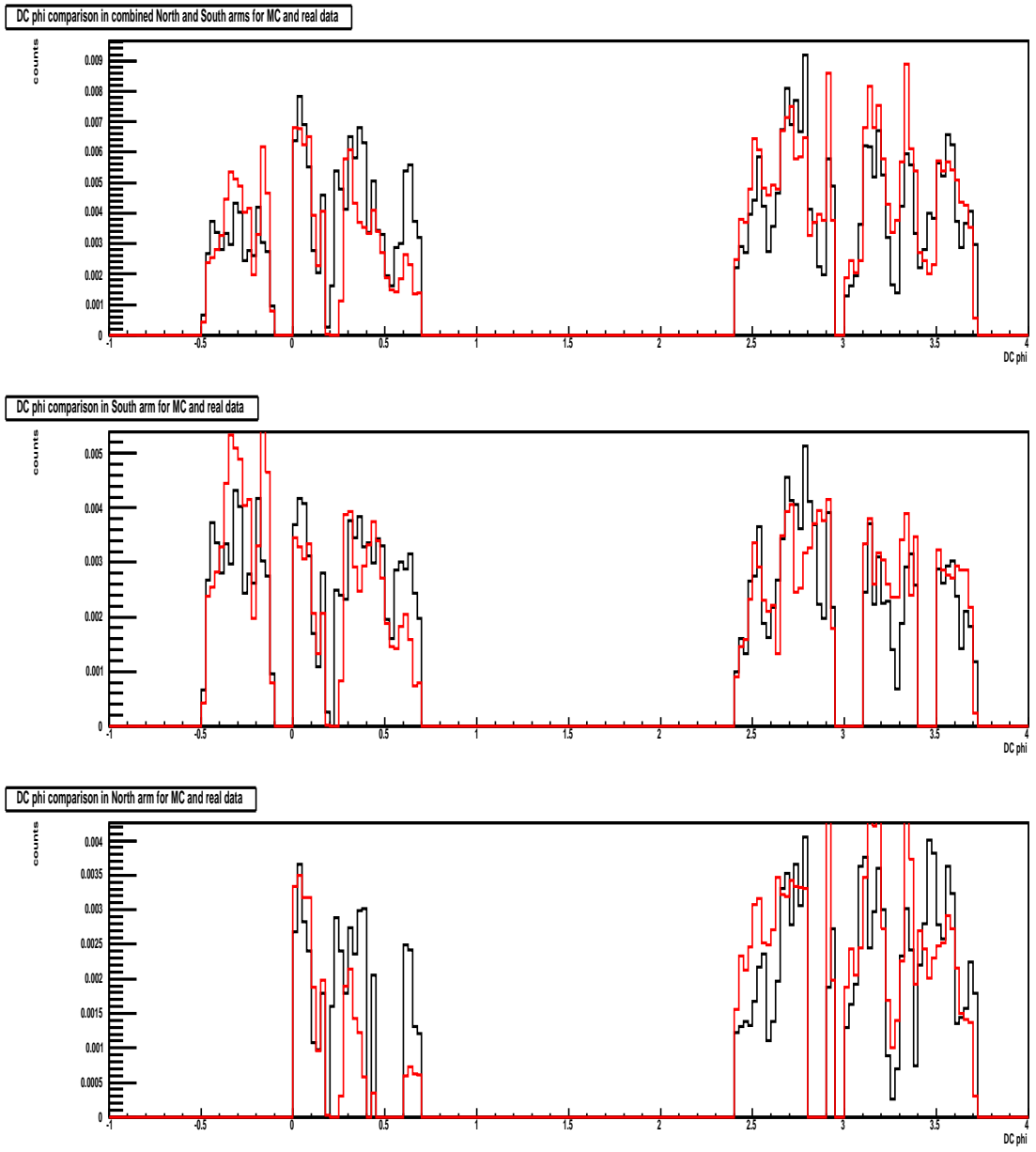


Figure 3.48: DC phi acceptance matching for simulation and ERT triggered real data. Red colored distribution is simulation and black colored distribution is real data. The real data is rescaled such that the integral of the phi distribution in the real data and in the simulation agrees. y axis is the rescaled counts. Top panel is for combined North and South arm of DC. Central panel is for South arm of DC and the bottom panel is for North arm of DC.

the input spectrum of generated electrons :

$$\epsilon = \frac{dN_{reco}/dp_T^{reco}}{dN_{gen}/dp_T^{gen}} \quad (3.23)$$

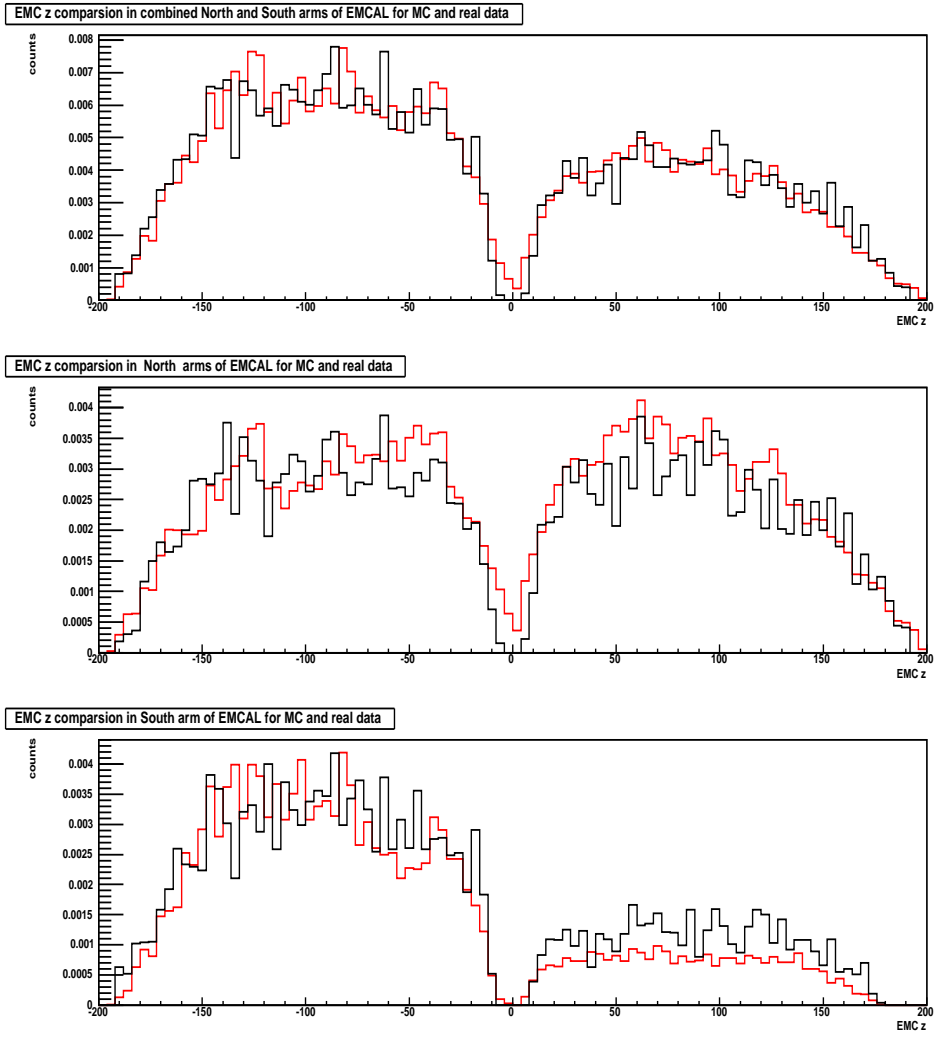


Figure 3.49: EMCAL z acceptance matching for simulation and ERT triggered real data. Red colored distribution is simulation and black colored distribution is real data. The real data is rescaled such that the integral of the EMCAL z distribution in the real data and in the simulation agrees. y axis is the rescaled counts. Top panel is for combined North and South arm of EMCAL. Central panel is for North arm of EMCAL and the bottom panel is for South arm of EMCAL.

where  $dN_{reco}/dp_T^{reco}$  is the yield of reconstructed single electron and  $dN_{gen}/dp_T^{gen}$  is the yield of generated single electron.

In order to get high statistics in high  $p_T$  region ERT data set is used. The ERT data set has been corrected for ERT trigger efficiency (Fig. 3.11) as in section 3.7.1. The complete expression for photonic single electron invariant yield

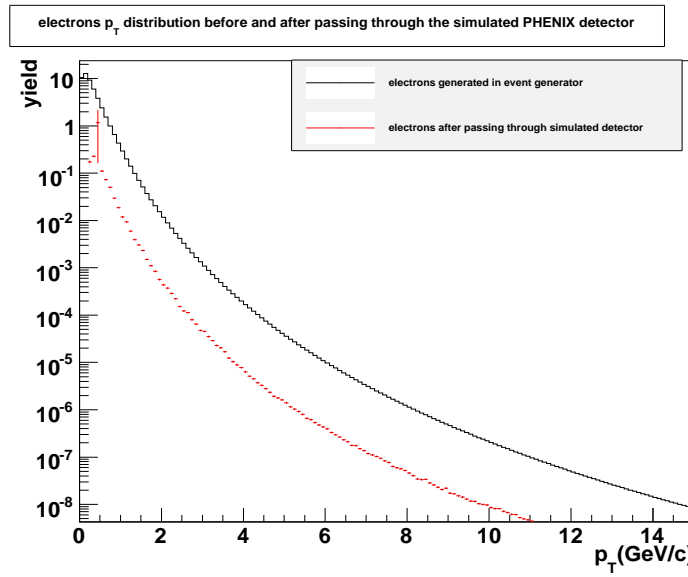


Figure 3.50: Spectra of single electron before passing through PISA (black curve) and after passing through PISA and reconstruction chain (red curve).

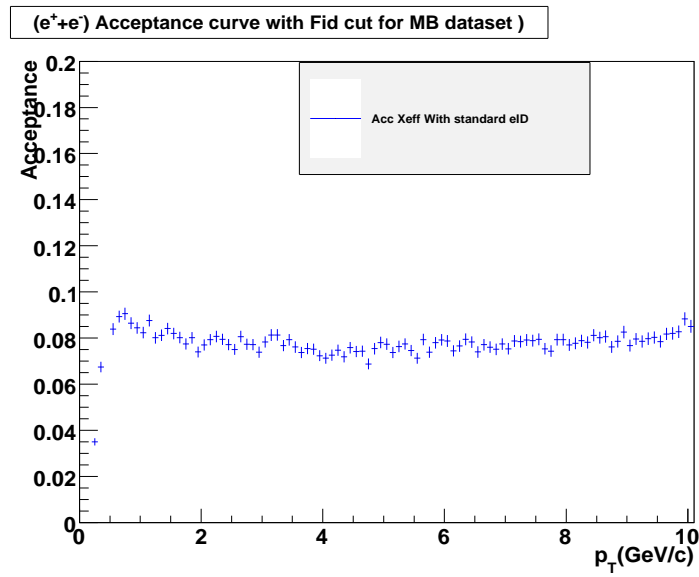


Figure 3.51: Acceptance plot for  $e^+ + e^-$  with fiducial cuts for MB triggered acceptance match for non-converter and converter data set

from MB and ERT data set is given by

$$\frac{d^2N}{2\pi p_T dp_T dy} = \frac{1}{2\pi p_T} \frac{1}{\Delta p_T} \frac{N_e^\gamma}{\epsilon_{trigg} \epsilon_{acc}} \quad (3.24)$$

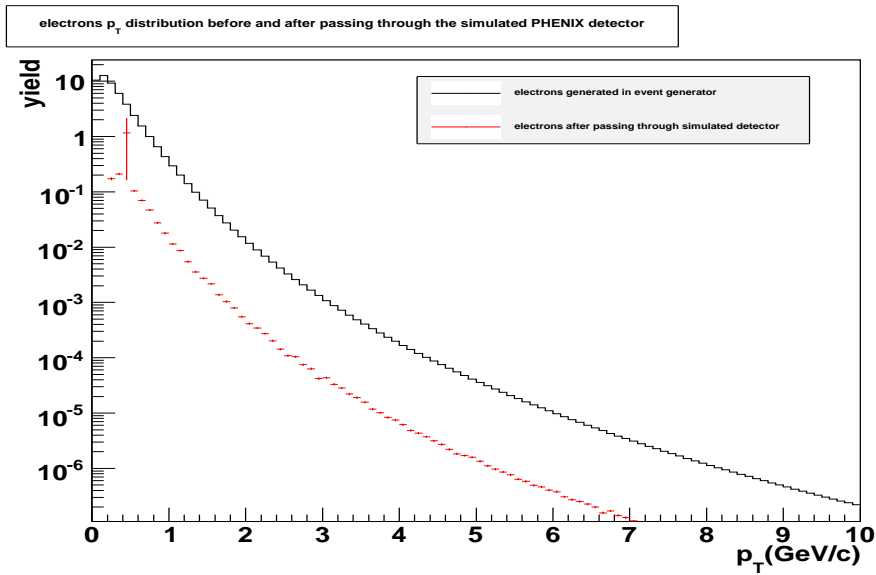


Figure 3.52: Spectra of single electron before passing through PISA (black curve) and after passing through PISA and reconstruction chain (red curve).

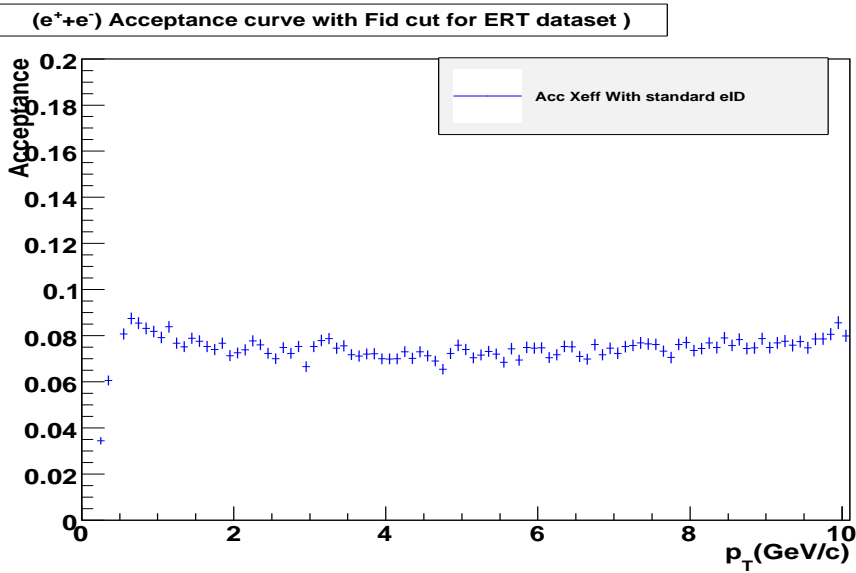


Figure 3.53: Acceptance plot for  $e^+ + e^-$  with fiducial cuts for ERT triggered acceptance match for non-converter and converter data set.

where

- $N_e^\gamma$  is the photonic electron component obtained from Eq. 3.18.
- $\epsilon_{trigg}$  is the ERT trigger efficiency and  $\epsilon_{acc}$  is the acceptance correction.

The cocktail calculation of the photonic electron invariant yield is then compared with the photonic electron invariant yield obtained in Eq. 3.24. If there is any difference then the photonic electron component of cocktail calculation is normalized by that factor before subtracting them from the inclusive single electron invariant yield.

### 3.11.1 Comparison of photonic electron invariant yield and cocktail photonic component

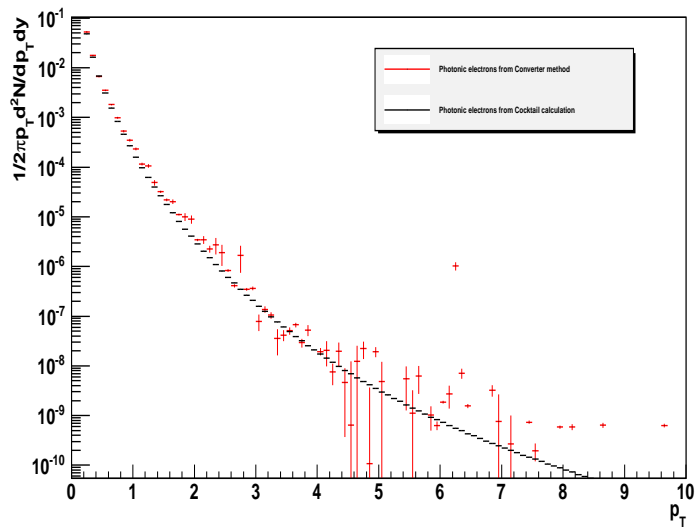


Figure 3.54: Invariant yield of photonic electrons obtained from converter method. Black curve is the photonic electrons from Cocktail method.

Fig. 3.54 is the invariant yield of the photonic electrons obtained from the converter method (red histogram) along with the photonic component of the cocktail calculation (black curve). The invariant yield of the photonic electron from converter method has MB triggered data for  $p_T < 1.6$  GeV and ERT triggered data corrected for ERT trigger efficiency for  $p_T \geq 1.6$  GeV. Further acceptance correction from Fig. 3.51 for MB triggered and from Fig. 3.53 has been applied. Fig. 3.55 is the ratio of photonic electron yield from the Converter method and the photonic component of cocktail. This ratio plot is further fitted by a constant

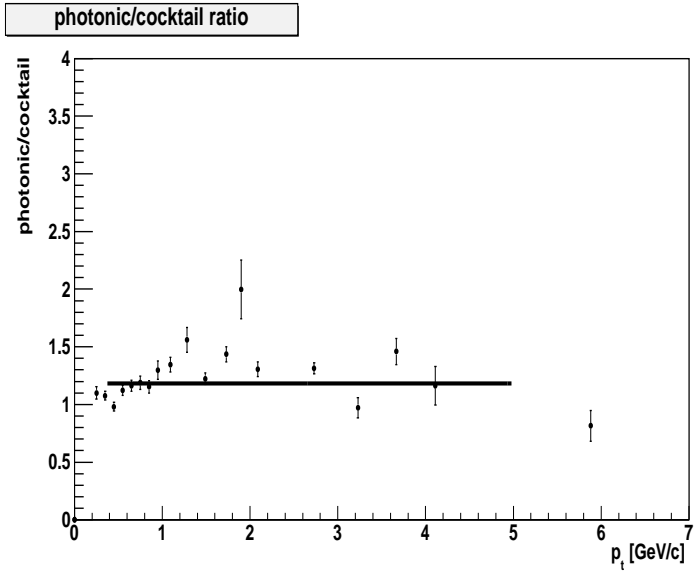


Figure 3.55: Ratio of the photonic electron invariant yield from converter method and the photonic cocktail component. The ratio is fitted with a constant value.

value fit. The fit value is being used as the scaling factor for the photonic components of the cocktail(Fig. 3.31) before subtracting it from the inclusive single electron spectra(Fig. 3.58).

### 3.11.2 Non-photonic single electron

The non-photonic single electron invariant yield from MB and ERT data set is given by

$$\frac{d^2N}{2\pi p_T dp_T dy} = \frac{1}{2\pi p_T} \frac{1}{\Delta p_T} \frac{N_e^{non-\gamma}}{\epsilon_{trigg} \epsilon_{accXeff}} \quad (3.25)$$

where  $N_e^{non-\gamma}$  is the non-photonic electron component obtained from Eq. 3.19. Fig. 3.56 shows the non-photonic single electron obtained from the Converter analysis along with the non-photonic single electron cocktail from the cocktail calculation in minimum bias centrality.

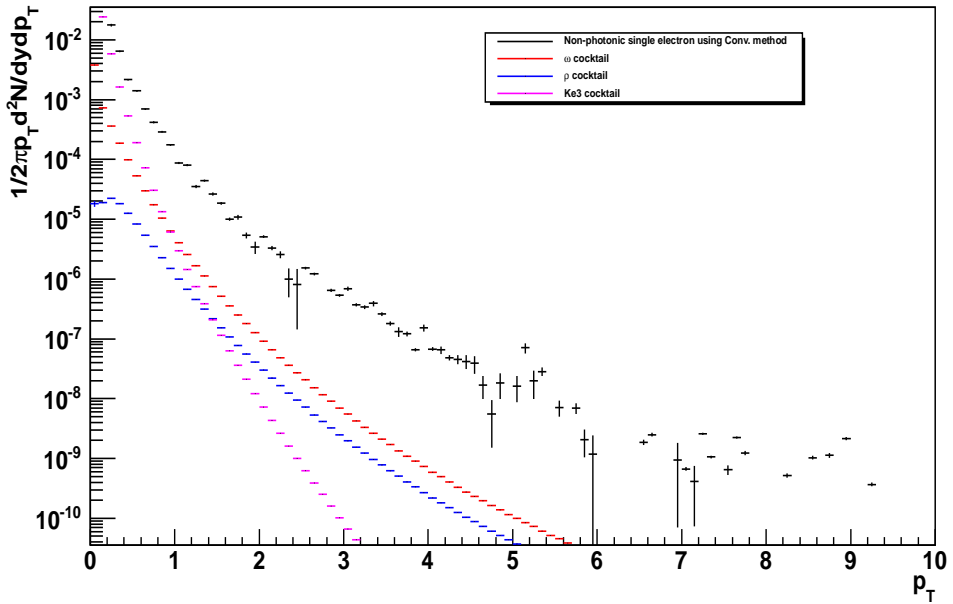


Figure 3.56: Non-photonic single electron from the converter analysis (black curve) in minimum bias centrality. Also shown are the single electron cocktail from  $Ke_3$  (magenta),  $\rho \rightarrow ee$  (blue) and  $\omega \rightarrow ee$  (red) from the cocktail calculation as in section 3.8.

### 3.12 Systematic error on Converter analysis

- $R_\gamma$  systematic error :  $R_\gamma$  is determined by PHENIX simulation of  $\pi^0$  with and without converter. The proper determination of  $R_\gamma$  requires the PHENIX simulation to be accurate with the material amounts of the converter and the PHENIX detectors. The study of the amount of material present in the PHENIX converter is done by the photon conversion pairs. The main source of conversion pairs( $e^+e^-$  pair due to conversion) is  $\pi^0$ . In order to determine the difference in the converter material in simulation and real data the  $e^+e^-$  pair yield is measured with and without converter in both real data and simulation and then they are compared with each other. The input to the PHENIX simulation is  $\pi^0$  which is generated using single particle generator called Exodus. If the material amounts in simulation are exactly the same as in real, the yield of the simulated conversion

pairs generated by the input of measured  $\pi^0$  should be almost consistent with the real data. By comparing the conversion pair yield in the real data and the simulation, we can examine the accuracy of the PHENIX detector simulation on the photonic conversion. Fig. 3.57 shows the invariant mass

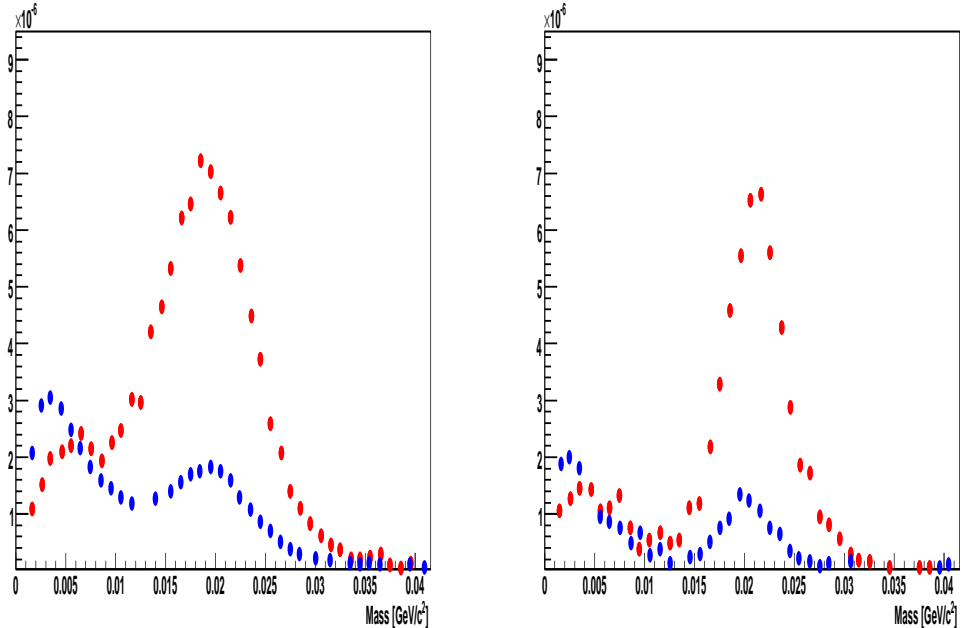


Figure 3.57: Left hand plot is the conversion pair( $e^+e^-$ ) invariant mass distribution in the real data from RUN4 of PHENIX. Right hand is for simulation. Red colored distribution is for converter and blue colored distribution is for non-converter. The data points for both the plots are taken from [95].

spectra of  $e^+e^-$  conversion electron pairs in converter and non-converter runs for both real data and simulation. The left hand side is for real data and the right hand side is for simulation. In both the left and right hand plots two mass peaks can be seen for invariant mass of conversion pair electrons  $M^{e^+e^-} < 50$  [ $MeV/c^2$ ]. The mass peak in  $M^{e^+e^-} < 10$  [ $MeV/c^2$ ] corresponds to Dalitz decay and the one for photon conversions at beam pipe appears in  $10 < M^{e^+e^-} < 35$  [ $MeV/c^2$ ]. In case of converter, the peak of  $M^{e^+e^-}$  is higher because of the presence of converter. For comparing the amount of material in simulation with that in real data a parameter  $R_\gamma^{pair}$

is defined given as :

$$R_{\gamma}^{pair} = \frac{N_{e^+e^-}^{conv-in}}{N_{e^+e^-}^{conv-out}} \quad (3.26)$$

where  $N_{e^+e^-}^{conv-in}$  is the number of electron pairs within  $M^{e^+e^-} < 35 [MeV/c^2]$  in the presence of converter and  $N_{e^+e^-}^{conv-out}$  is the number of electron pairs within  $M^{e^+e^-} < 35 [MeV/c^2]$  in absence of converter for  $0.5 < p_T < 5.0$  GeV/c.  $N_{e^+e^-}^{conv-in}$  includes photon conversion pairs by the converter, beam pipe and Dalitz decay.  $N_{e^+e^-}^{conv-out}$  includes photon conversion pairs by the beam pipe and Dalitz decay. The ratio of  $R_{\gamma}^{pair}$  in real data and simulation ( $[R_{\gamma}^{pair}]_{real}/[R_{\gamma}^{pair}]_{sim}$ ) gave value of  $0.99931 \pm 0.027$ . So the systematic error on  $R_{\gamma}$  here is taken as 2.7%.

- Blocking factor ( $\epsilon$ ) systematic error : Electrons emitted from inside the converter in the converter run lose its energy radiatively by the converter. This is known as the blocking factor and has been used in equations 3.18 and 3.19. This effect is absent in non-converter run. The blocking factor ( $\epsilon$ ) affects the shape of the invariant mass peak of conversion pair electrons as can be seen in Fig. 3.57. The invariant mass peak of  $e^+e^-$  pair for converter run is narrower than that in non-converter runs. The systematic error assigned to this  $\epsilon$  is 25%.
- Ratio of converter and non-converter ( $R_{CN}$ ) systematic error : The systematic error on  $R_{CN}$  depends on how well the acceptance in converter and non-converter runs matches. The acceptance matching plots for converter and non-converter runs are shown from Fig. 3.39 to Fig. 3.42. Though after applying extra fiducial cuts to force match the acceptance in converter and non-converter runs there is less than 1% difference in acceptance between converter and non-converter runs. This is determined by normalizing the converter run plots from Fig. 3.39 to Fig. 3.42 by the number of entries

in non-converter plots from Fig. 3.39 to Fig. 3.42 and then taking the ratio. The rms value is around 0.9% and so systematic uncertainty of 1% is assigned for  $R_{CN}$ .

## 3.13 Analysis of electron spectrum

### 3.13.1 Inclusive spectra

From Section 3.7.3 we have the acceptance uncorrected spectra which needs to be corrected by using the acceptance curve in Section 3.7.4. The complete expression for MB and ERT inclusive invariant yield can be written as

$$\frac{d^2N}{2\pi p_T dp_T dy} = \frac{1}{2\pi p_T} \frac{1}{N_{evt} \Delta p_T} \frac{N_e}{\epsilon_{trigg} \epsilon_{acc} X_{eff}} \quad (3.27)$$

where,  $N_{evt}$  is the total number of events recorded by the BBC within zvertex cut of  $\pm 20$  c.m.,  $N_e$  is the total number of electron counts recorded by PHENIX after applying all the electron identification criteria,  $\epsilon_{trigg}$  is the electron trigger efficiency,  $\epsilon_{acc}$  is the acceptance correction. After applying trigger efficiency and acceptance correction the resultant electron  $p_T$  distribution is being scaled by the following factors

- Scale by  $0.5 \rightarrow (e^+ + e^-)/2$
- Scale by  $1/2\pi$
- Scale by  $1/\Delta p_T = 1/\text{binwidth}$

in order to get the invariant inclusive yield of electrons. Fig. 3.58 shows inclusive spectra in minimum bias centrality bin.

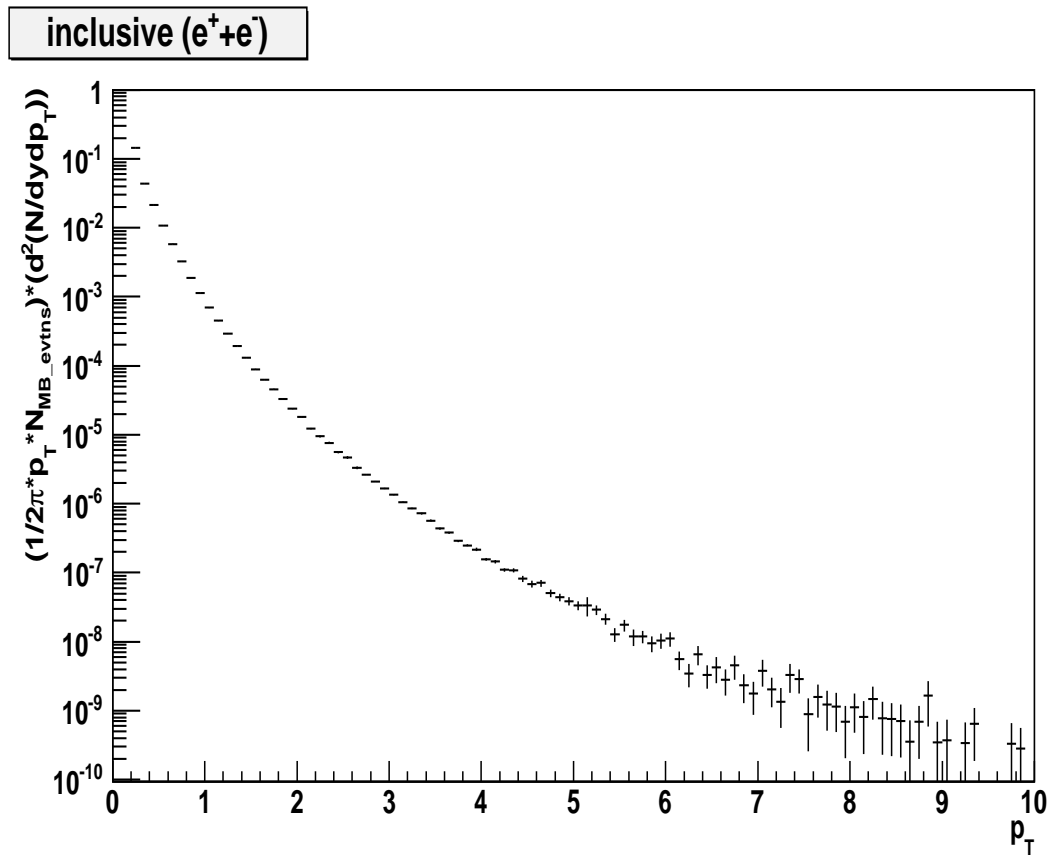


Figure 3.58: Single electron inclusive spectra in minimum bias centrality.

### 3.13.2 Heavy Flavor spectra

#### Cocktail subtraction method

The heavy flavor spectra is obtained by subtracting the inclusive spectra Fig. 3.58 from the Run8 d+Au single electron cocktail in fig. 3.31 for minimum bias centrality and fig. 3.32 for other centralities. The single electron is scaled by the constant fit value as shown in Fig. 3.55 in order to make the photonic electron component of cocktail calculation match with the photonic electron in real data. The statistical error is from inclusive spectra. The statistical error from cocktail has not been included as it is negligible and can be made more significantly negligible by running more events. The systematic error as determined in section 3.9 are added in quadrature and then are propagated to the final heavy flavor spectra.

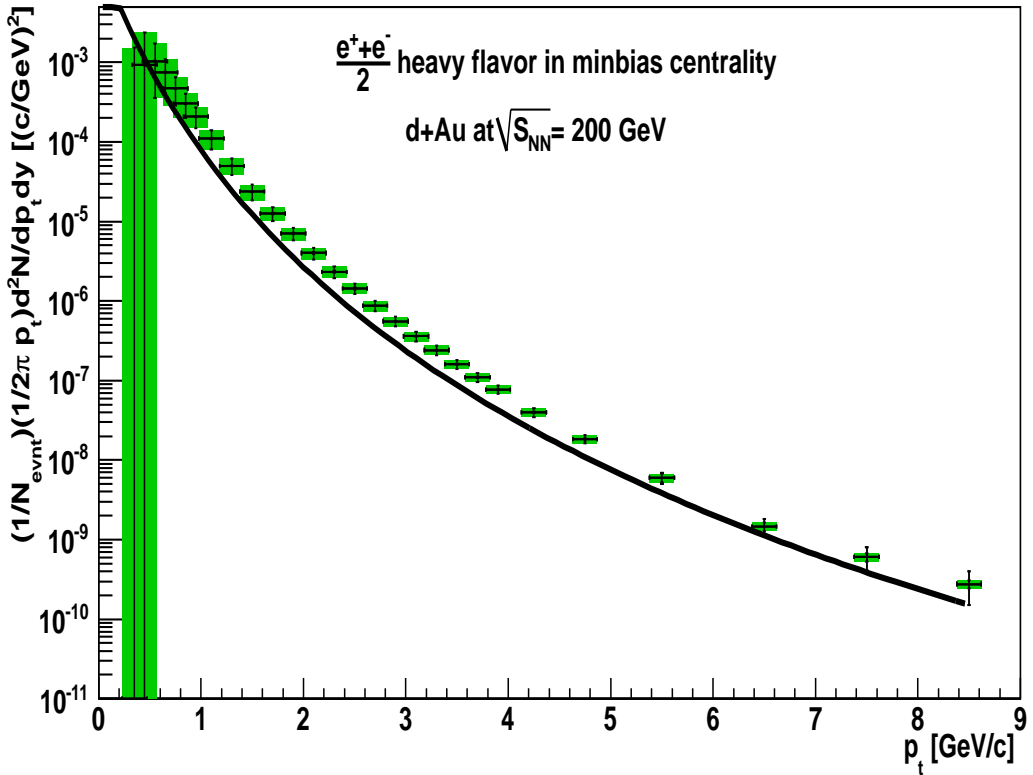


Figure 3.59: Single electron heavy flavour spectra from cocktail subtraction method in minimum bias centrality for d+Au collision species. The vertical bars at each data point are the statistical error whereas the systematic error is given by the block around each data point. The curve is the fit to the single electron from heavy flavor data from p+p collision species.

### Converter method

The heavy flavor from the converter method can be extracted from the non-photonic electron calculated from the converter analysis in section 3.11 by subtracting the non-photonic component of single electron from the non-photonic electron. The non-photonic components of single electron contributing to the background are from  $Ke_3$ ,  $\rho \rightarrow ee$  and  $\omega \rightarrow ee$  as mentioned in Table 3.11. The heavy flavor electron invariant yield ( $\frac{d^2N^{HQ}}{2\pi p_T dp_T dy}$ ) using the converter analysis

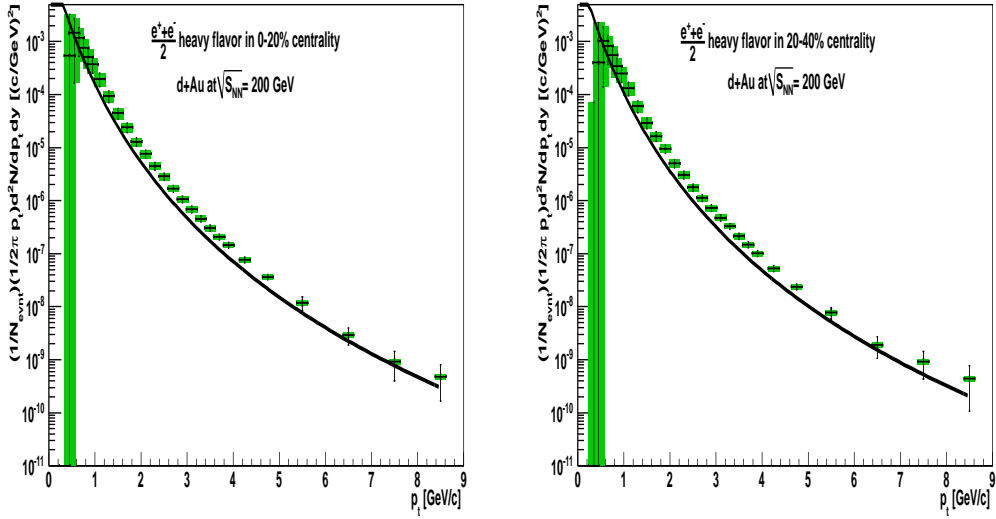


Figure 3.60: Single electron heavy flavor spectra for Run8 d+Au in 0-20% centrality (left plot) and in 20-40% centrality (right plot) for d+Au collisions species from cocktail subtraction method. The vertical bars at each data point are the statistical error whereas the systematic error is given by the block around each data point. The curves are the fit to the single electron from heavy flavor data from p+p collision species.

method is given by :

$$\frac{d^2 N^{HQ}}{2\pi p_T dp_T dy} = \frac{d^2 N^{non-\gamma}}{2\pi p_T dp_T dy} - \frac{d^2 N^{K_{e3}}}{2\pi p_T dp_T dy} - \frac{d^2 N^{\rho \rightarrow ee}}{2\pi p_T dp_T dy} - \frac{d^2 N^{\omega \rightarrow ee}}{2\pi p_T dp_T dy}, \quad (3.28)$$

where

- $\frac{d^2 N^{K_{e3}}}{2\pi p_T dp_T dy}$  is the single electron invariant yield from  $K_{e3}$  determined from simulation as described in section 3.8.1.
- $\frac{d^2 N^{\rho \rightarrow ee}}{2\pi p_T dp_T dy}$  is the single electron invariant yield from  $\rho$ . This is determined by the cocktail calculation as described in section 3.8.1.
- $\frac{d^2 N^{\omega \rightarrow ee}}{2\pi p_T dp_T dy}$  is the single electron invariant yield from  $\rho$  and is a component of cocktail as mentioned in section 3.8.1.

Fig. 3.62 shows the single electron heavy flavor invariant yield for minimum bias centrality using converter method. For other centralities the single electron

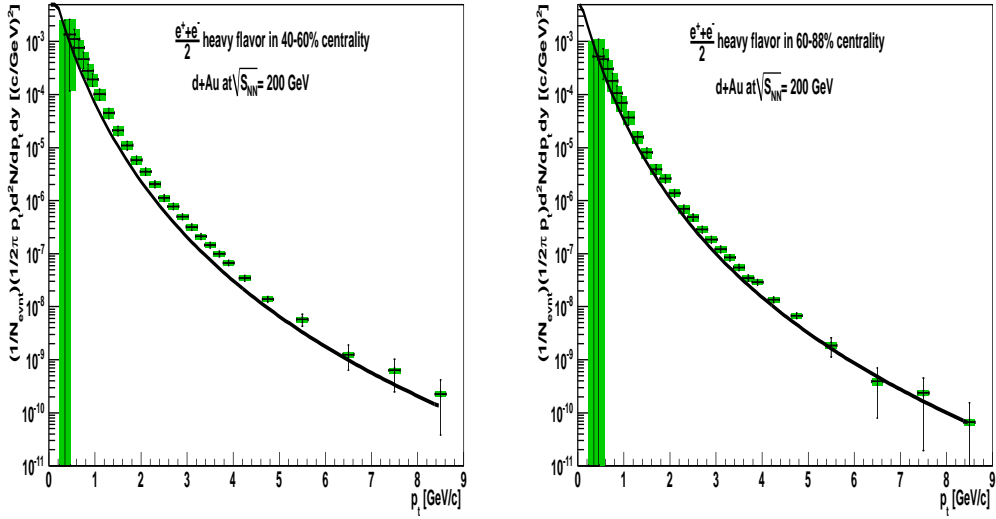


Figure 3.61: Single electron heavy flavor spectra for Run8 d+Au in 40-60% centrality (left plot) and in 60-88% centrality (right plot) for d+Au collisions species from cocktail subtraction method. The vertical bars at each data point are the statistical error whereas the systematic error is given by the block around each data point. The curves are the fit to the single electron from heavy flavor data from p+p collision species.

heavy flavor invariant yield is shown in Fig. 3.63. The systematic error propagation here is bit more cumbersome than the one in cocktail subtraction method. Other than the systematic errors as described in section 3.12 it also involves systematic error from high  $p_T$  extension, geometrical acceptance and acceptance X eID efficiency as described in section 3.9. For using the systematic from section 3.12, the parameters  $R_\gamma$ ,  $R_{CN}$  and  $\epsilon$  are changed by their assigned systematic and the new non-photonic electron is calculated for each of these changed parameters by using equation 3.19. Then the fractional changes in the non-photonic yield are added in quadrature along with the systematic from the inclusive yield of electrons as mentioned in section 3.9 to get the total systematic error on heavy flavor invariant yield from converter analysis.

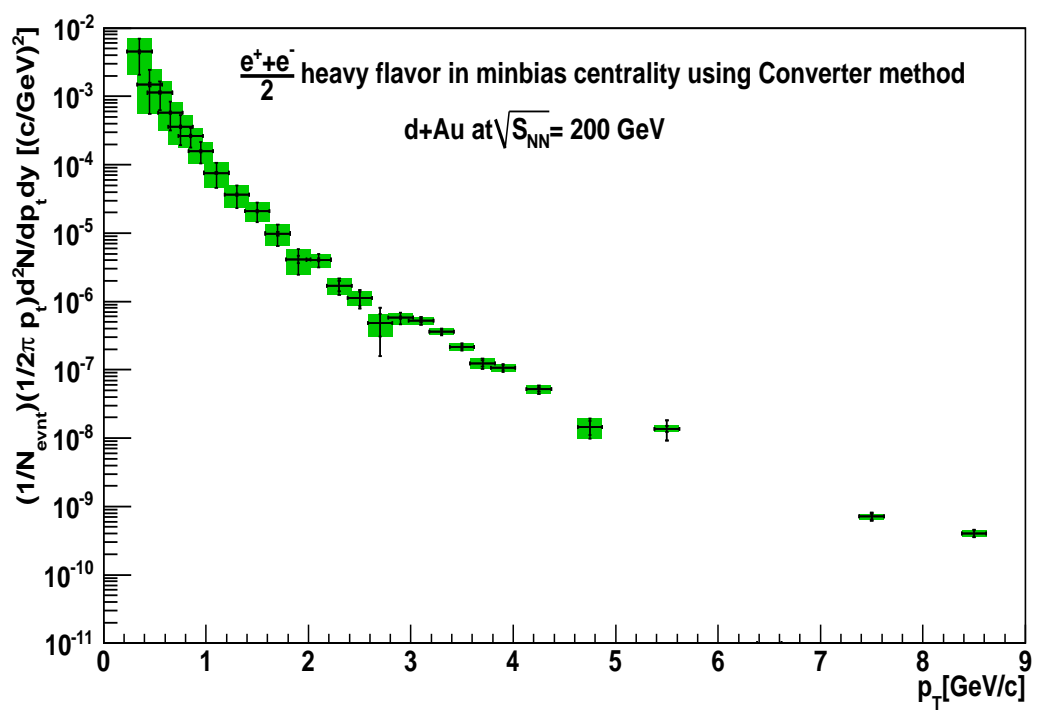


Figure 3.62: Single electron heavy flavour spectra using converter method in minimum bias centrality. The vertical bars are the statistical error around the central values and the systematics is shown by the boxes.

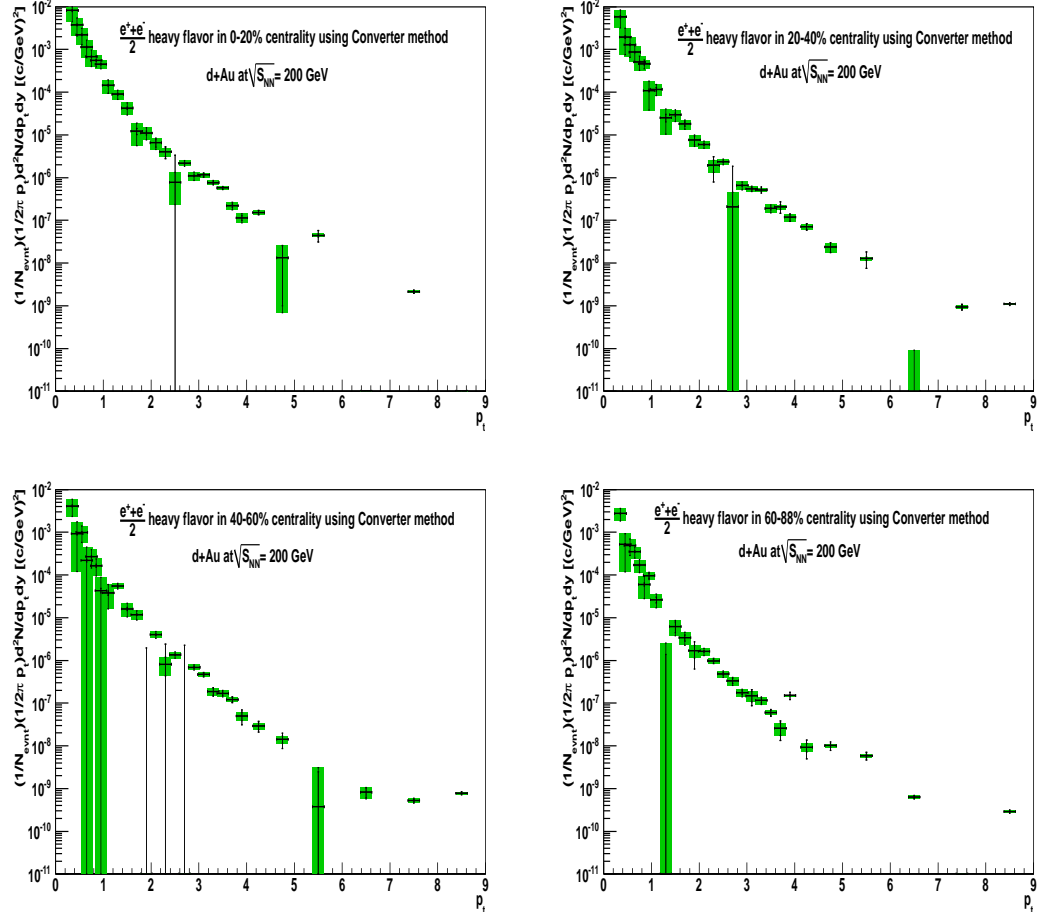


Figure 3.63: Single electron heavy flavor spectra using converter method for different centralities. The vertical bars are the statistical error around the central values and the systematics is shown by the boxes.

# Chapter 4

## Results and Discussions

The various results from the single electron analysis for  $d + Au$  collision at  $\sqrt{S_{NN}} = 200$  GeV has been summarized in this chapter. This includes heavy flavor single electron invariant yield obtained by cocktail subtraction method in different centrality as shown in section 4.1. Nuclear modification factor calculation in  $d + Au$  for heavy flavor is shown in section 4.2 by using the heavy flavor single electron yield for  $d + Au$  at  $\sqrt{S_{NN}} = 200$  GeV calculated from both converter analysis and cocktail subtraction method. The nuclear modification factor for  $d + Au$  is calculated by dividing the single electron invariant yield for  $d + Au$  obtained in this analysis by the  $N_{<coll>}$  for  $d + Au$  scaled  $p + p$  heavy flavor invariant yield. The nuclear modification result for single electron heavy flavor in  $d + Au$  obtained in this dissertation has been compared with a theoretical model prediction in section 4.3. Further a simple model to extract the cold nuclear matter effect present in  $Au + Au$  collision is being shown in section 4.4. The extraction of heavy flavor invariant differential cross section from invariant differential yield in shown in section 4.5. A small cross check of the behavior of nuclear modification factor in  $d + Au$  obtained by heavy flavor invariant yield is being done by comparing the heavy flavor invariant differential cross section for  $d + Au$  and properly scaled FONLL result for  $p + p$  in section 4.6.

## 4.1 Heavy Flavor single electron

### 4.1.1 Heavy Flavor single electron from cocktail subtraction method

The heavy flavor single electron invariant yield in different centrality is shown in Fig. 4.4. The statistical errors are displayed by the bars around the central values whereas the systematic is shown as boxes. The statistical error is only from the inclusive electron yield as the statistical error for cocktail calculation can be made negligibly small by generating more events.

### 4.1.2 Comparison of heavy flavor single electron invariant yield from converter and cocktail method

Fig. 4.2 shows the single electron heavy flavor invariant yield obtained from both the converter and cocktail subtraction method. In both the spectra the MB data set is used until  $p_T = 1.6$  GeV and ERT data set is used for  $p_T > 1.6$  GeV. All the corrections are being applied in both the heavy flavor single electron yield spectra. The error bars shown are only statistical.

Fig. 4.3 shows the single electron heavy flavor invariant yield obtained from both the converter and cocktail subtraction method. Systematic errors are shown in both the methods by the colored blocks around the data points. For cocktail subtraction method in  $p_T < 1.0$  GeV region the systematic error is larger compared to that from the converter subtraction method. Due to large systematic error from the cocktail method in the region of  $p_T < 1.0$  GeV heavy flavor determined from converter method is used for  $p_T < 1.0$  GeV.

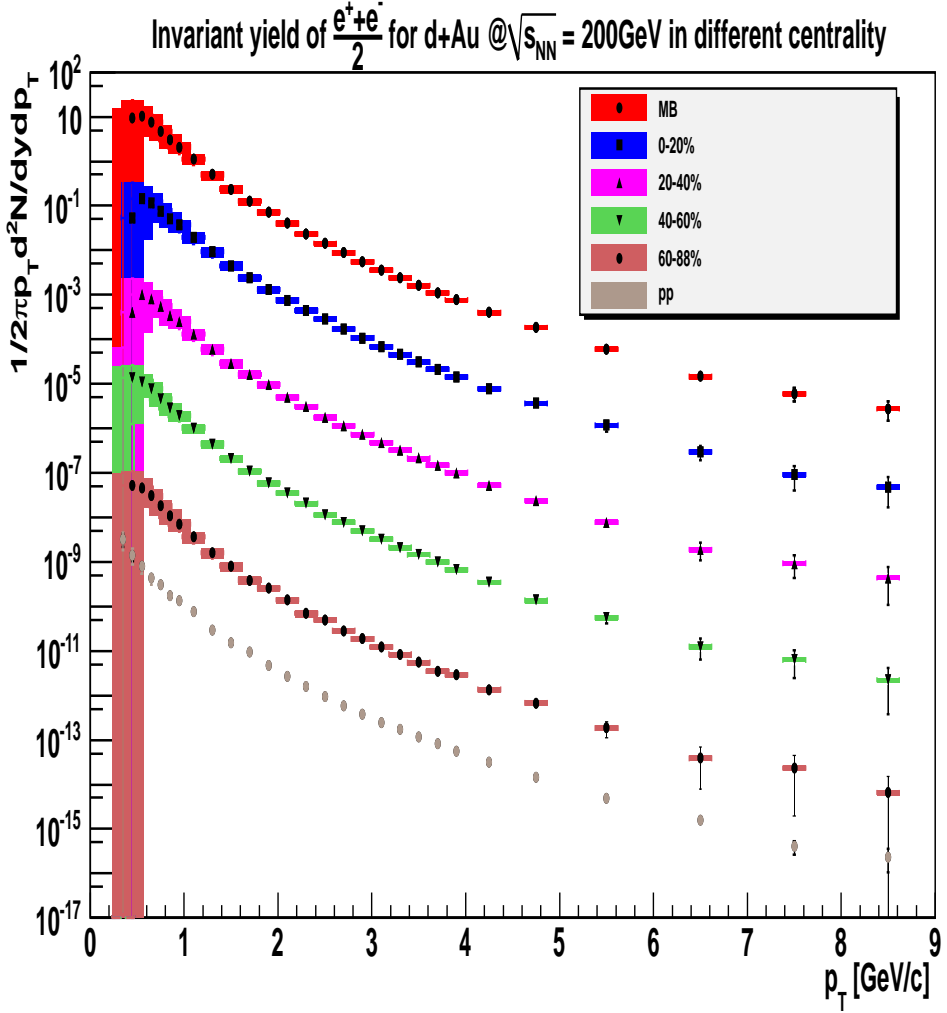


Figure 4.1: Heavy flavor single electron spectrum in different centrality using cocktail subtraction method.

## 4.2 Nuclear modification factor ( $R_{dA}$ )

The nuclear modification factor  $R_{dA}$  is found by dividing the heavy flavor for d+Au by the  $N_{coll}$  scaled  $p+p$  heavy flavor spectrum [96] and is given by

$$R_{dA} = \frac{dN_{dA}^e/dp_T}{\langle N_{coll} \rangle dN_{pp}^e/dp_T}. \quad (4.1)$$

Fig. 4.5 shows the nuclear modification factor of heavy flavor in  $d+Au$  collision at minimum bias centrality. For other centralities the  $R_{dA}$  is shown in Fig. 4.6. The

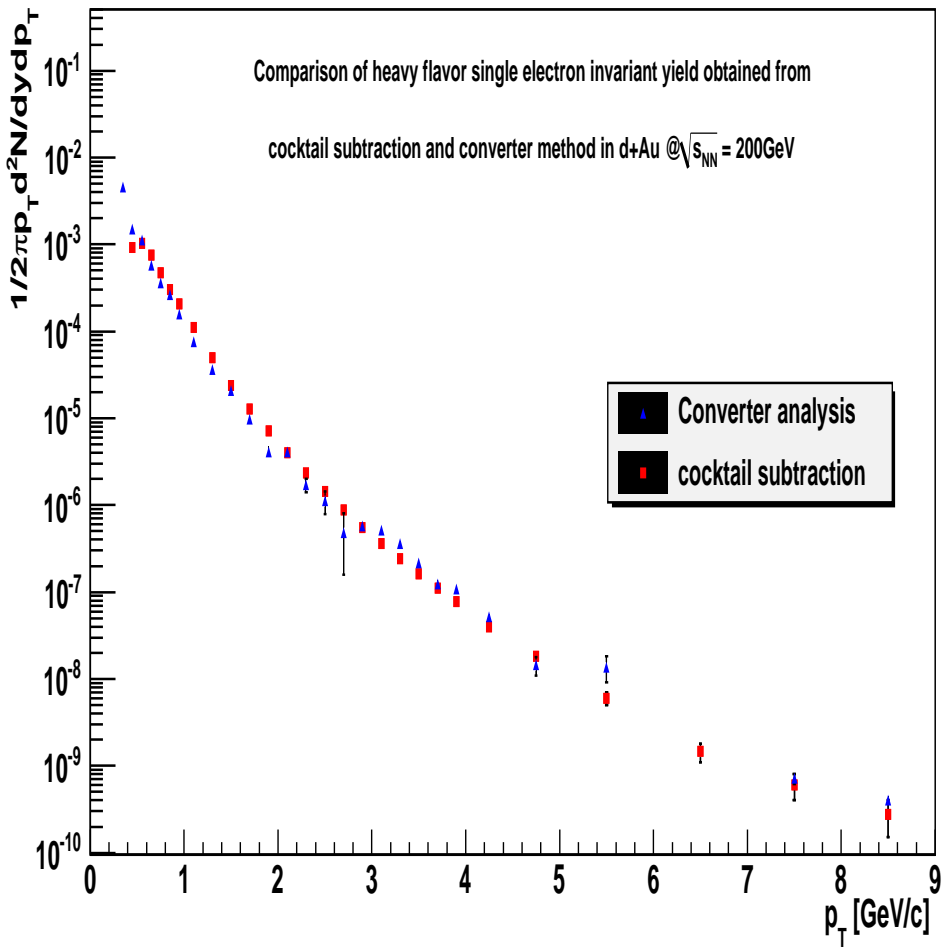


Figure 4.2: Heavy flavor single electron spectrum obtained from converter analysis and cocktail subtraction method. The statistical error is shown by the vertical bars around the central value.

heavy flavor single electron for d+Au used here is calculated from the cocktail subtraction method as shown in section 3.13.2.

Fig. 4.7 shows the nuclear modification factor of heavy flavor in  $d + Au$  collision at minimum bias centrality. For other centralities the  $R_{dA}$  is shown in Fig. 4.8. The heavy flavor single electron for d+Au used here is calculated from the converter method as shown in section 3.13.2.

Comparing Fig. 4.5 and Fig. 4.7 the  $R_{dA}$  from the heavy flavour single

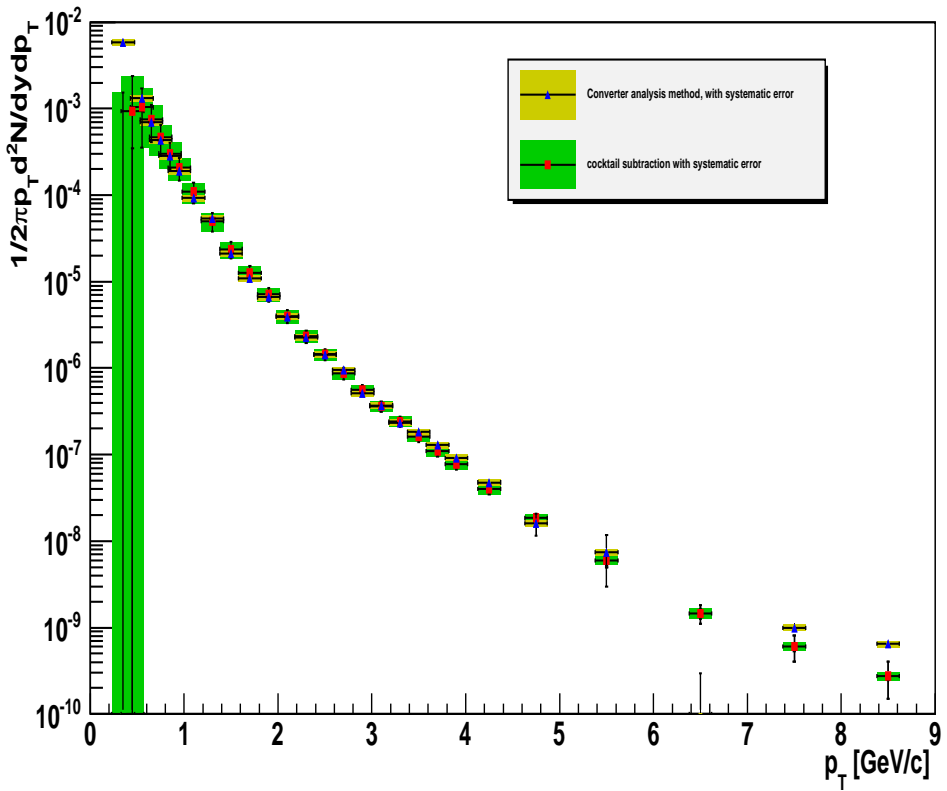


Figure 4.3: Heavy flavor single electron spectrum obtained from converter analysis and cocktail subtraction method. The statistical error is shown by the vertical bars around the central value. For cocktail subtraction method the systematic error are shown by green blocks whereas for converter subtraction method the systematic errors are shown by the yellow blocks.

electron, calculated by using cocktail subtraction method and Converter analysis method, are consistent with each other. Comparing Fig. 4.6 and Fig. 4.8 same can be said.

#### 4.2.1 Final Nuclear Modification for heavy flavor single electron in $d + Au$ collision

As already mentioned in section 4.1.2 and in Fig. 4.4 in  $p_T < 1.0$  GeV results from converter method has to be used due to less systematic error in comparison to the result from cocktail subtraction method, so the final  $R_{dA}$  is having values

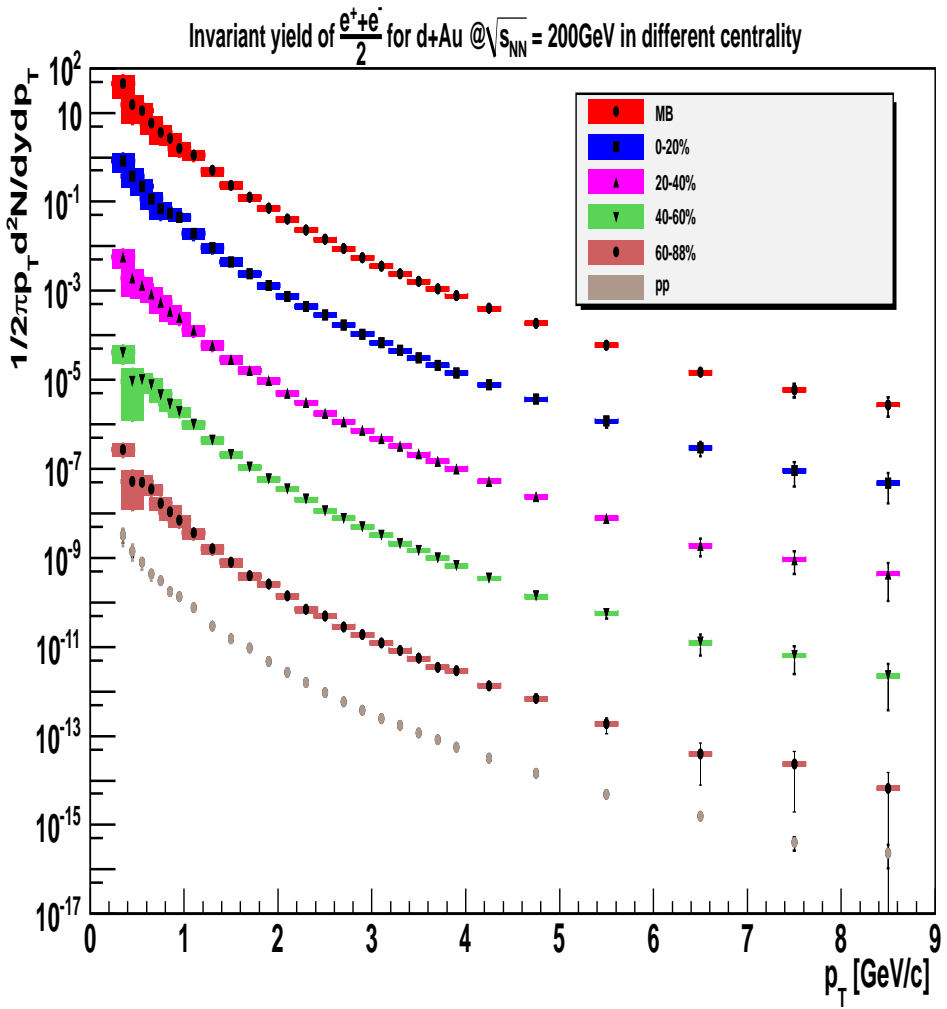


Figure 4.4: Heavy flavor single electron spectrum for different centrality. For  $p_T < 1.0$  GeV heavy flavor from converter analysis is used because of small systematic error in comparison to cocktail subtraction method. For  $p_T > 1.0$  GeV heavy flavor from cocktail subtraction method is used.

obtained from converter analysis method for  $p_T < 1.0$  GeV and for  $p_T > 1.0$  GeV results from cocktail subtraction method is used. Fig. 4.9 shows the final  $R_{dA}$  for minimum bias centrality with values obtained from converter analysis method for  $p_T < 1.0$  GeV and for  $p_T > 1.0$  GeV results from cocktail subtraction method is being used. Fig. 4.10 shows the final  $R_{dA}$  for other centralities.

Comparing the nuclear modification factor for single electron heavy flavor

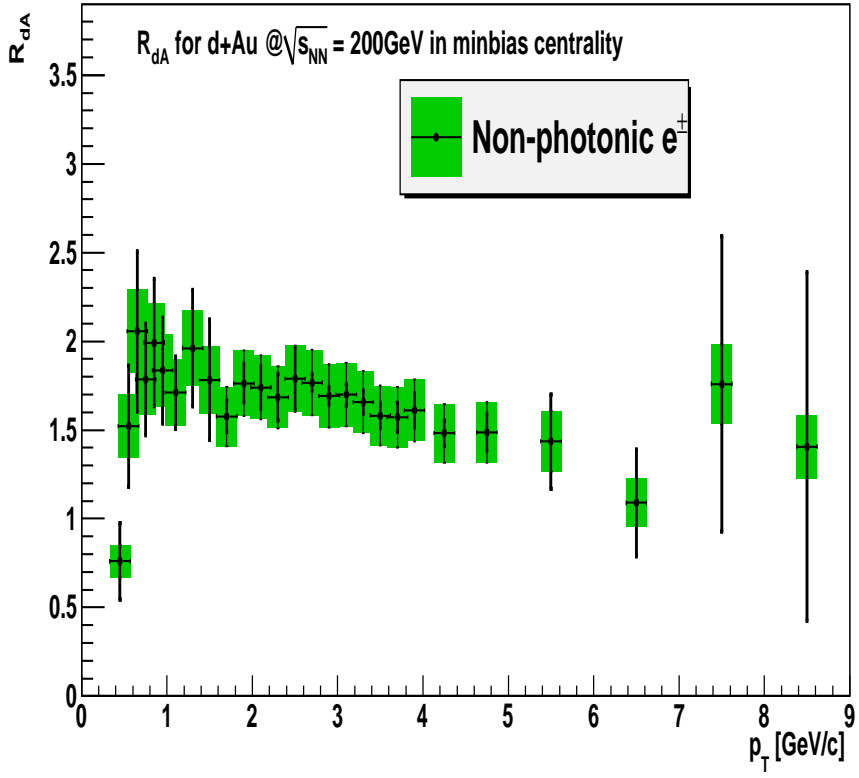


Figure 4.5:  $R_{dA}$  for minimum bias centrality using heavy flavor single electron invariant yield from cocktail subtraction method. The bars are statistical error and the systematic error is shown by boxes around the central value.

in  $d + Au$  and in  $Au + Au$ , as shown in Fig. 4.11, for minimum bias centrality, enhancement is seen for  $d + Au$  as compared to that in  $Au + Au$ . The peripheral (60-88%) centrality shows some enhancement for  $R_{dA}$  in the mid  $p_T$  region but otherwise it's consistent with the scaled  $p + p$  result within uncertainties. In the most central (0-20%) case the  $R_{dA}$  shows enhancement up to  $p_T = 5.0$  GeV. Though the converter analysis has less statistics, still in the mid  $p_T$  region ( $2.5 < p_T < 5.0$  GeV) a clear enhancement in  $R_{dA}$  can be seen.

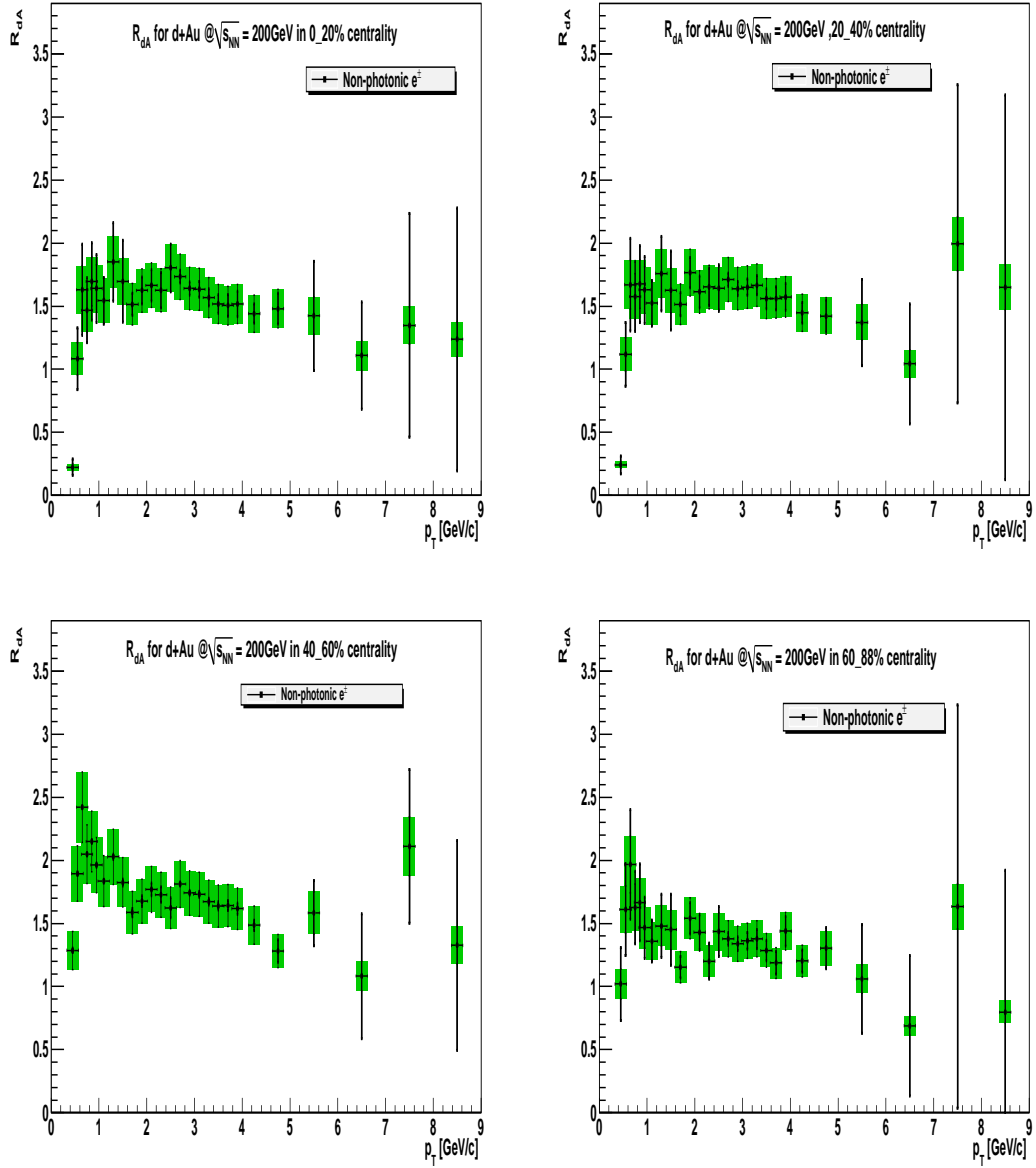


Figure 4.6:  $R_{dA}$  for other centralities starting from 0-20% from extreme left in top panel to 60-88% centrality in the extreme right of the bottom panel. The bars are statistical error and the systematic error is shown by boxes around the central value.

### 4.3 Model Comparison

The enhancement in the nuclear modification factors of  $d + Au$  collisions at  $\sqrt{S_{NN}} = 200$  GeV at RHIC observed in the present work matches qualitatively

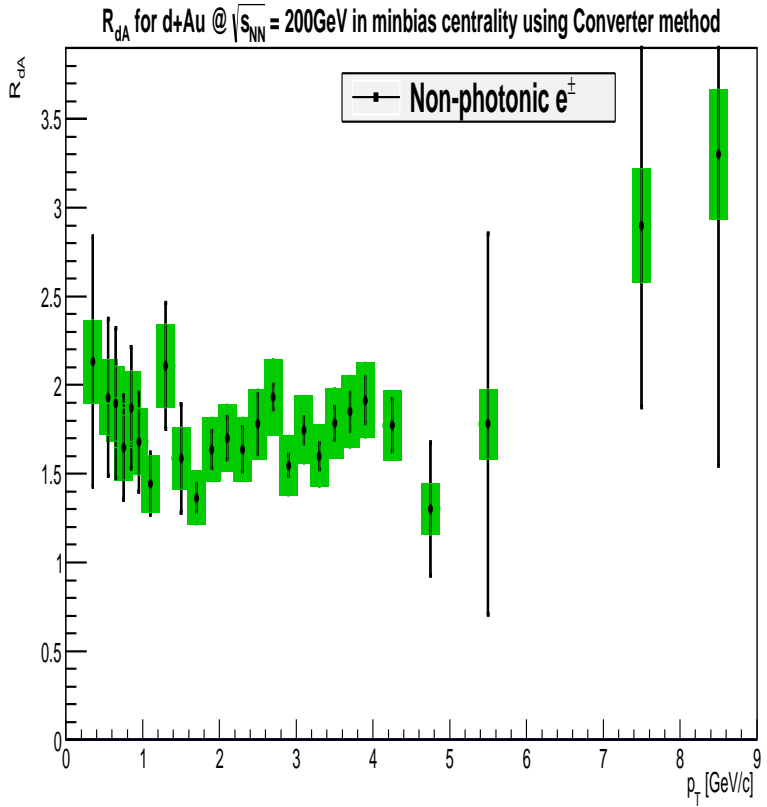


Figure 4.7:  $R_{dA}$  for minimum bias centrality from the converter method calculated heavy flavor single electron in  $d + Au$ . The bars are statistical error and the systematic error is shown by boxes around the central value.

with the theoretical calculation based on gluon saturation effect [98]. Heavy quark production at very small fraction of momentum transfer ( $x$ ) is affected in a similar way like that of gluon production by gluon saturation [99]. As  $x$  is proportional to the transverse mass, given by,  $m_T \sim \sqrt{(m^2 + p_T^2)}$  and rapidity is higher for higher mass quarks for same value of  $p_T$  and  $\sqrt{S_{NN}}$ , so in case of heavy quarks, the effect of gluon saturation appears only in higher energies/higher rapidities as compared to that of lighter quarks and gluons. Initial theoretical analysis [100, 101, 102] shows the phenomenological significance of coherent effects in hadron production at RHIC. Considering rest frame of the nucleus, these coherent effects consists of:

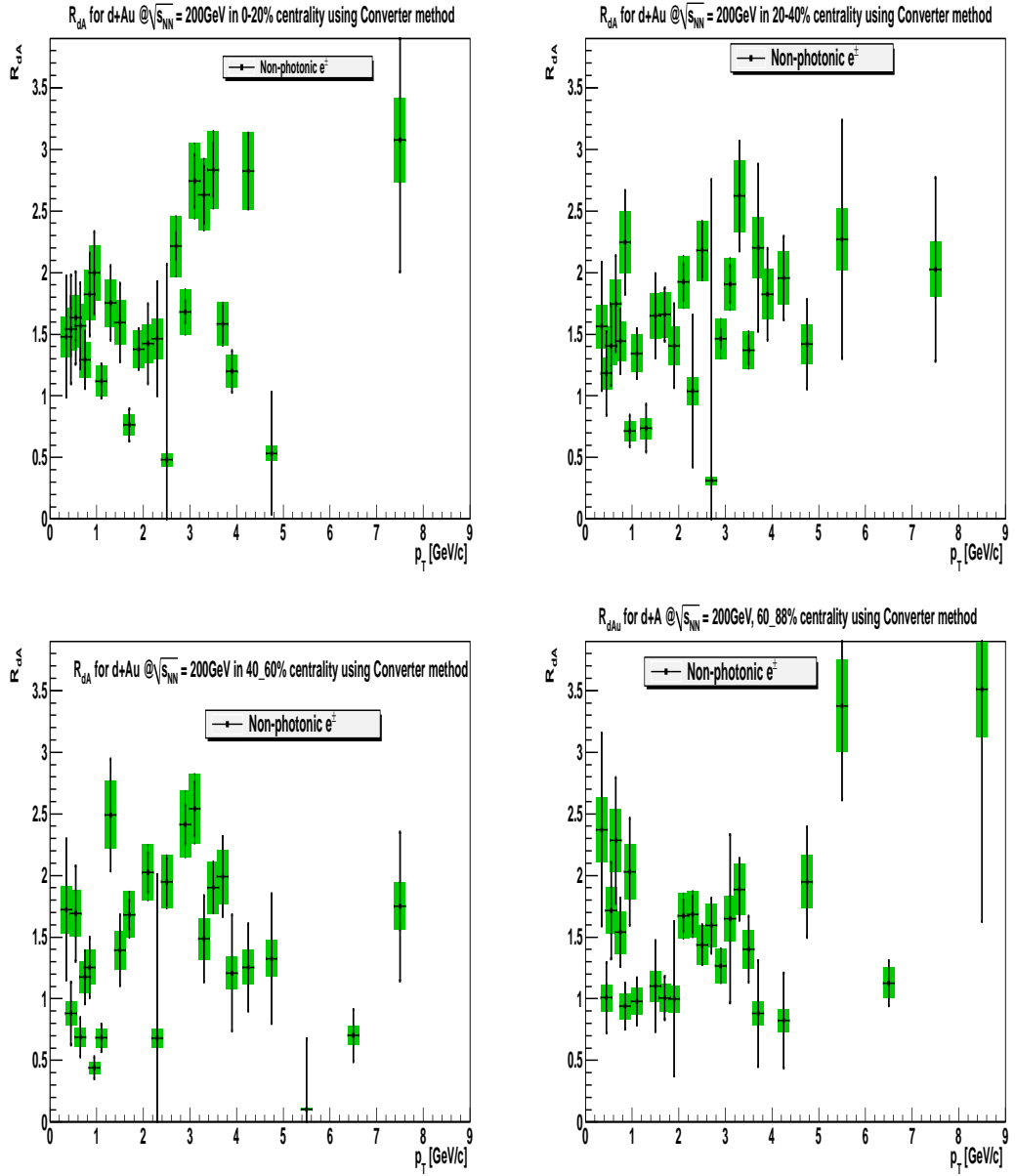


Figure 4.8:  $R_{dA}$  for other centralities starting from 0-20% from extreme left in top panel to 60-88% centrality in the extreme right of the bottom panel. The bars are statistical error and the systematic error is shown by boxes around the central value.

- Incoming parton system undergoing multiple re-scattering in the nucleus, controlled by the factor  $\alpha_s^2 A^{1/3} \sim 1$ . Here,  $A$  is the atomic number of the nucleus and  $\alpha_s$  is the running coupling constant.
- The quantum evolution of small fraction of momentum transfer being con-

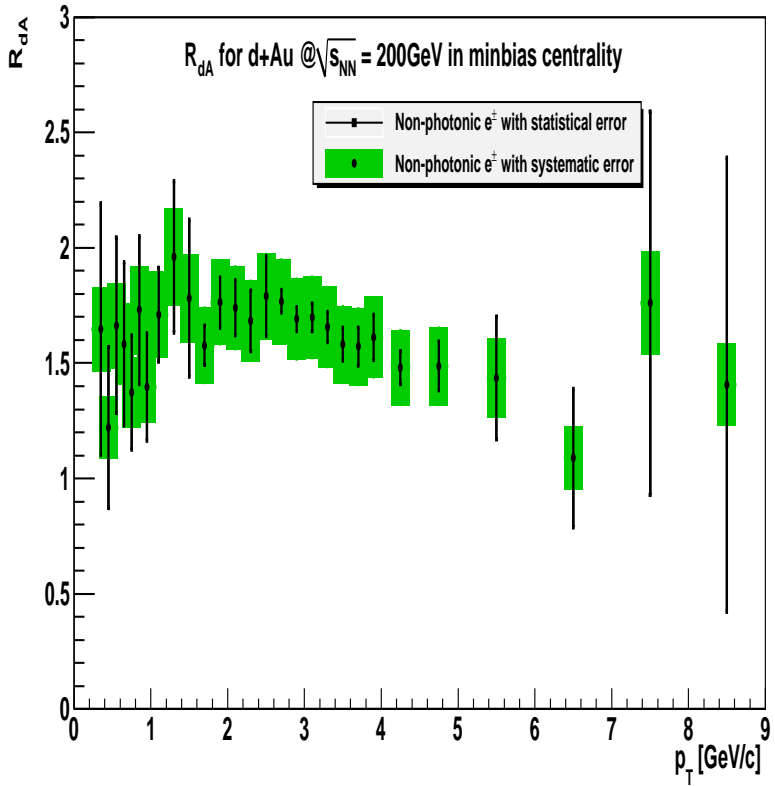


Figure 4.9: Final  $R_{dA}$  for minimum bias centrality. For  $p_T < 1.0$  GeV, results from converter analysis is used and for  $p_T > 1.0$  GeV results from cocktail subtraction method is used. The bars are statistical error and the systematic error is shown by boxes around the central value.

trolled by the parameter  $\alpha_s y = \alpha_s \ln(1/x) \sim 1$ .

The gluon saturation at small fraction of momentum transfer is the result of both the above mentioned effects. The theoretical calculations as in [103, 104, 105, 106] shows the effect of gluon saturation on nuclear modification factor for open charm measurement at forward rapidity. The calculations in [98] shows the effect of gluon saturation on nuclear modification factor for open charm in mid rapidity region and it explains the enhancement observed in nuclear modification factor in the present work.

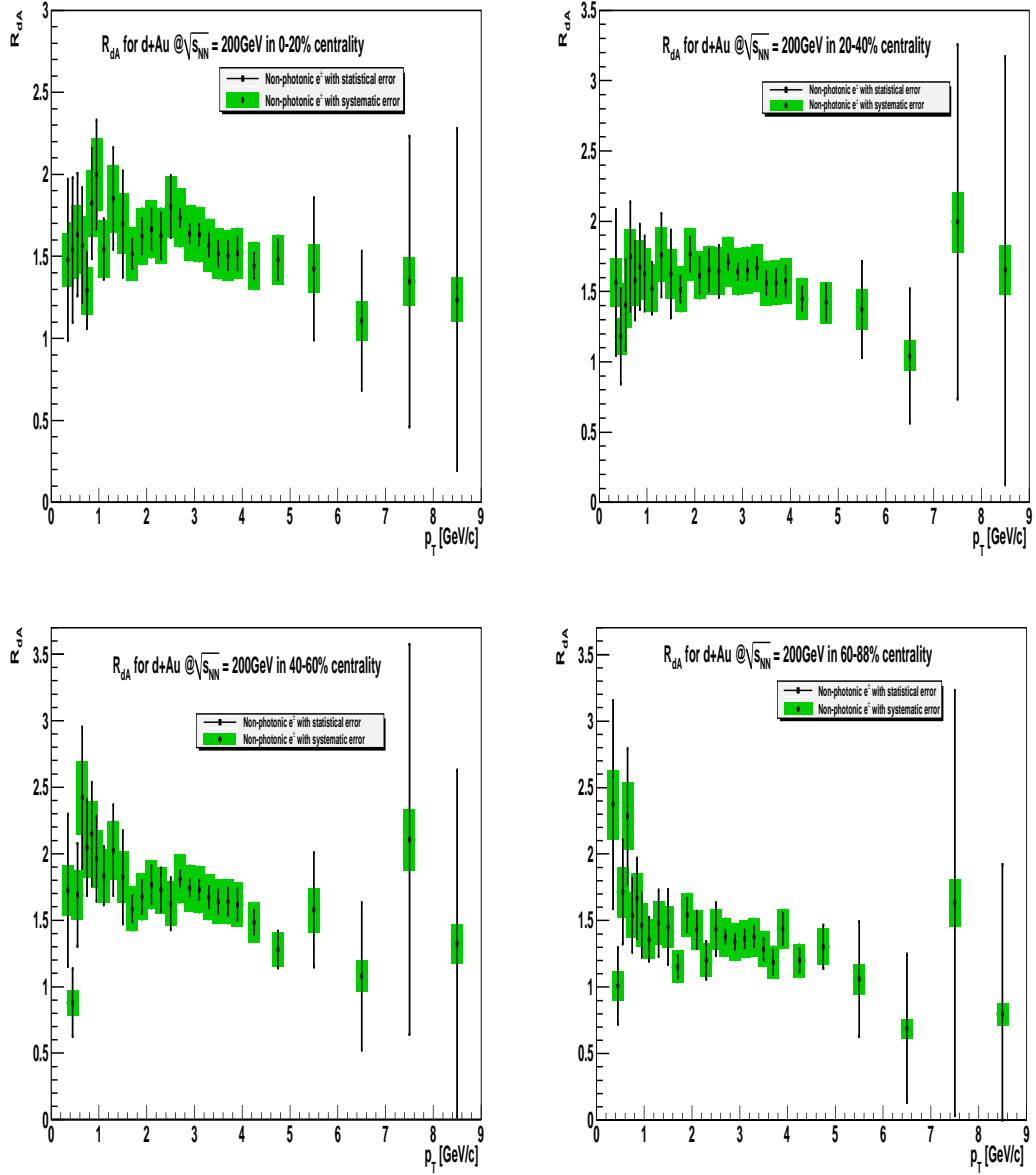


Figure 4.10: Final  $R_{dA}$  for other centralities starting from 0-20% from extreme left in top panel to 60-88% centrality in the extreme right of the bottom panel. For  $p_T < 1.0$  GeV, results from converter analysis is used and for  $p_T > 1.0$  GeV results from cocktail subtraction method is used. The bars are statistical error and the systematic error is shown by boxes around the central value.

#### 4.4 Ratio of $R_{AA}$ and $R_{dA}^2$ at $\sqrt{S_{NN}} = 200$ GeV

The calculation for nuclear modification factor of heavy flavor in  $d + Au$  in the theoretical model [98] is for the cold nuclear matter effect in  $d + Au$  collision

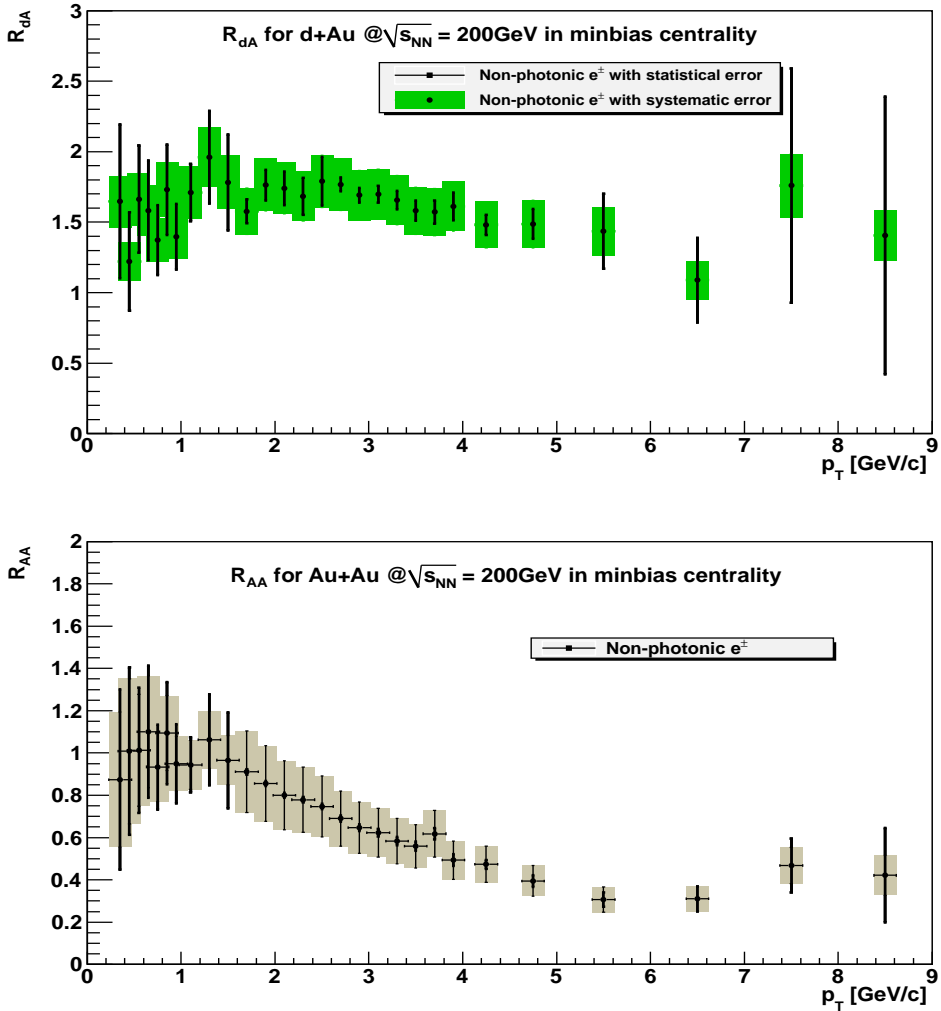


Figure 4.11: Nuclear modification factor in minimum bias centrality for  $d + Au$  (top panel) and  $Au + Au$  (bottom panel) at  $\sqrt{S_{NN}} = 200$  GeV. The bars are statistical error and the systematic error is shown by boxes around the central value. For  $d + Au$  collision enhancement in nuclear modification factor is seen as compared to the suppression in  $Au + Au$  collision from  $p_T > 2.0$  GeV.

which agrees qualitatively with the present work in this thesis. The cold nuclear matter is also produced in  $Au + Au$  collision during the early stage of the collision. However the dense hot nuclear medium produced during the  $Au + Au$  collision suppresses the effect of cold nuclear matter effect. The only thing that we see in  $Au + Au$  collision is the suppression effects of dense hot nuclear matter [107]. In order to properly understand the cold nuclear matter effects,  $d + Au$  collision

species is of importance where the collision species are asymmetric and the mass in between  $p + p$  and  $Au + Au$ . We don't expect to get the dense hot matter in  $d + Au$  unlike in  $Au + Au$ .

In order to isolate the medium effects in  $Au + Au$  and  $d + Au$  collision the ratio of  $R_{AA}$  and  $(R_{dA})^2$  is being calculated here and it is given by

$$\frac{R_{AA}}{(R_{dA})^2} = \frac{(N_{coll}^{dA})^2}{N_{coll}^{AA}} \frac{(dN/dy)_{AA} (dN/dy)_{pp}}{(dN/dy)^2} \quad (4.2)$$

where,  $N_{coll}^{AA}$  and  $N_{coll}^{dA}$  are the number of collisions in  $Au + Au$  and in  $d + Au$  respectively,  $(dN/dy)_{AA}$ ,  $(dN/dy)_{pp}$ ,  $(dN/dy)_{dA}$  are the electron yields from heavy flavor in  $Au + Au$ ,  $p + p$  and  $d + Au$  collision respectively at  $\sqrt{S_{NN}} = 200$  GeV. The electron yield for  $p + p$  is taken from [96] and that for  $Au + Au$  is taken from [108]. For  $d + Au$  the electron yield is taken from the present work.

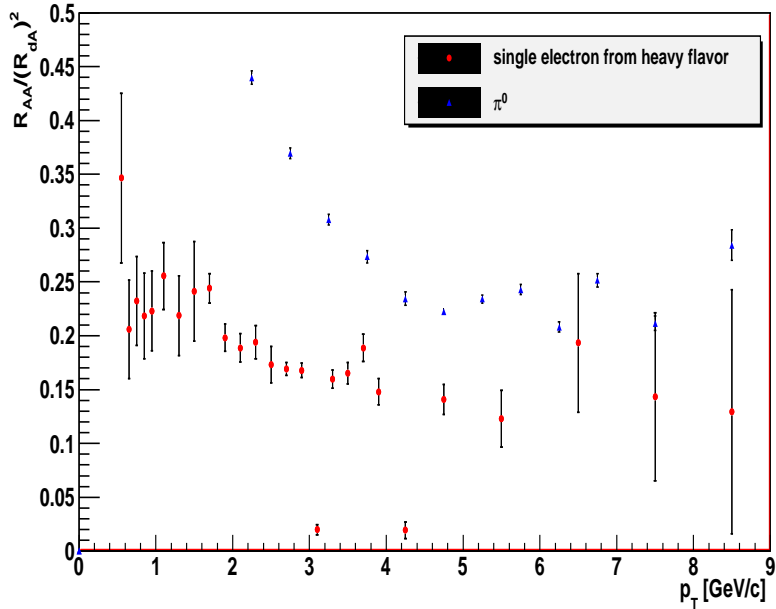


Figure 4.12:  $\frac{R_{AA}}{(R_{dA})^2}$  for single electron from heavy flavor. For comparison the light meson ( $\pi^0$ )  $\frac{R_{AA}}{(R_{dA})^2}$  is also shown. Heavy quarks suppression seems to be more than the light quark suppression.

Even though by looking at the expression 4.2 one can use directly the  $R_{AA}$  and  $R_{dA}$  values to find their ratios, here instead the electron yields are being used in order to make the error propagation more transparent. Fig. 4.12 shows the  $\frac{R_{AA}}{(R_{dA})^2}$  for heavy flavor single electron. Also shown in the figure is the same ratio for  $\pi^0$ . As is observed both  $Au + Au$  and  $d + Au$  cold nuclear matter effect shows heavy quarks getting suppressed more than the light quarks. This result is in complete contrast from the predictions based on suppression of gluon radiation from heavy quarks [109], according to which the heavy quarks will be suppressed less than the light quarks due to cold nuclear matter in hot nuclear medium.

## 4.5 Heavy flavor invariant cross section

The single electron inclusive differential cross section is given by

$$\frac{d^2\sigma^{incl}}{dp^3} = \frac{\sigma_{BBC}}{2\pi p_T} \frac{1}{N_{evt}\Delta p_T} \frac{N_e^{incl}}{\epsilon_{trigg}\epsilon_{accXeff}} \frac{1}{\epsilon_{bias}}, \quad (4.3)$$

where,

- $\sigma_{BBC}$  is the BBC trigger cross section.
- $\epsilon_{bias}$  is the fraction of electrons in the event that satisfies the BBC trigger and is termed as BBC trigger bias efficiency.
- $N_{evt}$  is the total number of events recorded by the BBC within z vertex cut of  $\pm 20$  c.m.
- $N_e^{incl}$  is the total number of electron counts recorded by PHENIX after applying all the electron identification criteria.
- $\epsilon_{trigg}$  is the electron trigger efficiency.
- $\epsilon_{accXeff}$  is the acceptance X efficiency correction.

The heavy flavor single electron invariant cross section can be obtained by subtracting the invariant cross section of the background single electron cocktail from eqn. 4.3. Comparing the right hand sides of eqn. 4.3 and the equation for invariant yield shown in eqn. 3.27, the only difference lies in the factors  $\sigma_{BBC}$  and  $\epsilon_{bias}$ , present in eqn. 4.3. Thus, just by multiplying the invariant yield of heavy flavor single electron by the factor  $\sigma_{BBC}/\epsilon_{bias}$  we can get the heavy flavor invariant cross section. The value of  $\sigma_{BBC}$  for  $d + Au$  collision as computed in PHENIX is 1920 mb and the  $\sigma_{BBC}$  value is 0.889. Thus scaling the heavy flavor single electron invariant yield of fig. 4.4, the heavy flavor single electron invariant cross section is obtained as shown in fig. 4.13 for minimum bias centrality. The systematic errors are shown in boxes around the central point and the vertical bars is the statistical error bars.

## 4.6 Comparison between data and FONLL calculation

The brief outline about FONLL calculation has already been given in section 1.2. Here the comparison of the invariant differential cross section of the single electron heavy flavor, obtained in section 4.5 is compared with the FONLL calculation [62]. The FONLL calculations, taken for comparison here, was done for  $p + p$  collision species. So the FONLL results is being scaled by the number of nucleons in deuterium multiplied by the number of nucleons in gold ions in order to make it at equal footing with the  $d + Au$  collision species. Fig. 4.15 shows the heavy flavor single electron invariant differential cross section calculated in this analysis (shown by data points). The curves are the FONLL calculation for the different decay channels of charm and bottom into single electron. The total invariant differential cross section from charm and bottom decaying into single electron is also shown along with the upper and lower limit of the FONLL calculation.

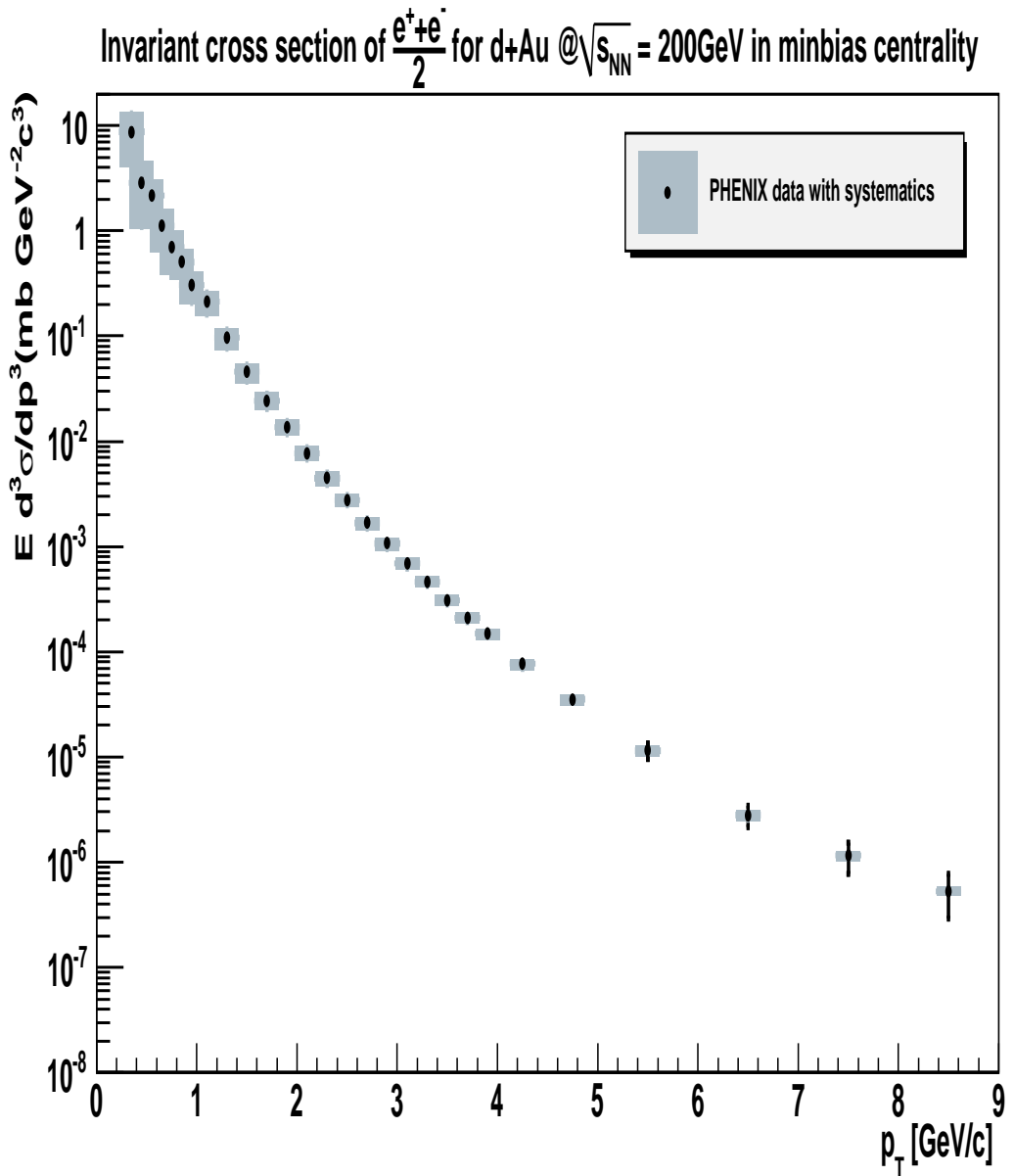


Figure 4.13: Heavy flavor invariant cross section for single electron in  $d + Au$  collisions at  $\sqrt{S_{NN}} = 200$  GeV in minimum bias centrality. The boxes are systematic error around the central value. The vertical bars are statistical error.

The data points are shown by red colour with the yellow colored bands as the systematic error in the measurement. The vertical bars are the statistical error in the measurement. In order to get clear picture of what's the extent of agreement between the single electron heavy flavor invariant differential cross section

obtained in this analysis with the FONLL result, the ratio of data points with the FONLL calculation is shown in Fig. 4.15. The upper and lower curves around the central curve shows the upper and lower limits of the uncertainty in FONLL calculation. Further the ratio of data and FONLL is fitted with polynomial of degree 0. The fit shows the value of 2.75. Considering the data/FONLL result in [96], it is to be noted that there is a difference of factor 1.7. So scaling the FONLL result for  $p + p$  by 1.7 in order to match by the PHENIX result of  $p + p$ , the data/FONLL ratio in this analysis should reduce to 1.6, which is consistent with the  $R_{dA}$  results obtained in section 4.2.

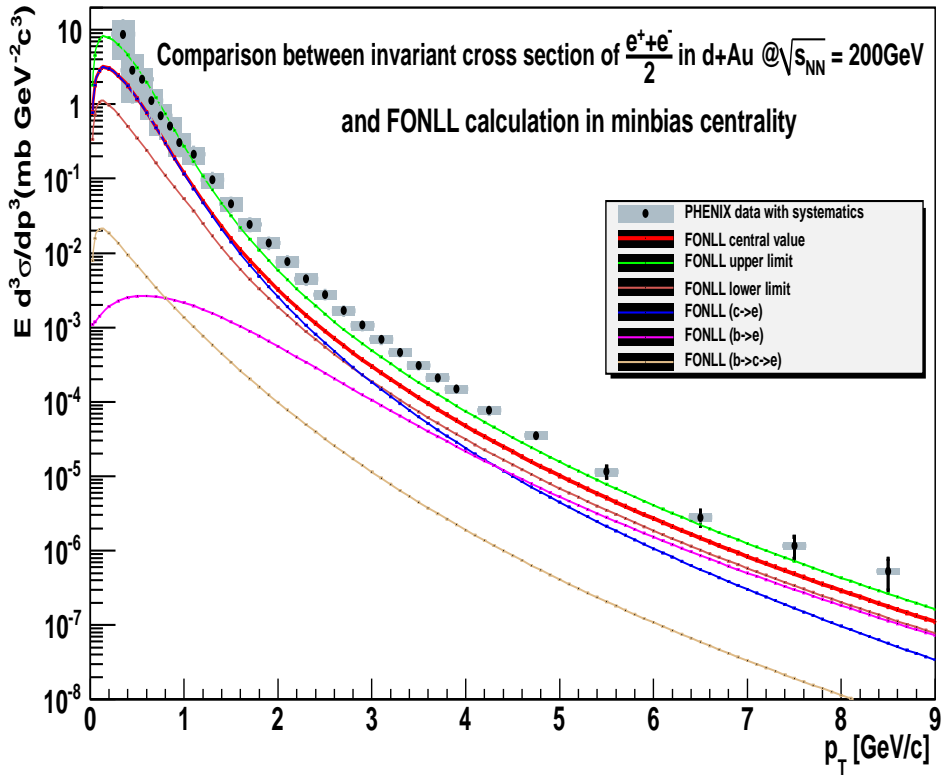


Figure 4.14: Comparison of heavy flavor invariant cross section for single electron in  $d + Au$  collisions at  $\sqrt{S_{NN}} = 200$  GeV obtained in this analysis with the FONLL prediction. The data points are obtained in this analysis and the different curves are the FONLL predictions for different decay channels of heavy flavors.

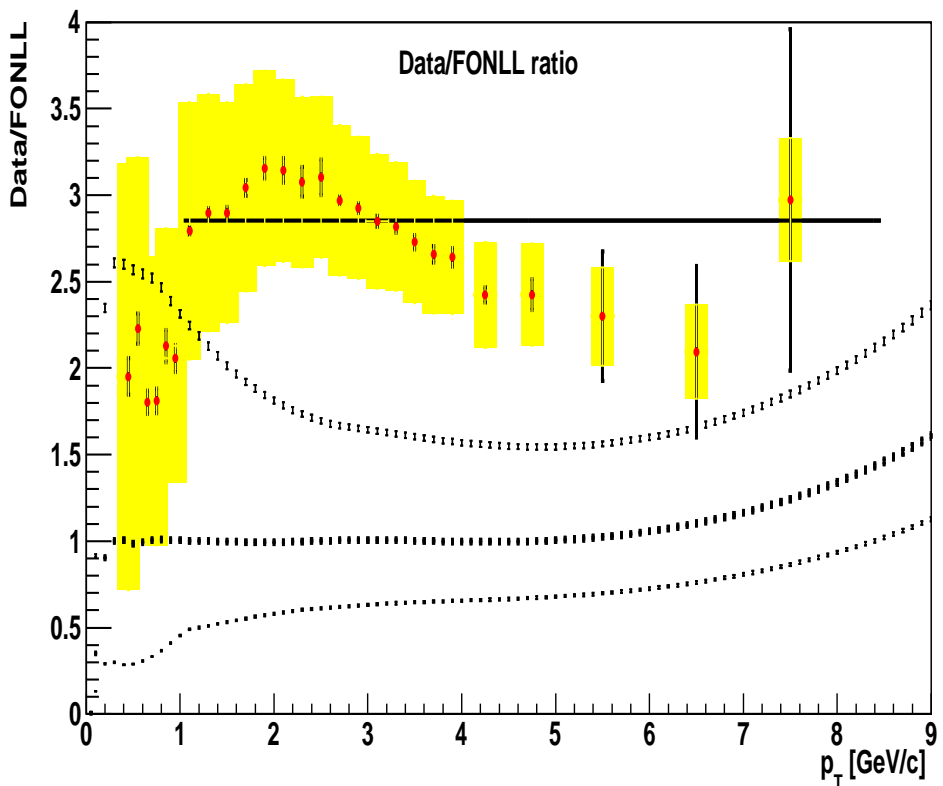


Figure 4.15: Data/FONLL calculation. The upper curve is the ratio of FONLL value upped by it's systematic with the FONLL central value. The lower curve is the ratio of FONLL value lowered by it's systematic with the FONLL central value. The upper and lower curve shows the upper and lower limits in the FONLL uncertainty band.

# Chapter 5

## Summary and Outlook

In this thesis I have presented the single electron invariant yield from heavy flavor for  $d + Au$  collisions at  $\sqrt{S_{NN}} = 200$  GeV. The invariant yield for the heavy flavor single electron is being extracted for different centrality and are further used for investigating the cold nuclear matter produced during the  $d + Au$  collision. The results derived from this analysis is important keeping in mind that the behaviour of cold nuclear matter is unknown. The cold nuclear matter is produced during the early stage of heavy ion collisions and is important for studying the evolution of the matter produced before the production of hot dense nuclear matter. Though the cold nuclear matter is present in  $Au + Au$  collision at  $\sqrt{S_{NN}} = 200$  GeV but hot dense matter produced in  $Au + Au$  collision suppresses the effect of cold nuclear matter and study of cold nuclear matter effects becomes impossible in  $Au + Au$  collision. Keeping this in mind the  $d + Au$  collision has been used which has the the collision species size between  $Au + Au$  and  $p + p$  and the colliding species are asymmetric.

The single electrons measured by the PHENIX detector has backgrounds from different photonic and non photonic sources as described in section 3.8.1. In order to extract the electrons coming from the heavy flavor these background electrons has to be subtracted. So calculation of the background single electron

cocktail was shown in section 3.8.1. Subtracting these calculated background electrons from the raw electrons provided the heavy flavor single electron invariant yield as shown in section 3.13.2. Another method as shown in section 3.11, called Converter method is used for extracting the heavy flavor single electron. This method also cross checks the results obtained by the cocktail subtraction method. The final heavy flavor single electron invariant yield consists of result obtained by Converter method and Cocktail subtraction method and is shown in Fig. 4.2.

The heavy flavor single electron invariant yield is then used for calculating the nuclear modification factor ( $R_{dA}$ ) of single electron from heavy flavor in  $d + Au$  collisions at  $\sqrt{S_{NN}} = 200$  GeV. The results obtained for the  $R_{dA}$  are shown in section 4.2. For most central collisions (0 – 20% centrality) enhancement in  $R_{dA}$  (Fig. 4.10) has been observed in mid  $p_T$  region. Calculations based on gluon saturation effect using the KKT model qualitatively shows the same effect [98]. In peripheral collision (60 – 88% centrality) enhancement in  $R_{dA}$  (Fig. 4.10) has also been seen though it is not pronounced like in most central collision. The  $Au + Au$  results [107] shows suppression in nuclear modification factor  $R_{AA}$  because of dense hot matter produced in  $Au + Au$  collision at  $\sqrt{S_{NN}} = 200$  GeV. The hot dense matter produced in  $Au + Au$  collision suppresses the cold nuclear matter produced in early stage of the collision and hence the enhancement effect is not seen here. Thus the  $R_{dA}$  results in this analysis is important in order to understand the cold nuclear matter effect and can be understood based on gluon saturation effect [98].

In order to entangle the cold nuclear matter in  $Au + Au$  collision, I tried to introduce a simple model by taking the ratio of  $R_{AA}$  and  $R_{dA}^2$ . This factor has been further calculated for light meson  $\pi^0$ . Fig. 4.12 shows the  $R_{AA}/R_{dA}^2$  for electrons from heavy flavor and for  $\pi^0$ . Both of them shows the same level of suppression which is a completely different behaviour as predicted based on suppression of gluon radiation from heavy quarks [109]. Gluon radiation suppression from heavy

quarks predicts that the suppression of heavy quarks will be less than the light quarks due to cold nuclear matter in hot nuclear medium.

The heavy flavor invariant differential cross section is also measured in this analysis and it has been compared with the FONLL [62] calculation for  $p + p$  as shown in section 1.2. The FONLL calculation for heavy flavor invariant differential cross section used here is for  $p + p$  collision species which has been scaled by proper factor in order to compare with the  $d + Au$  results shown here. The data/FONLL ratio shows that the nuclear modification factor obtained for  $d + Au$  using heavy flavor invariant yield is consistent with the ratio plot, provided the FONLL values here are scaled with the factor by which it differs from the PHENIX measurement of heavy flavor in  $p + p$  collision [96].

The present analysis don't have the means to separate the charm and bottom decays. The installation of Silicon Vertex Trackers (VTX) [110] provides the accurate measurement of the collision vertex as well as secondary vertex decay. The installation of VTX has been done during 2011. The installation of VTX will help to clearly distinguish the decays from charm and bottom in central arm of PHENIX. Thus the future measurement of heavy flavor will be of greatly improved quality as it will be possible to clearly distinguish between prompt decays and off-vertex decays of charmed and bottom meson.

# Bibliography

- [1] Donald H. Perkins, Introduction to High Energy Physics (Addison-Wesley), chap. History and Basic concepts, pp.26-29.
- [2] R. Nave, The Color Force, HyperPhysics. Georgia State University, Department of Physics and Astronomy, retrieved 26-4-2009.
- [3] F. Karsh, Lectures on Quark Matter (pringer, Berlin, Germany, 2002), vol. 583 of Lecture Notes in Physics, chap. Lattice QCD at high temperature and density, pp. 209-249, ISBN 978-3-540-43234-0.
- [4] M. Berenguer *et al.*, *The Role of quantum effects and nonequilibrium transport coefficients for relativistic heavy ion collisions*, J.Phys., G18, 655-679 (1992).
- [5] E. V. Shuryak, *Quark-gluon plasma and hadronic production of leptons, photons and psions*, Phys. Lett. **78B**, 150 (1978).
- [6] K. Kajantie and H. I. Miettinen, *Temperature measurement of quark-gluon plasma formed in high energy nucleus-nucleus collisions*, Z. Phys. C **9**, 341 (1981).
- [7] K. Geiger and J. I. Kapusta, *Dilepton radiation from cascading partons in ultrarelativistic nuclear collisions*, Phys. Rev. Lett. **70**, 1920 (1993).
- [8] E. Shuryak and L. Xiong, *Dilepton and photon production in the hot-glue scenario*, Phys. Rev. Lett. **70**, 2241 (1993).
- [9] B. Kampfer and O. P. Pavlenko, *Dilepton radiation from non-equilibrated parton matter produced in ultra-relativistic heavy-ion collisions*, Phys. Lett. B **289**, 127 (1992).
- [10] J. I. Kapusta, L. MacLerran, D. K. Srivastava, Phys. Lett. B **283**, 145 (1992).
- [11] T. Matsui and H. Satz, *J/ $\psi$  suppression by Quark-Gluon Plasma formation*, Phys. Lett. B **178**, 416 (1986).

- [12] R. Voigt, *J/ $\psi$  production and suppression*, Phys. Rep. **310**, 197 (1999).
- [13] B. Zhang, C. M. Ko, B. A. Li, Z. W. Lin and B. H. Sa, *J/ $\psi$  suppression in ultrarelativistic nuclear collisions*, Phys. Rev. C **62**, 054905 (2000).
- [14] B. Zhang, C. M. Ko, B. A. Li, Z. W. Lin and S. Pal, *J/ $\psi$  production in relativistic heavy ion collisions from a multi-phase transport model*, Phys. Rev. C **65**, 054909 (2002).
- [15] X. Zhao and R. Rapp, *Transverse Momentum Spectra of J/ $\psi$  in Heavy-Ion Collisions*, Phys. Lett. B **664**, 253 (2008).
- [16] L. Yan, P. Zhuang, and N. Xu, *J/ $\psi$  production in quark-gluon plasma*, Phys. Rev. Lett. **97**, 232301 (2006).
- [17] B. Alessandro *et al.* (NA50 Collaboration), *A New measurement of J/ $\psi$  suppression in Pb-Pb collisions at 158-GeV per nucleon*, Eur. Phys. J. C **39**, 335 (2005).
- [18] A. Adere *et al.* (PHENIX Collaboration), *J/ $\psi$  Production versus Centrality, Transverse Momentum, and Rapidity in Au+Au Collisions at  $\sqrt{s_{NN}} = 200\text{ GeV}$* , Phys. Rev. Lett. **98**, 232301 (2007).
- [19] A. Adere *et al.* (PHENIX Collaboration), *J/ $\psi$  suppression at forward rapidity in Au+Au collisions at  $\sqrt{s_{NN}} = 200\text{ GeV}$* , Phys. Rev. C **84**, 054912 (2011).
- [20] L. Grandchamp *et al.*, *In-Medium Effects on Charmonium Production in Heavy-Ion Collisions*, Phys. Rev. Lett. **92**, 212301 (2004).
- [21] A. Capella and E.G. Ferreiro, *J/ $\psi$  suppression at  $\sqrt{s} = 200\text{ GeV}$  in the comovers interaction model*, Eur. Phys. J. **C42**, 419 (2005).
- [22] M. Asakawa and T. Hatudsa, *J/ $\psi$  and  $\eta_c$  in the Deconfined Plasma from Lattice QCD*, Phys. Rev. Lett. **92**, 012001 (2004).
- [23] S. Datta, F. Karsch, P. Petreczky and I. Wetzorke, *Behavior of charmonium systems after deconfinement*, Phys. Rev. D **69**, 094507 (2004).
- [24] Shang-Yung Wang, D. Bayanovsky and Kin-Wang Ng, *Direct photons: a nonequilibrium signal of the expanding quark-gluon plasma*, arXiv:hep-ph/0101251v2 (2001).
- [25] S.S. Adler *et al.* (PHENIX Collaboration), *Measurement of Direct Photon Production in p+p Collisions at  $\sqrt{s} = 200\text{ GeV}$* , Phys. Rev. Lett. **98**, 012002 (2007).

- [26] S. Abachi *et al.* (D0 Collaboration), *The Isolated Photon Cross Section in the Central and Forward Rapidity Regions in p-pbar Collisions at  $\sqrt{s} = 1.8$  TeV*, Phys. Rev. Lett. **77**, 5011 (1996).
- [27] P. Koch, B. Muller and J. Rafelski, *Strangeness enhancement in central S + S collisions at 200 GeV/nucleon*, Phys. Rep. 142, 167 (1986).
- [28] J. Letessier, A. Tounsi, U. Heinz, J. Sollfrank and J. Rafelski, *Strangeness conservation in hot nuclear fireballs*, Phys. Rev. D **51**, 3408 (1995).
- [29] M. N. Asprouli, A. D. Panagiotou, *Strangeness as probe of quark-gluon plasma: Unconventional point of view*, Phys. Rev. C **51**, 1444 (1995).
- [30] C. P. Singh, *Signal for a quark-gluon plasma in the fragmentation region*, Phys. Lett. B **188**, 369 (1987).
- [31] C. P. Singh and S. Uddin, *Strangeness abundance as a signal for quark-gluon plasma*, Phys. Rev. D **41**, 870 (1990).
- [32] T. S. Biro, J. Zimanyi, *Quark-Gluon Plasma Formation in Heavy Ion Collisions and Quarkochemistry*, Nucl. Phys. A **395**, 525 (1983).
- [33] P. Koch, Prog. Nucl. Part. Phys. 26, 253 (1991).
- [34] Wong,C.Y.,Introduction to High Energy Heavy-Ion collisions, World Scientific, 1994.
- [35] Wong,C.Y.,Introduction to High Energy Heavy-Ion collisions, World Scientific, Chapter 2, pp.19 (1994).
- [36] K. Rajagopal, *Mapping the QCD Phase Diagram*, Nucl. Phys. A **661**, 150 (1999).
- [37] J. Peter *et al.*, *Phases of QCD: Summary of the Rutgers Long Range Plan Town Meeting*, arXiv:0705.1930 (2007).
- [38] F. Karsch, Progress of Theoretical Physics , 106 (2004).
- [39] F. Karsch, E. Laermann, and A. Peikert, *Quark mass and flavour dependence of the QCD phase transition*, Nuclear Physics B **605**, 579 (2001).
- [40] K. Adcox *et al.*, *Formation of dense partonic matter in relativistic nucleusnucleus collisions at RHIC: Experimental evaluation by the PHENIX Collaboration* (PHENIX Collaboration), Nuclear Physics A **757**, 184 (2005).

- [41] F. Karsch, *Lattice Results on QCD Thermodynamics*, Nucl. Phys. A **698**, 199 (2002).
- [42] W.K. Tung, Perturbative qcd and the parton structure of the nucleon, 2001.
- [43] R. Vogt, *The A Dependence of Open Charm and Bottom Production*, Int. J. Mod. Phys. E **12**, 211 (2003).
- [44] J. Adams *et al.* (STAR Collaboration), *Open Charm Yields in d+Au Collisions at  $\sqrt{s_{NN}} = 200 \text{ GeV}$* , Phys. Rev. Lett. **94**, 062301 (2005).
- [45] Y. Morino (PHENIX Collaboration), *Measurement of charm and bottom production in p + p collisions at  $\sqrt{s} = 200 \text{ GeV}$  at RHIC-PHENIX*, arXiv:0805.3871, 2008.
- [46] A. Adare *et al.* (PHENIX Collaboration), *Dilepton mass spectra in p+p collisions at  $\sqrt{s} = 200 \text{ GeV}$  and the contribution from open charm*, arXiv:0802.0050 (2008).
- [47] A. Ali and T. C. Yang, *Inclusive electron Spectrum in e+ e- Annihilation Near Charm Threshold*, Phys. Lett. **65B**, 275 (1976).
- [48] I. Hinchliffe and C. H. Llewellyn Smith, *Charm as a possible source of prompt leptons*, Nucl. Phys. B **114**, 45 (1976).
- [49] F. Bletzacker, H. T. Nieh and A. Soni, *Semileptonic decays of charmed mesons produced in electron-positron annihilation*, Phys. Rev. D **16**, 732 (1977).
- [50] W. J. Wilson, *Lepton Spectrum in the Semileptonic Weak Decays of Charmed Mesons*, Phys. Rev. D **16**, 742 (1977).
- [51] V. Barger, T. Gottschalk and R. J. N. Phillips, *Multi-Hadron Semileptonic Decays of Charmed Mesons*, Phys. Rev. D **16**, 746 (1977).
- [52] D. Fakirov and B. Stech, *F- and D-decays*, Nucl. Phys. **B133**, 315 (1978).
- [53] X. Y. Pham and J. M. Richard, *The decay  $D(1865) \rightarrow e \bar{\nu}_e K^*$  and the right-handed current*, Nucl. Phys. B **138**, 453 (1978).
- [54] K. Kudoh, *Sum Rules For The Four-Body Semileptonic Decays Of Charmed Mesons*, Prog. Theor. Phys. **60**, 1834 (1978).
- [55] M. Suzuki, *Gluon Correction To Semileptonic Decays Of Heavy Quarks*, Nucl. Phys. B **145**, 420 (1978).

- [56] N. Cabibo, G. Corbo and L. Maiani, *Lepton Spectrum in Semileptonic Charm Decay*, Nucl. Phys. B **155**, 93 (1979).
- [57] M. Gluck, *On The Free Parton Model For Weak Semileptonic Decays Of Charmed Particles*, Phys. Lett. **84B**, 459 (1979).
- [58] C. Amsler *et al.* (Particle Data Group), PL B **667**, 1(2008).
- [59] D. Drijard *et al.*, *Observation of charmed D meson production in pp collisions*, Phys Lett. B **81**, 250 (1979).
- [60] J. A. Appel *et al.*, *Observation of Direct Production of Leptons in p-Be Collisions at 300 GeV*, Phys. Rev. Lett. **33**, 722 (1974).
- [61] Yu. L. Dokshitzer and D. Kharzeev, *Heavy quark colorimetry of QCD matter*, Phys. Lett. B **519**, 199 (2001).
- [62] Matteo Cacciari, Paolo Nason and Ramona Vogt, *QCD predictions for charm and bottom production at RHIC*, Phys. Rev. Lett. **95**, 122001(2005).
- [63] P. Nason, S. Dawson, and R.K.Ellis, *The Total Cross-Section for the Production of Heavy Quarks in Hadronic Collisions*, Nucl. Phys. B **303**, 607 (1988).
- [64] P. Nason, S. Dawson, and R.K.Ellis, *The One Particle Inclusive Differential Cross-Section for Heavy Quark Production in Hadronic Collisions*, Nucl. Phys. B **327**, 49 (1989).
- [65] P. Nason, S. Dawson, and R.K.Ellis, Nucl. Phys. B **335**, 260(E) (1990).
- [66] W. Beenakker, W. L. van Neerven, R. Meng, G.A. Schuler and J. Smith, *QCD corrections to heavy quark production in hadron-hadron collisions*, Nucl. Phys. B **351**, 507 (1991).
- [67] M. Cacciari and M. Greco, *Large pt Hadroproduction of Heavy Quarks*, Nucl. Phys. B **421**, 530 (1994).
- [68] M. Allen *et al.* (PHENIX Collaboration), *PHENIX inner detectors*, Nucl.Instr. and Meth. A **499**, 549 (2003).
- [69] C. Adler *et al.*(PHENIX Collaboration), *The RHIC zero degree calorimeters*, Nucl. Instrum. Meth. A **470**, 488 (2001).
- [70] Schmalzle *et al.* , RHIC DX dipole magnet construction, Applied Superconductivity, IEE Transactions on, pp. 220 (2000)

- [71] E. Richardson *et al.*, *A reaction plane detector for PHENIX at RHIC*, Nuclear Instruments and Methods in Physics Research A636, 99 (2011)
- [72] A. M. Poskanzer and S. A. Voloshin, *Methods for analyzing anisotropic flow in relativistic nuclear collisions*, Phys. Rev. C **58**, 1671 (1998).
- [73] S. H. Aronson *et al.* (PHENIX Collaboration), *PHENIX magnet system*, Nucl. Instr. and Meth. A **499**, 480 (2003).
- [74] K. Adcox *et al.* (PHENIX Collaboration), *PHENIX central arm tracking detectors*, Nucl. Instr. and Meth. A **499**, 489 (2003).
- [75] Claus Grupen and Boris Shwartz, Particle Detectors, Cambridge University Press (2008), pp. 167, ISBN- 978-0-511-38866-8.
- [76] M. Aizawa *et al.* (PHENIX Collaboration), *PHENIX central arm particle ID detectors*, Nucl. Instr. and Meth. A **499**, 508 (2003).
- [77] D. J. Griffiths, Introduction to Electrodynamics, pp. 463-465.
- [78] S. Ichimaru, Basic Principles of Plasmas Physics: A Statistical Approach, p. 228.
- [79] J. H. Hubbell, Radiation Physics and Chemistry **75**, 614 (2006).
- [80] R. Nave, Relativity, HyperPhysics. Georgia State University, Department of Physics and Astronomy, retrieved 26-4-2009.
- [81] B. Rossi, High-Energy Particles, Prentice Hall Series (1965).
- [82] J.D. Jackson, Classical Electrodynamics, Wiley, New York (1975).
- [83] K. Kleinknecht, Detectors for particle radiation, Cambridge University Press (1998).
- [84] R.M. Barnett *et al.* (Particle Data Group), Review of particle properties, Phys. Rev. D **54**, 1 (1996).
- [85] L. Aphecetche *et al.* (PHENIX Collaboration), PHENIX calorimeter, Nucl. Instr. and Meth. A **499**, 521 (2003).
- [86] H. Akikawa *et al.*, Nuclear Instruments and Methods in Physics Research Section A: Accelerators, Spectrometers, Detectors and Associated Equipment , 537 (2003).
- [87] A. Kozlov *et al.*, *Development of a triple GEM UV-photon detector operated in pure CF<sub>4</sub> for the PHENIX experiment* , Nucl. Instr. Meth. A **523**, 345 (2004).

- [88] Z. Fraenkel *et al.*, *A hadron blind detector for the PHENIX experiment at RHIC*, Nucl. Instr. Meth. A **546**, 466 (2005).
- [89] G. David *et al.*, *Pattern recognition in the PHENIX PbSc electromagnetic calorimeter*, IEEE Trans. Nucl. Sci. **47**, 1982 (2000).
- [90] S. S. Adler *et al.* (PHENIX Collaboration), *Centrality dependence of charged hadron production in deuteron+gold and nucleon+gold collisions at  $\sqrt{s_{NN}} = 200 \text{ GeV}$* , Phys. Rev. C **77** (2008) 014905.
- [91] S. S. Adler *et al.* (PHENIX Collaboration), *Nuclear effects on hadron production in d+Au collisions at  $\sqrt{s_{NN}} = 200 \text{ GeV}$  revealed by comparison with p+p data*, Phys. Rev. C **74**, 024904 (2006).
- [92] S. S. Adler *et al.* (PHENIX Collaboration), *High transverse momentum  $\eta$  meson production in p+p, d+Au, and Au+Au collisions at  $\sqrt{s_{NN}} = 200 \text{ GeV}$* , Phys. Rev. C. **75**, 024909 (2007).
- [93] S. S. Adler *et al.* (PHENIX Collaboration), *Production of  $\omega$  mesons at large transverse momenta in p+p and d+Au collisions at  $\sqrt{s_{NN}} = 200 \text{ GeV}$* , Phys. Rev. C. **75**, 051902 (2007).
- [94] K. Adcox *et al.* (PHENIX Collaboration), *Measurement of Single Electrons and Implications for Charm Production in Au+Au Collisions at  $\sqrt{s_{NN}} = 130 \text{ GeV}$* , Phys. Rev. Lett. **88**, 192303 (2002).
- [95] Yasuyuki Akiba, Ralf Averbeck, Alan Dion, Fukutaro Kajihara (PHENIX Collaboration), *Run-4 Au+Au Single Electron Analysis Note*, PHENIX Internal Analysis Note **557**, 78 (2007).
- [96] A. Adare *et al.* (PHENIX Collaboration), *Measurement of High-pT Single Electrons from Heavy-Flavor Decays in p+p Collisions at  $\sqrt{s} = 200 \text{ GeV}$* , Phys. Rev. Lett. **97**, 252002 (2006).
- [97] A. Adare *et al.* (PHENIX Collaboration), *Measurement of Bottom Versus Charm as a Function of Transverse Momentum with Electron-Hadron Correlations in p+p Collisions at  $\sqrt{s} = 200 \text{ GeV}$* , Phys. Rev. Lett. **103**, 082002 (2009).
- [98] Y. L. Dokshitzer, D. E. Kharzeev, *Heavy quark colorimetry of QCD matter*, Phys. Lett. B **519**, 199 (2001).
- [99] D. Kharzeev and K. Tuchin, *Open charm production in heavy ion collisions and the Color Glass Condensate*, Nucl. Phys. A **735**, 248 (2004).
- [100] D. Kharzeev, E. Levin and L. McLerran, *Parton saturation and  $N_{part}$  scaling of semi-hard processes in QCD*, Phys. Lett. B **561**, 93 (2003).

- [101] D. Kharzeev, Y. V. Kovchegov and K. Tuchin, *Cronin effect and high- $p_T$  suppression in  $pA$  collisions. Abstract*, Phys. Rev. D **68**, 094013 (2003).
- [102] J. L. Albacete, N. Armesto, A. Kovner, C. A. Salgado and U. A. Wiedemann, *Energy Dependence of the Cronin Effect from Non-Linear QCD Evolution*, Phys. Rev. Lett. **92**, 082001 (2004).
- [103] F. Gelis and R. Venugopalan, *Large mass  $q\bar{q}$  production from the color glass condensate*, Phys. Rev. D **69**, 014019 (2004).
- [104] K. Tuchin, *Heavy quark production by a quasi-classical color field in proton-nucleus collisions*, Phys. Lett. B **593**, 66 (2004).
- [105] J. P. Blaizot, F. Gelis and R. Venugopalan, *High energy  $pA$  collisions in the color glass condensate approach II: quark pair production*, Nucl. Phys. A **743**, 57 (2004).
- [106] Y. V. Kovchegov and K. Tuchin, *Production of  $q\bar{q}$  pairs in proton-nucleus collisions at high energies*, Phys. Rev. D **74**, 054014 (2006).
- [107] A. Adere *et al.* (PHENIX Collaboration), *Energy Loss and Flow of Heavy Quarks in Au+Au Collisions at  $\sqrt{s} = 200$  GeV*, Phys. Rev. Lett. **98**, 172301 (2007).
- [108] S. S. Adler *et al.* (PHENIX Collaboration), *Centrality Dependence of Charm Production from Single Electrons in Au+Au Collisions at  $\sqrt{s} = 200$  GeV*, Phys. Rev. Lett. **94**, 082301 (2005).
- [109] Y. L. Dokshitzer and D.E. Kharzeev, *Heavy-quark colorimetry of QCD matter*, Phys. Lett. B **519**, 199 (2001).
- [110] J. M. Heuser (PHENIX), Vertex detector upgrade plans for the PHENIX experiment at RHIC, Nucl. Instr. Meth. A **511**, 210 (2003).

# Appendix A

## Kinematic Variables

The kinematic variables, introduced in heavy-ion collision experiments has simple properties under a change in reference frame making their use very convenient. The various kinematic variables usually used in heavy-ion collision experiments are discussed below.

### Light-Cone Variables

In high-energy reaction processes usually a detected particle originates from one of the colliding species. If  $c = (c_0, \mathbf{c}_T, c_z)$  is the four-momentum of detected particle (c) originating from beam particle (b) having four momentum represented by  $b = (b_0, \mathbf{b}_T, b_z)$ , then the quantity

$$c_+ = c_0 + c_z \quad (\text{A.1})$$

is called the *forward light-cone momentum* and the quantity

$$c_- = c_0 - c_z \quad (\text{A.2})$$

is called the *backward light-cone momentum* of the particle. Here  $c_0/b_0$  is the energy of the particle,  $\mathbf{c}_T/\mathbf{b}_T$  is the two dimensional transverse momentum in the plane perpendicular to the longitudinal axis and  $c_z/b_z$  is it's longitudinal momentum. Particles travelling along the beam direction (forward direction) the forward-light cone momentum  $c_+$  is larger compared to it's backward-light cone momentum and vice-versa. The forward light-cone momentum of any particle in one frame is related to the forward light-cone momentum of the same particle in another Lorentz boosted frame by a constant factor. Thus the ratio of forward light cone momentum of daughter particle to that of the beam particle is independent of Lorentz frame. This ratio is named as *forward light-cone variable*  $x_+$  of daughter particle relative to beam particle and is given by

$$x_+ = \frac{c_0 + c_z}{b_0 + b_z}. \quad (\text{A.3})$$

## Rapidity

The rapidity variable ( $y$ ) of a particle is a dimensionless quantity and is given in terms of the energy ( $E$ ) and longitudinal momentum ( $p_z$ ) of a particle as

$$y = \frac{1}{2} \ln \left( \frac{E + p_z}{E - p_z} \right). \quad (\text{A.4})$$

The rapidity variable can be both positive and negative. The rapidity is a convenient measurable variable under relativistic condition. For instance, under a Lorentz transformation, the rapidity  $y'$  of the particle in the moving frame is related to the rapidity  $y$  of the particle in rest frame by

$$y' = y - y_\beta \quad (\text{A.5})$$

where  $y_\beta$  can be called as rapidity of moving frame [35] and is given by

$$y_\beta = \frac{1}{2} \ln \left( \frac{1 + \beta}{1 - \beta} \right). \quad (\text{A.6})$$

## Pseudorapidity

In many experiments only angle of the detected particles is possible to measure. In such cases another variable called pseudorapidity ( $\eta$ ) has been introduced which is given by

$$\eta = -\ln[\tan(\theta/2)], \quad (\text{A.7})$$

where  $\theta$  is the angle between particle momentum ( $p$ ) and the beam direction. In terms of momentum the pseudorapidity can be expressed as

$$\eta = \frac{1}{2} \ln \left( \frac{|p| + p_z}{|p| - p_z} \right) \quad (\text{A.8})$$

Comparing equations A.8 and A.4 it is seen that under the condition large momentum, i.e.  $|p| \sim E$ , the  $\eta \sim y$ .

# Appendix B

## Collision geometry in heavy ion collision

Heavy ion collision geometry is defined by **impact parameter (b)**. It can be defined as the distance between the center of two colliding ion species giving us the information of overlapped region of ions colliding with each other. Fig. B.1 shows the schematic view of two ions about to collide and the impact parameter of the colliding ions. Depending on the value of this impact parameter, collision centrality is determined. For  $b \sim 0$  both the colliding species overlap almost completely with each other and this is known as **most central collision**. For  $b \sim R$ , where  $R$  being the radius of the colliding ions, the impact parameter is larger and this condition is known as **peripheral collision**.

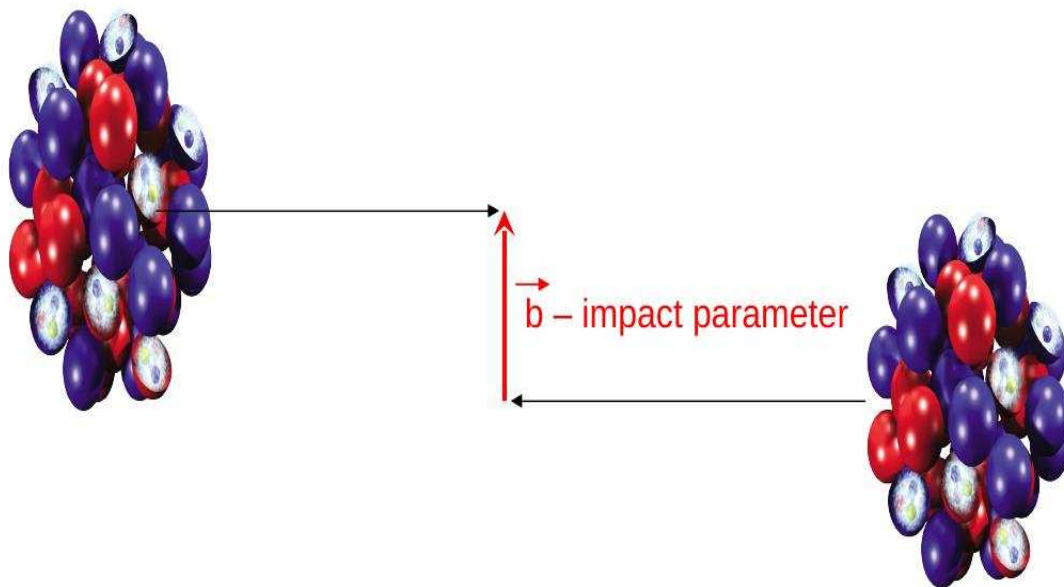


Figure B.1: Impact parameter.

## List of Publications

1. *Measurement of semi-electronic decay of heavy flavor mesons in d+Au collision at RHIC using PHENIX detector*, Sourav Tarafdar, Prashanta Kumar Khandai, Venktesh Singh, Nuclear Physics A **862-863**, 304 (2011).
2. *Nuclear modification factors of  $\phi$  mesons in d+Au, Cu+Cu, and Au+Au collisions at  $\sqrt{s_{NN}} = 200 \text{ GeV}$* , A. Adare....S.Tarafdar *et al.* (PHENIX Collaboration), Phys. Rev. C **83**, 024909 (2011).
3. *Cold Nuclear Matter Effects on  $J/\psi$  Yields as a Function of Rapidity and Nuclear Geometry in d+A Collisions at  $\sqrt{s_{NN}} = 200 \text{ GeV}$* , A. Adare....S.Tarafdar *et al.* (PHENIX Collaboration), Phys. Rev. Lett. **8107**, 142301 (2011).
4. *Measurements of Higher Order Flow Harmonics in Au+Au Collisions at  $\sqrt{s_{NN}} = 200 \text{ GeV}$* , A. Adare....S.Tarafdar *et al.* (PHENIX Collaboration), Phys. Rev. Lett. **107**, 252301 (2011).
5.  *$J/\psi$  suppression at forward rapidity in Au + Au collisions at  $\sqrt{s_{NN}} = 200 \text{ GeV}$* , A. Adare....S.Tarafdar *et al.* (PHENIX Collaboration), Phys. Rev. C **84**, 054912 (2011).
6. *Suppression of Back-to-Back Hadron Pairs at Forward Rapidity in d+Au Collisions at  $\sqrt{s_{NN}} = 200 \text{ GeV}$* , A. Adare....S.Tarafdar *et al.* (PHENIX Collaboration), Phys. Rev. Lett. **107**, 172301 (2011).
7. *Production of  $\omega$  mesons in p+p, d+Au, Cu+Cu, and Au+Au collisions at  $\sqrt{s_{NN}} = 200 \text{ GeV}$* , A. Adare....S.Tarafdar *et al.* (PHENIX Collaboration), Phys. Rev. C **84**, 044902 (2011) Published October 7, (2011).
8. *Suppression of away-side jet fragments with respect to the reaction plane in Au + Au collisions at  $\sqrt{s_{NN}} = 200 \text{ GeV}$* , A. Adare....S.Tarafdar *et al.* (PHENIX Collaboration), Phys. Rev. C **84**, 024904 (2011).
9. *Azimuthal correlations of electrons from heavy-flavor decay with hadrons in p+p and Au+Au collisions at  $\sqrt{s_{NN}} = 200 \text{ GeV}$* , A. Adare....S.Tarafdar *et al.* (PHENIX Collaboration), Phys. Rev. C **83**, 044912 (2011).

- 10.** *Cross Section and Parity-Violating Spin Asymmetries of  $W^\pm$  Boson Production in Polarized  $p+p$  Collisions at  $\sqrt{s_{NN}} = 500\text{GeV}$ , A. Adare....**S.Tarafdar** *et al.* (PHENIX Collaboration), Phys. Rev. Lett. **106**, 062001 (2011).*
- 11.** *Measurement of transverse single-spin asymmetries for  $J/\psi$  production in polarized  $p+p$  collisions at  $\sqrt{s_{NN}} = 200\text{GeV}$ , A. Adare....**S.Tarafdar** *et al.* (PHENIX Collaboration), Phys. Rev. D **82**, 112008 (2010).*
- 12.** *Azimuthal Anisotropy of  $\pi^0$  Production in  $Au+Au$  Collisions at  $\sqrt{s_{NN}} = 200\text{GeV}$ : Path-Length Dependence of Jet Quenching and the Role of Initial Geometry, A. Adare....**S.Tarafdar** *et al.* (PHENIX Collaboration), Phys. Rev. Lett. **105**, 142301 (2010).*
- 13.** *Elliptic and Hexadecapole Flow of Charged Hadrons in  $Au+Au$  Collisions at  $\sqrt{s_{NN}} = 200\text{GeV}$ , A. Adare....**S.Tarafdar** *et al.* (PHENIX Collaboration), Phys. Rev. Lett. **105**, 062301 (2010).*
- 14.** *Transverse momentum dependence of  $\eta$  meson suppression in  $Au+Au$  collisions at  $\sqrt{s_{NN}} = 200\text{GeV}$ , A. Adare....**S.Tarafdar** *et al.* (PHENIX Collaboration), Phys. Rev. C **82**, 011902 (2010).*
- 15.** *Transition in Yield and Azimuthal Shape Modification in Dihadron Correlations in Relativistic Heavy Ion Collisions, A. Adare....**S.Tarafdar** *et al.* (PHENIX Collaboration), Phys. Rev. Lett. **104**, 252301 (2010).*

## Symposium papers

- 1.** *Strategy of data analysis for Probing Quark Gluon Plasma with leptonic observable with PHENIX detector at RHIC, **S.Tarafdar**, B.K.Singh and V.Singh, Proceedings of the DAE Symp on Nucl. Phys. **52**, 545 (2007).*
- 2.** *Contribution of background from HBD component through conversion pair production, **S. Tarafdar**, B. K. Singh and V. Singh, Proceeding of the DAE Symp on High Energy Phys. **18**, 47 (2008).*

- 3.** *Study of minimum time, suitable position of inlet and outlet for uniform gas distribution inside the Resistive Plate Chamber (RPC) Detector*, **S.Tarafdar**, P. K. Khandai, L. Singh, A. K. Soma and V. Singh, Proceeding of the DAE Symp on High Energy Phys. **18**, 59 (2008).
- 4.** *Study of conversion pair production inside the Hadron Blind Detector*, **S. Tarafdar** and V. Singh, Proceeding of the DAE Symp on Nucl Phys. **53**, 771 (2008).